

Springer Theses

Recognizing Outstanding Ph.D. Research

Hong-Xin Zhang

Stellar Disk Evolution and Gaseous Disk Turbulence of Dwarf Irregular Galaxies



Springer

Springer Theses

Recognizing Outstanding Ph.D. Research

Aims and Scope

The series “Springer Theses” brings together a selection of the very best Ph.D. theses from around the world and across the physical sciences. Nominated and endorsed by two recognized specialists, each published volume has been selected for its scientific excellence and the high impact of its contents for the pertinent field of research. For greater accessibility to non-specialists, the published versions include an extended introduction, as well as a foreword by the student’s supervisor explaining the special relevance of the work for the field. As a whole, the series will provide a valuable resource both for newcomers to the research fields described, and for other scientists seeking detailed background information on special questions. Finally, it provides an accredited documentation of the valuable contributions made by today’s younger generation of scientists.

Theses are accepted into the series by invited nomination only and must fulfill all of the following criteria

- They must be written in good English.
- The topic should fall within the confines of Chemistry, Physics, Earth Sciences, Engineering and related interdisciplinary fields such as Materials, Nanoscience, Chemical Engineering, Complex Systems and Biophysics.
- The work reported in the thesis must represent a significant scientific advance.
- If the thesis includes previously published material, permission to reproduce this must be gained from the respective copyright holder.
- They must have been examined and passed during the 12 months prior to nomination.
- Each thesis should include a foreword by the supervisor outlining the significance of its content.
- The theses should have a clearly defined structure including an introduction accessible to scientists not expert in that particular field.

More information about this series at <http://www.springer.com/series/8790>

Hong-Xin Zhang

Stellar Disk Evolution and Gaseous Disk Turbulence of Dwarf Irregular Galaxies

Doctoral Thesis accepted by
University of Chinese Academy of Sciences, Beijing, China

 Springer

Author

Dr. Hong-Xin Zhang
Facultad de Física, Instituto de Astrofísica
Pontificia Universidad Católica de Chile
Santiago
Chile

Supervisors

Dr. Yu Gao
Purple Mountain Observatory
Nanjing, Jiangsu
China

Dr. Deidre Hunter
Lowell Observatory
Flagstaff, AZ
USA

ISSN 2190-5053

Springer Theses

ISBN 978-3-662-52865-5

DOI 10.1007/978-3-662-52867-9

ISSN 2190-5061 (electronic)

ISBN 978-3-662-52867-9 (eBook)

Library of Congress Control Number: 2016947487

© Springer-Verlag Berlin Heidelberg 2016

This work is subject to copyright. All rights are reserved by the Publisher, whether the whole or part of the material is concerned, specifically the rights of translation, reprinting, reuse of illustrations, recitation, broadcasting, reproduction on microfilms or in any other physical way, and transmission or information storage and retrieval, electronic adaptation, computer software, or by similar or dissimilar methodology now known or hereafter developed.

The use of general descriptive names, registered names, trademarks, service marks, etc. in this publication does not imply, even in the absence of a specific statement, that such names are exempt from the relevant protective laws and regulations and therefore free for general use.

The publisher, the authors and the editors are safe to assume that the advice and information in this book are believed to be true and accurate at the date of publication. Neither the publisher nor the authors or the editors give a warranty, express or implied, with respect to the material contained herein or for any errors or omissions that may have been made.

Printed on acid-free paper

This Springer imprint is published by Springer Nature
The registered company is Springer-Verlag GmbH Berlin Heidelberg

Supervisor's Foreword I

Time really flies. I cannot believe that it has been 4 years already since Dr. Hong-Xin Zhang's Ph.D. thesis defense in late May 2012. I am very pleased to have bright students like Hong-Xin who got the first Ph.D. degree under my supervision among my first Ph.D. students. With two more Ph.D. candidates planning to defend their theses later this year, becoming the 4th and 5th Ph.D. students with Ph.D. degrees under (co-)supervision of mine, I am so glad to know that Hong-Xin and the Springer are finally getting ready for this monograph of Hong-Xin's Ph.D. thesis. It is indeed the time for me to take this opportunity to reflect upon a bit while writing this forward for Hong-Xin's thesis. And I am grateful to Dr. Jian Li of the Springer for his help and efforts as well.

Prior to September 2009, Hong-Xin had already begun part of his Ph.D. thesis research and acquired the needed qualifications to carry out scientific research in astronomy. I have been his supervisor for more than 3 years since he joined my research group as a graduate student. Hong-Xin came to Purple Mountain Observatory (PMO) in Nanjing in 2006 from physics background and did quite well in all his astronomy course studies. By early fall 2009, he had gained a solid background in physics and mathematics and a good knowledge of various fields of astronomy. Before then he was already involved with the reduction and analysis of multiwavelength imaging data, and learned the stellar population synthesis technique among other things. For example, we worked on the multiband imaging data in the famous Antennae galaxies in tracking the star formation (SF) history, and Hong-Xin successfully gave a concise talk at the "Starburst-AGN Connection" international conference held in Shanghai in October 2008.

I think it was Hong-Xin's familiarity with the reduction and analysis of multi-wavelength imaging data through his hard working as well as his understanding and mastering of the stellar population synthesis technique, which is very useful in the study of multiband data in tracking SF history in galaxies, and that distinguished him as an outstanding candidate to obtain the Lowell Predoctoral Fellowship. The work about the Antennae galaxies with Hong-Xin as the first author was later submitted for publication and accepted before he started the predoctoral fellowship

at Flagstaff, AZ USA in the fall 2009 (Zhang et al. 2010, MNRAS). Hong-Xin showed great intelligence and diligence in this work. Independent thinking is his most prominent characteristics. He was also interested in the SF phenomena in very low density environments, e.g., XUV-disks, which is very relevant to the dwarf galaxies studied by the LITTLE THINGS project at Flagstaff. Besides these works, Hong-Xin was always attempting to probe the spatially resolved dust extinction of galaxies from multiband observations of stellar emission (far-UV to near-IR). Dust extinction in star-forming galaxies is a fundamentally important, yet a poorly understood problem in astrophysics. And all these preparations helped Hong-Xin gain success in his proposed thesis studies and his thesis research work at Lowell Observatory. And he had developed a quite nice research proposal with Dr. Deidre Hunter and me while working on finalizing the work on the Antennae galaxies. Most importantly, Hong-Xin found his lover during this period and married her before going to Flagstaff to start his thesis research studies.

Hong-Xin was also the only student of mine who could remember to write up at least half-year progress reports of their studies about SF in galaxies. And he continued to do so while he was at Lowell. Hong-Xin had the willingness and abilities to take an active role in a large research project, such as the LITTLE THINGS, under the leadership of Dr. Hunter. The other parts of Hong-Xin's Ph.D. thesis studies at Lowell focused on the understanding of the stellar disk-building process of nearby dwarf irregular galaxies by utilizing the excellent database of the LITTLE THINGS survey project. Hong-Xin's thesis work can be broadly divided into two parts, and Deidre's forward should explain these in depth since I was only involved in the first one, as follows:

- (1) Probing the stellar disk-building process of dwarf irregular galaxies by studying the radial variations of recent SF histories of a representative sample of nearby dwarf irregular galaxies. Zhang et al. (2012, AJ) developed a novel spectral energy distribution modeling code to interpret the multiwavelength data available for the LITTLE THINGS galaxies. The results suggest that the majority of dwarf irregular galaxies have been experiencing an outside-in shrinking of their star-forming disks, which is in contrast to the classical "inside-out" disk growth scenario suggested for luminous spiral galaxies. Although the outside-in quenching trend was suggested for a few dwarf irregular galaxies before, it is for the first time that the "outside-in" scenario is established for a relatively large sample of dwarf irregular galaxies.
- (2) Besides the stellar population analysis, Hong-Xin already got himself familiar with the reduction and analysis of the VLA HI-line emission data. He had been investigating the radial variations of the Fourier transform power spectra of HI gas distribution and stellar emission for a subsample of face-on LITTLE THINGS dwarf galaxies. Previous observations suggest that the SF density exhibits very weak correlation with the HI gas surface density in dwarf

galaxies, even though gas is the raw material for SF. By deriving the power spectra, the study of how SF, stellar mass, and gas are related to each other on different physical scales and as a function of galactocentric radius can be performed. Therefore, a better understanding of the relationship between the gas disk and the stellar disk can be achieved through this study.

Hong-Xin presented a nice talk at IAUS 284 in 2011 for the first part of his thesis work. In fact, we had our PMO research group reunion at Preston, UK during this conference with presence of four students of mine. After Hong-Xin's thesis defense in China, he went back to Flagstaff to plan on moving his family back in China. I was so glad to host his family visit to Los Angeles and our place in Thousand Oaks, CA on their way coming back China in early fall 2012. Particularly, his son was already running around then and had lots of fun visiting LA (another achievement of Hong-Xin at Lowell besides Ph.D. thesis). Hong-Xin was recently awarded with the excellent thesis of Chinese Academy of Sciences in 2013.

Since Hong-Xin has continued to have done a lot of excellent work, I would also like to briefly mention what I know of his most recent work after this Ph.D. thesis. Hong-Xin's first postdoctoral research was on working with the Next Generation Virgo Survey (NGVS) data. In one word, he has been focusing on working toward the understanding of what is a ultra-compact dwarf (UCD) galaxy? Specifically, he identified compact sources, either globular clusters (GC) or UCDs, belonging to the Virgo cluster from a multifiber spectroscopic survey with the 2dF/AAT instrument. Hong-Xin had reduced the spectra, compiled a clean catalog of GCs/UCDs, analyzed the kinematics of UCDs around the cD galaxy M87 in center of the Virgo cluster. He also needed to do some SED modeling of the newly identified UCDs/GCs in order to obtain their mass/age/metallicities. He was also trying to do stacking of NGVS images of all known Virgo UCDs (~ 130) to study the radial profiles of UCDs as well as further planning to cross-match the NGVS ugrizK photometry with GALEX F/NUV data to construct SEDs of UCDs from FUV to Ks. And then the SEDs of UCDs can be compared with that of GCs. Hong-Xin also leads several observing campaigns to do high-resolution multiobject spectroscopic observations of identified UCDs in order to study the internal dynamics of UCDs. And he was planning to select/study the GCs in late-type galaxies in order to investigate how the environment is related to the richness of GCs in different types of galaxies. If indeed late-type dwarf galaxies have fewer or more GCs than dEs, then it would strongly argue against the scenario that dEs were environmentally transformed from late-type dwarfs.

Considering his ample knowledge, background and research experiences, Hong-Xin should be an excellent young fellow, particularly in the studies of SF in galaxies, gas and star clusters. For this NGVS project, Hong-Xin has been actively working on with Prof. Eric Peng since the fall in 2012 and has done so much work

already. In conclusion, Dr. Hong-Xin Zhang is well motivated in various aspects of studies about SF in galaxies and has the willingness and abilities to take an active role in large research projects, such as demonstrated by his role in the LITTLE THINGS and NGVS projects. Therefore, I am fully supportive of his endeavor and have no reservation in writing him this forward for his Ph.D. thesis to share my joy of having worked with him over the previous years.

Nanjing, Jiangsu, China
June 2016

Dr. Yu Gao

Supervisor's Foreword II

Galaxies are the primary bodies in which the evolution of the universe takes place; gas is turned into stars, which evolve and die, and new stars are born. The attention of theorists, who are trying to explain how galaxies make new stars, is primarily on giant spiral galaxies. However, another class of galaxies, dwarf irregular galaxies, the tiniest but most numerous galaxies in the universe, challenge their models of SF and galaxy evolution. These tiny galaxies form new stars under conditions where the models say no SF should take place. Furthermore, stars have been traced far from the centers of galaxies, and no model explains how such extended stellar disks are produced and maintained.

Dr. Hong-Xin Zhang came to Lowell Observatory in 2009 to work with me on the SF histories of the LITTLE THINGS dwarf irregular galaxies. LITTLE THINGS is a multiwavelength project aimed at determining the drivers for SF in dwarf galaxies. The data include wavelengths from the far-ultraviolet to the near-IR, but the core of the project is radio interferometric HI-line data on 41 dwarf galaxies in three configurations of the VLA. Dr. Zhang contributed to the team effort by calibrating and mapping the HI data of several of the LITTLE THINGS galaxies, collected the ultraviolet *GALEX* and *Spitzer* data, and performed surface photometry. He has been a very valuable member of the LITTLE THINGS team.

For the first part of his Ph.D. dissertation, Dr. Zhang used stellar population fitting of broad-band colors to determine the stellar mass profiles and SF histories of the LITTLE THINGS dwarfs. Dr. Zhang developed the spectral-energy-distribution fitting code that he used, paying very careful attention to a large array of issues from different flavors of filter types, reddening, weighting, uncertainties, and biases. Dr. Zhang applied his SED-fitting program to the azimuthally averaged surface photometry of the LITTLE THINGS dwarfs and determined the stellar mass surface density profiles and broad SF histories as a function of radius. Dr. Zhang was particularly interested in determining the underlying cause of the correlation between the current SF and the older stars. But Dr. Zhang discovered that his work has important implications on the issue of disk assembly. In fact, his first paper has a remarkable and unexpected result: dwarf

galaxy disks are shrinking from the *outside-in*, in contrast to the current paradigm of *inside-out* disk growth in spirals.

For the next part of his dissertation, Dr. Zhang chose to look at structures in the LITTLE THINGS galaxies through Fourier transform power spectra. In his characteristic fearless fashion, Dr. Zhang built on forefront analysis techniques in the literature to develop a two-dimensional protocol and analyze structures as a function of radius in galaxies. He applied this to HI data cubes of the LITTLE THINGS galaxies to put limits on turbulence in the gas and its relationship to SF. He also discovered evidence that low luminosity dwarfs are more three-dimensional in nature. That paper, another fundamental result, formed the second part of his Ph.D. dissertation.

Finally, Dr. Zhang used his SED-fitting technique to measure the masses and ages of stellar clumps in a sample of LITTLE THINGS Blue Compact Dwarfs, systems that have become centrally concentrated and are believed to have undergone a burst of SF. That work, with Dr. Bruce Elmegreen, showed that torques can cause these clumps to spiral into the center on a time scale of 1 Gyr. This work helps us understand how the central concentration of stars and gas can grow and feed a long-lived starburst. Furthermore, this could be similar to the process that builds bulges in spiral galaxies.

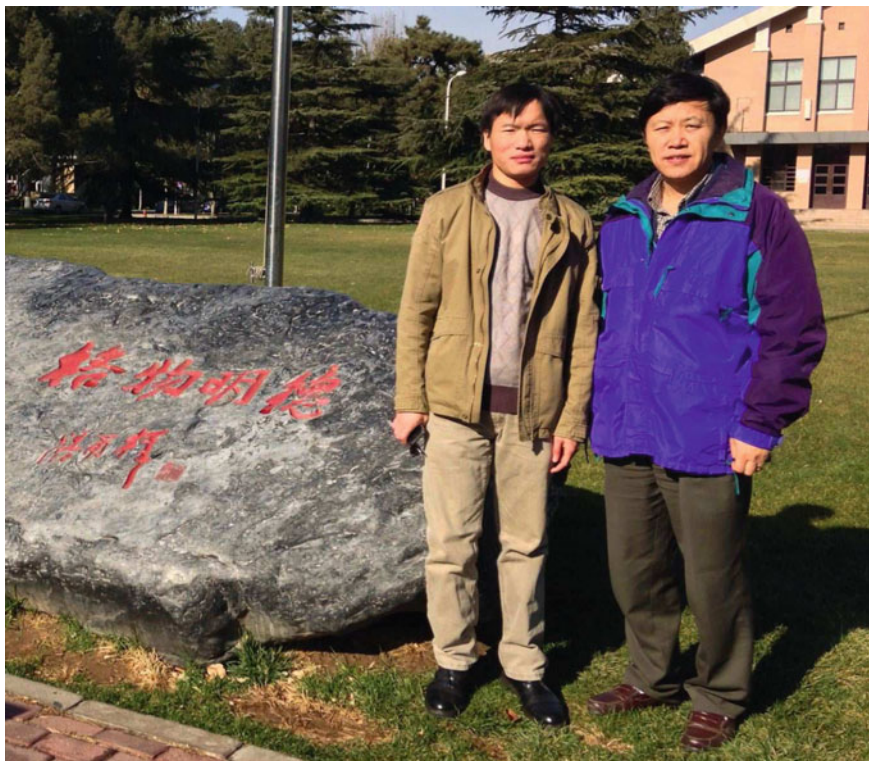
Dwarf irregular galaxies stress models of SF and galaxy evolution, and constraints produced by observations of these little galaxies will make the models more robust and inclusive. Altogether, Dr. Zhang's Ph.D. dissertation yielded basic and very significant contributions to our understanding of the structure and evolution of dwarf irregular galaxies and, hence, to galaxy evolution in general.

Flagstaff, AZ, USA
May 2016

Dr. Deidre Hunter



Photograph of some members of the Purple Mountain Observatory's Star Formation In Galaxies group, taken in the UK during the IAU Symposium #284 (September, 2011) on The Spectral Energy Distribution of Galaxies. From *left to right*, Zhiyu Zhang, Lijie Liu, Yu Gao, Qinghua Tan, Man I Lam, Hong-Xin Zhang



Photograph of Hong-Xin Zhang (*left*) and his thesis advisor Yu Gao (*right*), taken after the award ceremony of 2013 Excellent Ph.D. Thesis of Chinese Academy of Sciences in November 2013



Photograph taken at Flagstaff/US in July 2012. From *left to right*, Hong-Xin Zhang (the author), Jing-Xia Zhang (the author's wife), Kevin Zhang (the author's son), Deidre Hunter (the author's thesis advisor)

Acknowledgments

First and foremost, I would like to show my sincerest gratitude to my supervisors Dr. Yu Gao and Dr. Deidre Hunter. I entered into the fascinating world of astronomy through Dr. Yu Gao, and it is my honor to be among his first few Ph.D. students. Dr. Yu Gao is a world-renowned expert on star formation in galaxies. He was the one who led me to the field of population synthesis, which is a key technique used in my thesis work. His deep knowledge and his insightful guidance have been and will continue to be of great value for my astronomical life. I consider myself very fortunate for being able to work with Dr. Deidre Hunter. Deidre has been working on multiwavelength studies of nearby dwarf galaxies for more than 30 years, and she is among the world-leading researchers on observational studies of dwarf galaxies. Deidre is a very considerate, patient, supportive guider. I will never forget the numerous moments that she patiently taught and guided me when we did observing together. I learned from her the way to do research. Without her encouragements and enlightening guidance, I would have not finished my thesis work. I am also deeply grateful to Dr. Bruce Elmegreen. His numerous enlightening suggestions have been of great value to my thesis work. Collaborating with Bruce has been a very enjoyable experience, from which I gained a lot. I am fascinated by his in-depth thoughts on various astrophysical problems. I am much indebted to Dr. Xu Kong. He put a lot of time and effort into my first academic paper. His rigorous research attitude is infectious, and I have benefited a lot from his insightful knowledge on population analysis.

I am thankful to many of my colleagues at Purple Mountain Observatory (Ying-He Zhao, Xian-Zhong Zheng, Jun-Zhi, Wang, Hong-Jun Ma, Zhi-Yu Zhang, Fan Liu, Yan Sun, Li-Yun Zhang, Min Fang, Qing-Hua Tan, Jing-Bo Wang, Yuan Wang, Zhang-Zheng Wen, Li-Jie Liu et al.) and Lowell Observatory (Kimberly Herrmann, Megan Johnson, Dagmara Oszkiewicz, Simon Porter, Christopher Crockett, Lisa Prato, Will Grundy, Ted Bowell, Robin Melena, Brian Skiff, Brian Taylor, Phil Massey, Padraig Houlahan, Len Bright, Wes Lockwood, Lauren Amundson, Melinda Linzey, Jeff Hall, Larry Wasserman et al.) for providing me a stimulating and fun environment in which to learn and grow. I owe many thanks to

my brothers and sisters in office #619 of Purple Mountain Observatory. They made my study time enjoyable in the first 4 years of graduate study. I am very grateful to Dr. Ying-He Zhao who read very carefully my first paper draft and gave me a lot of extremely helpful suggestions and comments. Dr. Ying-He Zhao is a decent, prolific astronomer, and my helpful friend. I am also thankful to Prof. Xian-Zhong Zheng who gave me a lot of very useful suggestions on my work, and there is no doubt that I have been significantly inspired by his contagious enthusiasm for research. It is difficult to overstate my gratitude to Hong-Jun Ma for her help. She always remains pleasant, optimistic, and prepared for helping others. I would like to express my sincere thanks to Zhi-Yu Zhang, Jun-Zhi Wang, and Fan Liu. We had lots of happy and fun time together. I can say without exaggeration that the three of them were indispensable during the few years of my graduate study. I am very grateful to Dr. Kimberly Herrmann for her numerous help and for the happy time we spent together. I will never forget the happy time we had together in Sedona, Germany, Socorro, Grand Falls, Petrified Forest, etc. I also benefited a lot from her comments and suggestions on my paper and telescope proposals. I thank Dr. Megan Johnson very much for the much happy time we spent together. I thank Brian Taylor for many helpful discussions about observing with the MIMIR instrument on the Lowell 72-inch telescope. I appreciate Len Bright, Wes Lockwood, and Brian Skiff for their kindness and offering me rides to the 72-inch telescope for my observing runs. I am grateful to Robin Melena for helping me with many important paperworks. I thank Simon Porter for many happy and helpful conversions.

I must express deep gratitude to my family for all their love and encouragement. I am grateful to my parents who raised me with love and always support me in all my pursuits. I am also grateful to my two sisters who have been taking on my duty to take care of our parents. I am also much obliged to my wife Jing-Xia for her persistent love, understanding, and support. Jing-Xia has been taking nearly all the jobs on taking care of our precious son. She is a perfect wife and mother. Lastly, I thank my precious son Kevin whose arrival brought enjoyable change to my life. I dedicate this dissertation to all of my family members.

For this dissertation I would like to thank my thesis defense committee members: Prof. Houjun Mo (University of Massachusetts), Prof. Xue-Bing Wu (Peking University), Prof. Qiusheng Gu (Nanjing University), Prof. Xu Kong (University of Science and Technology of China), and Prof. Eric Peng (Peking University) for their time and extremely helpful comments.

Lastly, I thank very much the *Springer Theses* for offering an opportunity to publish this thesis work.

Contents

1	An Introduction to Disk Evolution of Dwarf Galaxies	1
1.1	Dwarf Irregular Galaxies	1
1.2	Star Formation in Dwarf Irregular Galaxies	4
1.3	Star Formation Histories of Dwarf Irregular Galaxies	5
1.3.1	The Technique: Evolutionary Population Synthesis	6
1.4	Evolution of Galactic Disk: Spirals Versus dIrrs	10
1.5	Turbulence, Power Spectra and Multiphase Neutral H I	12
1.5.1	The ISM Turbulence and Power Spectra	12
1.5.2	Velocity Channel Analysis and Cold H I in dIrr Galaxies	13
1.6	Dwarf Galaxies in a Λ CDM Cosmological Context	14
	References	15
2	Stellar Disk Evolution of Nearby Dwarf Galaxies	21
2.1	The Sample	21
2.1.1	Parent Sample of LITTLE THINGS	22
2.1.2	LITTLE THINGS: A Representative Sample of Nearby Dwarf Irregular Galaxies	23
2.1.3	A Subsample of LITTLE THINGS for Studying the Stellar Disk Evolution	29
2.2	Data	33
2.2.1	<i>GALEX</i> FUV/NUV	33
2.2.2	Optical <i>UBV</i>	33
2.2.3	Narrow-Band H α Imaging	34
2.2.4	<i>Spitzer</i> 3.6 μ m	34
2.3	Surface Photometry	35
2.4	Multi-wavelength Surface Brightness Profiles	37
2.5	SED Modeling Technique	40
2.5.1	Creating a Library of Star Formation Histories	40
2.5.2	Determining the Physical Parameters	41

2.5.3	Correcting the <i>GALEX</i> NUV Data for Galactic Extinction	42
2.5.4	Testing the SED Modeling Technique on Mock Dataset	43
2.6	Results of SED Modeling to Our Sample Galaxies	46
2.6.1	Integrated SED-Based Versus Stellar CMD-Based SF Histories	49
2.6.2	Globally Integrated SF Histories	50
2.6.3	Azimuthally Averaged Radial Star Formation Histories	52
2.6.4	Stellar Mass Surface Density Profiles	65
2.7	Discussions	67
2.7.1	The Disk Assembly Mode of dIrr Galaxies: Outside-In	67
2.7.2	The Relationship Between Σ_{SFR} , Σ_{\star} and Star Formation History	73
2.8	Summary	75
	References	76
3	Gaseous Disk Turbulence of Nearby Dwarf Irregular Galaxies	81
3.1	Sample and Observing	81
3.2	Data Reduction	84
3.3	Power Spectrum Variations with Channel Width	88
3.4	Comparison with a Visibility-Based Estimation of Power Spectra	94
3.5	Effective Velocity Slice Width and Multiphase Neutral H I	96
3.6	Power Spectral Index Versus SF	101
3.7	Power Spectral Index Versus Baryonic Mass	107
3.8	The Turbulent Velocity Field	108
3.9	Summary	110
	References	111
4	Blue Compact Dwarf Galaxies Formed Through Gravitational Torques	115
4.1	The Context: “BCD” as an Extreme Version of Dwarf Irregulars	115
4.2	Clump Accretion in BCDs	118
4.2.1	The Case with a Few Giant Clumps	118
4.2.2	Clumps with a Power Law Mass Function	122
4.2.3	Clump–Clump Interactions	123
4.3	Observations of Clump Properties in Dwarf Irregulars and BCD Galaxies	124
4.3.1	Clump Mass Fractions and Accretion Times	124
4.3.2	Galaxy Thickness and Scale Length Ratios	128

- 4.4 Summary 129
- References 130
- 5 Summary 135**
 - 5.1 Main Findings of This Thesis Work 135
 - 5.2 Recent Development in the Literature 136
 - 5.2.1 Observational Studies 136
 - 5.2.2 Theories and Numerical Simulations 138
 - 5.3 Closing Remarks 141
 - References 141
- Appendix A: Starburst Triggering Process in “Giant” Irregular
Galaxies: Spiral–Spiral Merger 143**

Chapter 1

An Introduction to Disk Evolution of Dwarf Galaxies

Abstract As an introduction to this thesis work on formation and evolution of dwarf galaxies, here we give a brief review on our current knowledge of various aspects of dwarf galaxies in the local universe. In particular, we will introduce the definition of dwarf irregular galaxies, the star formation (SF) properties of dwarf irregular galaxies, the SF histories of dwarf galaxies, the techniques used for studying the stellar populations of dwarf galaxies, and the difference and similarities of the evolutionary properties of dwarf and spiral galaxies. We will also cover the topics related to turbulent properties of the interstellar medium in dwarf galaxies. At the end, we will give the cosmological context in which dwarf galaxies play a unique role in our understanding of the standard cosmological models.

1.1 Dwarf Irregular Galaxies

In the classical Hubble sequence (Hubble 1936), ellipticals, lenticulars, unbarred and barred spirals together form the famous Hubble tuning fork diagram. These galaxies seem to form a continuous and smooth sequence, in terms of the relative size of the bulge, extent to which the arms are unwound, etc. Outside of this tuning fork sequence are the irregulars. In contrast with the axially symmetrical “Regular” galaxies, irregulars tend to show chaotic, nonsymmetrical blue light distributions. The Large Magellanic Cloud and Small Magellanic Cloud (LMC and SMC) are two of the most well-known, nearby examples of irregular galaxies. Generally speaking, the irregular morphology may arise from a variety of physical causes. One well-known type of irregulars are the stellar systems involved in galaxy–galaxy interactions (e.g., Toomre and Toomre 1972; Schweizer 1982). Besides galaxy–galaxy interactions, in galaxies with low background stellar density levels and spatially incoherent SF patterns, patches of young stars, which have very low mass-to-light ratios, easily stand out against symmetrically distributed older stars and give rise to irregular blue light brightness structures. This thesis work focuses on the second class of irregulars, which usually fall into the category of dwarf galaxies.

At an influential conference held at the Observatoire de Haute-Provence in 1993, G. Tammann gave a working definition of dwarf galaxies: All galaxies that are fainter

than $M_B \leq -16$ and more spatially extended than globular clusters are dwarf galaxies (Tammann 1994). This is broadly consistent with the limit of mass at which outflows tend to significantly affect the baryonic mass of a galaxy. Besides dIrrs, other common types of dwarf galaxies include dwarf spheroidals (dSphs), ultrafaint dwarfs (uFd), centrally concentrated actively star-forming blue compact dwarfs (BCDs), and ultracompact dwarfs (UCDs). BCDs probably can be regarded as an extreme kind of dIrrs, which are experiencing very intense starburst in the central regions. Among these different types of dwarfs, only dIrrs are usually found to be experiencing active SF. Stellar mass is the most important factor in determining the evolution of a star, likewise, the mass of galaxies also largely determines the evolution of a noninteracting galaxy. The low potential wells of dwarfs means that they are much more susceptible to the internal regulation (e.g., stellar feedback) and external influences (galactic interaction, ram pressure stripping, galaxy harassment, starvation). Actually, except for the MCs, all close companions of our Galaxy and of M 31 are dSphs. Almost all distant companions are dIrrs, with the exception of three free-flying dSphs, Cetus, Tucana, and And XVIII. It has long been suggested that dSphs may be simply transformed from dIrrs, induced by the internal and external influences mentioned above (e.g., Dekel and Silk 1986; Gunn and Gott 1972; Moore et al. 1996; Dressler 1980). Motivated by the idea that Sph galaxies are transformed, “red and dead” Scd-Irr galaxies, in the same way that many S0 galaxies are transformed, red and dead Sa-Sc spiral galaxies, Kormendy and Bender (2012) suggested a revised parallel-sequence morphological classification of galaxies. Figure 1.1 illustrates the morphological classification adapted from Kormendy and Bender (2012). This classification scheme places the dwarf galaxies in a continuous sequence with disks of other “regular” galaxies. The bulge-to-total light defines the position of a galaxy in this tuning fork diagram. In fact, in the three-dimensional plane (Fig. 1.2) involving effective radius, surface brightness at the effective radius, and absolute magnitude,

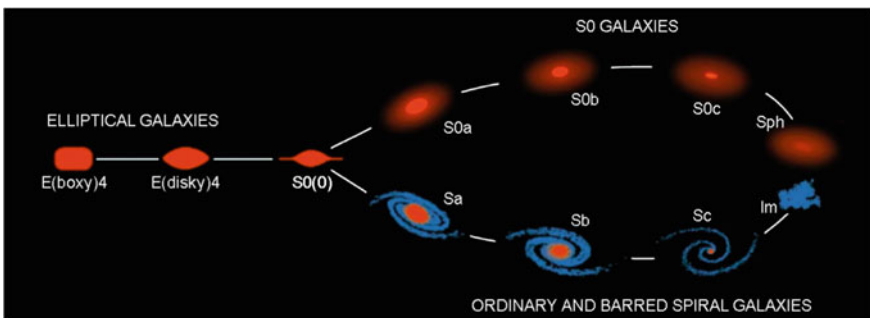


Fig. 1.1 Revised parallel-sequence morphological classification of galaxies. E types are from Kormendy and Bender (1996). Transition objects between spirals and S0s (van den Bergh’s anemic galaxies) exist but are not illustrated. Bulge-to-total ratios decrease toward the right; Sc and S0c galaxies have tiny or no pseudobulges. Sph and Im (or Irr) galaxies are bulgeless. This figure is adapted from Kormendy and Bender (2012)

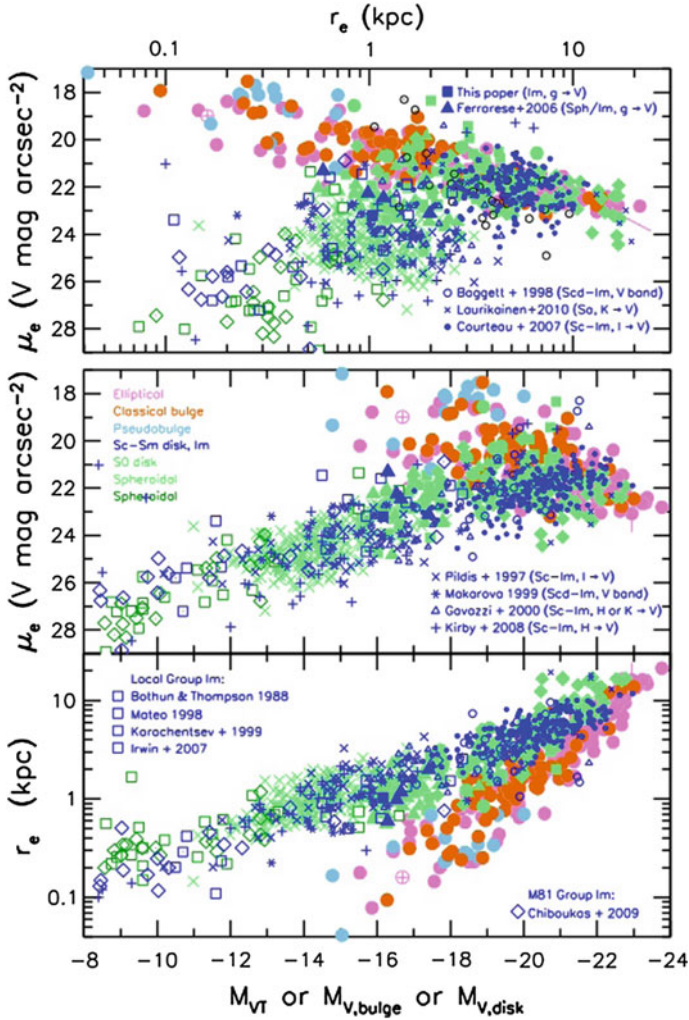


Fig. 1.2 Parameter correlations for ellipticals, bulges, Sphs, and S0 disks, plus disks of Sa C Im (or Irr) galaxies (*blue points*). When (pseudo)bulge–disk decomposition is necessary, the two components are plotted separately. All S0 galaxies from the ACS VCS survey (Ferrarese et al. 2006) are plotted (*light brown and light green points*). Also, blue points show four galaxies from Ferrarese et al. (2006) that they note are Sph/Im transition galaxies and one galaxy (VCC 1512) from the above paper that is classified as Im. Most disks that have lower-than-normal surface brightnesses are in galaxies that have outer rings, and most disks that have higher-than-normal surface brightnesses are either edge-on or starbursting. However, starbursting BCDs are omitted; they would add a few galaxies that scatter to higher surface brightnesses. This figure is adapted from Kormendy and Bender (2012)

different morphological types of disk galaxies, including dSphs and dIrrs, form a continuum (Tolstoy et al. 2009; Kormendy and Bender 2012).

dIrr galaxies numerically dominate active star-forming galaxies in the local universe (van den Bergh 1966; Gallagher et al. 1984; Dale et al. 2009). Compared to local spiral galaxies, dIrr galaxies are generally smaller, bluer, less luminous, and gas-rich. dIrr galaxies tend to have low metallicity and a flat metallicity gradient within measurement uncertainties in the ISM (e.g., Kobulnicky and Skillman 1996; Hunter and Hoffman 1999; van Zee and Haynes 2006; Croxall et al. 2009).

1.2 Star Formation in Dwarf Irregular Galaxies

Early models of SF activity in dIrrs indicated that small disks would be unstable to SF activity. In particular, episodic bursts of SF appeared to arise naturally from stochastic self-propagating SF (SSPSF) models (Gerola et al. 1980). As mentioned below, the gas density in dIrrs usually is well below the threshold for SF across the entire stellar disk, suggesting that it is difficult to initiate a global burst of SF. Thus, a more accurate representation of the SF process in dIrrs may be that of random percolation of SF activity across the stellar disk. This picture is fundamentally different from classic SSPSF since the SF activity does not propagate from one cell to another; rather, SF occurs only in a few localized regions where the local gas density is sufficient to permit molecular cloud formation and subsequent SF. The onset of SF activity in this type of model is still a stochastic process, but the SF activity across the galaxy is expected to be more quiescent since it is unlikely that the entire disk will have sufficient gas density to permit a sudden starburst (van Zee 2001).

The SF process in seemingly simple dIrrs is unclear. The classical Toomre gravitational instability model (Toomre 1964; Quirk 1972), which seems to explain the SF threshold successfully in spiral galaxies (Kennicutt 1989; Martin and Kennicutt 2001) and elliptical galaxies (e.g., Vader and Vigroux 1991), predicts that the gas surface density of dIrrs, both at intermediate radii and outer radii, is usually well below the threshold of large-scale SF for a single-fluid gas disk (Hunter et al. 1998, hereafter H98; Leroy et al. 2008). Even though recent studies (e.g., Yang et al. 2007) suggest that incorporation of the gravitational contribution of the stars may make the gas disk marginally stable, the uncertainties (e.g., the gas/stellar velocity dispersion, the disk scale height) included in the stability analysis are substantial. Nevertheless, widely distributed SF, although apparently inefficient, has been observed in dIrrs, which implies that some other internal or local process must play an important role. H98 suggests that cloud formation involving a competition between self-gravity and shear rather than an instability in the usual sense is more successful in defining the threshold for SF, even though this alternative model does not predict where SF ends. It is definitely true that, whatever is the formation mechanism, the cloud can last for a long time once formed, because dIrr galaxies have very low rotational shear, thanks to the solid-body rotation for most part of the disks.

H98 found that, for most dIrrs, the current SF rate (SFR; traced by $H\alpha$) correlates with the optical (e.g., V) starlight profiles better than with the usually mass-dominant atomic gas surface density. The correlation with older stars indicates that SF may be a self-regulating process and/or the SF may be affected by the existing stars to a certain degree. By analyzing optical and near-infrared (NIR) broadband data, Bell and de Jong (2000) and Bell et al. (2000) found that the SF histories (described as luminosity-weighted ages there) primarily correlate with the K -band surface brightness in both spiral galaxies and low-surface brightness (LSB) galaxies. Recently, Leroy et al. (2008) found that the SF efficiency ($\sim \text{SFR}/M_{\text{atomic gas}}$) shows a strong relationship with the stellar mass surface density, rather than with the gas, in atomic gas-dominated regions, such as dIrr galaxies and the outer disks of spiral galaxies. Shi et al. (2011) proposed an “extended Schmidt law” with explicit dependence of the SF efficiency on the stellar mass surface density.

SF in galaxies should be triggered by a combination of processes, including gravitational instabilities, spiral wave shocks, stellar compression, and turbulence compression. In dIrr galaxies and the outer parts of spiral disks, some of these processes shut down completely. There should be no strong stellar spirals. Cold cloud formation should also be more difficult at low ambient pressure. However, a low level of SF may sustain itself by driving shells and turbulence and by compressing the existing clouds. According to Elmegreen and Hunter (2006), the small but nonzero Mach number of the low-surface-density disks of dIrr galaxies gives turbulence and other dynamical processes the ability to form clouds that locally exceed the stability threshold, although these processes are not likely to be successful very often. Therefore, SF becomes very patchy. Turbulence has been implicated in SF processes because it readily accounts for the power-law luminosity functions of H II regions and the power-law mass functions of clouds and clusters (Mac Low and Klessen 2004). Turbulence also explains the power-law shape of Fourier Transform power spectra of HI (Stanimirović et al. 1999; Elmegreen et al. 2001) and $H\alpha$ (Willett et al. 2005), the log-normal distribution of $H\alpha$ intensity (Hunter and Elmegreen 2004), and the correlation between region size and the SF time scale (Efremov and Elmegreen 1998) in dwarfs. However, the relative importance of SF triggered by turbulence compression in dIrr galaxies is far from clear.

1.3 Star Formation Histories of Dwarf Irregular Galaxies

By studying the ground-based broadband UBV and $H\alpha$ imaging data of a large sample of isolated dIrrs, van Zee (2001) suggests that the observed optical colors are best fitted by composite stellar populations that have had approximately constant SFR for at least 10 Gyr. The HST ACS Nearby Galaxy Survey Treasury (ANGST: Weisz et al. 2011) survey covers 60 nearby ($D \lesssim 4$ Mpc) dwarfs of both early and late types. Weisz et al. (2011) conclude that the average dwarf formed $\gtrsim 50\%$ of its stars by $z \sim 2$ and 60% of its stars by $z \sim 1$, regardless of its current morphological type, and that the mean SF histories of dIrrs, dwarf transition galaxies, and dSphs

are similar over most of cosmic time, and only begin to diverge a few Gyr ago, with the clearest differences between the three appearing during the most recent 1 Gyr. Nevertheless, the observational depth of the ANGST sample is very shallow ($M_I \sim 0$), which means that the SF histories determined for older ($>1\text{--}2$ Gyr) ages are subject to large uncertainties. Stellar CMDs from very deep (reaching the ancient MSTOs) HST observations suggest very different SF histories for different types of dwarfs. In dIrrs IC 1613 (Skillman et al. 2003) and Leo A (Cole et al. 2007), the SF has occurred predominantly at intermediate ages ($\lesssim 5$ Gyr), and the SF has declined during the recent ~ 1 Gyr. The dSphs Cetus (Monelli et al. 2010a) and Tucana (Monelli et al. 2010b), and the transition-type galaxy LGS 3 (Hidalgo et al. 2011) are very old, metal-poor stellar systems, which experienced the strongest initial bursts of SF at very early epochs (>10 Gyr).

1.3.1 The Technique: Evolutionary Population Synthesis

The SF history of galaxies is imprinted in their integrated light. Evolutionary population synthesis, pioneered by Tinsley (1968), has become the standard technique to interpret galaxy colors and spectra. Especially, *isochrone synthesis* introduced by Charlot and Bruzual (1991) improved significantly upon the earlier evolutionary synthesis. The improvement on the calculation of stellar evolutionary tracks and theoretical models of stellar atmospheres, together with the accumulation of high-resolution observations of stellar spectra with different metallicities, has enabled more and more accurate studies of SF histories by comparing high-quality observations and state-of-the-art population synthesis tools. The basic assumption of modern population synthesis is that any SF history can be expanded in a series of instantaneous single stellar populations (SSPs), which can be described with the following expression

$$F_\lambda(t) = \int_0^t \text{SFR}(t-t') S_\lambda[t', Z(t-t'), \text{IMF}(t-t')] 10^{-0.4A(\lambda)} dt' \quad (1.1)$$

where SFR stands for SF rate, $S_\lambda[t', Z(t-t')]$ is the power radiated per unit wavelength per unit initial mass by an SSP of age t' , metallicity $Z(t-t')$ and a given initial mass function (IMF) at age t' which describes the fraction of stars with different stellar masses. $A(\lambda)$ is the dust extinction at wavelength λ . $F_\lambda(t)$ represents the observed integrated emission from an extended regions at age t . Ideally, with a reasonable assumption of the IMF, the SF history can be extracted by comparing observations to population synthesis models.

1.3.1.1 Two Big Uncertainties: IMF and Extinction Law

The IMF is usually assumed to be nonevolving with time in population modeling. Salpeter (1955) introduced a power-law stellar IMF to parametrize the relative

number of stars as a function of mass in the solar neighborhood. The single power-law stellar IMF with exponent ~ -2.35 as derived by Salpeter (1955) was found to be nearly invariant for stars with mass higher than $1 M_{\odot}$ in different environments. Later, a shallower mass function below a solar mass was proposed by Miller and Scalo (1979). Kroupa et al. (1993) adopted a multi-segment power law to fit the volume density distribution of stars with mass $< 1 M_{\odot}$. Chabrier (2003) parametrized the IMF as a log-normal form for the low-mass stars. The log-normal formalism of the stellar IMF may be physically preferred if the SF is determined by various independent processes. However, Dabringhausen et al. (2008) showed that the Chabrier IMF is extremely similar to the Kroupa-type IMF. Although the theories based on pure Jeans fragmentation implies a dependence of the mass function on the environment, such as density, radiation field, SFR (e.g., Krumholz et al. 2011), observations of resolved stellar populations in the field, local young clusters and associations are consistent with a nearly “universal” IMF (Bastian et al. 2010), i.e., the Kroupa or Chabrier-type IMF.

The dust extinction law, which describes the wavelength dependence of the dust extinction, is a very open issue. The extinction curve of single star (or a background quasar or Gamma-ray burst) by foreground dust should be distinguished from the attenuation curve of an extended object such as star-forming regions in galaxies. The extinction for a single star depends simply on the column density and is determined by both the absorption and the scattering properties of the grains in the foreground dusty screen. In the case of an extended object, the emitted light suffers an effective attenuation that also depends strongly on the geometrical relations between dust and stars. As pointed out by Witt et al. (1992), equal amounts of dust in different dust–star configurations produce very different reddening and attenuation effects. Furthermore, the clumpy multiphase structure of the interstellar medium (ISM) leads to a significant reduction in the opacity produced by a given amount of dust (e.g., Witt and Gordon 2000). Therefore, the relationships between reddening and dust column density is usually nonlinear. For example, assuming a uniformly mixed distribution of dust and stars, the dust attenuation at a wavelength λ would be

$$A_{\lambda} = -2.5 * \log_{10} \left(\frac{1 - e^{(-\tau_{\lambda})}}{\tau_{\lambda}} \right) \quad (1.2)$$

where τ_{λ} is the dust optical depth with is determined by the grain properties and dust column densities. Based on this equation, for a given intrinsic dust extinction curve (i.e., τ_{λ}), the A_{λ} - λ relation becomes shallower than the τ_{λ} - λ relation as τ increases. Taking advantage of the similarly young stellar populations in local starburst galaxies, Calzetti and her coworkers (Calzetti 1997, 2001; Calzetti et al. 2000) derived the empirical attenuation law, assuming the foreground dust geometry. This Calzetti curve has been very extensively used in extragalactic studies. One interesting finding of Calzetti et al. is that the nebular emission from H II regions experience higher attenuation than the stellar continuum emission. Motivated by the apparent discrepancy between the attenuation of nebular emission and stellar continuum found by Calzetti et al. Charlot and Fall (2000) developed a simple model for computing the effects

of dust on the integrated spectral properties of galaxies. Based on their model, the finite lifetime of the birth clouds, the emission (including both the nebular emission and stellar continuum) from young ($\lesssim 10^7$) stars are attenuated by dust in the outer HI envelopes of the birth clouds and the ambient ISM, whereas the emission from older stars is only attenuated by the ambient ISM. Fischera et al. (2003) provided a physical explanation for the Calzetti curve based on a a turbulent ISM.

1.3.1.2 Full-Spectrum Fitting

Modern telescopes have been extensively used to obtain high spectral resolution spectra of galaxies. In particular, large ground-based surveys, such as the Sloan Digital Sky Survey (SDSS, York et al. 2000), 2dF Galaxy Redshift Survey (2dFGRS, Colless et al. 2001), Galaxy And Mass Assembly (GAMA, Driver et al. 2009), have provided the community with an enormous amount of high-quality optical spectra for the local universe to intermediate redshift. These spectra have been and are being used to study the SF histories (e.g., Cid Fernandes et al. 2005) through comparison with the modern population synthesis models (e.g., Leitherer et al. 1999; Bruzual and Charlot 2003). One important result from the comparison between spectra and population models is the existence of a significant amount of very old stellar populations (e.g., Guseva et al. 2001; Kong et al. 2003; Zhao et al. 2011) in many Blue Compact Dwarfs (BCDs) which as a class were once thought to be primeval galaxies undergoing the first episode of SF (Sargent and Searle 1970). The notoriously known age-metallicity degeneracy in population analysis with spectral continuum can be largely broken by appealing to refined spectral diagnostics involving individual stellar absorption-line features (e.g., Jones and Worthey 1995; Vazdekis and Arimoto 1999; Bruzual and Charlot 2003). Nevertheless, spectroscopic observations are almost impossible for low-surface brightness (LSB, $\mu(B) > 23$, de Blok and Walter 2000) regions, with current telescopes. For example, the SDSS spectroscopic survey reaches a depth of $r_{AB} < 17.77$, the GAMA survey reaches a depth of $r_{AB} < 19.8$.

1.3.1.3 Color–Magnitude Diagram Fitting

Generally speaking, the SF history can be derived directly from analysis of resolved stellar color–magnitude diagrams (CMDs). A significant fraction of Local Group galaxies have been studied using the synthetic CMD method to infer their SF histories (e.g., Gallart et al. 1996; Mateo 1998; Dolphin 2002; Skillman et al. 2003; Cole et al. 2007; Hidalgo et al. 2011), primarily using the Hubble Space Telescope (HST). Recently, by modeling the stellar CMDs obtained by HST, the ANGST (The ACS Nearby Galaxy Survey) team determined the star formation histories (Weisz et al. 2011) for a large sample of nearby dwarf irregular galaxies (dIrrs). Most of these galaxies are only observed with a single HST pointing toward the galactic center. Due to the observational depth ($M_V \sim 0.7$, corresponds to the MSTO ages ≤ 500 Myr) of the ANGST galaxies, reliable SF histories are determined over the past 0.5 to ~ 1 Gyr,

while the SF histories at older ages ($\geq 1-2$ Gyr) are only loosely constrained by the poorly modeled post-main sequence phases (e.g., RGB, RC), with the problems mentioned above. Their study shows the diversity of the most recent SF histories of nearby dIrrs. Nevertheless, obtaining deep CMDs which reach the old main-sequence turnoffs (MSTOs) is crucial to reconstructing the whole SF history of a galaxy. As pointed out by Gallart et al. (2005), beyond ~ 2 Gyr ago, shallow (e.g., completeness limit $M_I < 2$) CMDs at best can reliably constrain the integrated SF. Presently, only four late-type dIrrs, namely Magellanic Clouds, Leo A and IC 1613, have been observed deep enough to reach close to the ancient MSTOs. Furthermore, the CMD modeling works often only study a small spatial area of galaxies. In addition, in galaxies beyond the Local Group, distance makes crowding very severe, and even HST cannot resolve stars as faint as the MSTO of old populations. The further the distance, the worse the crowding conditions and the shorter the look-back time reachable even with the deepest, highest resolution photometry (Tolstoy et al. 2009).

1.3.1.4 Broadband Fitting

Besides spectroscopy and CMD fitting, integrated broadband photometry is still an indispensable method to study the stellar populations in high redshift galaxies and LSB galaxies in the local universe. Except for the rare bursting BCD, most of the dIrr galaxies (Elmegreen and Hunter 2006) in the local universe have central surface brightness significantly fainter (more than one magnitude) than $21.65 \text{ mag arcsec}^{-2}$ (Freeman's brightness). Through analyzing the UBV broadband data, Larson and Tinsley (1978) found that their noninteracting normal disk galaxies are consistent with a monotonically decreasing SFR, whereas the morphologically peculiar and interacting galaxies have colors that are consistent with a "burst" mode of SF. The optical wavelength emissions from galaxies are usually dominated by intermediate-type main-sequence stars (A-F) to G-K giants Kennicutt (1998). Gallagher et al. (1984) showed that the blue band photometry can be used to constrain the SF during the past \sim Gyr. To study the stellar populations younger than a few hundred Myr, ultraviolet (UV) data is required. During the past few decades, several space telescopes, such as HST (e.g., Meurer et al. 1995), the Ultraviolet Imaging Telescope (Smith et al. 1996), and especially the Galaxy Evolution Explorer (GALEX; Martin et al. 2005), have provided the community with an enormous amount of UV data for galaxies. At wavelengths longer than the optical, the near-infrared (NIR) emission, which is dominated by the mass-dominant low-mass stars and the red giant stars, gives the tightest constraint on the total stellar mass (e.g., Elmegreen and Elmegreen 1984; Kendall et al. 2008), and thus the lifetime averaged SFR. The Two Micron All Sky Survey (2MASS) survey and the *Spitzer* Infrared Array Camera (IRAC; Fazio et al. 2004) have collected high-sensitive, high-resolution NIR and mid-infrared (MIR) imaging data for over millions of galaxies. With the availability of these multiwavelength broadband data, studying the rough SF history throughout the lifetime of galaxies has become possible. We will show in this thesis work that

the averaged SFR during the past 0.1 Gyr, 1 Gyr and a Hubble time can be very well constrained by modeling these multiband data with a complete library of model SF histories.

1.4 Evolution of Galactic Disk: Spirals Versus dIrrs

Disks are the most prominent parts of late-type galaxies. The rotation curves of nearby spirals are usually, following a steep increase in the inner region, flat for most part of the disks (e.g., van der Kruit and Allen 1978; Roberts 2008). The radial starlight distribution of galactic disks always follows an exponential profile (e.g., Freeman 1970; van der Kruit 1990). In addition, a negative abundance gradient was usually found in local spiral galaxies (e.g., Shaver et al. 1983). Nevertheless, as mentioned above, the nearby dIrrs have flat metallicity gradients within measurement uncertainties. Furthermore, dIrrs usually have a solid-body rotation curves for a significant part of the disks (Swaters et al. 2002).

Stellar disks are close to centrifugal equilibrium, suggesting dissipation of baryons to a near equilibrium structure before the gas became dense enough to initiate the onset of the main epoch of SF. The basic discrete two-component structure of the edge-on galaxy NGC 7814 led van der Kruit and Searle (1982) to deduce that there are two discrete epochs of SF, one before and the other after virialization of the spheroid and the formation of the disk. The discovery of dark matter halos (as indicated by the flat rotation curves of spiral disks) led to the two-stage galaxy formation model of White and Rees (1978), in which hierarchical clustering of the dark matter took place under the influence of gravity, followed by collapse and cooling of the gas in the resulting potential wells. The standard paradigm of disk formation, as discussed by Dalcanton et al. (1997) and Mo et al. (1998), involves the dark matter halo forming gravitationally and relaxing to virial equilibrium; then infalling gas is shock-heated to the halo virial temperature and then cools radiatively from inside out, gradually building up the disk and forming stars quiescently. However, recent simulations point to the likelihood of cold gas accretion into disk galaxies (e.g., Keres et al. 2005). Rather than shock-heated to the virial temperature of the potential well, the cold gas falls in via cosmic filaments, allowing galaxies to draw their gas from a large volume. It was suggested that hot halos are seen only for dark halo masses larger than 2–3 times $10^{11} M_{\odot}$ (Dekel and Birnboim 2006). In halos with masses smaller than $10^{12} M_{\odot}$, the disks are built by cold streams, giving efficient early SF regulated by supernova feedback. Deep H I images of disk galaxies found spectacular H I arms and filaments, some of which are forming stars at a low level (Bigiel et al. 2010). This structure may represent a slow filamentary infall of H I into the disk.

Whatever the primary disk building process (hot haloes or cold streams), the higher density inner disk, due to its shorter gas cooling timescale and shorter dynamical timescale, should always experience an earlier and faster SF compared to the outer disk. This is the so-called inside-out disk growth scenario (e.g., Larson 1976;

Chiappini et al. 1997). In this scenario, the disk size or scale length of a galactic disk increases with time due to the slower/late accretion of gas at large radii and exhaustion of gas in the center. The gradients of colors (bluer in the outer disk) and current abundance (lower in the outer disk) observed in spiral galaxies fit well into this inside-out scenario. The “inside-out” disk growth mode has been clearly established for the outer disks of two very nearby spiral galaxies (i.e., M 33 and NGC 300) by modeling the CMDs obtained with HST (i.e., Williams et al. 2009; Gogarten et al. 2010).

However, unlike luminous spiral galaxies, late-type dIrrs exhibit a variety of behaviors in terms of color profiles (Kormendy and Djorgovski 1989; Tully et al. 1996; Jansen et al. 2000; Taylor et al. 2005; Elmegreen and Hunter 2006, hereafter HE06). Nevertheless, Tully et al. (1996) found that galaxies fainter than $M_B = -17$ become redder with radius in the Ursa Major cluster. Later, with a larger sample, Jansen et al. (2000) found that the reddening (with radius) trend may occur at a fainter absolute magnitude than that found by Tully et al. (1996). Of a sample of 94 dIrrs studied by HE06, 64% of the galaxies with a gradient in $B - V$ become redder with radius. In particular, all the galaxies with $M_B > -14$ become redder at least in one color (either $B - V$ or $U - B$) at outer radii. Recently, Tortora et al. (2010) analyzed the optical color gradients of $\sim 50,000$ nearby Sloan Digital Sky Survey (SDSS) galaxies. They found a good correspondence between the color gradients and the stellar mass of the galaxies. In particular, below a stellar mass of $10^{8.7} M_\odot$, the color gradient slopes become positive, which were mainly attributed to the positive metallicity gradients.

Additionally, from stellar CMD analysis of two different (HST/WFPC2) fields in IC 1613, Skillman et al. (2003; also Bernard et al. 2007) found that the SF activity in the outer field has been significantly depressed during the last Gyr, which is in contrast to the “inside-out” growth scenario. Similarly, by analyzing resolved stellar populations, the characteristics of more spatially extended older populations have been reported both for transition-type dwarf galaxies (e.g., DDO 210, McConnachie et al. 2006; Phoenix, Hidalgo et al. 2009) and dSph galaxies (e.g., Sculptor dSph, Tolstoy et al. 2004; Fornax dSph, Battaglia et al. 2006). A clear trend of “outside-in” quenching of recent SF was also found (Gallart et al. 2008; Indu and Subramaniam 2011) in the LMC. In this work, we will show that the “outside-in” scenario is a rule for nearby dIrrs. The “outside-in” scenario in low-mass dIrrs may be induced by various internal (stellar feedback) and external (see above) regulations, of which the effect is much weaker in high-mass spirals.

1.5 Turbulence, Power Spectra and Multiphase Neutral H I

1.5.1 *The ISM Turbulence and Power Spectra*

The ISM is characterized by very large Reynolds number, thus turbulent motions control the structure of nearly all components of the ISM. Turbulence is nonlinear fluid motion which results in the excitation of an extreme range of correlated spatial and temporal scales. von Weizsacker (1951) outlined a theory for interstellar matter (ISM) that is probably similar our to present-day interpretation: cloudy objects with a hierarchy of structures form in interacting shock waves by supersonic turbulence that is stirred on the largest scale by differential galactic rotation and dissipated on small scales by atomic viscosity. Kolmogorov (1941) derived, for the first time, a mathematical formula for the energy spectrum of turbulence, and this spectrum gave the distribution of energy among turbulence vortices as a function of vortex size. In Kolmogorov's model, kinetic energy is injected at large scale (the driving scale), and significant dissipation by viscosity occurs only at small scales (dissipation scale). The scale range in between the driving scale and dissipation scale, which has power-law energy power spectra (PS), is known as the inertial range. The kinetic energy injected on large-scale cascades to small scales without much loss in the inertial range. The scale-invariant Kolmogorov scaling was only applicable to incompressible turbulence. In compressible ISM turbulence, kinetic energy is not conserved between different scales. Furthermore, the driving and the dissipation of ISM turbulence may span a wide range of scales (Elmegreen and Scalo 2004). Magnetic fields can further complicate the ISM turbulence, where energy can be transferred between kinetic and magnetic energy. However, Kolmogorov-type scaling may still apply in the direction perpendicular to the magnetic field (Goldreich and Sridhar 1995; Cho and Lazarian 2003). In addition, self-gravity is also an important factor regulating the ISM turbulence. Larson (1981) found that the column density and linewidths of molecular clouds scale with the size of the studied region as power laws, reminiscent of the Kolmogorov scaling law. Nevertheless, the supersonic nature of the molecular clouds suggests the turbulence is highly compressible.

Pervasive ISM turbulence regulates SF by creating local density enhancements and countering gravitational collapse. Hierarchical SF (e.g., Gladwin et al. 1999; Efremov and Elmegreen 1998; Zhang et al. 2001) is a manifestation of a fractal, turbulent ISM. Kinematic support from turbulence prevents giant molecular clouds from collapsing on the order of a free-fall timescale (Mac Low and Klessen 2004). Turbulent motions are also the dominant contributor of the total mid-plane pressure in the solar neighborhood (Boulares and Cox 1990; Jenkins and Tripp 2001). In addition, the stellar initial mass function may also be primarily shaped by turbulent fragmentation (Padoan and Nordlund 2002). Fast decay (\sim a crossing time across the driving scale, Stone et al. 1998; Elmegreen 2000; Mac Low 1999) of the turbulent energy suggests a continuous driving mechanism is in operation. It has been suggested that among the various power sources for turbulence, such as magnetorotational instabilities (MRI, e.g., Sellwood and Balbus 1999), gravitational instabilities (e.g.,

Wada et al. 2002), thermal instabilities (e.g., Kritsuk and Norman 2002), and stellar energy (e.g., winds, supernovae), supernovae dominate the energy input to the ISM (e.g., Norman and Ferrara 1996; Mac Low and Klessen 2004). Nevertheless, as pointed out by Elmegreen and Scalo (2004), gravitational energy, which has an energy input rate an order of magnitude lower than that of supernovae, may have a higher efficiency for conversion into turbulence. Indeed, recent hydrodynamic galaxy simulations (Bournaud et al. 2010) found that ISM turbulence appears to be regulated by gravitational processes around the Jeans scale length. Observationally, it remains to be seen how ISM turbulence is related to SF.

Fourier transform power spectra (PS), which characterize the relative importance of structures at different scales, have been extensively used as a diagnostic for ISM structures. A power-law behavior of the PS of H I-emission line intensities was found in the Milky Way (e.g., Crovisier and Dickey 1983; Green 1993; Dickey et al. 2001; Khalil et al. 2006), SMC (Stanimirović et al. 2000), and LMC (Elmegreen et al. 2001). The self-similar power-law PS is usually attributed to ISM turbulence. In unmagnetized, incompressible Kolmogorov turbulence (Kolmogorov 1941), the energy spectrum is given as $E(k) \sim k^{-5/3}$. Whereas for highly compressible, supersonic turbulence, it is commonly thought that the energy spectrum is like a field of uncorrelated shocks (Saffman 1971), i.e., $E(k) \sim k^{-2}$.

In incompressible, subsonic turbulence, density fluctuations passively follow the velocity field, which obeys the Kolmogorov scaling (Lithwick and Goldreich 2001). In other words, density and velocity have similar Kolmogorov PS $\sim k^{-11/3}$, where k is the three-dimensional (3D) wavevector. Nevertheless, the transonic (e.g., warm neutral medium, WNM) or supersonic (e.g., cold neutral medium, CNM) nature of the ISM implies highly compressible turbulence. The ISM turbulence also involves self-gravity and magnetic fields. Numerical simulations (Kim and Ryu 2005; Kowal et al. 2007; Gazol and Kim 2010) suggest that the spatial PS are sensitive to the sonic Mach number and the Alfvénic Mach number, in the sense that higher sonic Mach number and Alfvén Mach number (i.e., weaker magnetic forces) lead to steeper velocity PS and shallower density PS due to the formation of stronger shocks. Krumholz and McKee (2005) proposed that the sonic Mach number M is an important factor in determining the SFR ($\propto M^{-0.32}$).

1.5.2 Velocity Channel Analysis and Cold H I in dIrr Galaxies

H I is an important component of the ISM. Especially in gas-rich dwarf irregular (dIrr) galaxies, neutral H I usually dominates the baryonic component (e.g., Zhang et al. 2012). Observationally, the intensity fluctuations of individual H I channel maps are caused by both 3D real space projection and velocity mapping. Lazarian and Pogosyan (2000, hereafter LP00) found that the intensity fluctuations within thin velocity slices (less than the turbulent velocity dispersion at the studied scale) of the observed position-position-velocity (PPV) data cubes are generated or significantly affected by the turbulent velocity field, whereas intensity fluctuations in thick

velocity slices are dominantly caused by density fluctuations because the velocity fluctuations are averaged out. By studying the PS index variations with the instrumental channel width, the turbulent velocity spectrum and density spectrum can be probed.

Stanimirović and Lazarian (2001) applied this velocity channel analysis technique to the H I-emission line data of the SMC. They found that the power-law PS become steeper with increasing velocity slice thickness, from which the power-law PS were derived for both the density and velocity fields.

Field et al. (1969) demonstrated that the CNM ($T \sim 50$ K) and WNM ($T \sim 8000$ K) could coexist in pressure equilibrium, so that the neutral atomic gas could be considered to be a two-phase medium. Wolfire et al. (1995, 2003) found that the condition for the pressure equilibrium is satisfied in the Galactic disk, and thus the two-phase description of the interstellar H I is approximately valid even in the presence of interstellar turbulence. However, as the principle H I tracer, 21-cm emission line brightness is independent of kinetic temperature when optically thin and proportional to temperature when optically thick. Therefore, it is not straightforward to detect the cold H I in emission, because of its low temperatures and low abundance compared to the WNM. However, cold H I is usually thought of as being the precursor of molecular clouds where the SF takes place. Ideally, the CNM may be easily distinguished from the WNM due to their radically different temperatures (thus very different linewidths). But the method of multi-Gaussian decomposition commonly used to identify the CNM in the emission line profiles (e.g., Haud and Kalberla 2007) is subject to big uncertainties. The most questionable point of the multi-Gaussian decomposition is nonuniqueness of the decomposition. Furthermore, the spectral decomposition method requires very high quality spectra, otherwise acceptable decomposition is only possible for (star-forming) regions with high concentration of cold H I (e.g., Young and Lo 1996, 1997; de Blok and Walter 2006). Other common ways to identify cold H I include H I continuum absorption (HICA, e.g., Heiles and Troland 2003) and H I self-absorption (HISA, e.g., Gibson et al. 2005).

Besides constraining the turbulent velocity and density spectral indices, the theory developed by LP00 can be used to probe the distribution of different temperature components of the H I. According to the results of LP00, in a medium with a few H I phases having different temperatures, the PS index variations with the channel width should reflect the distribution of temperatures of H I components along the line of sight. To investigate the relationship between the spatial PS and SF, I will present the velocity channel analysis for a subsample of LITTLE THINGS (see below) dIrr galaxies. With the variations of the spectral index as functions of channel width and radius, I will also give some constraints on the distribution of cold H I in dIrr galaxies.

1.6 Dwarf Galaxies in a Λ CDM Cosmological Context

In a Λ CDM cosmological context, structures grow hierarchically from smaller systems to larger systems. Small dark matter halos, and (if any) their dwarf galaxies, are the building blocks of larger halos and galaxies. As shown above, there exist

distinct structural–kinematic scaling relations for galaxies with M_B brighter and fainter than ~ -18 mag (e.g., Kormendy 1985; Binggeli 1994). Dekel and Silk (1986) attributed the observed distinct scaling relations to a critical condition for global gas loss as a result of the first burst of SF. Dwarf galaxies, including the dwarf irregulars and dwarf ellipticals, are systems with virial velocities below $\sim 100 \text{ km s}^{-1}$, and these relatively diffuse dwarf galaxies mostly originated from the typical $\sim 1\sigma$ density peaks, whereas the brighter galaxies (including the compact dwarf galaxies) originate from rarer $\sim 2\text{--}3\sigma$ density peaks (Dekel and Silk 1986).

The morphology–environment relation and the similar scaling relations between late-type dwarf irregulars and early type dwarf ellipticals lead to a prevailing idea that dwarf ellipticals formed from dwarf irregulars, either through tidal stripping or tidal stirring mechanisms (e.g., Mayer et al. 2001a, b) that remove the gas and (thus) suppress the SF. The relatively uniform and widespread distribution of dwarf galaxies throughout the Universe makes them suitable candidates for cosmic reionization (e.g., Stark et al. 2007). More and more studies of the ultraviolet luminosity function of galaxies at high redshift ($z \lesssim 8$) found that the far more numerous faint dwarf galaxies are sufficient to maintain the cosmic reionization (e.g., Atek et al. 2015).

Central to the few most pressing challenges, i.e., cusp-core problem (e.g., Flores and Primack 1994), missing satellites problem (e.g., Klypin et al. 1999), and too big to fail problem (e.g., Boylan-Kolchin et al. 2011), for the standard Λ CDM cosmological model are dwarf galaxies with stellar masses $\lesssim 10^7 M_\odot$ (e.g., Weinberg et al. 2013). In particular, cosmological simulations that incorporate only gravity and cold dark matter predict halos with cuspy central density profiles, whereas observations of gas-rich dwarf galaxies favor cored density profiles (cusp-core problem); cosmological simulations predict hundreds to thousands of subhalos around a halo that hosts Milky Way like galaxies, whereas the observed number of satellite galaxies around the Milky Way falls short of the predictions by orders of magnitude (missing satellites problem); cosmological simulations predict massive subhalos around Milky Way like galaxies that have mass higher than that inferred from the massive satellite galaxies by a factor of ~ 5 (too big to fail problem). The final solution to the above three problems has not yet emerged, but a common view is that a realistic account of the baryonic physics should be the direction to pursue. For instance, recent simulations start to make cored density profiles in dwarf galaxies by invoking SF and supernova feedback (Governato et al. 2010). This thesis work deals with the two most dominant baryonic components of nearby dwarf galaxies, i.e., the stellar disks and the atomic gas.

References

- Atek H, Richard J, Jauzac M et al (2015) *ApJ* 814:69
 Bastian N, Covey KR, Meyer MR (2010) *ARA&A* 48:339
 Battaglia G, Tolstoy E, Helmi A et al (2006) *A&A* 459:423
 Bell EF, de Jong RS (2000) *MNRAS* 312:497
 Bell EF et al (2000) *MNRAS* 312:470
 Bernard EJ, Aparicio A, Gallart C et al (2007) *AJ* 134:1124

- Bigiel F, Leroy A, Walter F et al (2010) AJ 140:1194
- Binggeli B (1994) Dwarf galaxies. In: Meylan G, Prugniel P (eds) ESO conference and workshop proceedings, lc1994. ESO, Garching, p 13
- Boulares A, Cox DP (1990) ApJ 365:544
- Bournaud F, Elmegreen BG, Teyssier R, Block DL, Puerari I (2010) MNRAS 409:1088
- Boylan-Kolchin M, Bullock JS, Kaplinghat M (2011) MNRAS 415:40
- Bruzual G, Charlot S (2003) MNRAS 344:1000
- Calzetti D (1997) AJ 113:162
- Calzetti D (2001) PASP 113:1449
- Calzetti D, Armus L, Bohlin RC et al (2000) ApJ 533:682
- Chabrier G (2003) PASP 115:763
- Charlot S, Bruzual AG (1991) ApJ 367:126
- Charlot S, Fall SM (2000) ApJ 539:718
- Chiappini C, Matteucci F, Gratton R (1997) ApJ 477:765
- Cho J, Lazarian A (2003) MNRAS 345:325
- Cid Fernandes R, Mateus A, Sodré L, Stasińska G, Gomes JM (2005) MNRAS 358:363
- Cole AA, Skillman ED, Tolstoy E et al (2007) ApJ 659:17
- Colless M, Dalton G, Maddox S et al (2001) MNRAS 328:1039
- Crovisier J, Dickey JM (1983) A&A 122:282
- Croxall KV, van Zee L, Lee H, Skillman ED, Lee JC, Côté S, Kennicutt RC Jr, Miller BW (2009) ApJ 705:723
- Dabringhausen J, Hilker M, Kroupa P (2008) MNRAS 386:864
- Dalcanton JJ, Spergel DN, Summers FJ (1997) ApJ 482:659
- Dale DA, Cohen SA, Johnson LC et al (2009) ApJ 703:517
- de Blok WJG, Walter F (2000) ApJ 537:95
- de Blok WJG, Walter F (2006) AJ 131:343
- Dekel A, Birnboim Y (2006) MNRAS 368:2
- Dekel A, Silk J (1986) ApJ 303:39
- Dickey JM, McClure-Griffiths NM, Stanimirović S, Gaensler BM, Green AJ (2001) ApJ 561:264
- Dolphin AE (2002) MNRAS 332:91
- Dressler A (1980) ApJ 236:351
- Driver SP, Norberg P, Baldry IK et al (2009) Astron Geophys 50:12
- Efremov YN, Elmegreen BG (1998) MNRAS 299:588
- Elmegreen BG (2000) ApJ 530:277
- Elmegreen DM, Elmegreen BG (1984) ApJS 54:127
- Elmegreen BG, Hunter DA (2006) ApJ 636:149
- Elmegreen BG, Scalo J (2004) ARA&A 42:211
- Elmegreen BG, Kim S, Staveley-Smith L (2001) ApJ 548:749
- Fazio GG, Hora JL, Allen LE et al (2004) ApJS 154:10
- Ferrarese L, Côté P, Jordán A et al (2006) ApJS 164:334
- Field GB, Goldsmith DW, Habing HJ (1969) ApJ 155:149
- Fischera J, Dopita MA, Sutherland RS (2003) ApJ 599:21
- Flores RA, Primack JR (1994) ApJ 427:1
- Freeman KC (1970) ApJ 160:811
- Gallagher JS III, Hunter DA, Tutukov AV (1984) ApJ 284:544
- Gallart C, Aparicio A, Bertelli G, Chiosi C (1996) AJ 112:2596
- Gallart C, Zoccali M, Aparicio A (2005) ARA&A 43:387
- Gallart C, Stetson PB, Meschin IP et al (2008) ApJ 682:89
- Gazol A, Kim J (2010) ApJ 723:482
- Gerola H, Seiden PE, Schulman LS (1980) ApJ 242:517
- Gibson SJ, Taylor AR, Higgs LA et al (2005) ApJ 626:195
- Gladwin PP, Kitsionas S, Boffin HMJ, Whitworth AP (1999) MNRAS 302:305
- Gogarten SM et al (2010) ApJ 712:858

- Goldreich P, Sridhar S (1995) ApJ 438:763
Governato F, Brook C, Mayer L et al (2010) Nature 463:203
Green DA (1993) MNRAS 262:327
Gunn JE, Gott JR (1972) ApJ 176:1
Guseva NG, Izotov YI, Papaderos P et al (2001) A&A 378:756
Haud U, Kalberla PMW (2007) A&A 466:555
Heiles C, Troland TH (2003) ApJ 586:1067
Hidalgo SL, Aparicio A, Martínez-Delgado D, Gallart C (2009) ApJ 705:704
Hidalgo SL, Aparicio A, Skillman E et al (2011) ApJ 730:14
Hubble E (1936) The realm of the nebulae. Yale University Press, New Haven
Hunter DA, Elmegreen BG (2004) AJ 128:2170
Hunter DA, Hoffman L (1999) AJ 117:2789
Hunter DA, Elmegreen BG, Baker AL (1998) ApJ 493(H98):595
Indu G, Subramaniam A (2011) A&A 535:115
Jansen RA, Franx M, Fabricant D, Caldwell N (2000) ApJS 126:271
Jenkins EB, Tripp TM (2001) ApJS 137:297
Jones LA, Worthey G (1995) ApJ 446:31
Kendall S, Kennicutt RC, Clarke C, Thornley MD (2008) MNRAS 387:1007
Kennicutt RC Jr (1989) ApJ 344:685
Kennicutt RC, Stetson PB Jr, Saha A et al. (1998) ApJ 498:181
Keres D, Katz N, Weinberg DH, Davé R (2005) MNRAS 363:2
Khalil A, Joncas G, Nekka F, Kestener P, Arneodo A (2006) ApJS 165:512
Kim J, Ryu D (2005) ApJ 630:45
Klypin A, Kravtsov AV, Valenzuela O, Prada F (1999) ApJ 522:82
Kobulnicky HA, Skillman ED (1996) ApJ 471:211
Kolmogorov A (1941) DoSSR 30:301
Kong X, Charlot S, Weiss A, Cheng FZ (2003) A&A 403:877
Kormendy J (1985) ApJ 295:73
Kormendy J, Bender R (1996) ApJ 464:119
Kormendy J, Bender R (2012) ApJS 198:2 doi:[10.1088/0067-0049/198/1/2](https://doi.org/10.1088/0067-0049/198/1/2)
Kormendy J, Djorgovski S (1989) ARA&A 27:235
Kowal G, Lazarian A, Beresnyak A (2007) ApJ 658:423
Kritsuk AG, Norman ML (2002) ApJ 569:L127
Kroupa P, Tout CA, Gilmore G (1993) MNRAS 262:545
Krumholz MR, McKee CF (2005) ApJ 630:250
Krumholz MR, Klein RI, McKee CF (2011) ApJ 740:74
Larson RB (1976) MNRAS 176:31
Larson RB (1981) MNRAS 194:809
Larson RB, Tinsley BM (1978) ApJ 219:46
Lazarian A, Pogosyan D (2000) ApJ 537(LP00):720
Leitherer C, Schaerer D, Goldader JD et al (1999) ApJS 123:3
Leroy AK, Walter F, Brinks E et al (2008) AJ 136:2782
Lithwick Y, Goldreich P (2001) ApJ 562:279
Mac Low MM (1999) ApJ 524:169
Mac Low M-M, Klessen RS (2004) Rev Mod Phys 76:125
Martin CL, Kennicutt RC Jr (2001) ApJ 555:301
Martin DC, Fanson J, Schiminovich D et al (2005) ApJ 619:1
Mateo ML (1998) ARA&A 36:435
Mayer L, Governato F, Colpi M et al (2001a) ApJ 547:123
Mayer L, Governato F, Colpi M et al (2001b) ApJ 559:754
McConnachie AW, Arimoto N, Irwin M, Tolstoy E (2006) MNRAS 373:715
Meurer GR, Heckman TM, Leitherer C et al (1995) AJ 110:2665
Miller GE, Scalo JM (1979) ApJS 41:513

- Mo HJ, Mao S, White SDM (1998) MNRAS 295:319
- Monelli M, Gallart C, Hidalgo SL et al (2010a) ApJ 722:1864
- Monelli M, Hidalgo SL, Stetson PB et al (2010b) ApJ 720:1225
- Moore B, Katz N, Lake G, Dressler A, Oemler A (1996) Nature 379:613
- Norman CA, Ferrara A (1996) ApJ 467:280
- Padoan P, Nordlund A (2002) ApJ 576:870
- Quirk WJ (1972) ApJ 176:9
- Roberts MS (2008) Frontiers of astrophysics. In: Astronomical society of the Pacific conference series, vol 395, p 283
- Saffman PG (1971) Stud. Appl. Math. 50:377–83
- Salpeter EE (1955) ApJ 121:161
- Sargent WLW, Searle L (1970) ApJ 162:155
- Schweizer F (1982) ApJ 252:455
- Sellwood JA, Balbus SA (1999) ApJ 511:660
- Shaver PA, McGee RX, Newton LM, Danks AC, Pottasch SR (1983) MNRAS 204:53
- Shi Y et al (2011) ApJ 733:87
- Skillman ED, Tolstoy E, Cole AA et al (2003) ApJ 596:253
- Smith EP, Pica AJ, Bohlin RC et al (1996) ApJS 104:287
- Stanimirović S, Lazarian A (2001) ApJ 551:53
- Stanimirović S, Staveley-Smith L, Dickey JM, Sault RJ, Snowden SL (1999) MNRAS 302:417
- Stanimirović S, Staveley-Smith L, van der Hulst JM et al (2000) MNRAS 315:791
- Stark D, Ellis RS, Richard J et al (2007) ApJ 663:10
- Stone JM, Ostriker EC, Gammie CF (1998) ApJ 508:99
- Swaters RA, van Albada TS, van der Hulst JM, Sancisi R (2002) A&A 390:829
- Tammann GA (1994) Dwarf galaxies. In: Meylan G, Prugniel P (eds) European south observatory astrophysics symposium, vol 49. ESO, Garching, pp 3–9
- Taylor VA, Jansen RA, Windhorst RA, Odewahn SC, Hibbard JE (2005) ApJ 630:784
- Tinsley BM (1968) ApJ 151:547
- Tolstoy E, Irwin MJ, Helmi A et al (2004) ApJ 617:119
- Tolstoy E, Hill V, Tosi M (2009) ARA&A 47:371
- Toomre A (1964) ApJ 139:1217
- Toomre A, Toomre J (1972) ApJ 178:623
- Tortora C, Napolitano NR, Cardone VF, Capaccioli M, Jetzer Ph, Molinaro R (2010) MNRAS 407:144
- Tully RB, Verheijen MAW, Pierce MJ, Huang J, Wainscoat RJ (1996) AJ 112:2471
- Vader JP, Vigroux L (1991) A&A 246:32
- van den Bergh S (1966) AJ 71:922
- van der Kruit PC (1990) The milky way as a galaxy. University Science Books, California
- van der Kruit PC, Allen RJ (1978) ARA&A 16:103
- van der Kruit PC, Searle L (1982) A&A 110:61
- van Zee L (2001) AJ 121:2003
- van Zee L, Haynes MP (2006) ApJ 636:214
- Vazdekis A, Arimoto N (1999) ApJ 525:144
- von Weizsacker CF (1951) ApJ 114:165
- Wada K, Meurer G, Norman CA (2002) ApJ 577:197
- Weinberg DH, Bullock JS, Governato F et al (2013). [arXiv:1306.0913](https://arxiv.org/abs/1306.0913)
- Weisz DR, Dalcanton JJ, Williams BF et al (2011) ApJ 739:5
- White SDM, Rees MJ (1978) MNRAS 183:341
- Willett KW, Elmegreen BG, Hunter DA (2005) AJ 129:2186
- Williams BF et al (2009) ApJ 695:15
- Witt AN, Thronson HA Jr, Capuano JM Jr (1992) ApJ 393:611
- Witt AN, Gordon KD (2000) ApJ 528:799
- Wolfire MG, Hollenbach D, McKee CF et al (1995) ApJ 443:152

- Wolfire MG, McKee CF, Hollenbach D, Tielens AGGM (2003) ApJ 587:278
Yang CC, Gruendl RA, Chu YH (2007) ApJ 671:374
York DG, Adelman J, Anderson JE Jr et al (2000) AJ 120:1579
Young LM, Lo KY (1996) ApJ 464:59
Young LM, Lo KY (1997) ApJ 476:127
Zhang Q, Fall SM, Whitmore BC (2001) ApJ 561:727
Zhang H-X, Hunter DA, Elmegreen BG, Gao Y, Schrubba A (2012) AJ 143:47
Zhao Y, Gu Q, Gao Y (2011) AJ 141:68

Chapter 2

Stellar Disk Evolution of Nearby Dwarf Galaxies

Abstract We have studied multiband surface brightness profiles of a representative sample of 34 nearby dwarf irregular galaxies. Our data include *Galaxy Evolution Explorer* (GALEX) FUV/NUV, *UBV*, $H\alpha$, and *Spitzer* 3.6 μm images. These galaxies constitute the majority of the LITTLE THINGS survey (Local Irregulars That Trace Luminosity Extremes—The H I Nearby Galaxy Survey, <http://www.lowell.edu/users/dah/littlethings/index.html>). By modeling the azimuthal averages of the spectral energy distributions with a complete library of star formation (SF) histories, we derived the stellar mass surface density distributions and the SF rate (SFR) averaged over three different timescales: the recent 0.1 Gyr, 1 Gyr, and a Hubble time. We find that, for $\sim 80\%$ (27 galaxies) of our sample galaxies, radial profiles (at least in the outer part) at shorter wavelengths, corresponding to younger stellar populations, have shorter disk scale lengths than those at longer wavelengths, corresponding to older stellar populations. This indicates that the star-forming disk has been shrinking. In addition, the radial distributions of the stellar mass surface density are well described as piece-wise exponential profiles, and $\sim 80\%$ of the galaxies have steeper mass profiles in the outer disk than in the inner region. The steep radial decline of SFR in the outer parts compared to that in the inner disks gives a natural explanation for the down-bending stellar mass surface density profiles. Within the inner disks, our sample galaxies on average have constant ratios of recent SFR to stellar mass with radius. Nevertheless, $\sim 35\%$ (12 galaxies, among which 7 have baryonic mass $\lesssim 10^8 M_{\odot}$) of the sample exhibit negative slopes across the observed disk, which is in contrast with the so-called “inside-out” disk growth scenario suggested for luminous spiral galaxies. The tendency of SF to become concentrated toward the inner disks in low-mass dwarf irregular galaxies is interpreted as a result of their susceptibility to environmental effects and regulation through stellar feedback.

2.1 The Sample

In this section, we introduce the sample of dwarf galaxies compiled by LITTLE THINGS (Local Irregulars That Trace Luminosity Extremes, The H I Nearby Galaxy Survey; PI: Deidre Hunter). The galaxies studied in this work constitute a subsample of the 41 galaxies included in the LITTLE THINGS.

2.1.1 Parent Sample of *LITTLE THINGS*

To address the fundamental question of the driving mechanisms of SF in dwarf irregular galaxies, Hunter and Elmegreen (2004, 2006) carried out a systematic optical imaging survey (narrow band $H\alpha$, broadband UBV) of a large sample of nearby star-forming dwarf galaxies using telescopes, such as the KPNO 4 m, CTIO 1.5 m, Perkins 1.8 m Telescope, and Hall 1.1 m Telescope. The (2004, 2006) sample includes 94 Im, 26 blue compact dwarfs (BCDs), and 20 Sm galaxies, most of which are located within 30 Mpc from the Milky Way. While this sample is not complete in any sense, it spans a large range in galactic parameters including integrated luminosity ($-19 < M_V < -9$, Fig. 2.1), average surface brightness ($20 < \mu_{25} < 27$ B mag arcsec $^{-2}$, Fig. 2.1), gas mass to B -band luminosity ratio ($0.02 - 5 M_{\text{gas}}/L_B$, Fig. 2.1), and SF surface density ($0 < \Sigma_{\text{SFR}} < 1.3 M_{\odot} \text{ yr}^{-1} \text{ kpc}^{-2}$, Fig. 2.1), and thus constitute a large and representative sample of late-type dwarf galaxies in the local universe.

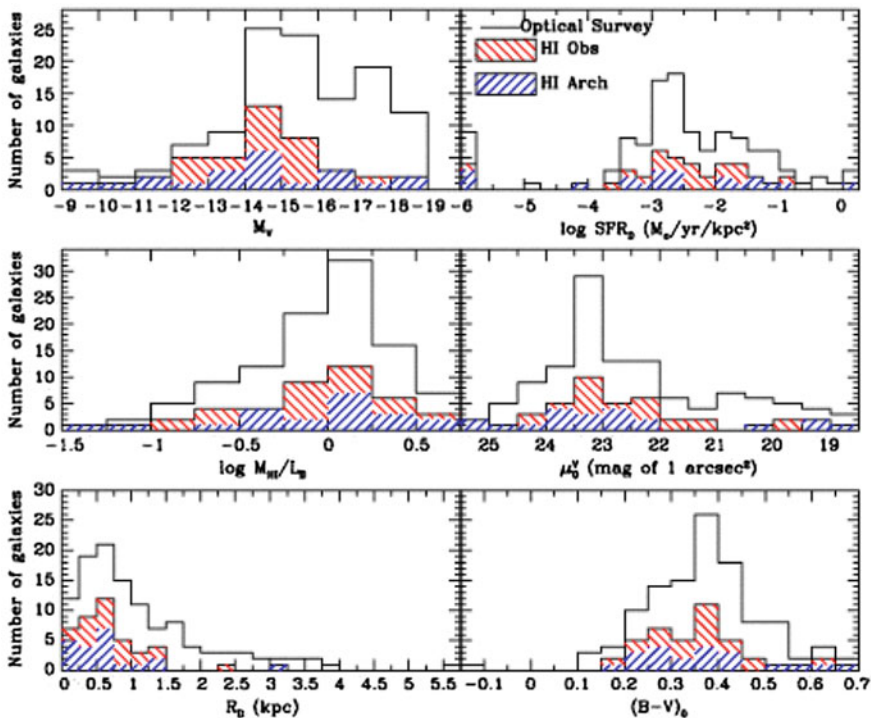
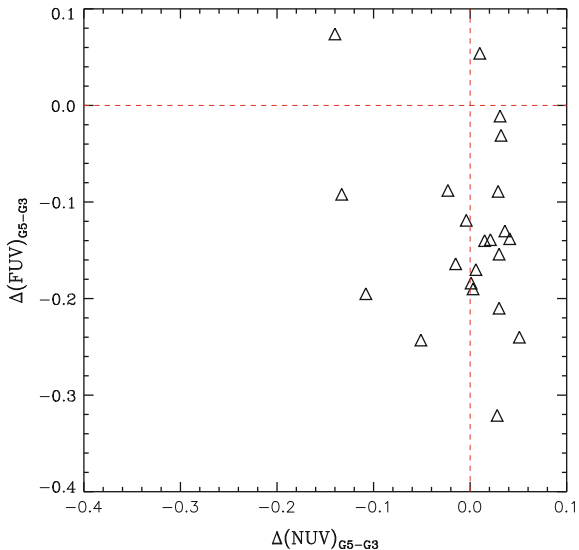


Fig. 2.1 Properties of the *LITTLE THINGS* sample (new VLA observations [*hashed +45°*] and archive data [*hashed -45°*]) compared to the entire optical survey of Hunter and Elmegreen (2006; *no hash*). The *LITTLE THINGS* sample covers the range of parameters of the full survey. SFR_D is the SFR, based on $H\alpha$ emission, normalized to πR_D^2 , where R_D is the disk scale length determined from a V -band image. A SF rate per unit area of 0 is plotted as a log of -6 . The parameter μ_0^V is the central surface brightness determined from a fit to the V -band surface brightness profile. This figure is adapted from Hunter et al. (2012)

Fig. 2.2 Comparison between integrated GALEX FUV (y -axis) and NUV (x -axis) photometry based on images from the GALEX GR5 pipeline and from the GALEX GR3 pipeline. Each *triangle* represents the photometry for one of our sample galaxies. The same elliptical apertures are used for GR5 and GR3 photometry of each galaxy. Note that the calibration of the GALEX (especially FUV) images changed/improved significantly from GR3 to GR5



2.1.2 *LITTLE THINGS: A Representative Sample of Nearby Dwarf Irregular Galaxies*

As an extension of the THINGS (The H I Nearby Galaxy Survey, PI: Fabian Walter) project to dwarf galaxies, the LITTLE THINGS (project AH927, PI: Deidre Hunter) embarked on a large H I emission line survey of a representative sample of 41 relatively isolated nearby dwarf irregular galaxies using the Very Large Array telescope (VLA) in B, C, and D configurations from December 2007 to August 2008. The sample includes 37 Im galaxies and 4 BCDs, which were drawn from the larger multi-wavelength survey as introduced in Sect. 2.1.1. The LITTLE THINGS galaxies were selected to be representative of its larger parent sample (Fig. 2.1). The sample galaxies were selected to be within $\lesssim 10$ Mpc, with an average distance of 3.7 Mpc. In addition, galaxies with W_{20} (full width at 20% of the peak of an integrated H I velocity profile) $> 160 \text{ km s}^{-1}$ were excluded from the sample in order to guarantee a good continuum subtraction. Moreover, galaxies with disk inclination greater than 70° were also excluded from the sample so that the disk structures can be reasonably resolved. The LITTLE THINGS benefits from a rich multi-wavelength collection of ancillary data on the sample galaxies, as summarized in Table 2.1. Details about the observations and data reduction of the VLA H I data will be presented in the next chapter, where we studied the spatial power spectra of the H I gas distribution.

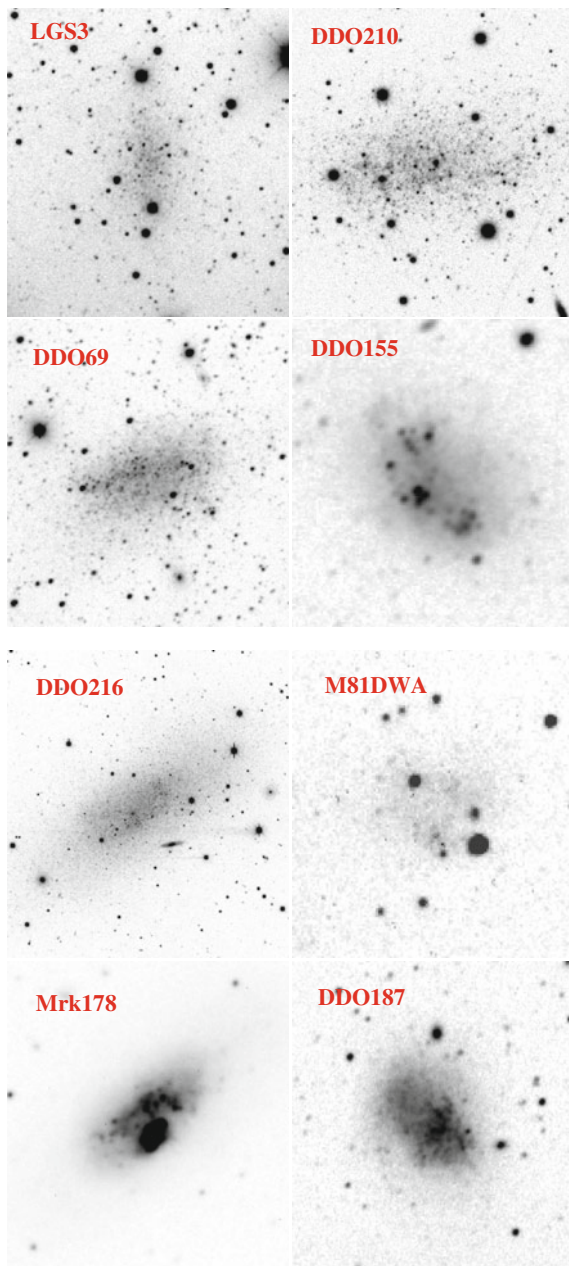


Fig. 2.3 Optical V-band images of the 34 galaxies studied in this work. These imaging data were collected by Deidre Hunter (Hunter and Elmegreen 2006)

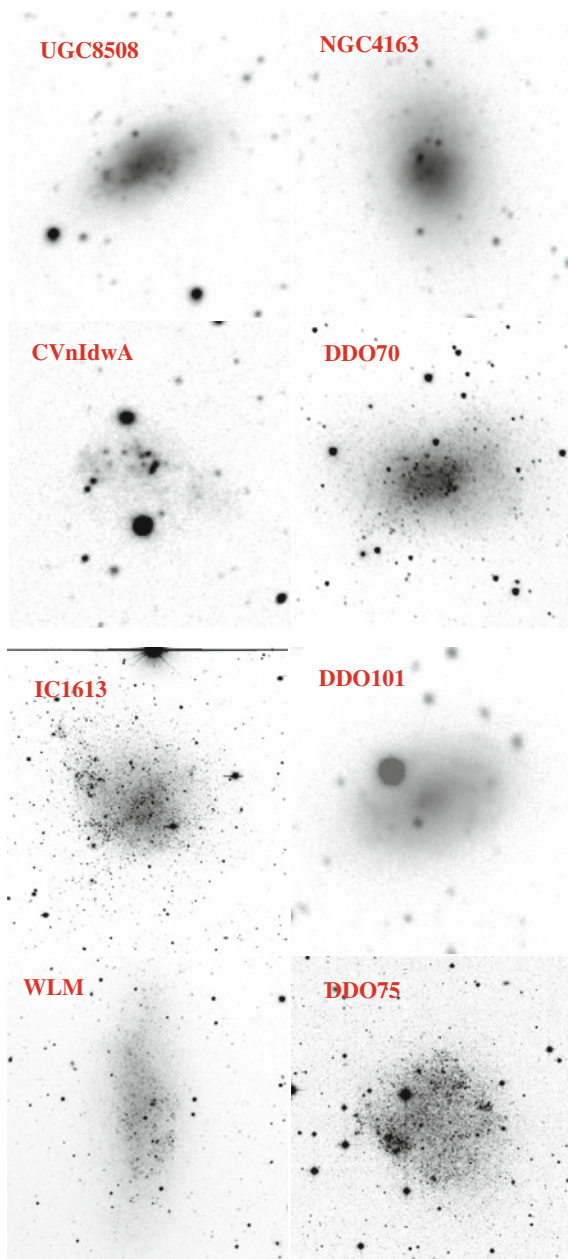


Fig. 2.3 (continued)

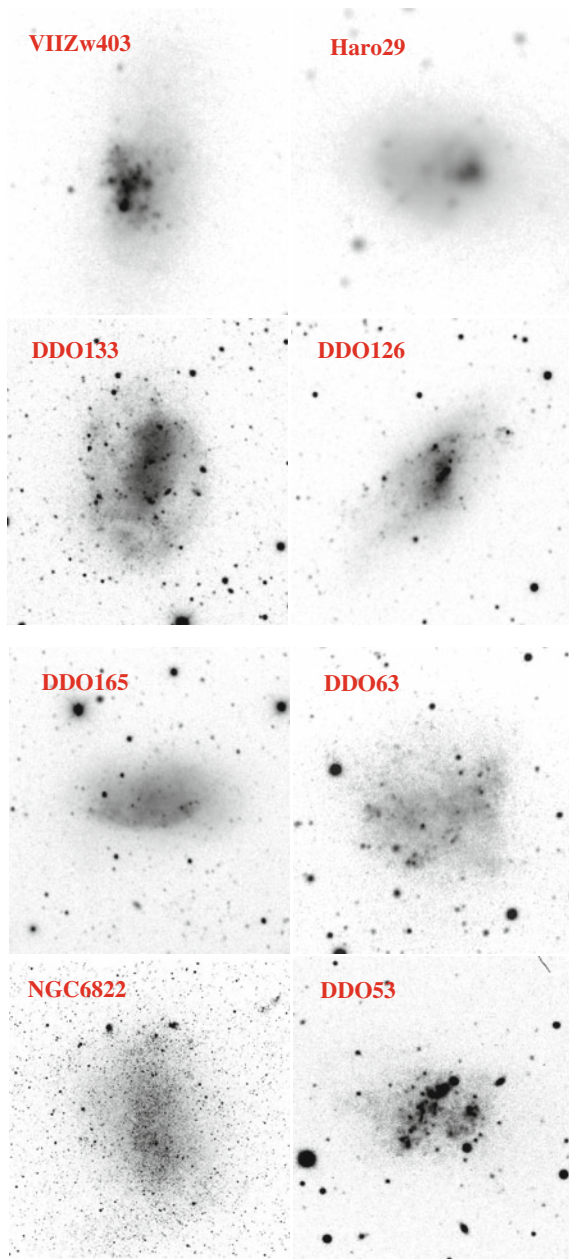


Fig. 2.3 (continued)

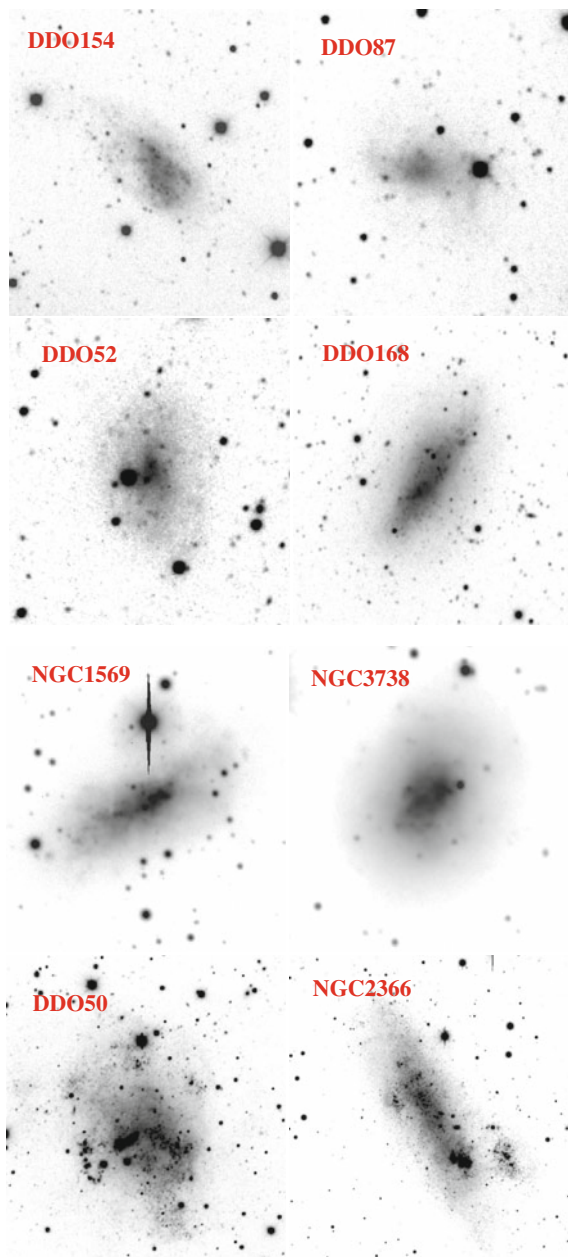


Fig. 2.3 (continued)

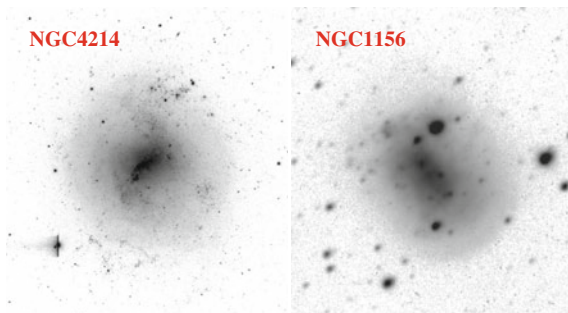


Fig. 2.3 (continued)

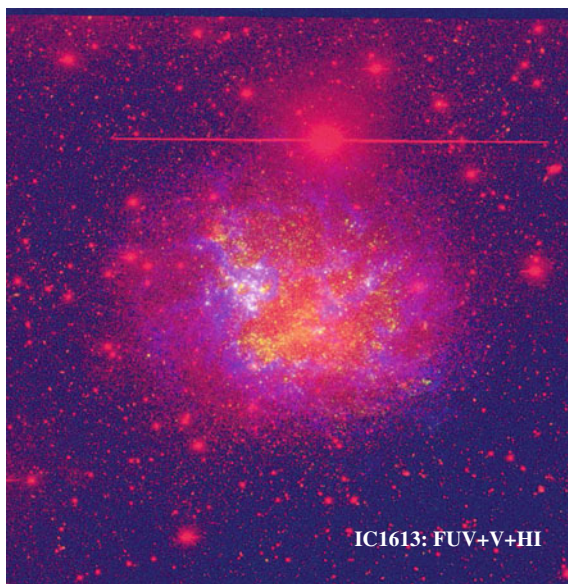


Fig. 2.4 Color composite image of IC1613. V-band is shown as *red*, FUV is shown as *green*, and HI integrated intensity is shown as *blue*. It is obvious that the atomic gas and the recent SF tracer FUV exhibit a more centrally concentrated distribution than the V-band emission, which traces relatively older stellar population. Note that the hole (or deficit) of HI distribution at the center is probably attributed to feedback from the recent cycle of starburst in the central region

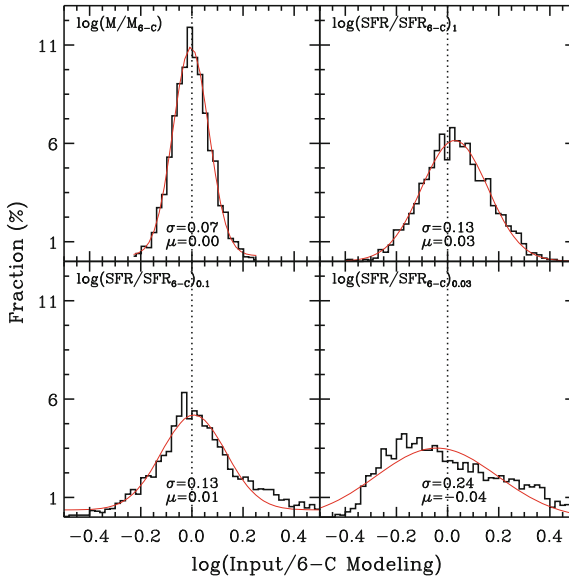


Fig. 2.5 Histograms of the ratios of the parameters (M_* , SFR_1 , $SFR_{0.1}$, and $SFR_{0.03}$) from the input mock SF histories to the best estimates derived from the 6-component (6-C) modeling. The *abscissa* in each panel is the logarithm of the relevant ratio (indicated in each panel) of the input and of the 6-C modeling results. The *ordinate* is the per cent of the data points in each bin. The *dotted line* in each panel marks the relationship of equality. The *red curve* in each panel is the gaussian fit to the relevant histogram. σ and μ indicate the best fitting parameters defining the gaussian curve. The figure is adapted from Zhang et al. (2012)

2.1.3 A Subsample of *LITTLE THINGS* for Studying the Stellar Disk Evolution

The 34 galaxies studied in this work were chosen to have the full complement of data available, including *GALEX* FUV/NUV, *UBV*, $H\alpha$, and *Spitzer* 3.6 μm . The Two Micron All Sky Survey (2MASS) *JHK_s* images are too shallow to be used in this work. However, UGC8508, which was not observed by *GALEX* due to a nearby bright star, and DDO165, which was not yet observed in *GALEX* FUV, are also included in our current sample. Moreover, another three galaxies (LGS3, M81dwA, DDO210) without $H\alpha$ detection were also included in our sample. Some global properties of this subsample are listed in Table 2.1.

Table 2.1 Galaxy sample

Galaxy	Other Names	D (Mpc)	b/a	$E(B - V)_f$	M_B	$\log(\Sigma_{\text{SFR}(\text{H}\alpha)})$ ($M_\odot \text{ yr}^{-1} \text{ kpc}^{-2}$)	M_{bary} (M_\odot)	M_{gas}/M_\star	Θ
(1)	(2)	(3)	(4)	(5)	(6)	(7)	(8)	(9)	(10)
LGS 3 ...	Pisces Dwarf	0.7	0.51	0.041	-9.11	...	5.68	0.76	1.7
DDO 210 .	Aquarius Dwarf	0.9	0.48	0.051	-10.38	...	6.60	4.90	-0.1
DDO 69 ..	UGC 5364, Leo A	0.8	0.56	0.021	-11.38	-3.28	7.16	13.19	0.2
DDO 155 .	UGC 8091, GR 8	2.2	0.71	0.026	-12.25	-1.50	7.22	4.54	-1.2
DDO 216 .	UGC 12613, Pegasus Dwarf	1.1	0.45	0.066	-13.06	-4.15	7.22	0.10	1.2
M81dwA .	KDG 052	3.6	0.73	0.021	-11.46	...	7.29	13.17	0.7
Mrk 178 ..	UGC 6541	3.9	0.46	0.018	-13.76	-1.53	7.39	1.21	-0.7
DDO 187 .	UGC 9128	2.2	0.80	0.024	-12.38	-2.64	7.43	6.78	-1.3
UGC 8508	IZw 60	2.6	0.54	0.015	-13.24	-2.12	7.63	4.54	-1.0
NGC 4163	NGC 4167, UGC 7199	2.9	0.64	0.020	-13.95	-2.43	7.69	0.81	0.1
CVn1dwA .	UGCA 292	3.6	0.78	0.016	-12.16	-2.64	7.83	15.66	-0.4
DDO 70 ..	UGC 5373, Sextans B	1.3	0.59	0.032	-13.74	-2.86	7.86	2.68	-0.7
IC 1613 ...	UGC 668, DDO 8	0.7	0.81	0.025	-14.17	-2.64	7.87	1.57	0.9
DDO 101 .	UGC 6900	6.4	0.69	0.022	-14.40	-2.99	7.89	0.19	...

(continued)

Table 2.1 (continued)

Galaxy	Other Names	D (Mpc)	b/a	$E(B - V)_f$	M_B	$\log(\Sigma_{\text{SFR}(\text{H}\alpha)})(M_{\odot} \text{ yr}^{-1} \text{ kpc}^{-2})$	$M_{\text{bary}} (M_{\odot})$	M_{gas}/M_{\star}	Θ
(1)	(2)	(3)	(4)	(5)	(6)	(7)	(8)	(9)	(10)
WLM	UGC 444, DDO 221	1.0	0.44	0.037	-13.98	-2.85	7.98	4.88	0.3
DDO75 ...	UGC 205, Sextans A	1.3	0.85	0.044	-13.72	-1.40	8.04	13.05	-0.6
VII Zw 403	UGC 6456, VV 574	4.4	0.85	0.036	-13.99	-1.82	8.05	5.37	-0.3
Haro 29 ...	UGC 281, Mrk 209, IZw 36	5.9	0.58	0.015	-14.39	-0.82	8.06	7.04	-1.0
DDO 133 .	UGC 7698	3.5	0.69	0.016	-14.36	-2.93	8.30	5.55	-1.1
DDO 126 .	UGC 7559	4.9	0.47	0.014	-14.56	-2.45	8.31	11.60	0.1
DDO 165 .	UGC 8201, II Zw 499	4.6	0.54	0.024	-15.38	-3.52	8.35	5.56	0.0
DDO 63 ..	UGC 5139, Holmberg I	3.9	1.00	0.048	-14.58	-3.44	8.40	6.45	1.5
NGC 6822	IC 4895, DDO 209	0.5	0.79	0.240	-14.76	-1.96	8.40	2.28	0.6
DDO 53 ..	UGC 4459, VII Zw 238	3.6	0.51	0.037	-13.43	-2.50	8.41	25.32	0.7
DDO 154 .	UGC 8024, NGC 4789A	3.7	0.50	0.009	-13.88	-2.60	8.50	36.97	-0.9
DDO 87 ..	UGC 5918, KDG 072, VII Zw 347	7.7	0.58	0.011	-14.52	-3.16	8.53	9.37	-1.5

(continued)

Table 2.1 (continued)

Galaxy	Other Names	D (Mpc)	b/a	$E(B - V)_f$	M_B	$\log(\Sigma_{\text{SFR}(H\alpha)}) (M_\odot \text{ yr}^{-1} \text{ kpc}^{-2})$	$M_{\text{bary}} (M_\odot)$	M_{gas}/M_*	Θ
(1)	(2)	(3)	(4)	(5)	(6)	(7)	(8)	(9)	(10)
DDO 52...	UGC 4426	10.3	0.67	0.037	-15.05	-3.27	8.63	7.04	-1.5
DDO 168.	UGC 8320	4.3	0.63	0.015	-15.35	-2.33	8.71	7.77	0.0
NGC 1569	UGC 3056, Arp 210, VIIZw 16	3.4	0.55	0.604 ^a	-17.35	0.11	8.78	0.66	-0.4
NGC 3738	UGC 6565, Arp 234	4.9	1.00	0.010	-16.70	-1.72	8.83	0.45	-1.0
DDO 50..	UGC 4305, Holmberg II	3.4	0.72	0.032	-16.39	-1.83	9.03	9.11	0.6
NGC 2366	UGC 3851, DDO 42	3.4	0.42	0.036	-16.49	-1.73	9.04	14.81	1.0
NGC 4214	UGC 7278	3.0	0.91	0.022	-17.26	-1.10	9.11	1.69	-0.7
NGC 1156	UGC 2455, VV 531	7.8	0.86	0.224	-18.29	-0.87	9.42	1.19	-1.7

Note—(1) Galaxy names adopted in this work. (2) The other commonly used names in the literature. (3) Distance from Hunter et al. (2012), and references therein. (4) Minor-to-major axis ratio measured on the V -band images. (5) The foreground reddening from Schlegel et al. (1998). (6) B -band absolute magnitude. (7) Integrated star formation rate (SFR) normalized to the area of the galaxy within one V -band disk scale length. The SFR is derived from $H\alpha$. (8) The baryonic (stellar plus atomic gas) mass. The stellar mass is derived from our SED modeling in this work. The atomic gas ($1.34 \times M_{H_I}$) mass is collected from single dish observations in the literature (see Hunter and Elmegreen (2004) for the references). (9) The atomic gas-to-stellar mass ratio. (10) Tidal index Θ from Karachentsev et al. (2004). Θ quantifies the density enhancement (thus the tidal action) caused by the main disturber. The larger the value of Θ is, the stronger gravitational disturbance exerted by the neighboring galaxies. Galaxies with zero or negative values of Θ could be considered as isolated objects.

^aThe average of the $E(B-V)$ derived by Burstein et al. (1982) (0.508) and by Schlegel et al. (1998) (0.700). See Johnson et al. (2012)

2.2 Data

This work utilized multi-wavelength photometry for constraining the radial variations of the SF history. This section briefly introduces the data.

2.2.1 GALEX FUV/NUV

FUV and NUV broadband images were obtained by the Galaxy Evolution Explorer (*GALEX*; Martin et al. 2005) satellite telescope. *GALEX* delivers images with a spatial resolution of $4''.3$ FWHM at FUV ($\lambda_{\text{eff}} = 1528\text{\AA}$, bandwidth $\sim 1344\text{--}1786\text{\AA}$), and $5''.3$ FWHM at NUV ($\lambda_{\text{eff}} = 2271\text{\AA}$, bandwidth $\sim 1771\text{--}2831\text{\AA}$). The field of view of a single *GALEX* pointing is $1^\circ 28'$ in FUV and $1^\circ 24'$ in NUV. Our images were mostly obtained from the *GALEX* Medium Imaging Survey (MIS), with a typical on-source exposure time of 1500 s in each of the two bands.

There have been significant improvement in the flat field and flux calibration of the *GALEX* imaging data from the general release GR2/3 pipeline to GR4/5 pipeline (Fig. 2.2). Therefore, we obtained the GR4/5 pipeline data for all of our galaxies from the Mikulski Archive for Space Telescopes (MAST). Note that the latest release GR6/7 improves further on flat field, flux calibration, and astrometry calibration with respect to GR4/5. However, the improvement is expected to be smaller than 1%, which is negligible in the full error budget of our surface photometry and spectral energy distribution modeling.

The ultraviolet continuum emission is dominated by young stellar populations with typical masses of $\gtrsim 3\text{--}5 M_{\odot}$ and typical ages of $<$ a few hundred Myr, and thus is a direct tracer of recent SF activity.

2.2.2 Optical UB V

The *UBV* images for the parent sample of LITTLE THINGS were obtained by Deidre Hunter in 27 observing runs using various ground-based telescopes. Most of the observations were made with a SITe 2048 \times 2048 CCD on either the Lowell Observatory Hall 1.1m Telescope or Perkins 1.8m Telescope. A few LITTLE THINGS galaxies, including DDO53, DDO210, DDO216, NGC1569, NGC2366, NGC4214, and SagDIG, were observed with the Kitt Peak National Observatory 4m Telescope (KPNO 4m). DDO75 was observed with the Cerro Tololo Inter-American Observatory 0.9m Telescope (CTIO 0.9m). The typical seeing condition during the observations is $\sim 1.5''\text{--}3.0''$.

The readers are referred to Hunter and Elmegreen (2006) regarding the details of observations and data reduction. Briefly, the telescope position was usually offset by $20''$ between each observation in order to average over flat-fielding defects and

eliminate cosmic rays, and twilight sky flats were taken for flat-fielding. The overscan region on each CCD was used for bias subtraction. In addition, the Landolt (1992) standards were observed in each observing run for flux calibration.

The optical emission through the UBV bands is mainly contributed by stellar populations formed over the past one to several Gyr in non-starbursting galaxies.

2.2.3 *Narrow-Band H α Imaging*

The narrow-band $H\alpha$ images, together with the accompanying continuum-only off-band images, of the parent sample of LITTLE THINGS were obtained in 22 observing runs by Deidre Hunter. The $H\alpha$ filters used in these observing runs usually have a FWHM of $\sim 30\text{\AA}$. All of the LITTLE THINGS galaxies were observed with either the Lowell Observatory Hall 1.1 m Telescope or Perkins 1.8 m Telescope. The typical seeing condition during the observations is $\sim 1.5'' \sim 3.0''$.

Details about the observations and data reduction were given in Hunter and Elmegreen (2004). In particular, the off-band continuum images were shifted, scaled, and subtracted from the narrow-band $H\alpha$ images to obtain images of pure $H\alpha$ emission. The $H\alpha$ emission was calibrated with the known $H\alpha$ flux from the H II regions NGC2363 and NGC604 and from spectrophotometric standard stars. In addition, correction for both the temperature shift of bandpass and the contamination from [N II] 6583 \AA and [N II] 6549 \AA nebular line was applied to the $H\alpha$ images.

The nebular recombination lines, including $H\alpha$, reemit the integrated stellar luminosity of galaxies shortward of the Lyman limit, so they offer a direct probe of the massive stellar populations with masses of $>8\text{--}10 M_{\odot}$ and lifetimes of $<10\text{--}20$ Myr. This means that these nebular emission lines provide a nearly instantaneous measure of the current SFR.

2.2.4 *Spitzer 3.6 μm*

The *Spitzer* IRAC (Fazio et al. 2004) 3.6 μm images were obtained and reduced by the Local Volume Legacy Survey (LVL; Dale et al. 2009) and the *Spitzer* Infrared Nearby Galaxy Survey (SINGS; Kennicutt et al. 2003). The two surveys adopted the same observing strategy. In particular, two sets of four dithered 30 s integrations were taken by constructing the Astronomical Observing Requests. For galaxies larger than the IRAC field of view ($\sim 5'$), a mosaicking strategy was used to cover the full optical size of each galaxy.

As detailed in Dale et al. (2009), besides the standard post-pipeline processing, additional processing, including distortion corrections, rotation of the individual frames, bias structure, and bias drift correction, image offset determinations via pointing refinements from the pipeline, detector artifact removal, constant level background subtraction, and image resampling to $0''.75$ pixels using a drizzling technique,

have been done with the MOPEX and self-developed reduction softwares by LVL and SINGS respectively. The spatial resolution of the resultant images in $3.6\ \mu\text{m}$ are $\sim 1''.6$.

The near-IR $3.6\ \mu\text{m}$ band is primarily stellar emission from the mass-dominant older populations (e.g., Helou et al. 2004), even though there could be a significant contribution from hot dust in intense starburst regions (e.g., Zhang et al. 2010). Furthermore, in low-metallicity dwarf irregular galaxies, the contribution of polycyclic aromatic hydrocarbon dust emission to $3.6\ \mu\text{m}$ passband is substantially weaker than that in high-metallicity massive galaxies (Engelbracht et al. 2008), which suggests that the IRAC $3.6\ \mu\text{m}$ band is a reliable tracer of underlying old stellar populations in typical dwarf irregular galaxies.

2.3 Surface Photometry

We follow the procedures as laid out in Hunter and Elmegreen (2004) for the surface photometry. First, the background-subtracted images were geometrically transformed and aligned with the V -band image. Background-and-foreground sources not belonging to the galaxy were masked. Then, the surface photometry was carried out with the Image Reduction and Analysis Facility (IRAF¹) task ELLIPSE, adopting the same geometrical parameters as derived by Hunter and Elmegreen (2004). Briefly, the center of the galaxy, position angle, and the ellipticity were determined from a contour in the outer half of the V -band image that was block-averaged by factors of a few to increase the signal-to-noise. Then, surface photometry was carried out along the semimajor axis of each galaxy, with the center being fixed as the geometrical center of the above determined isophote and the direction of the major axis being the longest bisector that passes through the center that, as much as possible, symmetrically divides the galaxy. The reader is referred to Hunter and Elmegreen (2004, 2006) for more details about the surface photometry of the UBV and $H\alpha$ images.

To perform photometry on the *GALEX* images, as described in Hunter et al. (2010), we masked foreground stars and background galaxies identified mainly in the higher resolution optical band images. For the removal of sky background, because the background was quite flat, we measured the sky level in tens of square regions (10 pixel by 10 pixel) sampled along an ellipse around the galaxy, but far enough from the galactic center to avoid emission from the target galaxy. The final sky level was determined as the average of the sky values in all sampled subregions. As to the uncertainties of the background removal, the standard deviation of the mean sky values $\sigma_{\langle sky \rangle}$ among the surrounding sky regions is usually an order of magnitude smaller than the mean of the standard deviation in individual regions $\langle \sigma_{sky} \rangle$. Therefore, only the $\langle \sigma_{sky} \rangle$ were considered.

¹IRAF is distributed by the National Optical Astronomy Observatory, which is operated by the Association of Universities for Research in Astronomy (AURA) under cooperative agreement with the National Science Foundation.

For the *Spitzer* 3.6 μm images, we first applied the same photometry mask as was used for the optical band images. Background galaxies can significantly affect the photometry on 3.6 μm images of faint dwarf galaxies. Whenever available, high-resolution archival Hubble Space Telescope (*HST*) imaging data were inspected to further remove the background galaxies based on morphology.

Finally, by dividing the luminosity differences between adjacent ellipses by the area of the annulus, we obtained azimuthally averaged surface brightness profiles. A value of 0.15 mag was taken as the calibration uncertainty for the *GALEX* UV data, and 0.1 mag for *Spitzer* 3.6 μm . The calibration uncertainties of the *UBV* data for each galaxy were given in Hunter and Elmegreen (2006). We adopt a 20% calibration uncertainty for all of the $H\alpha$ photometry.

Note that multiband surface photometry is carried out on the images that were geometrically transformed to match the *V*-band images, with the same elliptical isophotal parameters as that used for *V*-band images. The relative uncertainty in the surface photometry at each elliptical annulus was determined by assuming Poisson statistics and is the sum of the squares of the uncertainties in the galaxy counts in each of the two ellipses that form the annulus and in the sky for each ellipse, divided by the galaxy counts in the annulus, f_a :

$$\sigma_\mu = \frac{1.086}{f_a} \sqrt{(f'_2 + f'_1 + 2s(A_1 + A_2))/g}, \quad (2.1)$$

where subscript 1 and 2 refer to the first and second ellipses that bracket the annulus in question, f' is the sky-subtracted counts, s is the average sky per pixel in the image, A is the area of the ellipse in pixels, and g is the gain of the CCD (Hunter and Elmegreen 2006).

Routinely one uses the average Milky Way (MW) extinction curve ($R_V = A_V / E_{B-V} = 3.1$, Cardelli et al. 1989) to correct the photometry for the Galactic extinction. However, there is considerable scatter of the extinction curve shape from sightline to sightline through the Galaxy (Fitzpatrick 1999), which could significantly influence dereddening of the short-wavelength data (e.g., UV, *U*) when only an average extinction curve was adopted. Fitzpatrick (1999) gave the typical uncertainties ($\sigma_{E(\lambda-V)/E(B-V)}$, Table 2.1 in Fitzpatrick (1999)) when correcting the data with the average extinction curve. In this work, we included the uncertainty ($E(B-V) \times \sigma_{E(\lambda-V)/E(B-V)}$) of adopting the average MW extinction curve. The final uncertainties assigned to each annulus are a quadratic sum of four contributions: $\langle \sigma_{sky} \rangle$, photometric calibration uncertainties, Poisson noise, and $E(B-V) \times \sigma_{E(\lambda-V)/E(B-V)}$. The flux calibration uncertainties usually dominate all other contributions except in the outer disks.

2.4 Multi-wavelength Surface Brightness Profiles

The surface brightness profiles of $H\alpha$, FUV, B , and $3.6\ \mu\text{m}$ for all galaxies are presented in the first column of Fig. 2.13. The multiband surface brightness profiles broadly follow each other. Nevertheless, for about half of our galaxies, the surface brightness profiles of $H\alpha$ and FUV peak in the circumnuclear regions or even in the intermediate radii, rather than the center. The recent SF indicator $H\alpha$ (and FUV) usually follows the shorter wavelength stellar emission better than the longer wavelength emission, as is quantified below (Table 2.2; Fig. 2.18). Therefore, the correlation between $H\alpha$ and the optical bands seen by others was partly caused by a dominant contribution of recent SF to the optical passbands. The three BCD galaxies (Haro 29, VII Zw 403, Mrk 178) included in our sample show obvious central enhancements even at $3.6\ \mu\text{m}$, which suggests that the central regions have sustained the central starburst that characterizes BCDs for an extended period of time (e.g., Zhao et al. 2011).

To quantify the radial fall-off of the multi-wavelength emission, we obtained scale lengths of the exponential disk, R_D , of the FUV, NUV, U , B , V , and $3.6\ \mu\text{m}$ surface brightness profiles by fitting a single or multi-piece exponential to the profiles ($\mu = \mu_0 + 1.086R/R_D$) with the least squares method. The results are given in Table 2.2. Negative values of the scale lengths in Table 2.2 indicate that the relevant surface brightness increases toward larger radii. To visualize the difference of the scale lengths at different wavelengths, $R_D^{\text{FUV}}/R_D^{3.6\ \mu\text{m}}$ is plotted against $R_D^B/R_D^{3.6\ \mu\text{m}}$ for the galaxies (Fig. 2.18). For the double exponential profiles, we only plot the primary (the outer one for down-bending profiles, and the inner one for up-bending profiles) disk scale lengths in Fig. 2.18. The disk scale lengths measured at shorter wavelengths tend to be smaller than those measured at longer wavelengths.

FUV traces SF over the past ~ 100 Myr, B -band emission is dominated by stellar populations younger than a few Gyr, and $3.6\ \mu\text{m}$ is a very good proxy for SF over the whole lifetime of the galaxy (see references in the Introduction). The low metallicity of dIrr galaxies, combined with the lack of radial metallicity gradients, indicates that the multiband surface brightness profiles should be predominantly determined by the distribution of the different stellar populations, with negligible effects due to changing internal extinction. Therefore, the fact that shorter wavelengths have shorter scale lengths most probably implies that the star-forming disks are shrinking toward the inner regions for most of the dIrr galaxies in our sample. Below, we will come back to this point with the help of multiband SED modeling. The trends we see here in dIrr galaxies are in striking contrast with the findings in the luminous spiral galaxies (e.g., Ryder and Dopita 1994), for which the inside-out disk growth scenario has been suggested and the disk scale length decreases with age.

We note that for more than 50% of the sample galaxies the multiband surface brightness profiles show obvious breaks, especially at shorter wavelengths. $R_{D(\text{out})}^{\text{FUV}}/R_{D(\text{in})}^{\text{FUV}}$ is plotted against $R_{D(\text{out})}^{3.6\ \mu\text{m}}/R_{D(\text{in})}^{3.6\ \mu\text{m}}$ for galaxies exhibiting obvious surface brightness breaks in Fig. 3 of Zhang et al. (2012). As can be seen, most of the galaxies with broken profiles are characterized as down-bending profiles.

Table 2.2 Multiband disk scale length

Galaxy	Inner					Outer														
	R_D^{EUV} (kpc)	R_D^{NUV} (kpc)	R_D^{Z} (kpc)	R_D^{B} (kpc)	R_D^{V} (kpc)	$R_D^{3.6\ \mu\text{m}}$ (kpc)	R_D^{EUV} (kpc)	R_D^{NUV} (kpc)	R_D^{Z} (kpc)	R_D^{B} (kpc)	R_D^{V} (kpc)	$R_D^{3.6\ \mu\text{m}}$ (kpc)	R_D^{EUV} (kpc)	R_D^{NUV} (kpc)	R_D^{Z} (kpc)	R_D^{B} (kpc)	R_D^{V} (kpc)	$R_D^{3.6\ \mu\text{m}}$ (kpc)		
(1)	(2)	(3)	(4)	(5)	(6)	(7)	(8)	(9)	(10)	(11)	(12)	(13)	(8)	(9)	(10)	(11)	(12)	(13)		
LGS 3	0.07 ± 0.01	0.15 ± 0.00	0.20 ± 0.00	0.23 ± 0.00	0.35 ± 0.00	0.31 ± 0.00		
DDO 210 ..	0.12 ± 0.01	0.14 ± 0.00	0.13 ± 0.00	0.16 ± 0.00	0.17 ± 0.00	0.21 ± 0.00		
DDO 69 ..	0.72 ± 0.00	0.59 ± 0.00	0.65 ± 0.00	0.69 ± 0.00	0.83 ± 0.00	3.02 ± 0.05	0.17 ± 0.00	0.17 ± 0.00	0.17 ± 0.00	0.17 ± 0.00	0.18 ± 0.00	0.25 ± 0.00	0.17 ± 0.00	0.17 ± 0.00	0.17 ± 0.00	0.18 ± 0.00	0.18 ± 0.00	0.25 ± 0.00		
DDO 155 ..	0.07 ± 0.00	0.08 ± 0.00	0.09 ± 0.00	0.11 ± 0.00	0.12 ± 0.00	0.16 ± 0.00	
DDO 216 ..	0.16 ± 0.00	0.24 ± 0.00	0.42 ± 0.00	0.48 ± 0.00	0.56 ± 0.00	0.64 ± 0.00	0.48 ± 1.90	0.32 ± 0.01	0.61 ± 0.01	0.50 ± 0.00	0.50 ± 0.00	0.50 ± 0.00	0.48 ± 1.90	0.32 ± 0.01	0.61 ± 0.01	0.50 ± 0.00	0.50 ± 0.00	0.50 ± 0.00		
M81dwA ..	0.20 ± 0.00	0.25 ± 0.00	0.24 ± 0.00	0.25 ± 0.00	0.27 ± 0.00	0.30 ± 0.00	
Mrk 178 ..	0.01 ± 0.00	0.01 ± 0.00	0.18 ± 0.00	0.19 ± 0.00	0.21 ± 0.00	0.29 ± 0.00	0.36 ± 0.00	0.36 ± 0.00	0.36 ± 0.00	0.36 ± 0.00	0.36 ± 0.00	0.36 ± 0.00	0.36 ± 0.00	0.36 ± 0.00	0.36 ± 0.00	0.36 ± 0.00	0.36 ± 0.00	0.36 ± 0.00	0.83 ± 0.00	
DDO 187 ..	0.34 ± 0.00	0.32 ± 0.00	0.32 ± 0.00	0.34 ± 0.00	0.38 ± 0.00	0.56 ± 0.00	0.11 ± 0.00	0.12 ± 0.00	0.14 ± 0.00	0.15 ± 0.00	0.17 ± 0.00	0.15 ± 0.00	0.11 ± 0.00	0.12 ± 0.00	0.14 ± 0.00	0.15 ± 0.00	0.17 ± 0.00	0.15 ± 0.00	0.15 ± 0.00	
UGC 8508	0.21 ± 0.00	0.24 ± 0.00	0.26 ± 0.00	0.30 ± 0.00
NGC 4163 ..	0.11 ± 0.00	0.13 ± 0.00	0.19 ± 0.00	0.22 ± 0.00	0.24 ± 0.00	0.27 ± 0.00
CvldwA ..	0.12 ± 0.00	0.14 ± 0.00	0.20 ± 0.00	0.28 ± 0.00	0.44 ± 0.01	0.37 ± 0.00	0.42 ± 0.00	0.25 ± 0.00	0.36 ± 0.01	0.36 ± 0.00	0.47 ± 0.00	0.47 ± 0.00	0.25 ± 0.00	0.36 ± 0.01	0.28 ± 0.00	0.36 ± 0.00	0.47 ± 0.00	0.69 ± 0.01	0.69 ± 0.01	
DDO 70 ..	0.20 ± 0.00	0.23 ± 0.00	0.30 ± 0.00	0.33 ± 0.00	0.37 ± 0.00	0.42 ± 0.00	0.30 ± 0.00	0.36 ± 0.00	0.36 ± 0.00	0.36 ± 0.00	0.36 ± 0.00	0.36 ± 0.00	0.30 ± 0.00	0.36 ± 0.00	0.29 ± 0.00	0.55 ± 0.00	0.61 ± 0.00	0.61 ± 0.00	0.61 ± 0.00	
IC 1613 ...	-2.40 ± 0.00	-7.05 ± 0.01	2.46 ± 0.01	1.26 ± 0.00	1.12 ± 0.00	0.92 ± 0.00	0.94 ± 0.00	0.22 ± 0.01	0.26 ± 0.00	0.42 ± 0.00	0.45 ± 0.00	0.45 ± 0.00	0.22 ± 0.01	0.26 ± 0.00	0.42 ± 0.00	0.45 ± 0.00	0.47 ± 0.00	0.47 ± 0.00	0.44 ± 0.00	
DDO 101 ..	-3.5 ± 0.22	6.4 ± 0.13	1.30 ± 0.00	1.06 ± 0.00	0.94 ± 0.00	0.93 ± 0.00	0.94 ± 0.00	0.22 ± 0.01	0.26 ± 0.00	0.42 ± 0.00	0.45 ± 0.00	0.45 ± 0.00	0.22 ± 0.01	0.26 ± 0.00	0.42 ± 0.00	0.45 ± 0.00	0.47 ± 0.00	0.47 ± 0.00	0.44 ± 0.00	
WLM	1.03 ± 0.00	0.95 ± 0.00	0.90 ± 0.00	1.23 ± 0.00	1.18 ± 0.00	1.27 ± 0.00	1.18 ± 0.00	0.26 ± 0.00	0.29 ± 0.00	0.40 ± 0.00	0.46 ± 0.00	0.46 ± 0.00	0.26 ± 0.00	0.29 ± 0.00	0.40 ± 0.00	0.46 ± 0.00	0.52 ± 0.00	0.52 ± 0.00	0.53 ± 0.00	
DDO 75 ..	-3.48 ± 0.08	-5.75 ± 0.09	-6.17 ± 0.14	15.08 ± 0.74	9.86 ± 0.25	-1.15 ± 0.00	9.86 ± 0.25	0.16 ± 0.00	0.16 ± 0.00	0.18 ± 0.00	0.20 ± 0.00	0.32 ± 0.00	0.16 ± 0.00	0.16 ± 0.00	0.18 ± 0.00	0.18 ± 0.00	0.20 ± 0.00	0.20 ± 0.00	0.32 ± 0.00	
VII Zw 403 ..	0.18 ± 0.00	0.20 ± 0.00	0.23 ± 0.00	0.27 ± 0.00	0.32 ± 0.00	0.42 ± 0.00	
Haro 29 ...	0.16 ± 0.00	0.18 ± 0.00	0.16 ± 0.00	0.17 ± 0.00	0.17 ± 0.00	0.28 ± 0.00	0.54 ± 0.03	0.54 ± 0.02	0.34 ± 0.00	0.50 ± 0.00	0.50 ± 0.00	0.50 ± 0.00	0.54 ± 0.03	0.54 ± 0.02	0.34 ± 0.00	0.50 ± 0.00	0.50 ± 0.00	0.50 ± 0.00	1.78 ± 0.01	
DDO 133 ..	0.79 ± 0.08	3.70 ± 0.01	1.83 ± 0.01	1.46 ± 0.00	1.34 ± 0.00	1.16 ± 0.00	0.31 ± 0.01	0.37 ± 0.00	0.38 ± 0.00	0.42 ± 0.00	0.47 ± 0.00	0.47 ± 0.00	0.31 ± 0.01	0.37 ± 0.00	0.38 ± 0.00	0.42 ± 0.00	0.47 ± 0.00	0.47 ± 0.00	0.65 ± 0.00	
DDO 126 ..	0.72 ± 0.00	0.75 ± 0.00	0.74 ± 0.00	0.81 ± 0.00	0.82 ± 0.00	1.25 ± 0.00	
DDO 165	-21.4 ± 28.16	3.55 ± 0.01	2.50 ± 0.00	2.37 ± 0.00	2.40 ± 0.01	
DDO 63 ..	-4.87 ± 0.00	-31.25 ± 0.10	6.71 ± 0.11	2.84 ± 0.01	2.65 ± 0.01	2.14 ± 0.01	0.31 ± 0.00	0.38 ± 0.00	0.46 ± 0.00	0.65 ± 0.00	0.65 ± 0.00	0.65 ± 0.00	0.31 ± 0.00	0.38 ± 0.00	0.46 ± 0.00	0.65 ± 0.00	0.64 ± 0.00	0.64 ± 0.00	0.68 ± 0.00	
NGC 6822 ..	1.29 ± 0.00	0.74 ± 0.00	0.63 ± 0.00	0.59 ± 0.00	0.65 ± 0.00	0.65 ± 0.00	
DDO 53 ...	0.20 ± 0.00	0.24 ± 0.00	0.31 ± 0.00	0.43 ± 0.00	0.54 ± 0.00	0.35 ± 0.00	
DDO 154 ..	0.60 ± 0.00	0.56 ± 0.00	0.52 ± 0.00	0.51 ± 0.00	0.52 ± 0.00	0.53 ± 0.00	
DDO 87 ..	0.56 ± 0.01	0.71 ± 0.01	1.94 ± 0.01	1.84 ± 0.01	1.73 ± 0.00	1.75 ± 0.01	0.87 ± 0.03	1.40 ± 0.02	0.81 ± 0.01	1.03 ± 0.01	1.10 ± 0.00	1.35 ± 0.02	0.87 ± 0.03	1.40 ± 0.02	0.81 ± 0.01	1.03 ± 0.01	1.10 ± 0.00	1.35 ± 0.02	1.35 ± 0.02	

(continued)

Table 2.2 (continued)

Galaxy	Inner							Outer					
	R_D^{FUV} (kpc)	R_D^{NUV} (kpc)	R_D^U (kpc)	R_D^B (kpc)	R_D^V (kpc)	$R_D^{3.6\mu\text{m}}$ (kpc)	R_D^{FUV} (kpc)	R_D^{NUV} (kpc)	R_D^U (kpc)	R_D^B (kpc)	R_D^V (kpc)	$R_D^{3.6\mu\text{m}}$ (kpc)	
(1)	(2)	(3)	(4)	(5)	(6)	(7)	(8)	(9)	(10)	(11)	(12)	(13)	
DDO 52 ..	4.30 ± 0.03	3.07 ± 0.03	1.39 ± 0.00	1.45 ± 0.00	1.33 ± 0.00	2.09 ± 0.00	0.85 ± 0.03	0.89 ± 0.01	0.72 ± 0.07	0.93 ± 0.02	0.90 ± 0.01	0.87 ± 0.00	
DDO 168 ..	-10.15 ± 0.36	-15.31 ± 0.17	174.25 ± 19.25	-58.18 ± 0.89	82.50 ± 0.98	-17.72 ± 0.34	0.60 ± 0.00	0.60 ± 0.00	0.66 ± 0.00	0.69 ± 0.00	0.74 ± 0.00	0.83 ± 0.00	
NGC 1569	0.22 ± 0.00	0.23 ± 0.00	0.22 ± 0.00	0.22 ± 0.00	0.24 ± 0.00	0.31 ± 0.00	0.05 ± 0.17	0.16 ± 0.58	0.60 ± 0.12	1.99 ± 0.54	0.66 ± 0.02	0.83 ± 0.00	
NGC 3738	0.21 ± 0.01	0.24 ± 0.00	0.36 ± 0.00	0.42 ± 0.00	0.45 ± 0.00	0.45 ± 0.00	
DDO 50 ..	1.78 ± 0.01	1.67 ± 0.00	1.37 ± 0.00	1.40 ± 0.00	1.27 ± 0.00	0.99 ± 0.00	0.80 ± 0.01	0.75 ± 0.01	0.76 ± 0.01	0.82 ± 0.01	0.78 ± 0.01	...	
NGC 2366	1.49 ± 0.01	1.39 ± 0.00	1.50 ± 0.00	1.58 ± 0.00	1.58 ± 0.00	1.83 ± 0.00	1.07 ± 0.03	1.06 ± 0.01	1.08 ± 0.00	1.11 ± 0.00	1.12 ± 0.00	1.16 ± 0.03	
NGC 4214	0.49 ± 0.00	0.46 ± 0.00	0.50 ± 0.00	0.55 ± 0.00	0.57 ± 0.00	0.54 ± 0.00	0.85 ± 0.00	0.79 ± 0.00	0.71 ± 0.00	0.69 ± 0.00	0.67 ± 0.00	...	
NGC 1156	0.68 ± 0.00	0.78 ± 0.00	0.88 ± 0.00	0.94 ± 0.00	0.96 ± 0.00	1.04 ± 0.00	0.42 ± 0.02	0.52 ± 0.02	0.62 ± 0.00	0.72 ± 0.00	0.74 ± 0.00	0.87 ± 0.00	

Note (1) Galaxy names. (2–7) Inner disk scale lengths measured on the surface brightness profiles of FUV, NUV, U, B, V, and 3.6 μm , respectively. The typical uncertainties of the scale length are smaller than 0.01 kpc. (8–13) Disk scale lengths measured in the outer part of the disks, if an obvious break is present in the surface brightness profiles.

Furthermore, for the down-bending profiles, there is a trend that the breaks in FUV profiles are stronger (smaller ratio of $R_{D(out)}/R_{D(in)}$ for a down-bending profile) than that of in $3.6\ \mu\text{m}$, indicating that the recent SF histories may play an important role in shaping the broken profiles. We note that the smaller ratio of $R_{D(out)}^{FUV}/R_{D(in)}^{FUV}$ is primarily due to the much steeper radial decline of the FUV in the outer disk for most galaxies. A down-bending profile has been found in the majority of spiral (e.g., Pohlen et al. 2002; Pohlen and Trujillo 2006) and dIrr (Hunter and Elmegreen 2006; Herrmann et al. 2013) galaxies.

2.5 SED Modeling Technique

2.5.1 Creating a Library of Star Formation Histories

Detailed studies of high-quality stellar CMDs for very nearby dIrr galaxies (e.g., Dolphin 2000; Skillman et al. 2003; Cole et al. 2007; Tolstoy et al. 2009) suggest that low-mass dIrr galaxies exhibit a wide variety of SF histories over their lifetime. Therefore, rather than adopting the commonly used two-component form of SF histories for larger galaxies (an exponentially declining component superimposed by random bursts, e.g., Kauffmann et al. 2003; da Cunha et al. 2008), we used multicomponent population models to create our SF history library. Specifically, we divided logarithmically the lifetime from the present to 13.70 Gyr ago into six independent age bins (0–0.03, 0.03–0.10, 0.10–0.35, 0.35–1.18, 1.18–4.02, 4.02–13.70 Gyr), where each age bin has a constant SFR. The way we choose these age bins reflects the fact that the separation between isochrones of different ages strongly decreases with age. Our choice of the first age bin (0–0.03 Gyr) is justified by the nearly constant UV colors in the first ~ 0.03 Gyr of evolution (e.g., Leitherer et al. 1999). Similarly, the last age bin (from ~ 4 to 13.7 Gyr) is justified by the nearly un-evolving shape of the optical to NIR spectrum at ages older than ~ 4 Gyr (e.g., Bruzual and Charlot 2003).

In Appendix A, we show that the commonly assumed forms of SF histories tend to systematically bias the most probable estimates of the physical parameters. We make no assumptions here. Similarly, a common way to generate the SF history library is by Monte Carlo realizations of different SF histories. Instead, our library consists of a uniform, multidimensional grid of models without any prior assumption of the relevant physical parameters. This is necessary for exploring the complex SF histories of low-mass dIrr galaxies. When creating the SF history library, we allow the relative SFR among different age bins to logarithmically vary by an order of 1.5.

We use the Charlot and Bruzual (in preparation) stellar population models, which have implemented several important improvements compared to the Bruzual and Charlot (2003) models. In particular, the new models include the recently improved treatment (Marigo et al. 2008) of the thermally pulsing asymptotic giant branch (TP-AGB), which at maximum (from a few hundred Myr to ~ 1 Gyr for a single

stellar population) could dominate the NIR emission. We adopt the stellar initial mass function (IMF) parametrized by Chabrier (2003). We did not consider chemical evolution in the models, all the components of each model in the library have the same metallicity. The metallicities of the population models are allowed to vary among 0.02, 0.2, and $0.4 Z_{\odot}$, which are adequate for our dIrr galaxies.

To make use of the $H\alpha$ data in order to put critical constraint on the current SF rate, the nebular hydrogen emission lines from HII regions are also obtained for each model in the library. Collisionless Case B recombination for a 10,000 K gas is assumed. Using the recombination rates given by Hummer and Storey (1987), the $H\alpha$ luminosity is calculated from the UV stellar photons shortward of the Lyman limit. A systematic decline of the ratio of the integrated $H\alpha$ -to-FUV flux in low luminosity dwarf galaxies has been shown (e.g., Sullivan et al. 2004; Meurer et al. 2009; Lee et al. 2009a). Three interpretations have been suggested in the literature, namely, the leakage of ionizing photons (e.g., Hunter et al. 2010), the stochasticity of massive SF at low SFR (e.g., Cervino and Luridiana 2004), and nonuniversal stellar IMF (especially the upper end; e.g., Pflamm-Altenburg et al. 2009). These possibilities all imply that the observed $H\alpha$ emission only gives a lower limit to the current SFR, under the assumption of Case B recombination and a well-populated universal IMF, which is the case for our modeling. Therefore, our $H\alpha$ data are used to set a lower limit on the $H\alpha$ flux from the models. Considering, the uncertainties in the observed $H\alpha$ flux (HE04), we set the lower limit to be $0.8 \times L_{H\alpha, \text{obs}}$.

We use the two-phase dust attenuation recipes developed by Charlot and Fall (2000) as our standard dust extinction law. The effective absorption is proportional to $\lambda^{-0.7}$. Charlot and Fall (2000) found a typical value of ~ 3 for the ratio μ of the extinction experienced by the young stellar populations (≤ 10 Myr) to that by the older stellar populations. We adopt this value when creating our SF history library. The V-band dust extinction affecting the young stellar populations is allowed to vary linearly between 0.0 and 0.5 magnitude. The gray extinction curve derived by Charlot and Fall (2000) is in agreement with recent results for a large sample of nearby galaxies (Johnson et al. 2007).

2.5.2 Determining the Physical Parameters

Our final library consists of $\sim 4 \times 10^6$ different SF histories, which are created by allowing all the relevant parameters (i.e., dust extinction, metallicity, and relative SFR among different age bins) to vary uniformly (either logarithmically or linearly) among physically reasonable ranges. For each SF history in the library, we integrate respectively back to the past 0.03, 0.1, 1 Gyr, and the galaxy lifetime (here we adopt a Hubble time of 13.7 Gyr) in order to get the SFR averaged over these different timescales. In the following we denote the SFR averaged over the past 0.03, 0.1, 1 Gyr, and the whole lifetime as $\text{SFR}_{0.03}$, $\text{SFR}_{0.1}$, SFR_1 , and $\text{SFR}_{13.7}$, respectively. The accumulated present-day stellar mass is also derived. From our experiments, the broadband SED modeling is not expected to be very sensitive to the SFR averaged

over the past 0.03 Gyr (see the Appendix) and that averaged over the past 4 Gyr. So we concentrate on the interpretation of $\text{SFR}_{0.1}$, SFR_1 , $\text{SFR}_{13.7}$, and the stellar mass in this work. However, as mentioned above, our choice of six age bins guarantees that we have a relatively complete SF history library adequate for broadband SED modeling.

We use the Bayesian technique (e.g., Kauffmann et al. 2003; Kong et al. 2004) to find the most probable estimates of parameters related to each of the observed broadband SEDs. Specifically, given an observed SED, we construct the probability density function (PDF) and the related cumulative distribution function (CDF) for each parameter defining our SF history library by calculating the likelihood $\exp(-\chi^2/2)$ that an observed SED corresponds to each SF history model in our library. As described in the previous subsection, all the models with the emergent $H\alpha$ luminosity (scaled by a factor determined from the weighted least squares) smaller than $0.8 \times L_{H\alpha, \text{obs}}$ are excluded from the final determination of the parameters. The most probable value for a specific parameter is taken as the median of the corresponding PDF. The confidence interval is defined as the central 68% of the CDF. Simply adopting the single best-fitting value as the most probable estimate for the parameter is blind to degeneracies among relevant parameters. Our method is very robust, and the possible degeneracies are factored into the related confidence intervals.

2.5.3 Correcting the GALEX NUV Data for Galactic Extinction

Before feeding the data into the SED modeling, we correct the data for the foreground MW extinction (Schlegel et al. 1998), adopting the Cardelli et al. (1989) extinction curve with $R_V = A_V/E(B - V) = 3.1$. While there are nearly fixed, linear relations between A_λ and $E(B - V)$ for most bands, this is not the case for GALEX NUV (e.g., Wyder et al. 2007), due to the finite bandwidth ($\sim 1000 \text{ \AA}$) and the presence of the 2175 \AA bump in the MW extinction curve. The ratio $A_{\text{NUV}}/E(B - V)$ is sensitive to both the emergent extra-galactic SED and the foreground MW reddening $E(B - V)$. For example, the SED emergent from a constant SF and the SED from a 7 Gyr old single stellar population have $A_{\text{NUV}}/E(B - V) \sim 8.2$ and ~ 7.5 , respectively for 0.05 mag of MW reddening. Also, for the SED emergent from a constant SF, $A_{\text{NUV}}/E(B - V)$ would be 7.9 if the Galactic reddening was 0.5 mag. Therefore, unlike the other bands, the NUV data are not corrected for MW extinction with a fixed ratio of $A_{\text{NUV}}/E(B - V)$. Before comparing the data with each model in the library, the NUV is corrected for the Galactic extinction using the ratio of $A_{\text{NUV}}/E(B - V)$ predetermined from the emergent SED of the model and the Galactic $E(B - V)$ toward the specific galaxy. In other words, the MW extinction correction for NUV is consistently applied before comparing each model with a given galaxy.

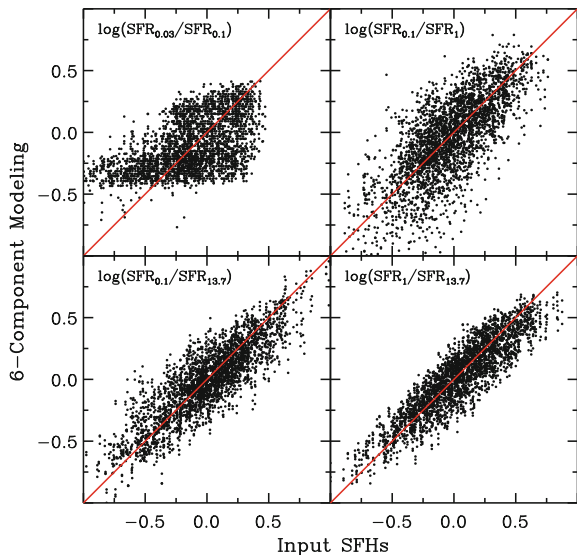
2.5.4 Testing the SED Modeling Technique on Mock Dataset

2.5.4.1 Recovery of Physical Parameters

Before proceeding to the results of our SED modeling of the real data, here we explore the reliability of multiband SED modeling in recovering the rough SF history of dIrr galaxies. In these tests, we first logarithmically divided the Hubble time (13.7 Gyr) into 14 independent age bins, and took the SF as constant within each age bin. Then a series of 3000 mock SF histories were generated by randomly changing the SFR for each independent age bin. The internal extinction was fixed at $A_V = 0.1$ when generating the SEDs related to each mock SF history. We then modeled the SEDs (*GALEX*FUV/NUV, *U*, *B*, *V*, 3.6 μ m) related to the mock SF histories with our library of 6-component superposition (6-C) SF histories used in this work. The calibration uncertainties of the real data were taken as the photometric uncertainties of the SED related to each mock SF history.

Figure 2.5 presents a comparison of the modeling results, including M_* , SFR_1 , $SFR_{0.1}$, and $SFR_{0.03}$, and relevant integrated quantities of the mock input SF histories. We fit each histogram in Fig. 2.5 with a gaussian curve, which is overplotted as a *red solid* line in each panel. The standard deviation (σ) and mean value (μ) of the gaussian curve is also indicated. As can be seen, except for $SFR_{0.03}$, all the parameters are well recovered in our SED modeling, with acceptable uncertainties related to the varying SF histories. Figure 2.6 further shows ratios of SFR averaged over different timescales. Again, except for $SFR_{0.03}$, the modeling with the 6-C library recovers

Fig. 2.6 Comparison between the ratios of the SFR averaged over different timescales (indicated in each panel) from the input SF histories (the *abscissa*) and the relevant quantities from the 6-C modeling (the *ordinate*). The *red solid* line in each panel marks the relationship of equality. The figure is adapted from Zhang et al. (2012)



the SF histories with negligible, if any, bias. Also plotted (Fig. 2.9) is the recovery rate of the input metallicities.

2.5.4.2 Bias Introduced by an Incomplete SF History Library

The incompleteness of the SF history library used in the SED modeling could significantly affect or bias the estimation of physical parameters (e.g., Kauffmann et al. 2003). To demonstrate this, we create another SF history library by assuming the real SF history can be approximated as an underlying component that varies exponentially with time plus a single random burst of finite length. Here, we denote this SF history library as ‘E + B.’ E + B is now the most commonly used SF history library in the literature. The exponential component is described with two parameters: the SF timescale τ and the age. The burst component is described with three parameters: the age, strength, and length of the burst. The Charlot and Fall (2000) extinction recipe was adopted here. All the parameters, including the extinction, are allowed to vary uniformly within physically reasonable ranges when creating the library. We model the same SEDs as related to the mock SF histories generated above. We obtained the

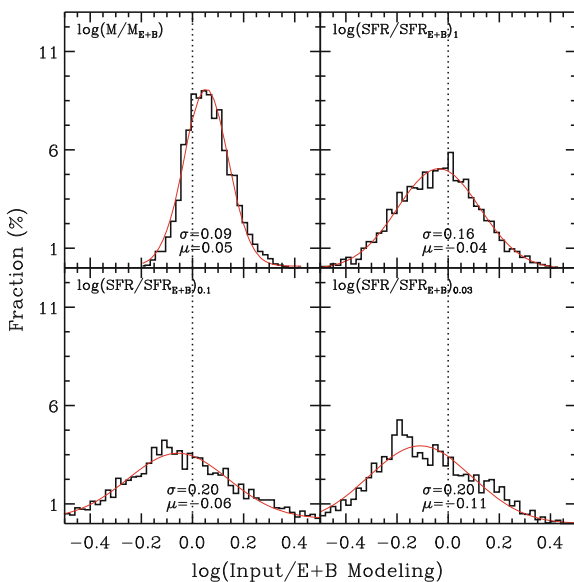


Fig. 2.7 Histograms of the ratios of the parameters (M_* , SFR_1 , $SFR_{0.1}$ and $SFR_{0.03}$) from the input mock SF histories to the best estimates from the exponential plus burst (E + B) modeling. The *abscissa* in each panel is the logarithm of the relevant ratio (indicated in each panel) of the input and of the E + B modeling results. The *ordinate* is the percent of the data points in each bin. The *red curve* in each panel is the gaussian fitting to the relevant histogram. σ and μ indicate the best-fitting parameters defining the gaussian curve. The *dotted line* in each panel marks the relationship of equality. The figure is adapted from Zhang et al. (2012)

Fig. 2.8 Comparison between the ratios of the SFR averaged over different timescales (indicated in each panel) from the input SF histories (the *abscissa*) and the relevant quantities from the E + B modeling (the *ordinate*). The red solid line in each panel marks the relationship of equality. The figure is adapted from Zhang et al. (2012)

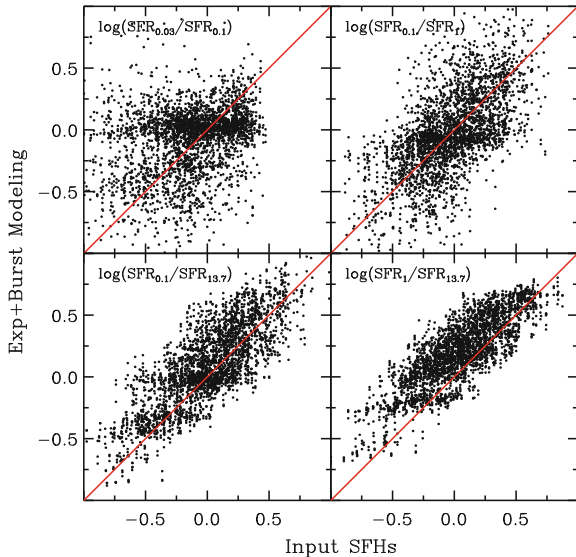
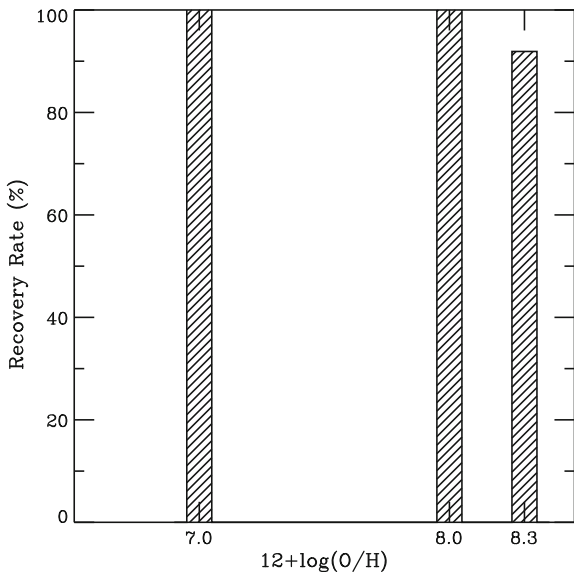


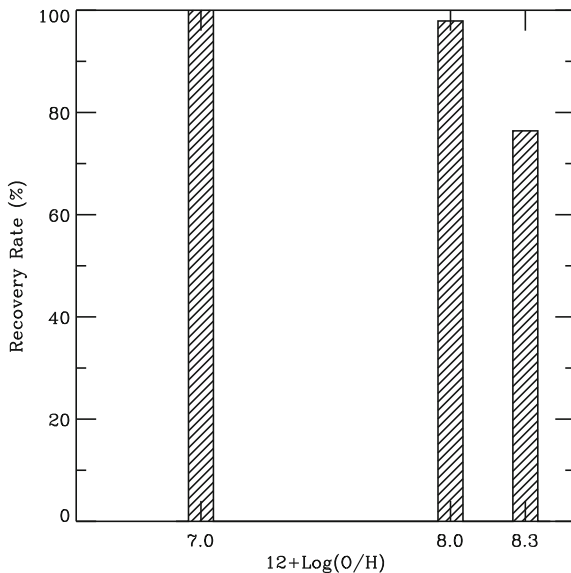
Fig. 2.9 Recovery rate of the metallicities of input mock models by using the 6-C SF history library



most probable physical parameters, including M_* , SFR_1 , $\text{SFR}_{0.1}$, and $\text{SFR}_{0.03}$, with the same method as described in Sect. 2.5.2.

Figures 2.7 and 2.8 show the modeling results of using the E + B library. Compared to the modeling results from our standard 6-C superposition method, the estimate of the relevant parameters exhibits a larger uncertainty and a considerable bias. For instance, the stellar mass M_* has a tendency to be slightly underestimated, and the

Fig. 2.10 Recovery rate of the metallicities of input mock models by using the E + B SF history library



recent SFR, i.e., $\text{SFR}_{0.1}$ and SFR_1 , tend to be overestimated. The problem of using the E + B library in modeling can be more clearly seen in Fig. 2.8. The E + B library tends to overestimate the SFR averaged over recent times, e.g., $\text{SFR}_{0.1}$, SFR_1 . As is expected for the more or less continuous nature of the SF histories in the E + B library, there is a very strong bias toward almost constant recent SF. The above bias could be ascribed to the fact that, while the SF averaged over a timescale of $\sim\text{Gyr}$ may be relevant to the overall evolution histories of the galaxies, the SF over shorter timescales (i.e., 0.1 Gyr) is not necessarily as important. In addition, the recovery rate of input metallicities is plotted (Fig. 2.10) for the E + B library. It can be seen that the performance of the E + B library in constraining the metallicities is not as good as the 6-C library (Fig. 2.9).

2.6 Results of SED Modeling to Our Sample Galaxies

The SF history variations as a function of radius within the galaxies, determined from our SED modeling, are shown for each galaxy in the middle column of Fig. 2.13. Specifically, the SFR averaged over the past 0.03, 0.1, 1 Gyr, and the Hubble time are shown, respectively, as *blue circles*, *green squares*, *brown triangles* and *red diamonds*. Stellar mass surface density profiles Σ_* are shown in the third column of Fig. 2.13. Table 2.3 gives the globally integrated stellar mass, lifetime averaged $\text{SFR}_{13.7}$, and ratios of $\text{SFR}_{0.1}$ to $\text{SFR}_{13.7}$ and SFR_1 to $\text{SFR}_{13.7}$ for each galaxy. All the photometry with uncertainties $\sigma > 0.3$ mag are excluded from the SED modeling.

Table 2.3 SED-fitting results

Galaxy	M_* [10^7 M_\odot]	$(SFR)_{13.7\text{Gyr}}$ [10^{-3} $M_\odot\text{yr}^{-1}$]	R_D^*		$R_{break,*}$ (kpc)	$\log(\Sigma_{*,break})$ ($\log(M_\odot\text{pc}^{-2})$)	$\log(\Sigma_{*,center})$ ($\log(M_\odot\text{pc}^{-2})$)	$C_{31,*}$	$b_{0.1\text{Gyr}}$	$b_{1\text{Gyr}}$
			Inner (kpc)	Outer (kpc)						
(1)	(2)	(3)	(4)	(5)	(6)	(7)	(8)	(9)	(10)	(11)
LGS 3 ...	0.027	0.038	0.49	0.09	0.26	-0.32	-0.20	2.04	0.10 ± 0.04	0.17 ± 0.06
DDO 210 .	0.068	0.094	0.44	0.19	0.29	-0.21	-0.05	2.63	1.72 ± 0.64	0.43 ± 0.14
DDO 69 ..	0.102	0.137	1.18	0.23	0.25	0.03	0.04	2.36	3.62 ± 0.56	1.55 ± 0.30
DDO 155 .	0.297	0.404	0.22	0.87	3.06	3.87 ± 0.98	0.84 ± 0.21
DDO 216 .	1.521	2.140	0.89	0.31	1.12	0.06	0.44	2.25	0.06 ± 0.02	0.09 ± 0.02
M81dwA .	0.138	0.182	-14.28	0.30	0.41	-0.12	-0.16	2.02	7.81 ± 1.12	1.22 ± 0.18
Mrk 178 ...	1.110	1.531	0.27	0.87	1.58	-1.14	0.69	2.78	2.04 ± 0.52	0.52 ± 0.12
DDO 187 .	0.345	0.451	0.53	0.23	0.30	0.48	0.71	2.51	0.55 ± 0.20	2.88 ± 0.62
UGC 8508	0.764	1.061	0.57	0.27	0.46	0.50	0.77	2.49	1.05 ± 0.29	0.56 ± 0.16
NGC 4163	2.708	3.807	0.43	0.29	0.61	0.83	1.40	2.62	0.51 ± 0.20	0.32 ± 0.10
CVn1dwA .	0.410	0.532	0.68	0.22	2.53	1.57 ± 0.41	1.43 ± 0.45
DDO 70 ..	1.960	2.668	0.50	1.59	0.77	0.14	0.76	2.77	1.03 ± 0.22	1.44 ± 0.25
IC 1613 ...	2.920	4.030	0.74	0.39	1.98	-0.20	0.96	2.64	0.81 ± 0.25	0.83 ± 0.21
DDO 101 .	6.543	9.325	0.68	0.41	1.54	0.39	1.37	2.52	0.08 ± 0.02	0.12 ± 0.05
WLM	1.629	2.268	1.24	0.57	1.34	-0.08	0.15	2.31	0.43 ± 0.11	0.27 ± 0.07
DDO75 ...	0.784	1.023	0.64	0.27	0.73	0.31	0.71	2.03	9.17 ± 1.49	2.21 ± 0.31
VIIZW 403	1.777	2.449	0.96	0.55	1.14	0.17	0.67	2.45	3.51 ± 0.89	1.10 ± 0.26
Haro 29 ...	1.443	1.921	0.20	1.98	1.12	-0.81	1.59	5.29	6.88 ± 2.02	1.70 ± 0.39
DDO 133 .	3.042	4.214	0.91	0.57	2.26	-0.28	0.77	2.54	0.72 ± 0.14	0.74 ± 0.14

(continued)

Table 2.3 (continued)

Galaxy	M_* [$10^7 M_\odot$]	$(\text{SFR})_{13.7\text{Gyr}}$ [$10^{-3} M_\odot \text{yr}^{-1}$]	R_D^*		$R_{break,*}$	$\log(\Sigma_{*,break})$ ($\log(M_\odot \text{pc}^{-2})$)	$\log(\Sigma_{*,center})$ ($\log(M_\odot \text{pc}^{-2})$)	$C_{31,*}$	$b_{0.1\text{Gyr}}$	$b_{1\text{Gyr}}$
			Inner (kpc)	Outer (kpc)						
(1)	(2)	(3)	(4)	(5)	(6)	(7)	(8)	(9)	(10)	(11)
DDO 126.	1.605	2.132	0.82	0.37	2.58	1.42 ± 0.33	1.71 ± 0.36
DDO 165.	3.453	4.631	1.82	0.92	1.34	0.22	0.45	2.30	3.84 ± 0.83	1.34 ± 0.25
DDO 63 ..	3.337	4.421	1.61	1.00	1.57	0.14	0.56	2.29	2.25 ± 0.52	2.27 ± 0.42
NGC 6822	7.630	10.451	1.47	0.36	0.38	1.59	1.66	2.35	0.51 ± 0.14	0.63 ± 0.14
DDO 53 ..	0.970	1.337	20.87	0.79	0.96	-0.06	-0.15	2.10	1.13 ± 0.18	0.69 ± 0.14
DDO 154.	0.835	1.131	1.00	0.49	0.68	0.10	0.28	2.47	3.82 ± 0.83	0.91 ± 0.17
DDO 87 ..	3.306	4.589	2.27	1.06	1.21	0.15	0.32	2.69	0.64 ± 0.15	0.53 ± 0.13
DDO 52 ..	5.273	7.296	1.05	0.52	3.15	-0.41	0.85	2.68	0.46 ± 0.17	0.86 ± 0.25
DDO 168.	5.865	7.953	32.04	0.99	0.73	0.65	0.63	2.64	1.43 ± 0.29	0.79 ± 0.17
NGC 1569	36.016	49.259	0.43	0.87	2.25	0.13	2.35	3.13	6.19 ± 1.36	1.02 ± 0.18
NGC 3738	46.571	65.325	0.68	0.61	1.59	1.16	2.20	2.95	0.62 ± 0.22	0.62 ± 0.17
DDO 50 ..	10.725	14.416	1.08	0.71	2.00	0.42	1.02	2.45	3.88 ± 0.51	1.47 ± 0.21
NGC 2366	6.954	9.186	3.69	1.11	2.66	-0.14	-0.18	2.70	2.64 ± 0.44	2.00 ± 0.30
NGC 4214	47.999	65.390	0.82	0.60	2.73	0.56	2.01	3.09	0.92 ± 0.15	1.26 ± 0.22
NGC 1156	121.759	164.914	0.97	0.64	3.92	0.55	2.30	2.64	1.73 ± 0.40	0.85 ± 0.22

Note—(1) Galaxy names. (2) Total stellar mass derived by applying the growth curve method to the stellar mass profiles from our SED modeling. (3) SFR averaged over the Hubble time (13.7 Gyr). (4–5) Disk scale length measured from the surface stellar mass density profiles. The scale lengths of the inner and the outer parts are listed, respectively. If there is no obvious break in the profile, the related scale length is listed in column 4. (6) Radius where the break of the surface stellar mass density profile happens. (7) Surface stellar mass density at the broken radius. $\Sigma_{*,break}$ has been inclination-corrected under the assumption that the intrinsic $(b/a)_0 = 0.3$. (8) Inclination-corrected central surface stellar mass density, extrapolated from the inner regions around the center. (9) Concentration index (see the text for details). (10) Ratio of the SFR averaged over the past 0.1 Gyr to the SFR averaged over the Hubble time. (11) Ratio of the SFR averaged over the past 1 Gyr to the SFR averaged over the Hubble time.

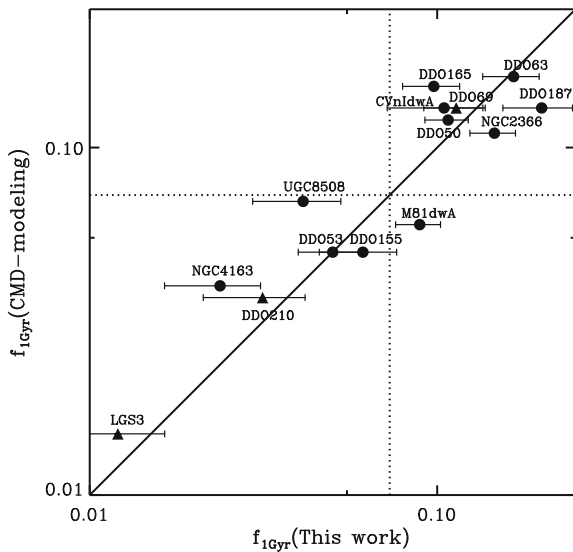
The global results are derived by integrating the relevant radial profiles across the whole disk.

2.6.1 Integrated SED-Based Versus Stellar CMD-Based SF Histories

Before proceeding to the interpretation of our SED modeling results, we compare our results with those derived from existing stellar CMD-based analysis. Half of our galaxies have stellar CMD-based SF histories obtained from *HST* data and available in the literature. Among these galaxies, 14 galaxies have CMD analysis for a significant part (the observing field covers more than 20% of the area enclosed by the Holmberg radius) of the stellar disk. The availability of *GALEX* FUV and *Spitzer* 3.6 μm data makes our results for $\text{SFR}_{0.1}$ and M_* particularly reliable. Therefore, we compare our results of the fraction of the SF accumulated during the recent 1 Gyr $f_{1\text{Gyr}}$ ($(\text{SFR}_1/\text{SFR}_{13.7})/13.7$) with that derived from CMD modeling. Among the 14 galaxies, the $f_{1\text{Gyr}}$ for 11 galaxies (denoted as *black circles* in Fig. 2.11) are from Weisz et al. (2011), and those of the other three galaxies (denoted as *triangles* in Fig. 2.11) are from Orban et al. (2008). From the comparison of these 14 galaxies, our globally integrated results from the SED-modeling are broadly consistent with those from the CMD-based analysis.

Generally speaking, studying the resolved stellar populations is the best way to derive a detailed SF history, provided the data are deep enough. We note that most of the above CMD analyses are carried out on relatively shallow data sets ($M_I \lesssim 0$).

Fig. 2.11 Fractions of the total stellar mass formed during the past 1 Gyr $f_{1\text{Gyr}}$ derived from our SED-modeling are compared to those determined from stellar CMD-based analysis. The galaxies with CMD analysis from Weisz et al. (2011) and from Orban et al. (2008) are denoted as *filled circles* and *filled triangles*, respectively. The (*solid*) line of equality is plotted to guide the eye. The *dotted lines* mark the expected value for a constant SF history over the Hubble time. The figure is adapted from Zhang et al. (2012)



This means that the SF history at older times ($\gtrsim 2$ Gyr) is mainly constrained by the age-insensitive red giant branch (RGB). The RGB alone at best could provide a good estimate of the total SF from its formation to a few Gyr ago (Greggio 2002) to within a factor of ~ 2 . Nevertheless, the results from the current CMD-fitting are also sensitive to the modeling techniques used by different works. For example, using the same *HST* data sets of WLM, Weisz et al. (2008) derived a two times higher $f_{1\text{Gyr}}$ than Dolphin et al. (2005). Even more, adopting different stellar evolution libraries can lead to differences of at least a factor of 2 in the derived SFR (Gallart et al. 2005). Our library of SF histories are created with stellar evolution tracks combining those of Padova (1994) (see Bruzual and Charlot 2003) and Marigo et al. (2008) for the evolution of AGB, whereas the above CMD-modeling adopted the tracks of Padova (2000) (Girardi et al. 2002) and Marigo et al. (2008). This undoubtedly leads to some differences in the SF histories. We also noticed that the CMD-modeling works listed above adopted different IMFs from ours. Finally, the CMD-modeling often covers a smaller spatial area on the galaxy than our SED fitting. Given these uncertainties and differences, the results from our SED-modeling are in reasonable agreement with those from CMD-modeling.

SF histories derived from broadband SED-modeling have been thought in the past to be biased toward younger, luminous populations. The above comparison shows that the average SFR during the past \sim Gyr is well constrained by modeling the broadband SED with a relatively complete library of SF histories. We point out that the availability of *U* and *B*-band data is essential in SED-modeling because the two bands straddle the age-sensitive 4000 Å break.

2.6.2 Globally Integrated SF Histories

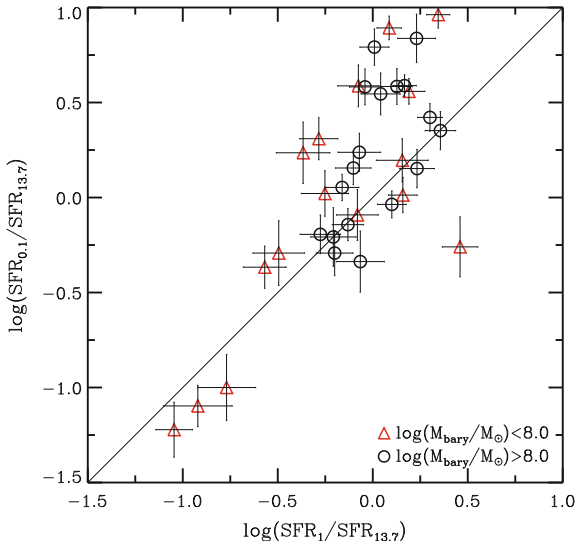
By integrating the relevant surface density profiles times the circumference over radius, we derived (in Table 2.3) the asymptotic total stellar masses M_* (See Fig. 2.19 for an example), $\text{SFR}_{13.7}$, $b_{0.1\text{Gyr}}$ ($\text{SFR}_{0.1}/\text{SFR}_{13.7}$), and $b_{1\text{Gyr}}$ ($\text{SFR}_1/\text{SFR}_{13.7}$). The galaxies are listed in order of increasing total baryonic mass in Table 2.3. A factor of 2–3 (e.g., Hunter and Gallagher 1986; Kennicutt et al. 2005; Lee et al. 2009b) enhancement of current SF compared the averaged past rate has been used as one way to define a starburst in the literature. Compared to $\text{SFR}_{13.7}$, 38% (13) of the sample galaxies have $\text{SFR}_{0.1}$ enhanced at least by a factor of 2, and 47% (16) have $\text{SFR}_{0.1}$ consistent with $\text{SFR}_{13.7}$ within a factor of 2. For SFR_1 , 12% (4 galaxies) have been enhanced at least by a factor of 2, and 71% (24 galaxies) have SFR_1 consistent with $\text{SFR}_{13.7}$ within a factor of 2. Among the 5 galaxies with $\text{SFR}_{0.1}/\text{SFR}_{13.7} < 0.5$, 4 (LGS 3, DDO 216, DDO 101, WLM) have baryonic mass (here approximated to be the stellar mass plus atomic gas mass, see below) smaller than $10^8 M_\odot$. Similarly, all 6 galaxies with $\text{SFR}_1/\text{SFR}_{13.7} < 0.5$ have baryonic mass smaller than $10^8 M_\odot$. The total atomic gas mass was derived by multiplying the HI gas mass by 1.34 to account for He. The HI masses used here were all from single dish HI emission line observations reported in the literature (see HE04 for

the references), and the total stellar mass is derived from our SED modeling (see Sect. 2.6.4).

We plot $b_{0.1\text{Gyr}}$ and $b_{1\text{Gyr}}$ for the galaxies (Table 2.3) in Fig. 2.12. The galaxies with baryonic mass smaller and higher than $10^8 M_\odot$ are denoted as different symbols. A mass of $10^8 M_\odot$ is about the median baryonic mass of our whole sample. There is almost no relationship between SF histories and total baryonic mass for our sample, except that all galaxies that exhibit extremely declining SF histories are relatively low-mass systems. Among the whole sample, five galaxies (LGS 3, DDO 216, NGC 4163, DDO 101, and WLM) have experienced a significant ($>30\%$) decline in SF activity (both $\text{SFR}_{0.1}$ and SFR_1) over the past $\sim\text{Gyr}$. We note that all of these five galaxies have baryonic masses smaller than $10^8 M_\odot$, and, except for WLM, the (atomic) gas to stellar mass ratios are smaller than 1.

The tidal indices (Table 2.1) of LGS 3 and DDO 216 are larger than 1, which indicates that their evolution has likely been significantly influenced by environment. Most of the gas in these two galaxies could have been removed by either ram pressure stripping or tidal disturbance. In particular, based on the morphology of the HI distribution, McConnachie et al. (2007) concluded that DDO 216 is currently undergoing ram pressure stripping caused by the intragroup/intracluster medium. The tidal index (Karachentsev et al. 2004) of a galaxy is defined as the maximum density enhancement caused by all neighboring galaxies, and higher values correspond to the likelihood of more significant tidal interaction with neighboring galaxies. This is consistent with the expectation that, lower mass systems (below a few times $10^8 M_\odot$) are more susceptible to significant influence of both the environment (Gunn and Gott 1972) and stellar feedback (e.g., winds and supernova explosions (SNE)),

Fig. 2.12 Ratios of globally integrated $\text{SFR}_{0.1}/\text{SFR}_{13.7}$ versus $\text{SFR}_1/\text{SFR}_{13.7}$ for the galaxy sample. The (solid) line of equality is plotted to guide the eye. The galaxies are divided into two groups according to total baryonic mass. Those with masses less than $10^8 M_\odot$ are denoted with red triangles, and those with masses greater than this are plotted as black circles. The figure is adapted from Zhang et al. (2012)



which could even induce blow-out of interstellar gas from the galaxy (e.g., Mac Low 1999).

A few galaxies deserve special mention. M81dwA, DDO 75, Haro 29 and NGC 1569 hold the largest ratio (>5) of $\text{SFR}_{0.1}/\text{SFR}_{13.7}$ among our sample. The recent starburst in NGC 1569, which has the highest current SF intensity in our sample, may be ascribed to an interaction of some kind (e.g., Stil and Israel 1998; Muhle et al. 2005; Johnson et al. 2011). Similarly, the recent rise of the SFR in M81dwA may be due to the recent interaction within the M81 group, which has several dramatic galaxy-galaxy interactions in progress. Haro 29 is a typical BCD galaxy undergoing a intense burst of SF in the central regions (Thuan and Martin 1981). DDO 75 and Haro 29 both have negative tidal indices (-0.6 for DDO 75, -1 for Haro 29), indicating that the recent enhancement of SF may be ascribed to internal processes. For DDO 154, Kennicutt and Skillman (2001) reported a factor of $\sim 2-4$ times lower recent SF compared to the past based on $\text{H}\alpha$ imaging, which is inconsistent with our results for $\text{SFR}_{0.1}$. We interpret the disagreement as being due to the fact that $\text{H}\alpha$ is not a robust SFR indicator in LSB dwarf galaxies (e.g., Meurer et al. 2009; Lee et al. 2009a; Hunter et al. 2010).

2.6.3 Azimuthally Averaged Radial Star Formation Histories

The sample as a whole exhibits a diversity of radial variations of SF histories (Fig. 2.13). However, some systematic trends do exist.

Figures 2.14 and 2.15 show the radial variations of $\log(\Sigma_{\text{SFR}_{0.1}}/\Sigma_{\star})$ and of $\log(\Sigma_{\text{SFR}_1}/\Sigma_{\star})$. The radius has been normalized by the V -band disk scale length. The galaxies in Figs. 2.14 and 2.15 are plotted in order of increasing total baryonic mass from the upper left panel to the lower right panel, and the galaxy names are listed in order of increasing baryonic mass in each panel. The *dashed* line in each panel marks a constant SF history over a Hubble time. Deep stellar CMD analysis of nearby dIrr galaxies (e.g., IC 1613; Skillman et al. 2003; Leo A; Cole et al. 2007) suggests that most of the SF in dIrr galaxies may take place at intermediate ages, rather than persisting constantly over a Hubble time. In contrast, LGS 3 (Hidalgo et al. 2011) consists of mostly old populations. Therefore, the data points lying above the *dashed* line in Figs. 2.14 and 2.15 do not necessarily mean elevated SFR compared to the past.

To quantify the radial trends of the SF history variation, we did linear least-squares fitting to the radial variations of $\log(\Sigma_{\text{SFR}_{0.1}}/\Sigma_{\star})$ and $\log(\Sigma_{\text{SFR}_1}/\Sigma_{\star})$. If there is an obvious break in the stellar mass surface density profiles (Fig. 2.13 and Table 2.3), we fit the slope for the inner and the outer parts separately. The *GALEX* data (thus the measure of recent SFR) of several galaxies (LGS 3, DDO 210, DDO 216, and NGC 1569) have high S/N ratios only in the inner disk, in this case we only fit the inner disk. We also fit the relevant ratios as a function of normalized (by the V -band scale length) radius. The slopes (or gradients) from the fitting are listed in Table 2.4. The weighted averages of the relevant slopes for the galaxies below and above a baryonic mass 10^8

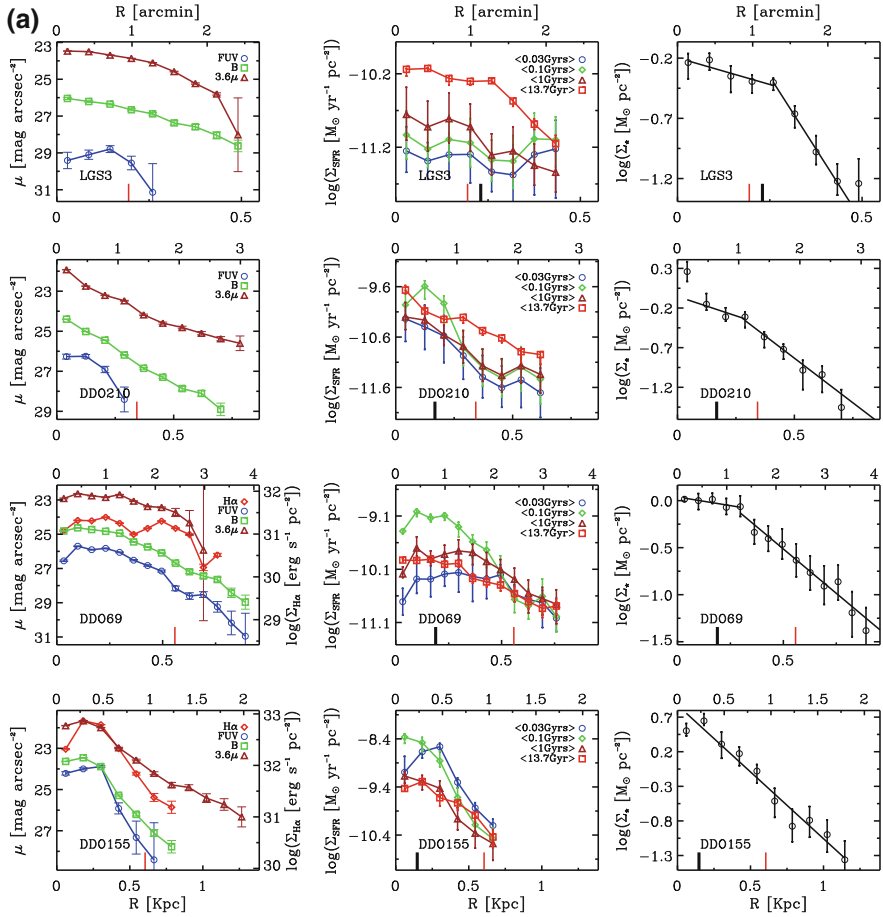


Fig. 2.13 *First column:* Azimuthally averaged surface brightness profiles of the $H\alpha$, FUV, B and $3.6\mu\text{m}$ images. The NUV and U -band profiles are plotted instead of FUV if there are no FUV observations. *Second column:* Radial variations of the SFR averaged over different timescales obtained from our multiband SED modeling. The averaging timescales are the most recent 0.03 Gyr, the most recent 0.1 Gyr, the past 1 Gyr, and the Hubble time. *Third column:* Inclination-corrected stellar mass surface density profiles from the SED modeling. The fitted exponential profiles are overlotted as *solid lines*. The *thin red line* marks the Holmberg radius, and the *thick black vertical line* marks the V -band scale length. The figure is adapted from Zhang et al. (2012)

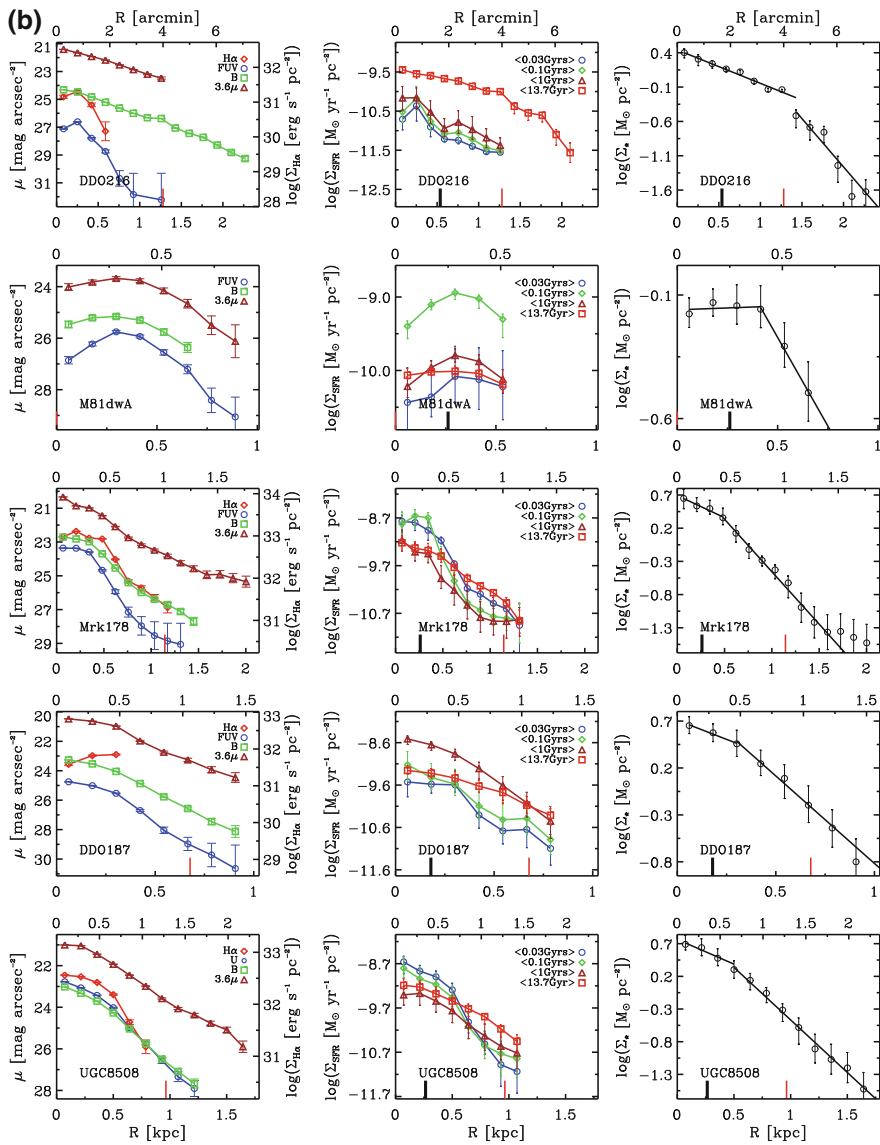


Fig. 2.13 (continued)

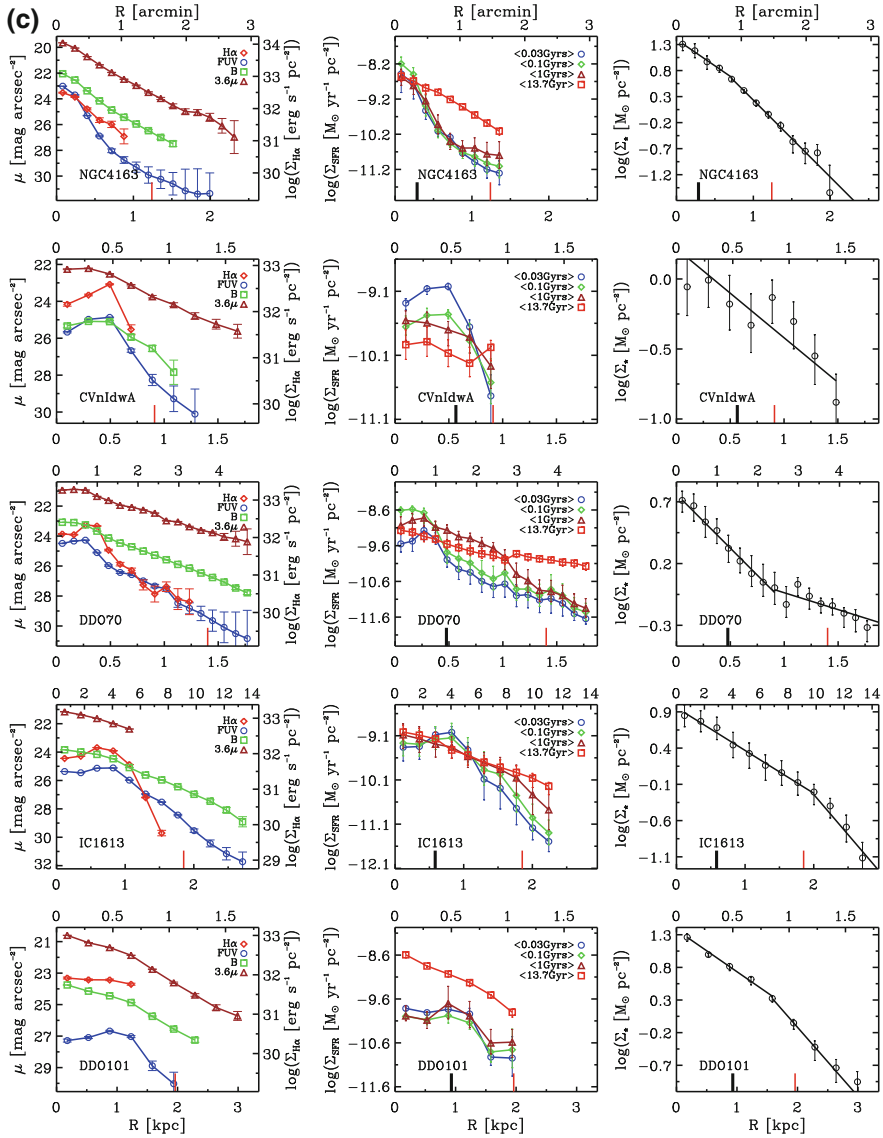


Fig. 2.13 (continued)

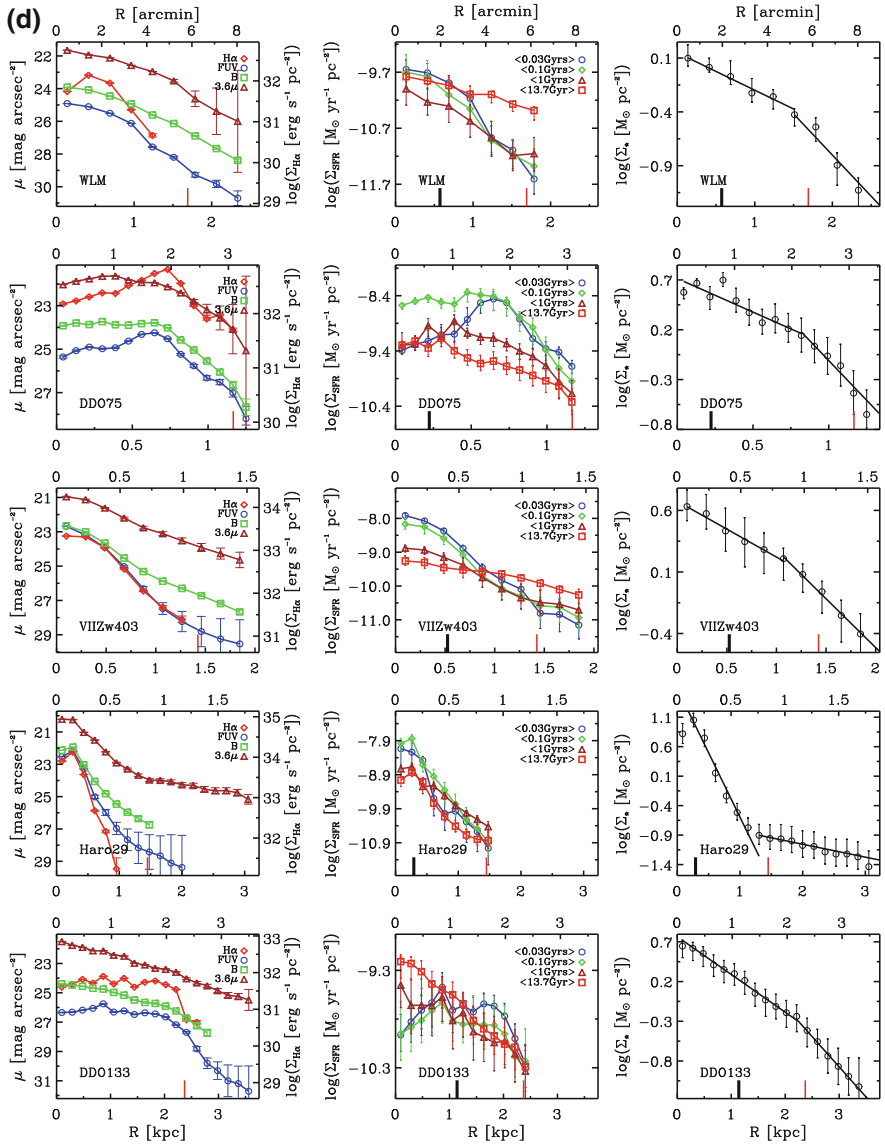


Fig. 2.13 (continued)

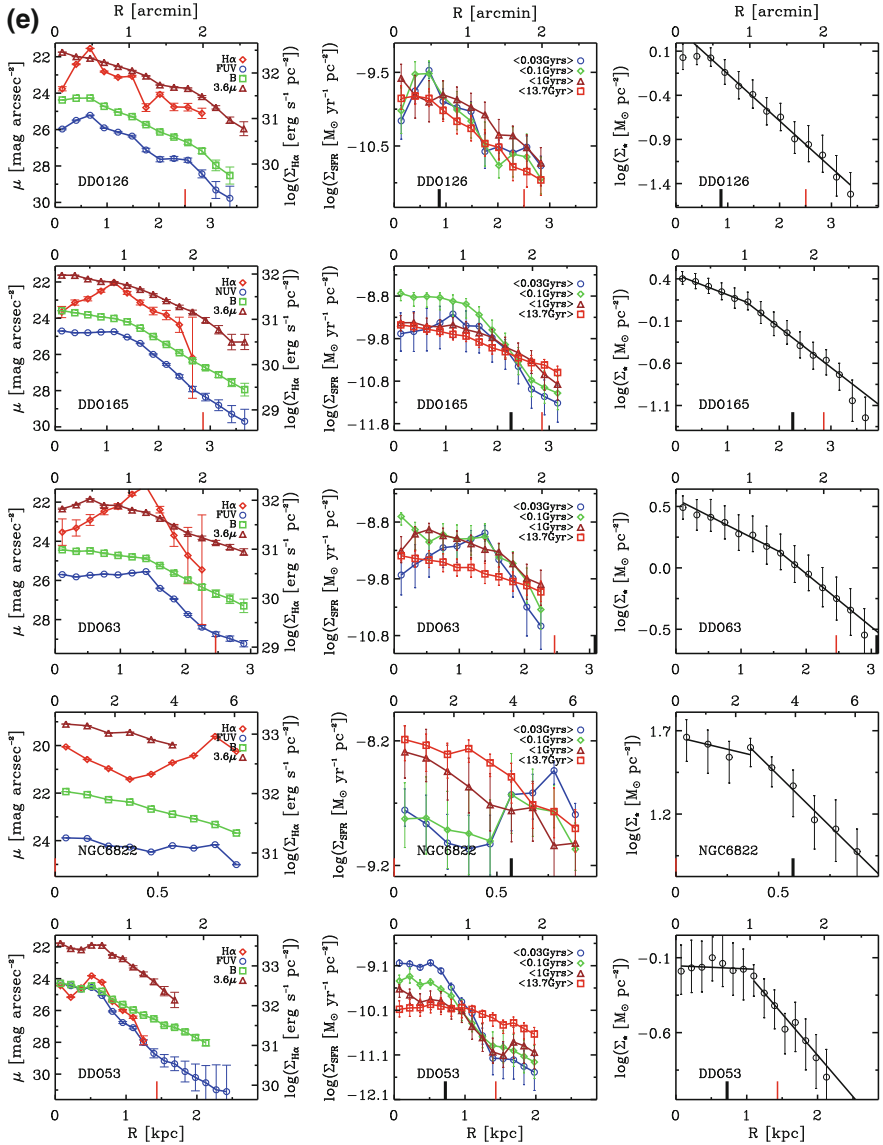


Fig. 2.13 (continued)

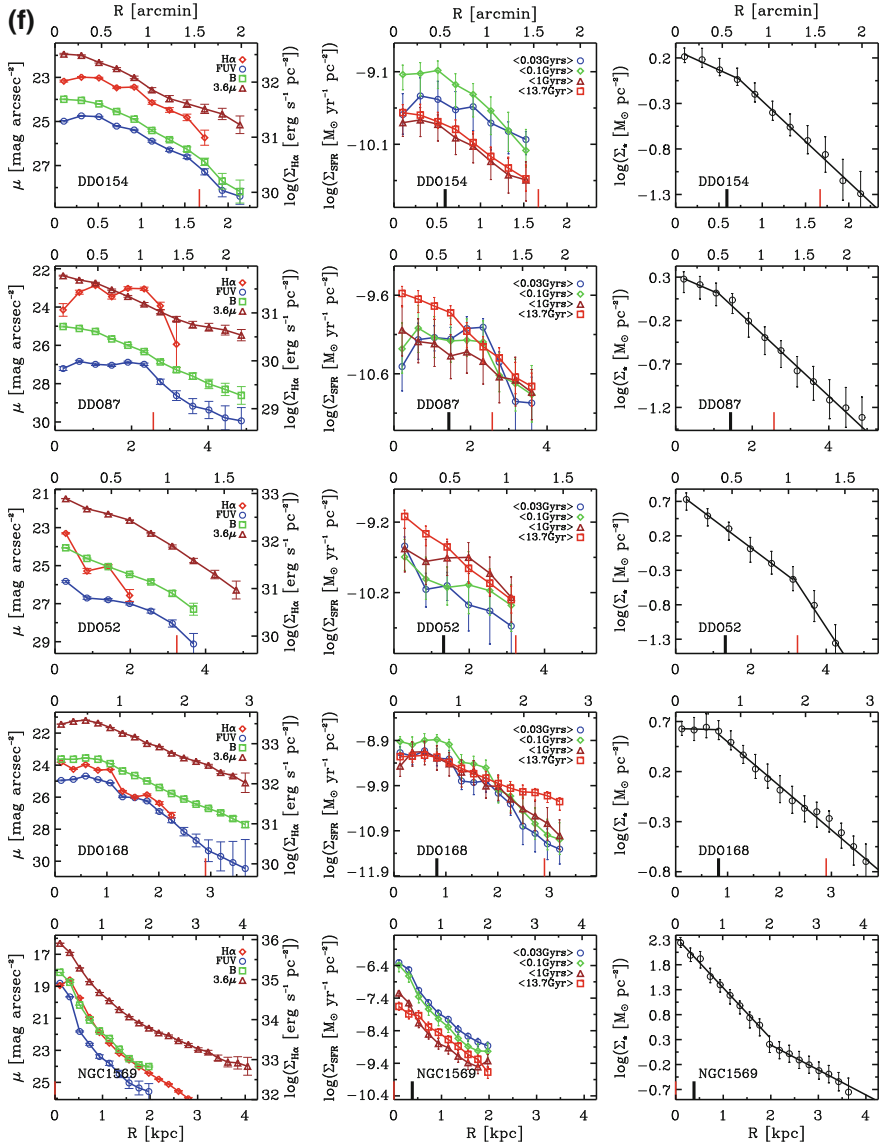


Fig. 2.13 (continued)

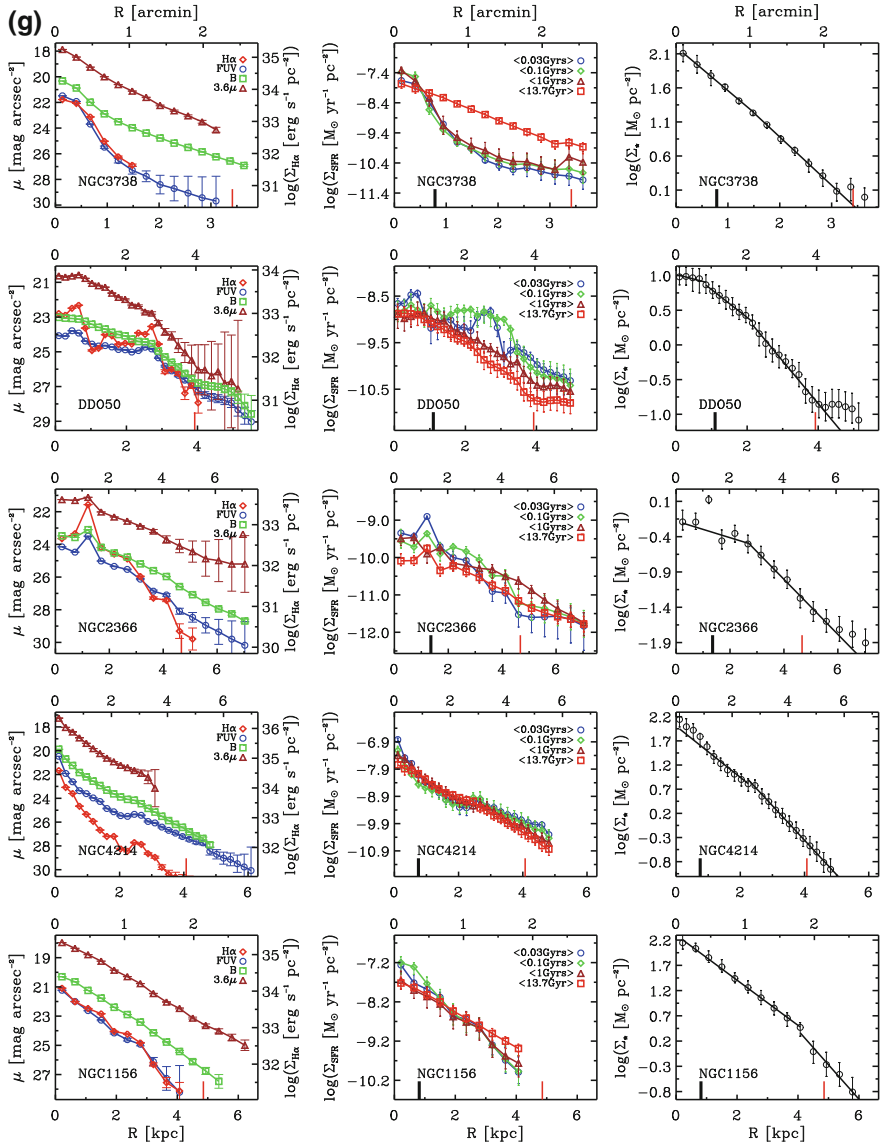


Fig. 2.13 (continued)

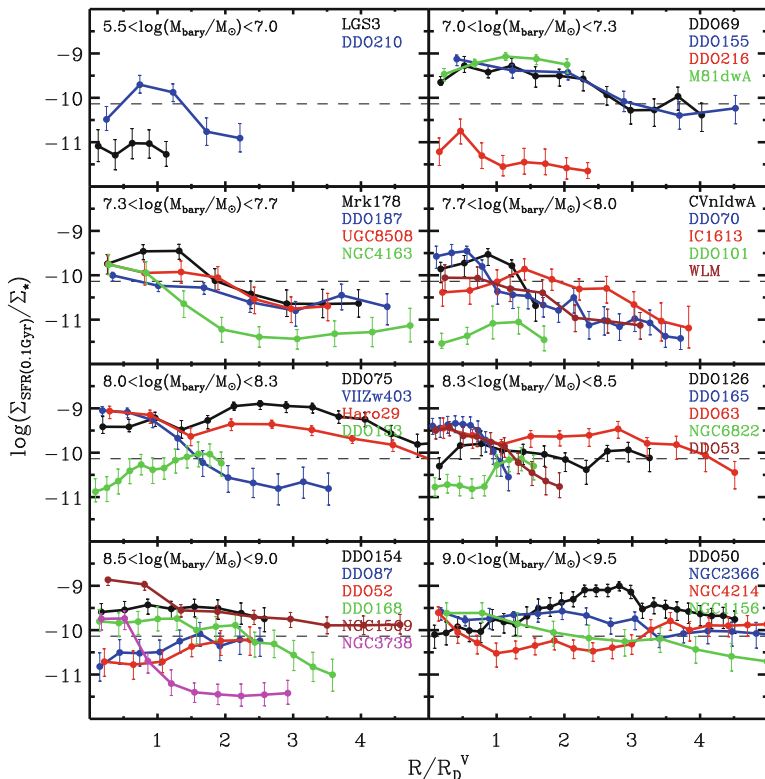


Fig. 2.14 $\log(\Sigma_{\text{SFR}_{0.1}}/\Sigma_*)$ is plotted as a function of radius, which is normalized by the V -band disk scale length. The galaxies are plotted in order of total baryonic mass from the *upper left* to the *lower right*, and within each panel galaxy names are listed in order of increasing baryonic mass. The *dashed line* in each panel marks a constant SF history over a Hubble time. The figure is adapted from Zhang et al. (2012)

M_{\odot} are also listed in Table 2.4. The slopes are further plotted in Figs. 2.16 and 2.17. Also shown in Figs. 2.16 and 2.17 are the weighted averages (*large diamonds*) of the whole sample. Negative slope indicates that the SFR averaged over the relevant timescale becomes more centrally concentrated compared to the past. As is shown, on average, our sample galaxies have more negative radial variations of $\log(\Sigma_{\text{SFR}_{0.1}}/\Sigma_*)$ and $\log(\Sigma_{\text{SFR}_1}/\Sigma_*)$ in the outer disks than the inner disks, and $\log(\Sigma_{\text{SFR}_{0.1}}/\Sigma_*)$ has a steeper radial decline than $\log(\Sigma_{\text{SFR}_1}/\Sigma_*)$. In the inner disks, 44% (15 galaxies) of the sample show negative radial slopes for both $\log(\Sigma_{\text{SFR}_{0.1}}/\Sigma_*)$ and $\log(\Sigma_{\text{SFR}_1}/\Sigma_*)$, and 9 of the 15 galaxies have $M_{\text{bary}} < 10^8 M_{\odot}$. A few galaxies with $M_{\text{bary}} > 10^8 M_{\odot}$ (i.e., DDO 165, DDO 63, DDO 154, DDO 168, NGC 2366, and NGC 4214) have almost flat slopes ($|\text{slope}| < 0.2$) in the inner disks. In the outer disks, 80% (27 galaxies) have negative slopes for both $\log(\Sigma_{\text{SFR}_{0.1}}/\Sigma_*)$ and $\log(\Sigma_{\text{SFR}_1}/\Sigma_*)$, and 14 of the 27 galaxies have $M_{\text{bary}} < 10^8 M_{\odot}$. Particularly, 35% (12 galaxies, 7 with

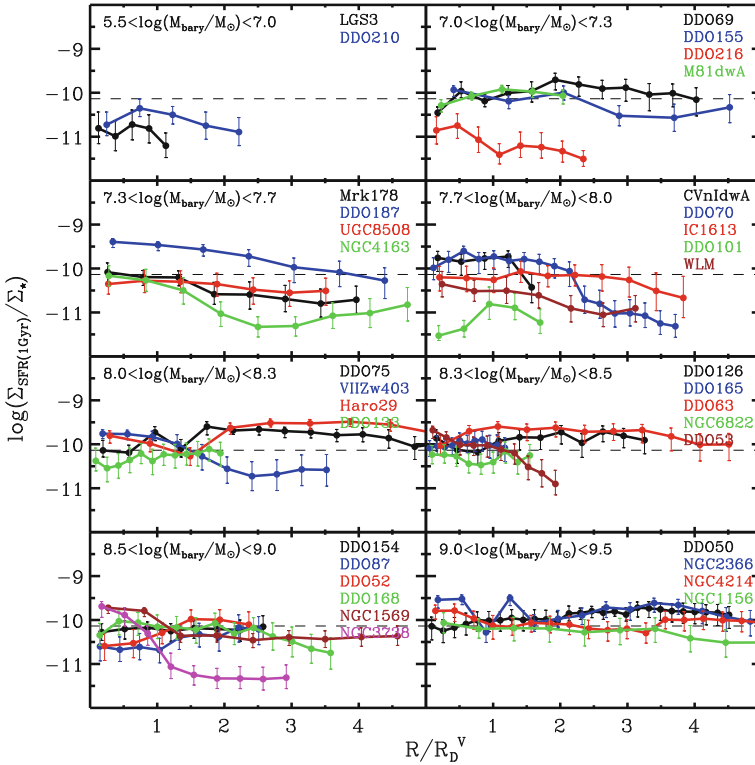


Fig. 2.15 $\log(\Sigma_{\text{SFR}_1}/\Sigma_*)$ plotted as a function of radius, which is normalized by the V -band disk scale length. The galaxies are plotted in order of total baryonic mass from the *upper left* to the *lower right*, and within each panel galaxy names are listed in order of increasing baryonic mass. The *dashed line* in each panel marks a constant SF history over a Hubble time. The figure is adapted from Zhang et al. (2012)

$M_{\text{bary}} \lesssim 10^8 M_{\odot}$) of the galaxies exhibit negative slopes across the observed disk. In NGC 4163 and NGC 3738, the recent SF has been suppressed by more than an order of magnitude in the outer regions, even though these two galaxies have almost constant ratios of $\log(\Sigma_{\text{SFR}_{0.1}}/\Sigma_*)$ and $\log(\Sigma_{\text{SFR}_1}/\Sigma_*)$ at large radii. These results are in line with Fig. 2.18, which shows the comparison between the scale length of FUV, B and $3.6 \mu\text{m}$.

Among the whole sample, the weighted averages of the slopes of $\Delta(\log(\Sigma_{\text{SFR}_{0.1}}/\Sigma_*))/\Delta(R)$ are 0.10 ± 0.42 and -0.64 ± 0.48 for the inner and the outer disks, respectively. The weighted averages of $\Delta(\log(\Sigma_{\text{SFR}_1}/\Sigma_*))/\Delta(R)$ are -0.05 ± 0.37 and -0.28 ± 0.39 for the inner and the outer disks, respectively. Furthermore, as listed in Table 2.4, the inner disks tend to have much shallower radial slopes of $\Delta(\log(\Sigma_{\text{SFR}}/\Sigma_*))/\Delta(R)$ than the outer disks. The SF activity in dIrr galaxies was suggested to be a random percolating process across the stellar disk (e.g., van Zee 2001). According to our results, *this randomly percolating scenario may be only*

Table 2.4 Slopes of the star formation history variations with radius

Galaxy	$\frac{\Delta(\log(\Sigma_{\text{SFR}0.1}/\Sigma_{\star}))}{\Delta(R/\text{kpc})}$		$\frac{\Delta(\log(\Sigma_{\text{SFR}0.1}/\Sigma_{\star}))}{\Delta(R/R_D)}$		$\frac{\Delta(\log(\Sigma_{\text{SFR}1}/\Sigma_{\star}))}{\Delta(R/\text{kpc})}$		$\frac{\Delta(\log(\Sigma_{\text{SFR}1}/\Sigma_{\star}))}{\Delta(R/R_D)}$	
	Inner	Outer	Inner	Outer	Inner	Outer	Inner	Outer
(1)	(2)	(3)	(4)	(5)	(6)	(7)	(8)	(9)
Galaxies with $M_{\text{barry}} < 10^8 M_{\odot}$								
LGS 3 ...	-0.10 ± 0.16	...	-0.02 ± 0.04	...	-1.25 ± 0.19	...	-0.29 ± 0.04	...
DDO 210 .	-2.59 ± 0.59	...	-0.43 ± 0.10	...	-0.85 ± 0.22	...	-0.14 ± 0.04	...
DDO 69 ..	-0.50 ± 0.06	-2.29 ± 0.28	-0.09 ± 0.01	-0.43 ± 0.05	1.01 ± 0.15	-0.95 ± 0.05	0.19 ± 0.03	-0.18 ± 0.01
DDO 155 .	-1.41 ± 0.06	-2.53 ± 0.24	-0.21 ± 0.01	-0.37 ± 0.03	-0.65 ± 0.15	-1.19 ± 0.26	-0.10 ± 0.02	-0.18 ± 0.04
DDO 216 .	-0.44 ± 0.04	...	-0.24 ± 0.02	...	-0.52 ± 0.04	...	-0.28 ± 0.02	...
M81dwA .	0.58 ± 0.03	-0.75 ± 0.02	0.15 ± 0.01	-0.20 ± 0.01	0.56 ± 0.03	-0.65 ± 0.01	0.14 ± 0.01	-0.17 ± 0.01
Mrk 178 ..	-2.53 ± 0.12	-1.86 ± 0.02	-0.66 ± 0.03	-0.48 ± 0.01	-1.28 ± 0.09	-0.35 ± 0.02	-0.33 ± 0.02	-0.09 ± 0.01
DDO 187 .	-1.01 ± 0.08	-2.09 ± 0.05	-0.18 ± 0.01	-0.37 ± 0.01	-0.64 ± 0.01	-1.42 ± 0.06	-0.11 ± 0.01	-0.26 ± 0.01
UGC 8508	-0.58 ± 0.02	-2.56 ± 0.07	-0.15 ± 0.01	-0.68 ± 0.02	0.07 ± 0.02	-0.72 ± 0.02	0.02 ± 0.01	-0.19 ± 0.01
NGC 4163	-0.74 ± 0.02	-0.06 ± 0.02	-0.74 ± 0.02	-0.06 ± 0.02	-0.55 ± 0.01	0.00 ± 0.04	-0.55 ± 0.01	0.00 ± 0.04
CVn1dwA .	0.24 ± 0.07	-2.50 ± 0.15	0.14 ± 0.04	-1.42 ± 0.09	0.07 ± 0.03	-1.40 ± 0.18	0.04 ± 0.02	-0.79 ± 0.10
DDO 70 ..	-1.58 ± 0.03	-0.82 ± 0.11	-0.75 ± 0.01	-0.39 ± 0.05	0.00 ± 0.05	-1.42 ± 0.11	0.00 ± 0.02	-0.68 ± 0.05
IC 1613 ...	0.11 ± 0.05	-1.22 ± 0.03	0.06 ± 0.03	-0.72 ± 0.02	0.04 ± 0.01	-0.67 ± 0.02	0.02 ± 0.01	-0.39 ± 0.01
DDO 101 .	0.52 ± 0.01	-0.24 ± 0.07	0.48 ± 0.01	-0.23 ± 0.06	0.68 ± 0.03	-0.18 ± 0.08	0.63 ± 0.03	-0.16 ± 0.07
WLM	-0.46 ± 0.02	-0.90 ± 0.04	-0.26 ± 0.01	-0.52 ± 0.02	-0.26 ± 0.01	-0.39 ± 0.06	-0.15 ± 0.01	-0.23 ± 0.03
Averages ..	0.01 ± 0.72	-1.26 ± 0.68	-0.10 ± 0.31	-0.37 ± 0.17	-0.29 ± 0.65	-0.71 ± 0.35	-0.14 ± 0.16	-0.19 ± 0.07
Galaxies with $M_{\text{barry}} > 10^8 M_{\odot}$								
DDO 75 ..	0.76 ± 0.03	-2.01 ± 0.06	0.17 ± 0.01	-0.45 ± 0.01	0.82 ± 0.03	-0.55 ± 0.05	0.18 ± 0.01	-0.12 ± 0.01
VIIZW 403	-1.42 ± 0.06	-0.95 ± 0.03	-0.75 ± 0.03	-0.50 ± 0.02	-0.52 ± 0.05	-0.71 ± 0.06	-0.27 ± 0.02	-0.37 ± 0.03
Haro 29 ...	-0.60 ± 0.09	-1.09 ± 0.05	-0.18 ± 0.02	-0.32 ± 0.01	0.63 ± 0.06	-0.13 ± 0.03	0.18 ± 0.02	-0.04 ± 0.01

(continued)

Table 2.4 (continued)

Galaxy	$\frac{\Delta(\log(\Sigma_{\text{SFR}_{0.1}}/\Sigma_{\star}))}{\Delta(R/\text{kpc})}$		$\frac{\Delta(\log(\Sigma_{\text{SFR}_{0.1}}/\Sigma_{\star}))}{\Delta(R/R_D)}$		$\frac{\Delta(\log(\Sigma_{\text{SFR}_1}/\Sigma_{\star}))}{\Delta(R/\text{kpc})}$		$\frac{\Delta(\log(\Sigma_{\text{SFR}_1}/\Sigma_{\star}))}{\Delta(R/R_D)}$	
	Inner	Outer	Inner	Outer	Inner	Outer	Inner	Outer
(1)	(2)	(3)	(4)	(5)	(6)	(7)	(8)	(9)
DDO 133 .	0.46 ± 0.01	-0.23 ± 0.05	0.52 ± 0.01	-0.26 ± 0.06	0.15 ± 0.01	0.02 ± 0.02	0.17 ± 0.01	0.02 ± 0.02
DDO 126 .	-0.23 ± 0.02	-0.02 ± 0.02	-0.20 ± 0.01	-0.02 ± 0.02	0.42 ± 0.03	-0.02 ± 0.01	0.36 ± 0.03	-0.01 ± 0.01
DDO 165 .	0.05 ± 0.01	-1.00 ± 0.02	0.12 ± 0.01	-2.27 ± 0.04	0.12 ± 0.01	-0.16 ± 0.01	0.26 ± 0.02	-0.35 ± 0.02
DDO 63 ..	-0.07 ± 0.02	-1.02 ± 0.03	-0.03 ± 0.01	-0.51 ± 0.02	0.19 ± 0.03	-0.39 ± 0.02	0.09 ± 0.02	-0.19 ± 0.01
NGC 6822	-0.07 ± 0.02	1.75 ± 0.14	-0.04 ± 0.01	1.00 ± 0.08	-0.67 ± 0.02	0.44 ± 0.13	-0.38 ± 0.01	0.25 ± 0.07
DDO 53 ..	-0.48 ± 0.02	-1.56 ± 0.05	-0.35 ± 0.01	-1.13 ± 0.04	-0.54 ± 0.02	-1.32 ± 0.03	-0.39 ± 0.02	-0.95 ± 0.02
DDO 154 .	0.03 ± 0.03	-0.45 ± 0.02	0.02 ± 0.02	-0.27 ± 0.01	-0.02 ± 0.01	0.03 ± 0.02	-0.01 ± 0.01	0.02 ± 0.01
DDO 87 ..	0.20 ± 0.03	-0.04 ± 0.01	0.29 ± 0.04	-0.06 ± 0.02	-0.05 ± 0.01	0.12 ± 0.01	-0.07 ± 0.01	0.17 ± 0.01
DDO 52 ..	0.19 ± 0.02	0.13 ± 0.01	0.25 ± 0.02	0.17 ± 0.02	0.31 ± 0.01	-0.10 ± 0.01	0.40 ± 0.02	-0.14 ± 0.01
DDO 168 .	-0.06 ± 0.01	-0.88 ± 0.02	-0.05 ± 0.01	-0.73 ± 0.02	0.01 ± 0.02	-0.40 ± 0.02	0.01 ± 0.02	-0.33 ± 0.02
NGC 1569	-0.64 ± 0.03	...	-0.25 ± 0.01	...	-0.46 ± 0.03	...	-0.18 ± 0.01	...
NGC 3738	-1.31 ± 0.04	-0.27 ± 0.01	-1.31 ± 0.04	-0.27 ± 0.01	-1.22 ± 0.02	-0.25 ± 0.02	-1.22 ± 0.02	-0.25 ± 0.02
DDO 50 ..	0.35 ± 0.01	-0.31 ± 0.02	0.38 ± 0.01	-0.34 ± 0.03	0.08 ± 0.01	0.00 ± 0.01	0.09 ± 0.01	0.00 ± 0.01
NGC 2366 .	0.04 ± 0.01	-0.07 ± 0.01	0.06 ± 0.01	-0.10 ± 0.02	-0.14 ± 0.01	-0.09 ± 0.01	-0.19 ± 0.02	-0.12 ± 0.02
NGC 4214 .	0.15 ± 0.01	...	0.11 ± 0.01	...	-0.01 ± 0.01	...	0.00 ± 0.01	...
NGC 1156 .	-0.30 ± 0.01	-0.41 ± 0.01	-0.24 ± 0.01	-0.33 ± 0.01	-0.05 ± 0.01	-0.25 ± 0.02	-0.04 ± 0.01	-0.20 ± 0.02
Averages ..	0.12 ± 0.29	-0.59 ± 0.44	0.08 ± 0.25	-0.44 ± 0.65	0.04 ± 0.21	-0.08 ± 0.20	0.02 ± 0.20	-0.09 ± 0.16

Note—(1) Galaxy names. (2–5) Slopes of the radial variations of $\Delta(\log(\Sigma_{\text{SFR}_{0.1}}/\Sigma_{\star}))/\Delta(R/\text{kpc})$ and $\Delta(\log(\Sigma_{\text{SFR}_{0.1}}/\Sigma_{\star}))/\Delta(R/R_D)$, for the inner disks and the outer disks, respectively. (6–9) Slopes of the radial variations of $\Delta(\log(\Sigma_{\text{SFR}_1}/\Sigma_{\star}))/\Delta(R/\text{kpc})$ and $\Delta(\log(\Sigma_{\text{SFR}_1}/\Sigma_{\star}))/\Delta(R/R_D)$, for the inner disks and the outer disks, respectively.

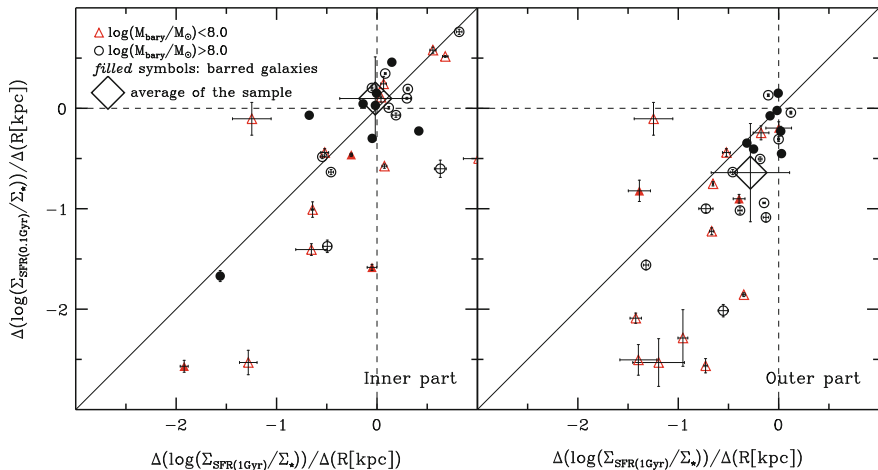


Fig. 2.16 Fitted slope of the radial variations of $\log(\Sigma_{\text{SFR}_{0.1}}/\Sigma_{\star})$ plotted against the slope of the radial variations of $\log(\Sigma_{\text{SFR}_{1}}/\Sigma_{\star})$. The *left panel* shows the results for the inner disks, and the *right panel* shows the results for the outer disks. The galaxies with baryonic mass larger and smaller than $10^8 M_{\odot}$ are denoted as *black open circles* and *red open triangles*, respectively. The *large diamonds* represent the averages among the whole sample galaxies. The *(solid)* line of equality is plotted to guide the eye. The *dashed* lines mark a flat gradient slope. Here the slope fitting was done on the physical (kpc) scales. The figure is adapted from Zhang et al. (2012)

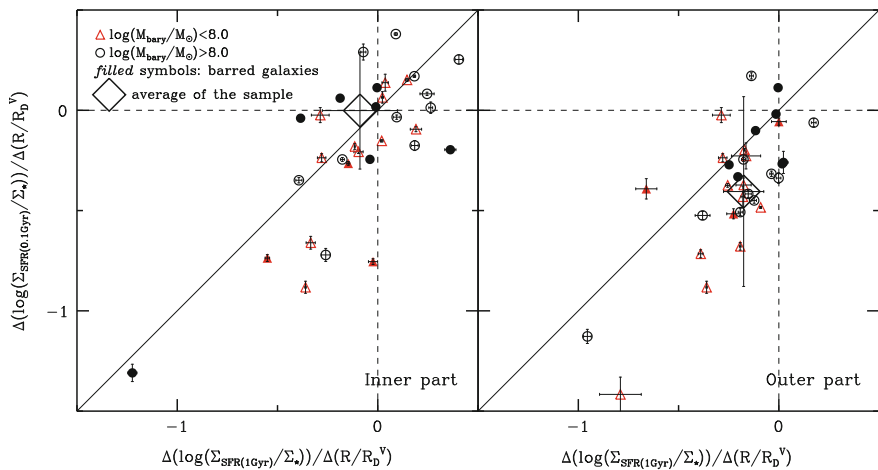


Fig. 2.17 Fitted slope of the radial variations of $\log(\Sigma_{\text{SFR}_{0.1}}/\Sigma_{\star})$ plotted against the slope of the radial variations of $\log(\Sigma_{\text{SFR}_{1}}/\Sigma_{\star})$. The *left panel* shows the results for the inner disks, and the *right panel* shows the results for the outer disks. The galaxies with baryonic mass larger and smaller than $10^8 M_{\odot}$ are denoted as *black open circles* and *red open triangles*, respectively. The *large diamonds* represent the averages among the whole sample galaxies. The *(solid)* line of equality is plotted to guide the eye. The *dashed* lines mark a flat gradient slope. Here the slope fitting was done on the radius normalized to the V-band disk scale length. The figure is adapted from Zhang et al. (2012)

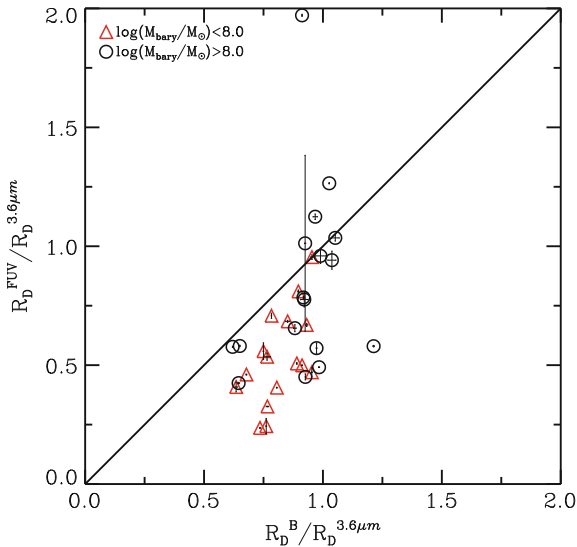


Fig. 2.18 Ratios of disk scale lengths $R_D^{\text{FUV}}/R_D^{3.6\mu\text{m}}$ plotted against $R_D^B/R_D^{3.6\mu\text{m}}$ for our sample of galaxies. R_D^{FUV} , R_D^B , and $R_D^{3.6\mu\text{m}}$ denote the disk scale lengths of the FUV, B, and $3.6\mu\text{m}$ passbands, respectively. The disk scale length measured at the outer disk is plotted for galaxies with broken surface brightness profiles. The galaxies with baryonic mass larger and smaller than $10^8 M_\odot$ are denoted as *black open circles* and *red open triangles*, respectively. The (solid) line of equality is shown to guide the eye, and galaxies below the line have larger R_D^B than R_D^{FUV} . The figure is adapted from Zhang et al. (2012)

appropriate for the inner disks of some galaxies (especially those relatively massive galaxies). As far as the whole disk of the low-mass dIrr galaxy is concerned, the star-forming disk has been shrinking from the outer part.

2.6.4 Stellar Mass Surface Density Profiles

The stellar mass surface density Σ_* profiles of the galaxies are shown in the last column of Fig. 2.13. The stellar mass surface density profiles are well fitted with a piece-wise exponential function, which is overplotted on the profiles. For some relatively faint galaxies, the high quality IRAC $3.6\mu\text{m}$ data reaches further radii than the other bands. In this case, considering the relative insensitivity of the M_*/L_{NIR} to the underlying stellar populations (Bell and de Jong 2001), we extend stellar mass surface density profiles derived from our multiband fitting to the radius reached by the $3.6\mu\text{m}$ surface photometry, adopting the $M_*/L_{3.6\mu\text{m}}$ ratio from the radius where our multiband SED fitting ends. The $3.6\mu\text{m}$ photometry for some galaxies with large angular size does not reach as far as the other bands due to the limited field of view of the *Spitzer* observations. In this case, we constrained the stellar mass profiles in

the outer part by modeling the UBV (and $GALEX$ FUV/NUV if available) data. We also derived the asymptotic total stellar mass by applying the “growth curve” method to the accumulated stellar mass surface density profiles (e.g., Muñoz-Mateos et al. 2009). Briefly, we obtained the radial gradient of the accumulated stellar mass surface density at each observed radius, then the accumulated stellar mass surface density was linearly fit as a function of the gradient and the y-intercept (zero gradient) of the fit was adopted as the asymptotic stellar mass. As an example, the stellar mass surface density profile, the corresponding accumulated stellar mass as a function of galactocentric radius, and the asymptotic total stellar mass (*horizontal dashed line*) based on the “growth curve” method for one of our sample galaxies—NGC 1569—are shown in Fig. 2.19. Table 2.3 lists the central stellar mass density $\Sigma_{\star,center}$ extrapolated from the inner exponential disk, stellar mass concentration index C_{31} , the inner/outer scale lengths of the stellar mass density profiles, and the asymptotic total stellar mass for each galaxy. C_{31} is defined here as the ratio of the radii that encompass 75 and 25 % of the total stellar mass (de Vaucouleurs 1977).

Like the radial light profiles, the stellar mass surface density profiles of dIrr galaxies usually can be described by either a single or piece-wise exponential profile over most of the disk. The most striking feature about our galaxies is that most of them have *broken* stellar mass surface density profiles. Specifically, $\sim 80\%$ (27) of the galaxies exhibit obvious down-bending profiles, in the sense that the outer disks have a steeper mass profile than the inner disks. Whereas three (DDO 70, Haro 29, NGC 1569) galaxies have obvious up-bending (flatter outer disk) profiles, in the sense that the outer disks exhibit shallower profiles than the inner disks. Both Haro 29 and NGC 1569 have experienced intense, extended starbursts in their inner regions. It has been shown that down-bending surface brightness profiles are very common in spiral galaxies (e.g., Ferguson and Clarke 2001; Pohlen and Trujillo

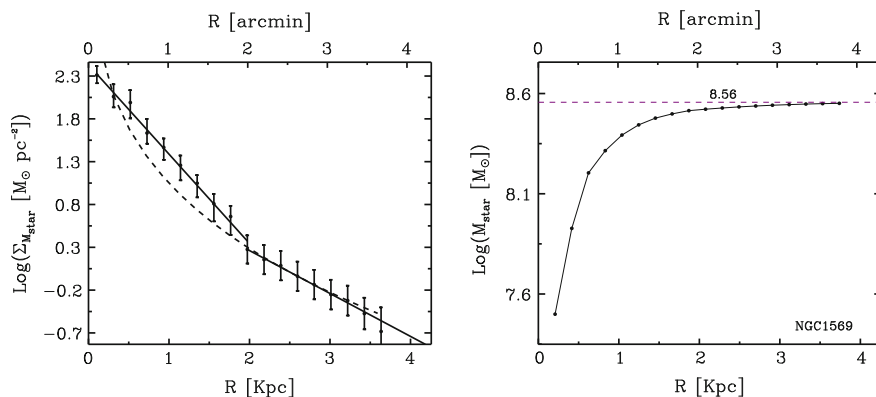


Fig. 2.19 Stellar mass surface density radial profile (*left panel*) and the accumulated stellar mass profile (*right panel*) of NGC 1569. The accumulated stellar mass profile is used to determine the asymptotic total stellar mass, as marked by the *horizontal dashed line* in the *right panel*, with the “growth curve” method

2006). Nevertheless, Bakos et al. (2008) found a pure exponential stellar mass profile for the spiral galaxies with down-bending surface brightness profiles. This is different from our dIrr galaxies which tend to have both down-bending stellar mass profiles and down-bending surface brightness profiles. Amorín et al. (2007) found that the LSB stellar hosts in BCD galaxies have near-exponential profiles. From our results for BCD galaxies, not only the LSB stellar hosts, but also the inner starburst regions have exponential stellar mass surface density profiles, although the scale length is different for the inner starburst region and the LSB stellar host (Fig. 2.13).

The present-day stellar mass surface density profile of dIrr galaxies should be primarily determined by the radial variations of SF history. As is shown above (Table 2.4), on average, the SF in the outer disks has been decreasing more significantly both over time (Figs. 2.14 and 2.15) and over radius (Figs. 2.16 and 2.17) compared to the inner disks, which would naturally lead to down-bending stellar mass surface density profile, seen in most of our galaxies. This scenario of outside-in depression of SF is different from what may be happening in typical BCD (e.g., Haro 29, NGC 1569, see Fig. 2.13) galaxies. The central starburst of BCD galaxies results in faster buildup of the inner stellar disk than the outer part, which could lead to up-bending stellar mass surface density profiles.

As can be seen, a local enhancement of the recent SF may affect the stellar mass density profile in these low-mass dIrr galaxies. For example, in NGC 2366, the supergiant H II complex (NGC 2363, Youngblood and Hunter 1999) ~ 1 kpc away from the center corresponds to the remarkable spike in the stellar mass surface density profile. The concentration index of the stellar mass surface density profile is generally close to, but lower than, that of a single exponential ($C_{31} = 2.81$).

Lower mass systems tend to have lower stellar mass concentrations (Table 2.3). However, the BCD galaxy Haro 29 is as centrally concentrated ($C_{31} = 5.3$) as a de Vaucouleurs $r^{1/4}$ bulge profile, which suggests that the centralized starburst has lasted an extended period of time. Assuming the $SFR_{0.1}$ in the central regions is representative of the recent episode of central starburst, and the central stellar mass is dominantly contributed by the burst, the starburst would have lasted more than 0.6 Gyr.

2.7 Discussions

2.7.1 *The Disk Assembly Mode of dIrr Galaxies: Outside-In*

The “inside-out” growth mode has long been suggested for the formation of galaxy disks (e.g., Larson 1976; Chiappini et al. 1997; Mo et al. 1998; Naab 2006). The “inside-out” scenario reproduces many observations of spiral galaxies, such as the radial gradients of both broadband colors (bluer outward) and metallicity (lower outward) (de Jong 1996; Bell and de Jong 2000; MacArthur et al. 2004; Wang et al. 2011), and the extended UV emission discovered in outer spiral disks

(e.g., Thilker et al. 2007a, b; Boissier et al. 2008). Muñoz-Mateos et al. (2007) found a moderate inside-out disk formation by studying the radial profiles of *GALEX* FUV and 2MASS *Ks* for a sample of relatively face-on nearby spiral galaxies. Recently, the “inside-out” growth mode has been confirmed for M 33 (Williams et al. 2009) and NGC 300 (Gogarten et al. 2010) from analysis of CMDs obtained with *HST*. For M 33, it was shown (Williams et al. 2009; Barker et al. 2011) that the “inside-out” scenario only applies to the inner disk, and the region beyond the surface brightness break exhibits positive age gradient.

However, unlike luminous spiral galaxies, late-type dIrr galaxies exhibit a variety of behaviors in terms of color profiles (Kormendy and Djorgovski 1989; Tully et al. 1996; Jansen et al. 2000; Taylor et al. 2005; HE06). Nevertheless, Tully et al. (1996) found that galaxies fainter than $M_B \sim -17$ become redder with radius in the Ursa Major cluster. Later, with a larger sample, Jansen et al. (2000) found that the reddening (with radius) trend may occur at a fainter absolute magnitude than that found by Tully et al. (1996). Of a sample of 94 dIrr galaxies studied by HE06, 64% of the galaxies with a gradient in $B-V$ become redder with radius. In particular, all the galaxies with $M_B > -14$ become redder at least in one color (either $B-V$ or $U-B$) at outer radii. Recently, Tortora et al. (2010) analyzed the optical color gradients of $\sim 50,000$ nearby Sloan Digital Sky Survey galaxies. They found a good correspondence between the color gradients and the stellar mass of the galaxies. In particular, below a stellar mass $M_\star \lesssim 10^{8.7} M_\odot$, the color gradient slopes become positive, which were mainly attributed to the positive metallicity gradients. The lowest mass galaxies in the sample of Tortora et al. (2010) have $M_\star \sim 10^{8.2} M_\odot$, compared to the median stellar mass $\sim 10^{7.2} M_\odot$ of our sample. All the above studies are based on optical broadband data alone, which makes the interpretation of the radial color gradients ambiguous, due to the degeneracy between age, metallicity, and extinction.

Additionally, from stellar CMD analysis of two different (*HST*/WFPC2) fields in IC1613, Skillman et al. (2003) (also Bernard et al. 2007) found that the SF activity in the outer field has been significantly depressed during the last Gyr, which is in contrast to the “inside-out” growth scenario. Similarly, by analyzing resolved stellar populations, the characteristics of more spatially extended older populations have been reported both for transition-type dwarf galaxies (e.g., DDO 210: McConnachie et al. 2006; Phoenix: Hidalgo et al. 2009) and dwarf spheroidal (dSph) galaxies (e.g., Sculptor dSph: Tolstoy et al. 2004; Fornax dSph: Battaglia et al. 2006). A clear trend of “outside-in” quenching of recent SF was also found (Gallart et al. 2008; Indu and Subramaniam 2011) in the Large Magellanic Cloud, which has a mass comparable to that of the most massive galaxy (i.e., NGC 1156) in our sample.

These studies are in agreement with our findings for our sample of dIrr galaxies. We point out that our analysis here is only sensitive to the SF during the recent \sim Gyr and the SF averaged over the whole lifetime. The radial variations of SF at the intermediate ages could be different from the recent past. For instance, in the late-type spiral galaxy NGC 2976, Williams et al. (2010) found a deficit of stellar populations younger than \sim Gyr beyond the break of the disk surface brightness profile, with similar ancient stellar populations at all radii. Nevertheless, since the suppression of SF in the outer disk was found in the majority of our sample galaxies, the trend

we found here must reflect the evolutionary process of the stellar disks of low-mass dIrr galaxies in general. In the following, we discuss possible interpretations of the observed radial variations of the stellar populations in dIrr galaxies.

2.7.1.1 In Situ SF Versus Secular Redistribution?

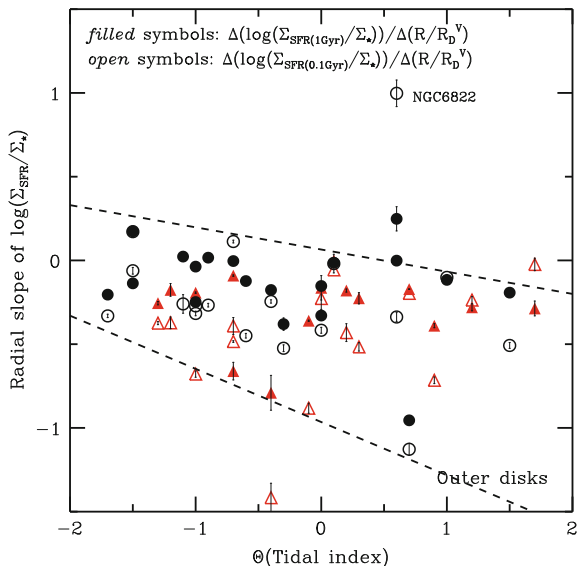
The present-day radial distribution of the stellar populations could be ascribed either to in situ SF or to a stellar redistribution process. For example, disk non-axisymmetric instabilities (e.g., spiral arms, bars) are capable of a large-scale redistribution of stars. In spiral galaxies, resonant scattering with transient spiral arms can lead to substantial radial stellar migration (e.g., Sellwood and Binney 2002; Roskar et al. 2008), which complicates determination of the in situ SF history. Likewise, the existence of bars can, besides inducing strong gas inflows, drive substantial redistribution of the stellar disk, even increasing the disk scale length (e.g., Hohl 1971; Debattista et al. 2006). However, dIrr galaxies usually lack large-scale instabilities (H98), which is a requisite of generating spiral arms and (probably) bar instabilities (e.g., Lin and Pringle 1987; Mihos et al. 1997).

Nevertheless, it has been shown that a slowly rising rotation curve naturally leads to the alignment of elongated orbits, and thus is more prone to bar formation (Lynden-Bell 1979). Even more, once the bar is made, it may exist for many dynamical times in a situation of solid body rotation, which is the case over a large part of the disk in most dIrr galaxies. Nevertheless, the bar growth of late-type galaxies may stop at a very early stage because the co-rotation radius moves out of the main disk (Combes and Elmegreen 1993). There exists a strong correlation between the strength of the bar and the central density (e.g., Elmegreen et al. 2007; Sheth et al. 2008). dIrr galaxies usually lack a central stellar mass excess, which implies that bar instabilities, if they exist, are very inefficient in transferring angular momentum across the disk of dIrr galaxies. Of our sample, 11 galaxies (32%) show evidence for a bar based on ellipse fitting of optical isophotes (HE06). Figures 2.16 and 2.17 suggest that there is no preference for barred galaxies exhibiting larger or smaller radial gradients of $\log(\Sigma_{\text{SFR}}/\Sigma_{\star})$. We note that identifying bars in dIrr galaxies is not as straightforward as in luminous spiral galaxies.

2.7.1.2 External Influences

External factors, such as interactions (both with the intragroup/intracluster medium and with neighboring galaxies) and the cosmic UV background (e.g., Gnedin 2000), can also lead to more centrally concentrated recent SF or depressed SF in outer disks. The tidal index (Table 2.1) suggests that less than 5 of the galaxies studied here could be noticeably affected ($\Theta \gtrsim 1$) by neighboring galaxies. The slopes of the radial variations of $\log(\Sigma_{\text{SFR}_{0.1}}/\Sigma_{\star})$ and $\log(\Sigma_{\text{SFR}_1}/\Sigma_{\star})$ for the outer disks are plotted against the tidal index in Fig. 2.20 (There is no calculation of Θ for DDO 101 in Karachentsev et al. (2004), so we arbitrarily set Θ as 0 when creating the plot).

Fig. 2.20 Fitted slope of the radial variations of $\log(\Sigma_{\text{SFR}_{0.1}}/\Sigma_*)$ and $\log(\Sigma_{\text{SFR}_1}/\Sigma_*)$ in the outer disks plotted as a function of the tidal index Θ . The *black circles* and the *red triangles* denote galaxies with baryonic mass larger and smaller than $10^8 M_\odot$, respectively. The *open* and the *filled* symbols denote the slope of $\log(\Sigma_{\text{SFR}_{0.1}}/\Sigma_*)$ and the slope of $\log(\Sigma_{\text{SFR}_1}/\Sigma_*)$, respectively. The *dashed lines* mark the upper and the lower envelopes of the distribution of most data points in the plot. The figure is adapted from Zhang et al. (2012)



There is no obvious correlation between the radial variations of the SF histories and the environment. However, most galaxies fall between an upper envelope and a lower envelope, as indicated by the *dashed* lines in the plot. NGC 6822 has such a large angular size projected on the sky that the observations only covered the central regions. As mentioned above, the SF of dIrr galaxies usually peaks in the circumnuclear regions, therefore, the slopes measured here for NGC 6822 do not reflect the SF history variations across the main star-forming disk. In fact, based on *HST* images of five fields in NGC 6822, Wyder (2001) found a higher ratio of the recent SFR to the average past rate in the inner bar regions than the outer regions, consistent with the trend we found in this study. The galaxies with larger Θ prefer lower (zero or negative) slopes of the radial variations of $\log(\Sigma_{\text{SFR}_{0.1}}/\Sigma_*)$ and $\log(\Sigma_{\text{SFR}_1}/\Sigma_*)$.

Two of the most obvious environmental effects studied in the literature are ram pressure stripping of the gas component caused by a hot gaseous intra-group/intracluster medium (Gunn and Gott 1972; Lin and Faber 1983) and tidal disturbance from neighboring galaxies (e.g., Mayer et al. 2001). By studying the dynamical properties of the dwarf galaxies in the Fornax cluster, Drinkwater et al. (2001) show that the dwarf galaxies are still falling into the cluster, and the fraction of dwarfs with active SF drops rapidly toward the cluster center. This is a clear indication of the environmental effect on the evolution of dwarf galaxies. Similarly, Pustilnik et al. (2002) found that the blue compact galaxies in higher density environment have on average less HI, which could be attributed to either ram pressure stripping of the gas or tidal interactions.

Presumably, both ram pressure stripping and tidal disturbance should be more effective on lower mass galaxies. The outer disk, especially in relatively low-mass

systems where the gravitational well and the gas surface density are relatively low, is more prone to gas removal due to ram pressure. Furthermore, significant tidal forces from neighboring galaxies could induce a bar instability and ensuing gas inflows toward the inner regions (e.g., Mayer et al. 2001), which leads to a more centrally concentrated SF. In our sample, lower mass galaxies tend to have more centrally concentrated SF than relatively higher mass galaxies, which is in general agreement with the expectation of the above two environmental effects.

By studying the HI distribution of spiral galaxies in the Virgo cluster, Cayatte et al. (1994) found that some galaxies close to the cluster core have normal gas densities (compared to field counterparts) in the inner disks but show a strong decline or cutoff of the HI intensity starting within the half-light radius of the stellar disk. These galaxies should have been undergoing remarkable ram pressure stripping. Actually, the radial HI distribution (Hunter et al. 2012) for some of our galaxies do show a strong decline starting well within the stellar disk. Numerical simulations (e.g., Vollmer 2003; Kapferer et al. 2008) suggest that both ram pressure stripping and tidal disturbance are needed to reproduce the observations. Figure 2.20 suggests that the tidal disturbance from neighboring galaxies should play some role in the inward movement of SF activity.

The presence of a UV background can heat the gas in low-mass halos, which prevents SF at least in the outer disk where the gas is not dense enough for self-shielding (Susa and Umemura 2004). By solving the radiative transfer equation for the diffuse UV background in a pre-galactic cloud, Tajiri and Umemura (1998) showed that, above a critical number density $n_{\text{crit}} \sim 1.4 \times 10^{-2} \text{ cm}^{-3}$ ($N_{\text{H}_I} \sim 1.3 \times 10^{19}$ for a gas disk ~ 0.3 kpc thick), which is almost independent of the UV background intensity, self-shielding of the ISM against the UV background is prominent. Based on our HI emission line maps of these galaxies, and according to this critical density, the typical gas column density ($\sim 10^{20} \text{ cm}^{-2}$) across the observed stellar disks of our galaxies should be sufficient for them to be self-shielded. Therefore, the cosmic UV background is unlikely to be the main driver of the centrally concentrated SF.

2.7.1.3 Regulation of the SFR Through Stellar-Feedback

Depressed SF in outer dwarf disks could be attributed to self-regulation due to stellar feedback. Feedback from both SNe and stellar winds has been shown to be a major factor shaping the evolution of dwarf galaxies due to their shallow potential wells (e.g., Dekel and Silk 1986; Mori et al. 2002; Mashchenko et al. 2008). From numerical simulations, the SNe/stellar winds-regulated evolution of isolated dwarf galaxies tends to be characterized by an episodic SF history (e.g., Chiosi and Carraro 2002; Stinson et al. 2007). Such SF histories have been suggested to explain the anomalously blue colors and low metallicities of dIrr galaxies (e.g., Searle et al. 1973).

In this SNe/stellar winds-regulated evolution scenario, the SN explosions and stellar winds from massive stars following one episode of SF trigger gas heating and expansion, and some gas may be blown away from the galaxy. Subsequent cooling

allows the remaining gas to sink deeper into the center and start another cycle of SF. The outside-in formation scenario has been suggested for low-mass elliptical galaxies (Martinelli et al. 1998; Pipino and Matteucci 2004) to explain the positive gradients of [Mg/Fe] and the blue colors in the center of dwarf elliptical galaxies. The outer regions, where the gravitational potential well is relatively low, are more susceptible to the galactic wind (thus blow-out/blow-away) compared to the inner regions. The blow-out/blow-away of the high angular momentum gas (compared to the inner regions) in the outer part of the dwarf disk results in a remarkable net loss of angular momentum, and thus the shrinking of the gas disk. This leads to a depression of SF in the outskirts and more prolonged SF in the central regions. Recent simulations (Valcke et al. 2008) indeed found that, for a self-regulated, SNe-driven evolution of low-mass ($M_{\text{bary}} \lesssim 10^8 M_{\odot}$) dwarf galaxies, the SF becomes more and more centrally concentrated with time, which is in agreement with what we see here. We point out that this scenario of outside-in shrinking may not apply to the early universe when the galaxy just started assembling and the potential was shallow (susceptible to stellar feedback) even in the inner region. Governato et al. (2010) found that the outflows resulting from stellar feedback may selectively remove low-angular momentum gas, especially at $z > 1$.

Recent high-resolution hydrodynamical simulations including cooling, SN feedback, and the UV background radiation (Sawala et al. 2010) suggest that, while the combined effects of SN feedback and UV heating are necessary to reproduce the observations, SN feedback is the key factor in determining the evolution of low-mass dwarf galaxies. The cosmic UV radiation has almost no effect on galaxy evolution if the SN feedback was ignored in the simulations.

2.7.1.4 Pressure Support in the Gas Disk

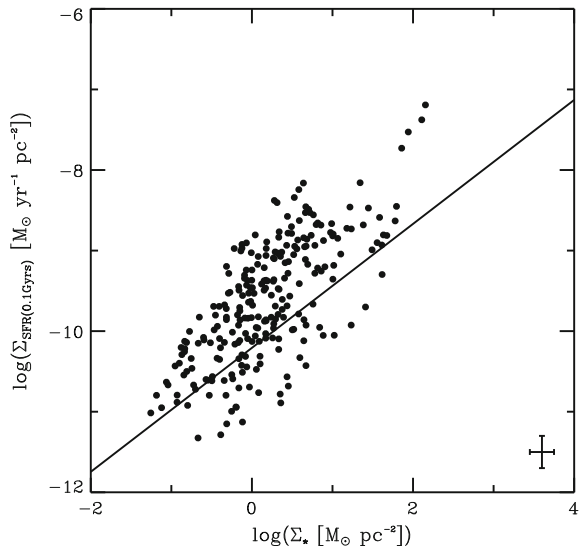
Low-mass dIrr galaxies are dynamically hot systems compared to luminous spiral galaxies. The (turbulent) gas velocity dispersion within dwarf galaxies can be comparable to the ordered rotational velocity, which means the gas pressure may provide significant radial support to the rotating gas disk (Stinson et al. 2009; Dalcanton and Stilp 2010). Since the gas density usually declines with radius, the pressure gradient, together with the centrifugal acceleration, will counteract the gravity. A higher efficiency of SF in the inner regions then leads to quicker consumption of gas, which results in an initial reduction of the gas density there. After the enhanced turbulence from SF subsides, the pressure in the center will drop too, and more gas will flow in so that pressure gradients and centrifugal force balance gravity again. Thus some shrinking of the gas disk might be possible, within the limits of angular momentum conservation. In their simulations of isolated low-mass dwarf galaxies, Stinson et al. (2009) found a positive age gradient with radius after gas contraction, stellar migration, and supernova-triggered SF, with the latter two effects being more important for lower mass galaxies. Dalcanton and Stilp (2010) further demonstrated that the impact of pressure support alone on the evolution of a gas disk may be weak.

2.7.2 The Relationship Between Σ_{SFR} , Σ_{\star} and Star Formation History

H98 found that the radial profiles of current SF activity correlate better with those of the older stellar emission (e.g., V-band) than with the atomic gas in dIrr galaxies. Since star-forming molecular clouds are forming from the atomic gas, this lack of a correlation between SF and gas is unexpected. Similarly, Ryder and Dopita (1994; see also James et al. 2009) discovered a good correlation between I-band surface brightness (a proxy for the mass dominant old stellar populations) and H α for a sample of nearby spiral galaxies. Recently, a good correspondence between the surface brightness in SDSS *r*-band and in FUV was also shown for a sample of LSB galaxies (Wyder et al. 2009). If the optical broadband emission traces the underlying mass-dominant old stellar populations, the above correlations would be equivalent to a relationship between SF and the stellar mass surface density. Is this correlation between Σ_{SFR} and Σ_{\star} causal or casual?

In spiral galaxies, the stellar component usually dominates the inner disk in terms of both surface density and volume density, so we might expect that the stellar component plays an important role in regulating the ISM and thus the SF process (e.g., Wong and Blitz 2002; Blitz and Rosolowsky 2006; Shi et al. 2011). However that is not necessarily the case in dIrr galaxies, where the atomic gas usually dominates the baryonic component. In Fig. 2.21, $\Sigma_{\text{SFR}_{0.1}}$ is plotted against Σ_{\star} for the whole sample. The data points are extracted from the azimuthal averages of the relevant surface density profiles. Although there is rough correspondence between $\Sigma_{\text{SFR}_{0.1}}$ and Σ_{\star} , the scatter is substantial. The Spearman rank correlation coefficient between Σ_{\star} and $\Sigma_{\text{SFR}_{0.1}}$ is ~ 0.6 .

Fig. 2.21 $\Sigma_{\text{SFR}_{0.1}}$ plotted against Σ_{\star} for the galaxy sample. The data points are from the azimuthal averages of the relevant surface density profiles, so each galaxy is represented by many points. The *solid line* in the plot indicates the expected relationship between $\Sigma_{\text{SFR}_{0.1}}$ and Σ_{\star} for a constant SFR over a Hubble time. The figure is adapted from Zhang et al. (2012)



As is shown in Fig. 2.14, the inner regions of our galaxies tend to have higher ratios of $\Sigma_{\text{SFR}_{0.1}}$ to Σ_{\star} than outer parts, which is especially significant for relatively lower mass systems. In other words, $\Sigma_{\text{SFR}_{0.1}}$ usually has a steeper radial dependence than Σ_{\star} . This is consistent with our finding that shorter wavelengths tend to have shorter scale lengths than longer wavelengths (Fig. 2.18). Within the inner disks, our sample galaxies, on average, have almost zero radial gradients of $\Sigma_{\text{SFR}}/\Sigma_{\star}$ (Figs. 2.16 and 2.17). Therefore, the correlation between Σ_{SFR} and Σ_{\star} is only good within the inner disk.

Recently, Leroy et al. (2008) found that, in dIrr galaxies and outer disks of spiral galaxies, the ratio of SFR surface density to atomic gas surface density exhibits an almost linear relationship to the stellar mass surface density. Given the narrow range of the HI surface density ($5\text{--}10 M_{\odot} \text{ pc}^{-2}$, Leroy et al. (2008) within the optical disk, the above correlation actually reflects the correlation between the SFR and the stellar mass surface density. We note that all of the dIrr galaxies studied by Leroy et al. (2008) have baryonic masses well above $10^8 M_{\odot}$. For the four galaxies in common with the sample of Leroy et al. (i.e., DDO 154, DDO 63, DDO 50, and NGC 4214), except for DDO 50, all the other three have shallow ($|\Delta(\log(\Sigma_{\text{SFR}_{0.1}}/\Sigma_{\star}))/\Delta(R)| < 0.2$, Table 2.4) radial slopes of $\log(\Sigma_{\text{SFR}_{0.1}}/\Sigma_{\star})$ across the inner disks, which extend to more than \sim three disk scale lengths, in agreement with Leroy et al. (2008). Nevertheless, some galaxies (DDO 52, NGC 1569, NGC 3738, and NGC 1156) in our sample with baryonic masses larger than $10^8 M_{\odot}$ show obvious gradients (either positive or negative, see Table 2.4) of $\log(\Sigma_{\text{SFR}_{0.1}}/\Sigma_{\star})$ across the whole disks.

The star formation efficiency (SFE) in dIrr galaxies generally is very low (e.g., van Zee 2001; Lee et al. 2011), as is evidenced by high gas-to-stellar mass ratios (e.g., see Table 2.1). Therefore, the stellar disk may have always been a small perturbation on the gas-dominated baryonic disk. The constant average ratios of $\Sigma_{\text{SFR}_{0.1}}$ to Σ_{\star} and Σ_{SFR_1} to Σ_{\star} seen in the inner disks of dIrr galaxies could imply that the SFE at a given radius in the inner disk may have been nearly the same for most of the galaxy's lifetime. This would naturally lead to similar radial profiles of the SFR to the accumulated stellar mass. In agreement with this evolutionary picture, Elmegreen and Hunter (2006) considered multicomponent SF triggering processes, including turbulent compression, to interpret SF in outer spiral disks and in dIrr galaxies. They suggested that the SF profile should be about the same as the accumulated stellar mass profile when the baryonic component of the disk is still dominated by atomic gas. In this scenario, the stellar mass distribution naturally follows the inefficient, patchy SF. On the other hand, for the outer disks, the SF process has been significantly affected by stellar feedback (e.g., SNe) and the external disturbances. As discussed in the previous section, feedback-regulated evolution or environmental effects may result in shrinking of the star-forming gas disk toward the inner part, and thus more and more centrally concentrated SF, without a remarkable correlation between SFR and stellar mass. We noticed that the ‘‘inner disk’’ of galaxies with $M_{\text{bary}} > 10^8 M_{\odot}$ could extend over more than ~ 3 disk scale lengths.

2.8 Summary

We present multiband (*GALEX* FUV/NUV, *UBV*, $H\alpha$ and *Spitzer* 3.6 μm) surface brightness profiles for a representative sample of nearby dIrr galaxies. The median of the stellar mass and of the total baryonic mass of our sample galaxies are $\sim 10^{7.2} M_{\odot}$ and $10^8 M_{\odot}$, respectively. By modeling the multiband SEDs with a relatively complete library of SF histories, we constrained: the radial variations of the SFR averaged over the recent 0.1 Gyr, $\text{SFR}_{0.1}$, the SFR averaged over the recent 1 Gyr, SFR_1 , and the stellar mass surface density profiles. To summarize the results:

1. We show that, with a relatively complete library of model SF histories, the average SFR during the past 1 Gyr can be well constrained by modeling integrated multi-band data. The exponential plus burst SF history library commonly used for spirals tends to systematically overestimate recent SF of dIrr galaxies, which are characterized as having much more complex SF histories than the larger spiral galaxies.
2. For $\sim 80\%$ (27) of the dIrr galaxies studied in this work, and all (15) with baryonic mass less than $10^8 M_{\odot}$, surface brightness profiles determined from shorter wavelength passbands have shorter exponential disk scale lengths than those based on passbands at longer wavelengths at least in the outer disks. This trend suggests that the star-forming stellar disk may be shrinking for most dIrr galaxies. This produces an “outside-in” disk formation scenario for dIrr galaxies.
3. The recent SF activity of $\sim 38\%$ of our galaxies has been enhanced by a factor of at least 2 compared to the lifetime averaged SFR. Even though no obvious correlation between global SF histories and total baryonic mass was found in our sample, all of the galaxies with significantly declining global SF activity have baryonic masses smaller than $10^8 M_{\odot}$. This may be ascribed to the susceptibility of low-mass dwarf galaxies to significant influence by both internal and external processes.
4. Consistent with the “outside-in” scenario, 80% of our sample galaxies have negative slopes of radial variations of $\log(\Sigma_{\text{SFR}_{0.1}}/\Sigma_{\star})$ and of $\log(\Sigma_{\text{SFR}_1}/\Sigma_{\star})$ at least in the outer disks (beyond the breaks of stellar mass surface density profiles). In the inner disks, especially for the galaxies with $M_{\text{bary}} > 10^8 M_{\odot}$, the slopes are much shallower (consistent with zero slopes on average) than that in the outer disks. Both internal (stellar feedback, gas pressure support) and external (ram pressure stripping of gas and tidal disturbance) processes are discussed as the possible explanation for the “outside-in” shrinking of the star-forming disk.
5. The radial distribution of the stellar mass density of dIrr galaxies is well described as a single or, for the majority, a piece-wise exponential profile. In particular, the majority ($\sim 80\%$) of our sample galaxies exhibit steeper outer (down-bending) stellar mass profiles. Since the outer disks on average have much steeper radial declining $\Sigma_{\text{SFR}}/\Sigma_{\star}$ than the inner regions, we interpret the down-bending stellar mass surface density profiles as a natural result of a gradual shrinking of the star-forming disks. A few galaxies exhibit much steeper stellar mass profiles in the inner disk than the outer disk, which may be caused by an intense starburst

in their inner regions. Spiral galaxies with double exponential surface brightness profiles and inside-out SF may require a different explanation for the steep outer profiles. In spirals, the outer disks are sometimes younger than the inner disks, while in dwarfs, the outer disks are usually older than the inner disks. Perhaps spirals are still accreting gas in their outer parts, whereas the dwarfs have lost gas in their outer parts and have other dynamical effects not present in larger galaxies.

6. The previously found correlation between surface density of the stellar mass and recent SFR is only remarkable in the inner disks, which could extend over more than three disk scale lengths for the relatively massive ($M_{\text{bary}} \gtrsim 10^8 M_{\odot}$) dIrr galaxies. The correlation can be explained by inefficient, constant SF at a given radius during most of the galaxy's lifetime. For the outer disks of most (80% for the present sample) dIrr galaxies, on the other hand, the correlation between SFR and stellar mass surface densities is not strong, due to effects of internal feedback, turbulent gas pressure support, and external disturbances (Elmegreen and Elmegreen 1984; Hunter and Hoffman 1999; McQuinn et al. 2009; Rafikov 2001).

References

- Amorín RO, Muñoz-Tuñón C, Aguerri JAL, Cairós LM, Caon N (2007) *A&A* 467:541
- Bakos J, Trujillo I, Pohlen M (2008) *ApJ* 683:103
- Barker MK, Ferguson AMN, Cole AA, Ibata R, Irwin M, Lewis GF, Smecker-Hane TA, Tanvir NR (2011) *MNRAS* 410:504
- Battaglia G et al (2006) *A&A* 459:423
- Bell EF, de Jong RS (2000) *MNRAS* 312:497
- Bell EF, de Jong RS (2001) *ApJ* 550:212
- Bernard EJ, Aparicio A, Gallart C, Padilla-Torres CP, Panniello M (2007) *AJ* 134:1124
- Blitz L, Rosolowsky E (2006) *ApJ* 650:933
- Boissier S, Gil de Paz A, Boselli A et al (2008) *ApJ* 681:244
- Bruzual A (1000) G., & Charlot, S. (2003). *MNRAS* 344:
- Burstein D, Heiles C (1982) *AJ* 87:1165
- Cardelli JA, Clayton GC, Mathis JS (1989) *ApJ* 345:245
- Cayatte V, Kotanyi C, Balkowski C, van Gorkom JH (1994) *AJ* 107:1003
- Cervino M, Luridiana V (2004) *A&A* 413:145
- Chabrier G (2003) *ApJ* 586:133
- Charlot S, Fall SM (2000) *ApJ* 539:718
- Chiappini C, Matteucci F, Gratton R (1997) *ApJ* 477:765
- Chiosi C, Carraro G (2002) *MNRAS* 335:335
- Cole AA, Skillman ED, Tolstoy E et al (2007) *ApJ* 659:17
- Combes F, Elmegreen BG (1993) *A&A* 271:391
- da Cunha E, Charlot S, Elbaz D (2008) *MNRAS* 388:1595
- Dale DA, Cohen SA, Johnson LC et al (2009) *ApJ* 703:517
- Dalcanton JJ, Stilp AM (2010) *ApJ* 721:547
- de Jong RS (1996) *A&A* 313:377
- de Vaucouleurs G (1977) In: Larson RB, Tynsley BM (eds) *Evolution of Galaxies and Stellar Populations*, vol 43. Yale Univ, New Haven
- Debbastista V, Mayer L, Carollo CM, Moore B, Wadsley J, Quinn T (2006) *ApJ* 645:209

- Dekel A, Silk J (1986) *ApJ* 303:39
- Dolphin AE (2000) *ApJ* 531:804
- Dolphin AE, Weisz DR, Skillman ED, Holtzman JA (2005) [arXiv:astro-ph/0506430](https://arxiv.org/abs/astro-ph/0506430)
- Drinkwater MJ, Gregg MD, Holman BA, Brown MJI (2001) *MNRAS* 326:1076
- Elmegreen DM, Elmegreen BG (1984) *ApJS* 54:127
- Elmegreen BG, Hunter DA (2006) *ApJ* 636:149
- Elmegreen BG, Elmegreen DM, Knapen JH, Buta RJ, Block DL, Puerari I (2007) *ApJ* 670:97
- Engelbracht CW, Rieke GH, Gordon KD et al (2008) *ApJ* 678:804
- Fazio GG et al (2004) *ApJS* 154:10
- Ferguson AMN, Clarke CJ (2001) *MNRAS* 325:781
- Fitzpatrick EL (1999) *PASP* 111:63
- Gallart C, Zoccali M, Aparicio A (2005) *ARA&A* 43:387
- Gallart C, Stetson PB, Meschin IP, Pont F, Hardy E (2008) *ApJ* 682:89
- Girardi L, Bertelli G, Bressan A, Chiosi C, Groenewegen MAT, Marigo P, Salasnich B, Weiss A (2002) *A&A* 391:19
- Gnedin N (2000) *ApJ* 542:535
- Gogarten SM et al (2010) *ApJ* 712:858
- Governato F et al (2010) *Nature* 463:203
- Greggio, L. (2002) *ASP Conf. Proceedings, Ser. Vol. 274, p. 444*. Editor: Lejeune, T., & Fernandes, J
- Gunn JE, Gott JR III (1972) *ApJ* 176:1
- Helou G et al (2004) *ApJS* 154:253
- Herrmann KA, Hunter DA, Elmegreen BG (2013) *AJ* 146:104
- Hidalgo SL, Aparicio A, Martinez-Delgado D, Gallart C (2009) *ApJ* 705:704
- Hidalgo SL et al (2011) *ApJ* 730:14
- Hummer DG, Storey PJ (1987) *MNRAS* 224:801
- Hunter DA, Elmegreen BG (2004) *AJ* 128(HE04):2170
- Hunter DA, Elmegreen BG (2006) *ApJ* 162(HE06):49
- Hunter DA, Hoffman L (1999) *ApJ* 117:2789
- Hunter DA, Gallagher JS (1986) *PASP* 98:5
- Hunter DA, Elmegreen BG, Ludka BC et al (2010) *AJ* 139:447
- Hunter DA, Ficut-Vicas D, Ashley T et al (2012) *AJ* 144:134. doi:[10.1088/0004-6256/144/5/134](https://doi.org/10.1088/0004-6256/144/5/134)
- Hohl F (1971) *ApJ* 168:343
- Indu G, Subramaniam A (2011) [arXiv:1109.1061](https://arxiv.org/abs/1109.1061)
- James PA, Bretherton CF, Knapen JH (2009) *A&A* 501:207
- Jansen RA, Franx M, Fabricant D, Caldwell N (2000) *ApJS* 126:271
- Johnson BD et al (2007) *ApJS* 173:392
- Johnson M, Hunter DA, Oh S-H, Zhang H-X et al (2012) *AJ* 144:152
- Kapferer W, Kronberger T, Ferrari C, Riser T, Schindler S (2008) *MNRAS* 389:1405
- Karachentsev ID, Karachentseva VE, Huchtmeier WK, Makarov DI (2004) *AJ* 127:2031
- Kauffmann G et al (2003) *MNRAS* 341:33
- Kennicutt RC Jr, Skillman ED (2001) *AJ* 121:1461
- Kennicutt RC Jr et al (2003) *PASP* 115:928
- Kennicutt RC, Jr, Lee JC, Funes JG, Sakai S, Akiyama S (2005) *ASSL Volume 329, Starbursts from 30 Doradus to Lyman Break Galaxies*, eds., De Gris, R. & Gonzalez Delgado, R. M., Springer (the Netherlands), 187
- Kong X, Charlot S, Brinchmann J, Fall SM (2004) *MNRAS* 349:769
- Kormendy J, Djorgovski S (1989) *ARA&A* 27:235
- Landolt AU (1992) *AJ* 104:340
- Larson RB (1976) *MNRAS* 176:31
- Lee JC et al (2009a) *ApJ* 706:599
- Lee JC, Kennicutt RC, Funes JG, Sakai S, Akiyama S (2009b) *ApJ* 692:1305
- Lee JC et al (2011) *ApJS* 192:6

- Leitherer C, Schaerer D, Goldader JD et al (1999) *ApJ* 123:3
- Leroy AK et al (2008) *AJ* 136:2782
- Lin DNC, Faber SM (1983) *ApJ* 670:21
- Lin DNC, Pringle JE (1987) *MNRAS* 225:607
- Lynden-Bell D (1979) *MNRAS* 187:101
- Marigo P, Girardi L, Bressan A et al (2008) *A&A* 482:883
- Martin DC, Fanson J, Schiminovich D et al (2005) *ApJ* 619:1
- Martinelli A, Matteucci F, Colafrancesco S (1998) *MNRAS* 298:42
- Mashchenko S, Wadsley J, Couchman HMP (2008) *Science* 319:174
- MacArthur LA, Courteau S, Bell E, Holtzman JA (2004) *ApJS* 152:175
- Mac Low M, Ferrara A (1999) *ApJ* 523:391
- Mayer L, Governato F, Colpi M, Moore B, Quinn T, Wadsley J, Stadel J, Lake G (2001) *ApJ* 547:123
- Meurer GR et al (2009) *ApJ* 695:765
- McQuinn KBW, Skillman ED, Cannon JM, Dalcanton JJ, Dolphin A, Stark D, Weisz D (2009) *ApJ* 659:561
- Mihos JC, McGaugh SS, de Blok WJG (1997) *ApJ* 477:79
- McConnachie AW, Arimoto N, Irwin M, Tolstoy E (2006) *MNRAS* 373:715
- McConnachie AW, Venn KA, Irwin MJ, Young LM, Geehan JJ (2007) *ApJ* 671:33
- Mo HJ, Mao S, White SDM (1998) *MNRAS* 295:319
- Mori M, Ferrara A, Madau P (2002) *ApJ* 571:40
- Muhle S, Klein U, Wilcots EM, Huttemeister S (2005) *AJ* 130:524
- Muñoz-Mateos JC, de Paz Gil A, Boissier S, Zamorano J, Jarrett T, Gallego J, Madore BF (2007) *ApJ* 658:1006
- Muñoz-Mateos JC, Gil de Paz A, Zamorano J et al (2009) *ApJ* 703:1569
- Naab T, Ostriker JP (2006) *MNRAS* 366:899
- Orban C, Gnedin OY, Weisz DR, Skillman ED, Dolphin AE, Holtzman JA (2008) *ApJ* 686:1030
- Pflamm-Altenburg J, Weidner C, Kroupa P (2009) *MNRAS* 395:394
- Pipino A, Matteucci F (2004) *MNRAS* 347:968
- Pohlen M, Trujillo I (2006) *A&A* 454:759
- Pohlen M, Dettmar R-J, Luticke R, Aronica G (2002) *A&A* 392:807
- Pustilnik SA, Martin J-M, Huchtmeier WK, Brosch N, Lipovetsky VA, Richter GM (2002) *A&A* 389:405
- Rafikov RR (2001) *MNRAS* 323:445
- Roskar R, Debattista VP, Quinn TR, Stinson GS, Wadsley J (2008) *ApJ* 684:79
- Ryder SD, Dopita MA (1994) *ApJ* 430:142
- Sawala T, Scannapieco C, Maio U, White S (2010) *MNRAS* 402:1599
- Searle L, Sargent WLW, Bagnuolo WG (1973) *ApJ* 179:427
- Sellwood JA, Binney JJ (2002) *MNRAS* 336:785
- Sheth K et al (2008) *ApJ* 675:1141
- Skillman ED, Tolstoy E, Cole AA, Dolphin AE, Saha A, Gallagher JS, Dohm-Palmer RC, Mateo M (2003) *ApJ* 596:253
- Sullivan M, Treyer MA, Ellis RS, Mobasher B (2004) *MNRAS* 350:21
- Schlegel DJ, Finkbeiner DP, Davis M (1998) *ApJ* 500:525
- Shi Y et al (2011) *ApJ* 733:87
- Stil JM, Israel FP (1998) *A&A* 337:64
- Stinson GS, Dalcanton JJ, Quinn T, Kaufmann T, Wadsley J (2007) *ApJ* 667:170
- Stinson GS, Dalcanton JJ, Quinn T, Gogarten SM, Kaufmann T, Wadsley J (2009) *MNRAS* 395:1455
- Susa H, Umemura M (2004) *ApJ* 600:1
- Tajiri Y, Umemura M (1998) *ApJ* 502:59
- Taylor VA, Jansen RA, Windhorst RA, Odewahn SC, Hibbard JE (2005) *ApJ* 630:784
- Thilker DA et al (2007a) *ApJS* 173:538
- Thilker DA et al (2007b) *ApJS* 173:572
- Thuan TX, Martin GE (1981) *ApJ* 247:823

- Tolstoy E, Hill V, Tosi M (2009) *ARA&A* 47:371
- Tully RB, Verheijen MAW, Pierce MJ, Huang J, Wainscoat RJ (1996) *AJ* 112:2471
- Tolstoy E et al (2004) *ApJ* 617:119
- Tortora C, Napolitano NR, Cardone VF, Capaccioli M, Jetzer Ph, Molinaro R (2010) *MNRAS* 407:144
- Valcke S, de Rijcke S, Dejonghe H (2008) *MNRAS* 389:1111
- van Zee L (2001) *AJ* 121:2003
- Vollmer B (2003) *A&A* 398:525
- Wang J et al (2011) *MNRAS* 412:1081
- Weisz DR, Skillman ED, Cannon JM, Dolphin AE, Kennicutt RC Jr, Lee J, Walter F (2008) *ApJ* 689:160
- Weisz DR et al (2011) *ApJ* 739:5
- Williams BF et al (2009) *ApJ* 695:15
- Williams BF et al (2010) *ApJ* 709:135
- Wong T, Blitz L (2002) *ApJ* 569:157
- Wyder TK (2001) *AJ* 122:2490
- Wyder TK, Martin DC, Schiminovich D et al (2007) *ApJS* 173:293
- Wyder TK et al (2009) *ApJ* 696:1834
- Youngblood AJ, Hunter DA (1999) *ApJ* 519:55
- Zhang H-X, Gao Y, Kong X (2010) *MNRAS* 401:1839
- Zhang H-X, Hunter DA, Elmegreen BG et al (2012) *AJ* 143:47
- Zhao Y, Gu Q, Gao Y (2011) *AJ* 141:68

Chapter 3

Gaseous Disk Turbulence of Nearby Dwarf Irregular Galaxies

Abstract HI spatial power spectra (PS) were determined for a sample of 24 nearby dwarf irregular galaxies selected from the LITTLE THINGS (Local Irregulars That Trace Luminosity Extremes—The HI Nearby Galaxy Survey) sample. The two-dimensional (2D) power spectral indices asymptotically become a constant for each galaxy when a significant part of the line profile is integrated. For narrow channel maps, the PS become shallower as the channel width decreases, and this shallowing trend continues to our single-channel maps. This implies that even the highest velocity resolution of 1.8 km s^{-1} is not smaller than the thermal dispersion of the coolest, widespread HI component. The one-dimensional PS of azimuthal profiles at different radii suggest that the shallower PS for narrower channel width is mainly contributed by the inner disks, which indicates that the inner disks have proportionally more cooler HI than the outer disks. Galaxies with lower luminosity ($M_B > -14.5 \text{ mag}$) and star formation (SF) rate (SFR, $\log(\text{SFR } (M_\odot \text{ yr}^{-1})) < -2.1$) tend to have steeper PS, which implies that the HI line-of-sight depths can be comparable with the radial length scales in low mass galaxies. A lack of a correlation between the inertial-range spectral indices and SFR surface density implies that either non-stellar power sources are playing a fundamental role in driving the interstellar medium (ISM) turbulent structure, or the nonlinear development of turbulent structures has little to do with the driving sources.

3.1 Sample and Observing

The 24 dIrr galaxies studied in this work (Table 3.1) are drawn from the LITTLE THINGS sample. LITTLE THINGS is a large NRAO Very Large Array (VLA¹) project, which was granted nearly 376 h of VLA time in the B-, C-, and D-array configurations to perform 21-cm HI-emission line observations of a representative sample of 41 nearby ($D \lesssim 10 \text{ Mpc}$) dIrr galaxies. The sub-sample of 24 galaxies is chosen to be relatively face-on (inclination $< 55^\circ$), and these galaxies cover a

¹The VLA is a facility of the National Radio Astronomy Observatory (NRAO), itself a facility of the National Science Foundation operated under cooperative agreement by Associated Universities, Inc.

Table 3.1 Galaxy sample

Galaxy (1)	Other names (2)	D (Mpc) (3)	M_B (mag) (4)	$\log(\text{SFR})$ ($M_{\odot} \text{ yr}^{-1}$) (5)	$\log(M_{\text{atomic gas}})$ (M_{\odot}) (6)	R_{HI} (kpc) (7)	R_D^V (kpc) (8)	Incl. (degrees) (9)
DDO 210 .	Aquarius Dwarf	0.9	-10.38	-4.07	6.52	0.78	0.17	47
M81dwA .	KDG 052	3.6	-11.46	-3.14	7.26	2.04	0.26	0
CVn1dwA	UGCA 292	3.6	-12.16	-2.68	7.81	2.22	0.57	41
DDO 155 .	UGC 8091, GR 8	2.2	-12.25	-2.71	7.13	1.35	0.15	48
DDO 187 .	UGC 9128	2.2	-12.38	-3.14	7.37	1.23	0.18	32
DDO 53 ..	UGC 4459, VIIZ _w 238	3.6	-13.43	-2.34	8.39	3.14	0.72	43
DDO 75 ..	UGCA 205, Sextans A	1.3	-13.72	-2.18	8.01	3.09	0.22	34
F564-V3 .	LSBC D564-08	8.7	-13.67	-3.05	7.56	3.37	0.53	53
DDO 70 ..	UGC 5373, Sextans B	1.3	-13.74	-2.59	7.72	3.22	0.48	24
NGC 4163	UGC 7199	2.9	-13.95	-1.73	7.34	0.60	0.10	0
IC 1613 ..	UGC 668, DDO 8	0.7	-14.17	-2.23	7.66	2.66	0.58	38
Haro 29 ..	UGCA 281, Mrk 209, IZw 36	5.9	-14.39	-1.87	8.01	4.52	0.29	42
DDO 46 ..	UGC 3966	6.1	-14.36	-2.05	8.35	4.76	1.14	29
DDO 133 .	UGC 7698	3.5	-14.36	-2.13	8.23	3.82	1.14	43
DDO 63 ..	UGC 5139, Holmberg I	3.9	-14.58	-2.09	8.33	4.22	3.09	0

(continued)

Table 3.1 (continued)

Galaxy (1)	Other names (2)	D (Mpc) (3)	M_B (mag) (4)	$\log(\text{SFR})$ ($M_{\odot} \text{ yr}^{-1}$) (5)	$\log(M_{\text{atomic gas}})$ (M_{\odot}) (6)	R_{HI} (kpc) (7)	R_D^V (kpc) (8)	Incl. (degrees) (9)
DDO 87 ..	UGC 5918, KDG 072, VIIZw 347	7.7	-14.52	-2.15	8.49	8.51	1.43	28
DDO 101 .	UGC 6900	6.4	-14.40	-2.68	7.10	2.36	0.93	49
DDO 43 ..	UGC 3860	7.8	-14.75	-2.03	8.40	5.82	0.61	46
DDO 52 ..	UGC 4426	10.3	-15.05	-2.03	8.57	6.99	1.32	53
DDO 47 ..	UGC 3974	5.2	-15.17	-1.83	8.73	10.97	1.36	19
IC 10	UGC 192	0.7	-15.75	-1.73 ^a	8.16	4.00	0.40	41
DDO 50 ..	UGC 4305, Holmberg II	3.4	-16.39	-1.18	8.99	8.67	1.10	47
NGC 3738	UGC 6565, Arp 234	4.9	-16.70	-1.45	8.32	5.42	0.78	46
NGC 4214	UGC 7278	3.0	-17.26	-1.03	8.91	8.62	0.75	26

Note—(1) Galaxy name. (2) The other commonly used names in the literature. (3) Distance from Hunter et al. (2012). (4) B -band absolute magnitude. (5) Logarithm of SFR derived from the FUV luminosity (Hunter et al. 2010; Zhang et al. 2012). (6) Logarithm of the atomic gas mass ($1.34 \times M_{\text{HI}}$) is collected from single-dish observations in the literature (see Hunter and Elmegreen 2004 for the references). (7) The radius where the HI column density falls off to 10^{19} cm^{-2} . (8) Disk scale length measured on the V -band images. (9) The inclination angles derived by fitting the iso-intensity contours on the velocity-integrated HI maps

^aNo FUV observations, so the SFR is derived from $\text{H}\alpha$ luminosity

large range of galactic parameters, such as integrated luminosity ($-18 < M_B < -10$ mag), central surface brightness ($18.5 < \mu_0^V < 25.5$ mag arcsec $^{-2}$), SFR surface density ($-4 < \log(\Sigma_{\text{SFR}}(M_{\odot} \text{ yr}^{-1} \text{ kpc}^{-2})) < -1.3$), and atomic gas richness ($0.2 < M_{\text{gas}}/M_* < 26$). Note that all but three (DDO 50, NGC 3738, NGC 4214, Table 3.1) of our galaxies are fainter than the SMC ($M_B = -16.35$ mag, Bekki and Stanimirović 2009).

3.2 Data Reduction

The VLA data reduction was done with AIPS (Astronomical Image Processing System). Basically, the reduction could be divided into two major steps, i.e., calibration and mapping. Our new VLA observations took place when the VLA started to be upgraded to EVLA. So the array was a mixture of VLA and EVLA antennas, which made our calibration process slightly different from the common practice. First, during the VLA-EVLA transition period, the hardware used to convert the digital signals from the EVLA antennas into analog signals to be fed into the VLA correlators caused power to be aliased into the bottom 500 kHz of baseband. To guarantee the high quality of the final data products, the EVLA-EVLA baselines were discarded (UVFLG) in the beginning of the calibration process. Second, because the channel 0 data created by the task FILLM contained closure errors on VLA-EVLA baselines, we created a bandpass table with BPASS, and then a new channel 0 data was created using AVSPC with the bandpass solutions applied.

In the calibration process, the uv data were inspected by eye for each configuration and bad data points due to either interference or cross talk between antennae were removed using the tasks UVFLG and TVFLG. Then the data were calibrated with the tasks CALIB and CLCAL. In the mapping process, we first combined the calibrated data sets of the three array configurations with DBCON. Then the continuum was subtracted in the uv plane with UVLSF. Finally, imagery data cubes were produced using the task IMAGR. To better handle extended emission, LITTLE THINGS adopted the multi-scale CLEAN (MSCLEAN) algorithm implemented in AIPS. In particular, four different scale sizes, i.e., $0''$, $15''$, $45''$, and $135''$, were chosen for mapping both small- and large-scale emission. After the mapping, only those regions, which show emission in three consecutive channels above at least 2σ in standard cubes that have been convolved to $25''$ resolution, were considered as areas of genuine emission. These areas of genuine emission were stored as masks in a master cube (BLANK), which were then used to blank the full resolution cubes.

For this work, we used the HI data cubes created with the ROBUST=0.5 weighting scheme in the task IMAGR. The cubes were cleaned down to a flux level of 2 times the rms noise, determined in line-free channels. The typical spatial resolution of these ROBUST maps is $\sim 7''$. Thirteen galaxies have a velocity resolution $\sim 1.3 \text{ km s}^{-1}$, with a real velocity resolution of 1.8 km s^{-1} . The other 11 galaxies have a channel

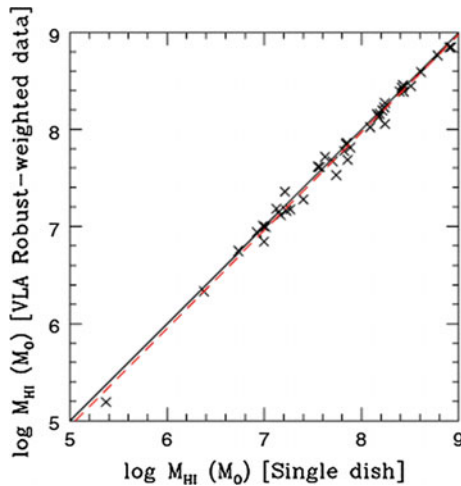


Fig. 3.1 Comparison of the integrated H I masses from the LITTLE THINGS (y-axis) with those from single-dish radio telescope observations (x-axis) in the literature. Both measurements are relative to the same distance. The LITTLE THINGS H I masses are measured on the VLA integrated H I ROBUST-weighted map. The *solid black line* marks equal masses, and the *red dashed line* is the best fit to the data. The average difference between the masses measured from the ROBUST-weighted maps and those measured from the Natural-weighted maps is 11%. The best fit line lies slightly below the line of equal masses, indicating that the VLA has systematically missed a small fraction of flux compared to single-dish values. The figure is adapted from Hunter et al. (2012)

width $\sim 2.6 \text{ km s}^{-1}$, with a real velocity resolution of 2.6 km s^{-1} . Limited by the shortest baseline of the VLA’s compact array configuration, our observations are blind to emission from structures with angular scales $> \sim 15'$. Figure 3.1 shows a comparison between the integrated H I gas masses from the LITTLE THINGS and the H I gas masses from single-dish radio telescope observations in the literature. There is a decent agreement between two measurements, with the masses being only marginally underestimated by the LITTLE THINGS interferometer observations for some galaxies.

Figure 3.2 shows the moment zero (i.e., integrated intensity) maps of the 24 galaxies analyzed in this work. For our sample, except for IC 10, all the galaxies have an H I extent (the largest scale for PS analysis) well below $15'$. The VLA primary beam is $32'$. The imagery data cubes were corrected for primary beam attenuation, and then de-projected using geometrical parameters (galactic center, position angle and axial ratio) derived from ellipse fitting (task ELLIPSE in IRAF) to the moment zero maps. An intrinsic axial ratio of 0.3 (Hodge and Hitchcock 1966) was adopted when converting the axial ratios to inclination angles.

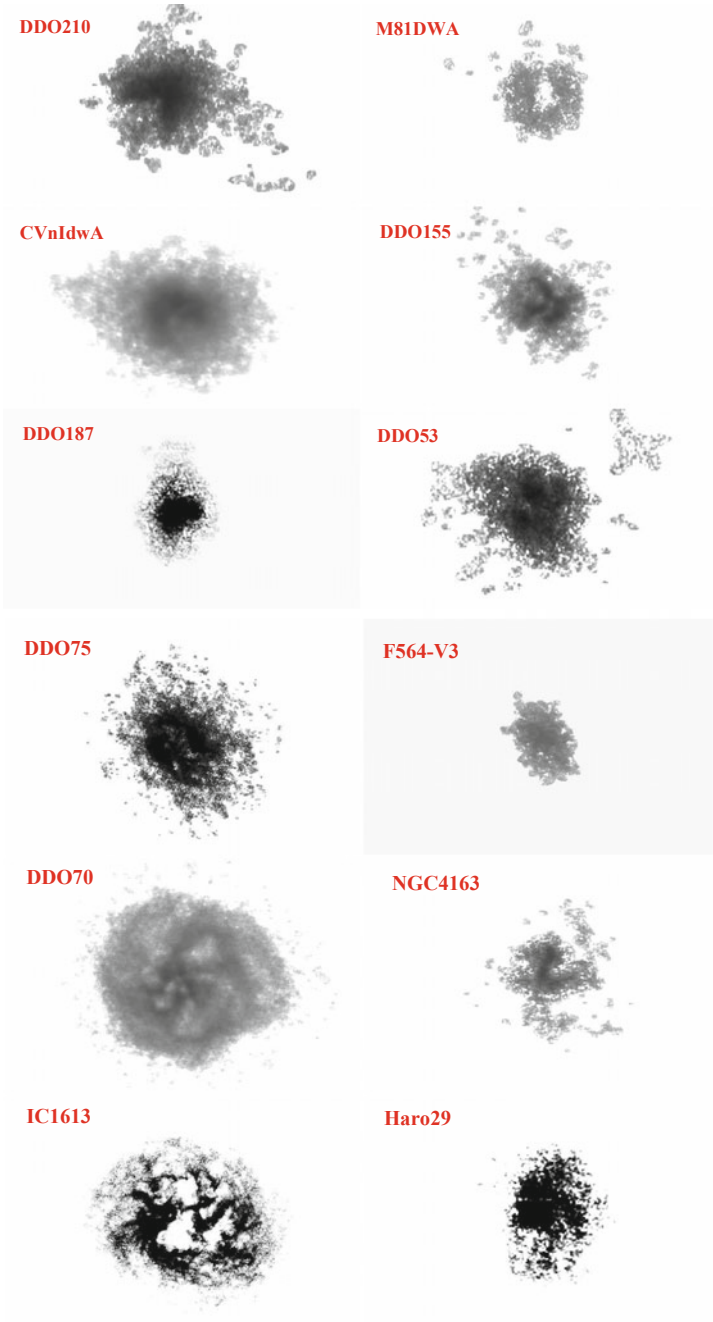


Fig. 3.2 Integrated H I intensity maps (moment 0) of the 24 galaxies studied in this work. These maps were obtained by the LITTLE THINGS (Hunter et al. 2012)

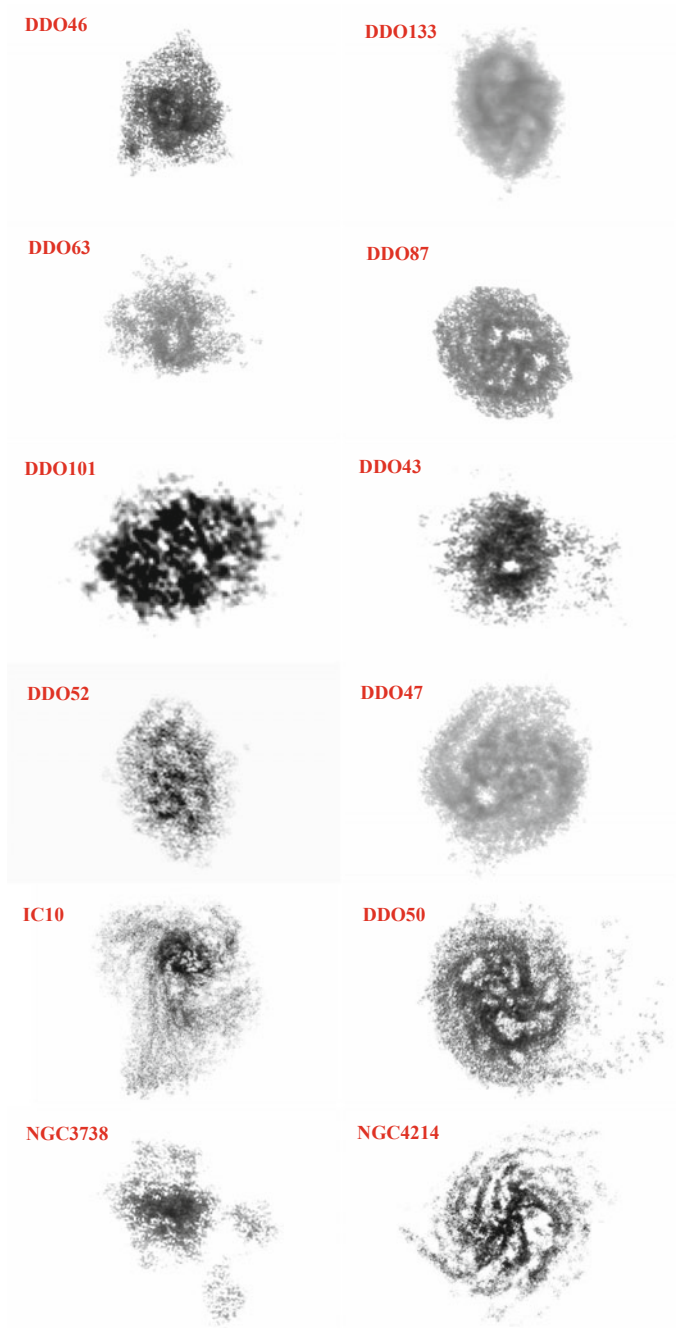


Fig. 3.2 (continued)

3.3 Power Spectrum Variations with Channel Width

Individual channel maps of the observed HI PPV data cube have intensity fluctuations resulting from density statistics distorted by velocity perturbations. According to the theoretical results of LP00, the velocity and density statistics can be extracted from narrow channel maps and velocity-integrated maps, respectively. The PS power-law indexes of density and velocity fluctuations can be obtained by changing the thickness of the velocity slices of the PPV data cube. The velocity slice is regarded to be thin if the effective slice thickness (see below) is smaller than the turbulent velocity dispersion on the scales under study. Velocity fluctuations lead to shallower PS for thinner velocity slices. Intuitively, within individual channel maps, there are more small scale structures that are not from physically distinct clumps, but from the projection effect along the line of sight that have the same velocity (velocity crowding). Thus the narrow channel maps may contain more information of the velocity structure. Whereas for very thick (e.g. velocity-integrated) slices, the perturbation from velocity fluctuations is averaged out, and thus the density field dominates the intensity fluctuations in that case.

We determined the two-dimensional (2D) spatial power spectra of velocity slices with different width, by gradually rebinning the channels with bin size increasing from the single channel width of 1.3 km s^{-1} (or 2.6 km s^{-1}) to a sum over whole line profiles. Line-emission channels with at least 20 per cent of the peak flux of the global HI velocity profile were used in the analysis. The power spectra were obtained using the Fast Fourier Transform algorithm. Note that the power spectra presented in this paper are the average within each annulus (1 spatial frequency unit wide) in the 2D wavenumber k (k_x, k_y) space. The finite size of the synthesized beam results in a pronounced decline at high spatial frequencies of the power spectrum (Fig. 3.3). Also, toward the lowest spatial frequencies of the power spectrum, some galaxies exhibit an obvious up-bending trend compared to higher spatial frequencies, which may be caused by some large-scale symmetric structures in the galaxies. Therefore, we fit each power spectrum with a power law ($P \propto k^\beta$) for linear scales from 1.5 times the beam size up to the point where the power spectrum starts bending upward.

For a given slice width, the power spectral indices of individual velocity slices with the same width are averaged to get the average spectral index $\langle \beta \rangle$ for that width. Most of our galaxies have nonzero inclinations, which means that an individual channel map shows only part of galaxy, due to galactic rotation. Thus galactic rotation may restrict the lowest spatial frequencies of the power spectra of narrow channel maps. If the fitted power spectral indices with and without the lowest one or two spatial frequencies are significantly different, we removed the lowest one or two spatial frequencies from the power spectrum fitting. As an example, Fig. 3.4 shows some 2.6 km s^{-1} channel maps (*black contours*) of DDO 133 overlaid on the integrated map (grayscale image). Our result suggests that, at a given channel width, different channel maps have about the same power spectrum, although they may show different parts of the galaxy.

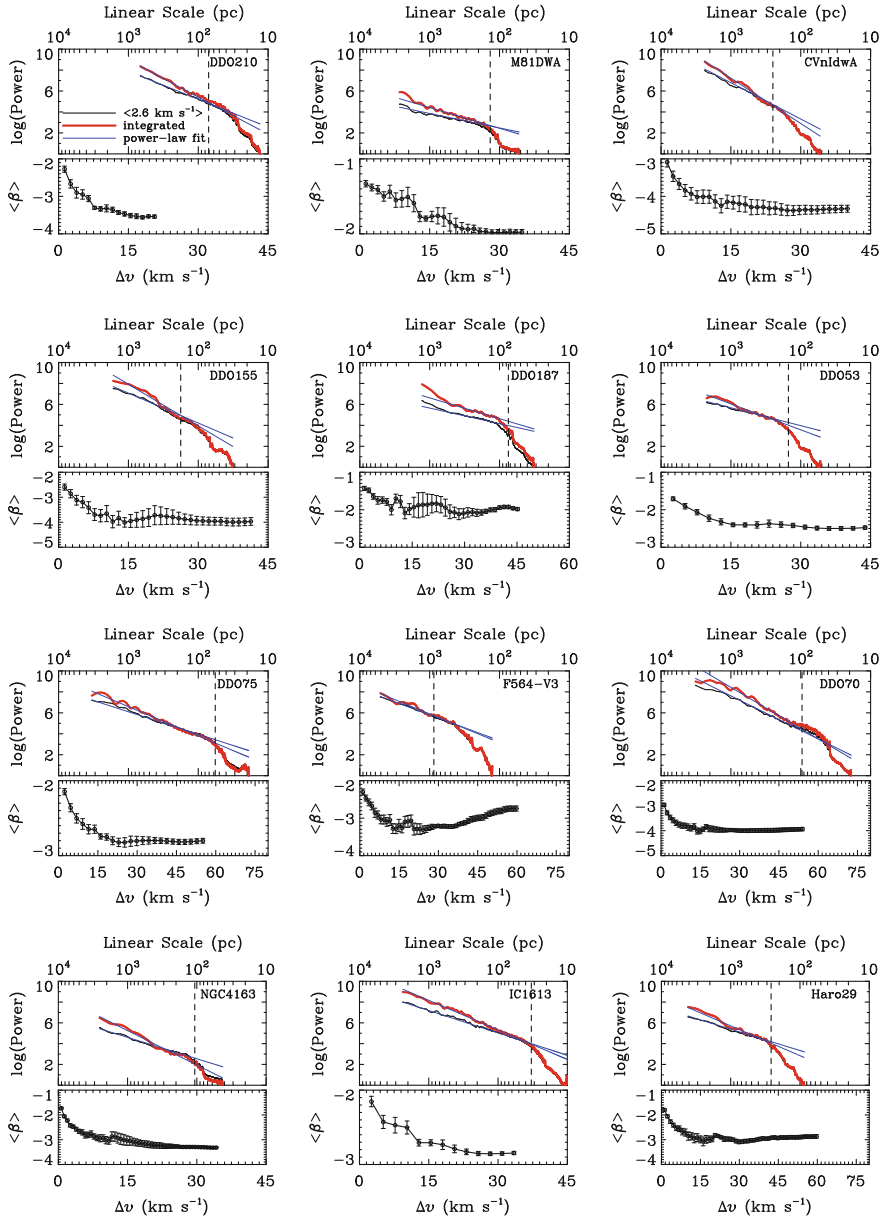


Fig. 3.3 Power spectrum variations as a function of channel width. The average power spectra of 2.6 km s^{-1} thick channel maps (*thin black solid line*), and power spectra of velocity-integrated maps (*thick red solid line*) are shown in the upper panel of each galaxy plot. The power-law fit to the power spectrum is overlotted as *thin blue solid line*. The power spectra have been arbitrarily shifted vertically. The vertical *dashed* lines mark the linear scales of the synthesized beam. Note that finite size of the synthesized beam causes the decline of power on linear scales smaller than the beam size. Variations of power-law spectral indices with channel width (in velocity units) are shown in the lower panel of each galaxy plot. The figure is adapted from Zhang et al. (2012)

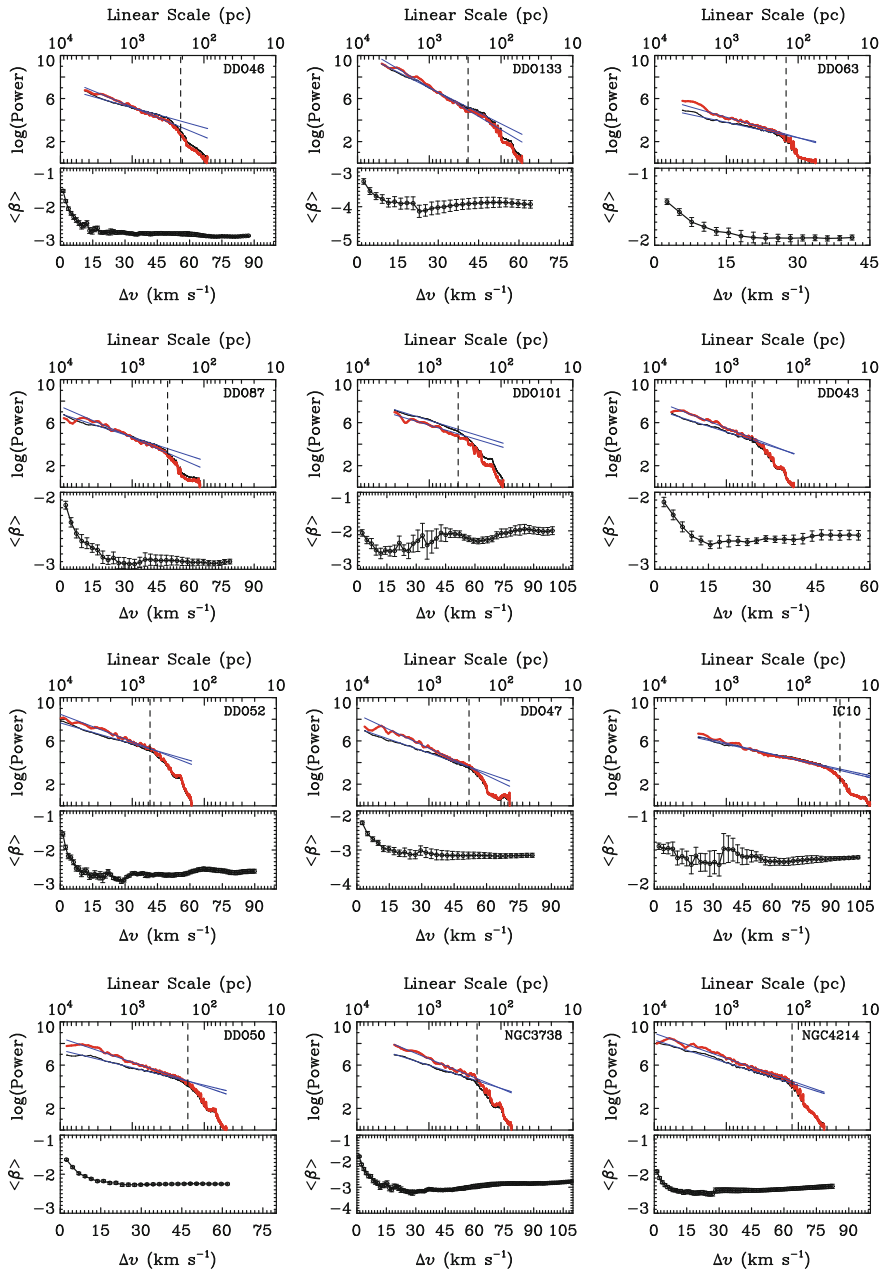


Fig. 3.3 (continued)

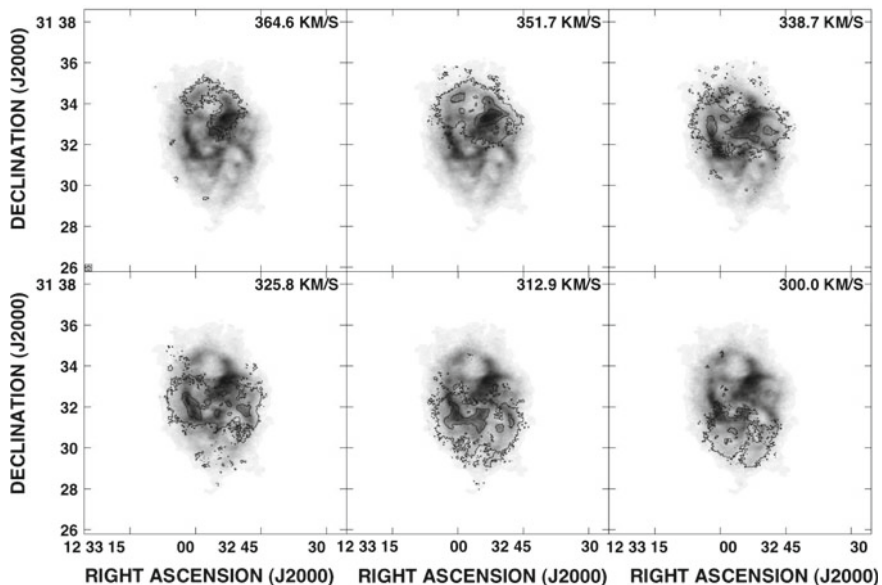


Fig. 3.4 Every fifth 2.6 km s^{-1} channel map of DDO 133 used in our power spectrum analysis is shown as *black contours*. The *grayscale* image in each panel is the integrated intensity map. The synthesized beam is indicated at the left-bottom corner of the *upper-left panel*. The contour levels are 2, 10, and 20 times the rms noise. The figure is adapted from Zhang et al. (2012)

The variations of $\langle \beta \rangle$ with increasing slice width are shown in Fig. 3.3. The error bars in Fig. 3.3 are determined as the standard deviation of β divided by \sqrt{n} , where n is the number of slices that were averaged together. In Fig. 3.3, we also present the average power spectra of the 2.6 km s^{-1} channel maps (*thin black solid lines*) and the power spectra of the velocity-integrated maps (*thick red solid lines*). The *vertical dashed lines* in Fig. 3.3 mark the linear scales of the synthesized beam. Table 3.2 lists the linear ranges used in the power-law fitting, the spectral indices of the velocity-integrated and the 1.3 and 2.6 km s^{-1} channel maps, the approximate slice width at which the power spectra start getting shallower for smaller slice widths, and the velocity spectral indices, discussed below.

As shown in Fig. 3.3, the power spectra are described very well by a single power law on large scales. Except for the two nearest galaxies (i.e., IC 1613, IC 10), the robust linear scales of the derived power spectra are $\gtrsim 100$ pc. DDO 187 and F564-V3 have the smallest range (less than a factor of 5) of linear scales used in the power spectrum fitting. As the slice width decreases, the power spectra of F564-V3 and DDO 101 get steeper first, then get shallower. Except for F564-V3 and DDO 101, the others exhibit gradually steeper power spectra as the velocity slice gets thicker, and the spectral index approaches a constant as a significant part of the line profile is integrated together.

Table 3.2 Power spectra

Galaxy (kpc) (1)	Min _{scale} (kpc) (2)	Max _{scale} (3)	$\langle \beta_{1.3} \rangle$ (4)	σ_β (5)	$\langle \beta_{2.6} \rangle$ (6)	σ_β (7)	$\beta_{\text{integrated}}$ (8)	σ_β (9)	Ch _{change} (km s ⁻¹) (10)	β_{velocity} (11)
DDO 210 .	0.11	0.68	-2.17	0.09	-2.47	0.11	-3.66	0.05	15	-4.05
M81DWA	0.20	1.35	-1.33	0.04	-1.38	0.04	-1.98	0.04	27	-4.19
CVnIdwA	0.38	2.37	-3.09	0.13	-3.47	0.14	-4.33	0.09	23	-2.07
DDO 155 .	0.27	1.65	-2.59	0.12	-2.86	0.16	-3.97	0.15	6	-3.28
DDO 187 .	0.11	0.43	-1.43	0.05	-1.48	0.06	-1.98	0.04	9	-4.00
DDO 53 ..	0.23	2.23	-1.71	0.05	-2.48	0.04	15	-4.54
DDO 75 ..	0.09	1.67	-2.15	0.04	-2.80	0.03	23	-4.31
F564-V3 .	1.31	5.09	-2.30	0.08	-2.46	0.08	-2.74	0.07	9	-3.56
DDO 70 ..	0.14	1.61	-2.97	0.06	-3.29	0.08	-3.94	0.07	12	-2.42
NGC 4163	0.16	2.54	-1.73	0.04	-2.06	0.05	-3.32	0.04	24	-4.88
IC 1613 ..	0.05	2.37	-2.15	0.07	-2.85	0.02	26	-4.38
Haro 29 ..	0.39	2.07	-1.80	0.05	-2.06	0.06	-2.87	0.07	17	-4.62
DDO 46 ..	0.32	2.29	-1.59	0.04	-1.85	0.04	-2.75	0.02	14	-4.80
DDO 133 .	0.43	4.61	-3.34	0.07	-3.94	0.10	13	-2.31
DDO 63 ..	0.22	2.05	-1.44	0.04	-1.90	0.03	28	-3.93
DDO 87 ..	0.48	4.50	-2.17	0.05	-2.90	0.03	15	-4.46

(continued)

Table 3.2 (continued)

Galaxy (kpc) (1)	Min _{scale} (kpc) (2)	Max _{scale} (3)	$\langle \beta_{1,3} \rangle$ (4)	σ_β (5)	$\langle \beta_{2,6} \rangle$ (6)	σ_β (7)	$\beta_{\text{integrated}}$ (8)	σ_β (9)	Ch _{change} (km s ⁻¹) (10)	β_{velocity} (11)
DDO 101 .	0.59	3.06	-2.05	0.08	-2.00	0.10	10	-2.88
DDO 43 ..	0.65	5.87	-2.13	0.06	-2.56	0.06	13	-3.86
DDO 52 ..	0.85	4.93	-1.59	0.05	-1.93	0.05	-2.54	0.05	14	-4.23
DDO 47 ..	0.42	3.91	-2.30	0.05	-3.14	0.05	21	-4.39
IC 10 ...	0.04	2.46	-1.45	0.04	-1.59	0.02	13	-3.28
DDO 50 ..	0.25	2.72	-1.63	0.02	-2.25	0.02	26	-4.25
NGC 3738	0.32	3.04	-1.82	0.04	-2.13	0.05	-2.75	0.04	13	-4.24
NGC 4214	0.18	9.26	-1.92	0.03	-2.10	0.03	-2.31	0.05	14	-3.43

Note—(1) Galaxy name. (2) The minimum linear scale in the power-law fitting to the power spectra. Min_{scale} is equal to 1.5 times the beam size. (3) The maximum linear scale in the power-law fitting to the power spectra. (4) The average 2D power spectral index of the 1.3 km s⁻¹ velocity slices. (5) The uncertainty of the power spectral index of the 1.3 km s⁻¹ velocity slices. (6) The average power spectral index of the 2.6 km s⁻¹ velocity slices. (7) The uncertainty of the power spectral index of the 2.6 km s⁻¹ velocity slices. (8) The power spectral index of the velocity-integrated map. (9) The uncertainty of the power spectral index of the velocity-integrated map. (10) The approximate channel width smaller than which the power spectra start to get shallower. (11) The velocity spectral index determined under the assumption that 1.3 km s⁻¹ velocity slices reach the thin regime and the line-of-sight depth is comparable to the maximum transverse scales

The turbulent velocity field is correlated with spatial scales, in the sense that the velocity dispersion on larger scales is usually larger than that on smaller scales. In incompressible turbulence, the turbulent density field passively follows the velocity field. In a narrow channel map, small-scale structures from independent gas elements on the line of sight combine to give relatively more power on smaller scales. This results in a shallower power spectrum for a narrower channel map. However, if the spatially uncorrelated thermal velocity is nonnegligible in a given channel map, then small-scale structures with turbulent velocity dispersions smaller than the thermal speed will lose their distinction. If the thermal velocity is much larger than the turbulent velocity dispersion even on the largest scales, then the thermal velocity component will totally smooth out the spatial correlation present in the turbulent velocity field. Therefore, the shallowing trend for power spectra of narrower channel maps is a reflection of the spatially-correlated turbulent velocity field, modulated by the thermal velocity.

According to the theoretical calculations of LP00, the power-law indices of turbulent density and velocity power spectra can be obtained by changing the width of velocity slices of the PPV data cube. If the effective velocity slice width, which is jointly determined by the instrumental channel width and the thermal velocity (see below), is significantly smaller than the turbulent velocity dispersion on the studied scales, then the velocity slice is regarded to be thin, and the power spectral indices remain constant as the slice width further decreases. If the effective velocity slice width is significantly larger than the turbulent velocity dispersion on the studied scales, then the velocity slice is regarded to be thick, and the power spectral indices remain constant as the slice width further increases. The spectral indices of thick slices are determined solely by the turbulent density fluctuations. In the β - Δv plot of Fig. 3.3, the asymptote on the side of thick velocity slices suggests that density fluctuations determine the intensity fluctuations there. The shallower power spectra of intensity fluctuations in narrower velocity slices implies more influence from velocity fluctuations.

3.4 Comparison with a Visibility-Based Estimation of Power Spectra

Dutta et al. (2009b) have determined HI power spectra of a sample of dwarf galaxies using a different method. They used data from the Giant Metrewave Radio Telescope (GMRT), and the range of baselines roughly corresponds to those of the VLA D and C array configurations. They determined the power spectra directly from the observed visibilities in the uv plane rather than producing maps first and then taking the Fourier Transform and determining the power spectra. This avoids an unnecessary step (converting visibilities into maps) since the uv data are already in the Fourier domain. Here we prefer to identify real emission from the target by working in the image plane. Also, the correction for inclination and primary beam can only be properly done in the image plane.

The Dutta et al. (2009b) study has two galaxies in common with our sample: DDO 210 and DDO 155. They found that DDO 210 has power spectral indices of -2.1 ± 0.6 and -2.3 ± 0.6 for velocity-integrated and single-channel (1.7 km s^{-1}) velocity slices, respectively, and DDO 155 has power spectral indices of -0.7 ± 0.3 and -1.1 ± 0.4 for velocity-integrated and single channel velocity slices, respectively. These are compared to our values of -3.66 ± 0.05 and -2.17 ± 0.09 for DDO 210, and -3.97 ± 0.15 and -2.59 ± 0.12 for DDO 155. Recall that the single channel of 1.3 km s^{-1} is narrower than the real velocity resolution of $\sim 1.8 \text{ km s}^{-1}$. The power spectra of DDO 155 are not a power law for linear scales above 1.5 times the beam size, and thus the quality of power-law fitting is very poor (Fig. 3.3). We notice that the power spectra of DDO 155 determined by Dutta et al. (2009b) show similar behavior on large scales. So DDO 155 may not be a good case for comparison. For DDO 210, our single channel spectral index is consistent with that determined by Dutta et al. within the uncertainty of their measurement. Our velocity-integrated spectral index of DDO 210 is much steeper than that determined by Dutta et al. (2009b). Based on Fig. 3.8 of Dutta et al. (2009b), the multichannel-integrated power spectrum of DDO 210 is a very good power law for linear scales above ~ 0.18 kpc, below which the spectrum becomes very noisy and (thus) flat. Dutta et al. included the noisy, flat part of the power spectrum in their power-law fitting, which leads to a much less negative spectral index.

The key difference between the image-domain-based and visibility-based power spectra lies in the different ways used to avoid noise bias. Noise present in the visibilities or images shallows the derived power spectrum. To reduce the effect of noise in the uv plane, Dutta et al. determined the power spectrum by correlating the visibilities at slightly different baselines for which the noise is assumed to be uncorrelated. This method works on the assumption that the angular extent of the galaxy is much smaller than the primary beam of the telescope. The compromise present in this method is that, on the one hand, sufficient visibility pairs are needed to get good statistics and on the other hand, the baseline differences should be as small as possible ($< 1/\theta_0$, where θ_0 is the angular extent of the target galaxy) to have strong enough correlations between visibilities of different baselines.

In the image plane, we distinguish between real emission and noise primarily in two steps. First, in the dirty map, only peaks 2σ above the noise level are regarded as signal and MSCLEAN-ed. Second, as described above, only regions with flux $> 2-3\sigma$ in at least three consecutive channels in the smoothed cubes are regarded as real emission, and the rest is blanked. We found that the power spectral indices of both DDO 210 and DDO 155 would be about -1.5 regardless of the channel width if we do not apply blanking to the cubes. This implies that non-blanked cubes are predominantly affected by noise on small scales. MSCLEAN has been shown to work excellently in recovering extended structures (Cornwell 2008; Rich et al. 2008). Compared to the classical CLEAN, MSCLEAN with its scale-sensitive nature, can clean down to the noise level without leaving skewed noise on the residual map. Furthermore, the recovered fluxes from MSCLEAN (and BLANK) were found to be consistent with those from single-dish observations (Hunter et al. 2012)). Nevertheless, the noise present

in the uv data can definitely affect the nonlinear deconvolution involved in the image restoration process.

Given these different approximations and assumptions in the two methods, it is not obvious which method is better in determining power spectra. In this work, however, we point out that, (1) by including the deep VLA B-array data, the outer part (longer baseline length) of the uv plane is better sampled in our data; (2) the two galaxies in common all have nonnegligible inclinations.

3.5 Effective Velocity Slice Width and Multiphase Neutral HI

The distinction between the thin and thick regimes depends on a comparison between the squared turbulent velocity dispersion on the studied scale $\sigma_{turb, l}^2$ and the squared effective velocity slice width δV^2 (LP00)

$$\begin{aligned} \sigma_{turb, l}^2 &\ll \delta V^2, \text{ thick} \\ \sigma_{turb, l}^2 &\gg \delta V^2, \text{ thin} \end{aligned} \quad (3.1)$$

The thermal motion (v_T), which is spatially incoherent, acts like a smoothing along the velocity dimension. Thermal broadening, together with the instrumental channel width, determine the effective velocity slice width. Assuming a uniform sensitivity across individual channels, the effective velocity slice width is given by

$$\delta V \sim 2(\Delta v^2/6 + 2v_T^2)^{1/2} \quad (3.2)$$

where Δv and v_T are the individual channel width and typical thermal velocity, respectively (LP00). It is the effective velocity slice width, rather than the channel width, that determines the effective slice thickness, and thus the variation of power spectral indices.

The thermal velocity of the gas restricts the minimum effective velocity slice width that can be achieved. For an isothermal gas with temperature T , the effective velocity slice width remains nearly constant when the channel width becomes smaller than the thermal velocity v_T ($\sqrt{2k_B T/m\pi}$), and thus the power spectral indices do not change. Empirically, the median channel width at the point where the power spectra start to get shallower for narrower channel width is $\sim 15 \text{ km s}^{-1}$ for our sample galaxies (Table 3.2). A two-phase (WNM and CNM) description of the neutral HI was suggested by Field et al. (1969). Wolfire et al. (2003) demonstrate that the interstellar HI at a temperature of $\sim 100 \text{ K}$ and of $\sim 8000 \text{ K}$ can coexist in thermal equilibrium. Therefore, if there is only a thermally stable WNM, the power spectral indices would not change for channel widths narrower than $\sim 6.5 \text{ km s}^{-1}$ (the thermal velocity of HI gas with a temperature of 8000 K). For the thirteen galaxies with a channel width of 1.3 km s^{-1} , the power spectra keep getting shallower for narrower

channel width, down to 1.3 km s^{-1} . This suggests widespread HI with a temperature $\sim 600 \text{ K}$ (corresponds to a thermal velocity of 1.8 km s^{-1}) or even lower, considering that the real velocity resolution is 1.8 km s^{-1} . In the Milky Way, Heiles and Troland (2003) found that more than 48% of the WNM, which accounts for $\sim 60\%$ of the total HI, is in the thermally unstable regime with a broad temperature range from $\sim 500\text{--}5000 \text{ K}$. A temperature of $\sim 600 \text{ K}$ lies in the broad boundary between the WNM and CNM.

The typical velocity dispersion from HI emission line observations of nearby star-forming galaxies is $\sim 10 \text{ km s}^{-1}$ (e.g. Co   et al. 2000; Leroy et al. 2008), which is the combination of turbulent and thermal velocity dispersions. Therefore, $\sim 10 \text{ km s}^{-1}$ can be regarded as an upper limit on the turbulent velocity on galactic scales. Also, since the maximum temperature T_{max} of neutral HI is $\sim 10^4 \text{ K}$, the minimum possible turbulent velocity dispersion σ_{turb} should be $\sim 4 \text{ km s}^{-1} (\sqrt{10^2 - v_T^2})$. For a given scale, the thin (thick) regime is reached if the squared effective slice width is much smaller (larger) than the squared turbulent velocity dispersion (Inequality 1). In the β versus Δv plot, two asymptotes are expected for the two regimes of thin and thick effective velocity slices. As mentioned above, the HI gas with a temperature of $\sim 600 \text{ K}$ has a thermal velocity $v_T \sim 1.8 \text{ km s}^{-1}$ which is the highest spectral resolution for our data. With $v_T = 1.8 \text{ km s}^{-1}$ and $\Delta v = 1.8 \text{ km s}^{-1}$, Eq. 3.2 gives an effective velocity slice width of $\sim 5 \text{ km s}^{-1}$. Since we do not see the asymptotic behavior toward the single-channel width in the β versus Δv plot (Fig. 3.3), the single channel, and thus the effective velocity slice width of 5 km s^{-1} does not reach the thin regime, at least for the thermally unstable WNM components with a temperature $\lesssim 600 \text{ K}$. Based on Inequality 1, the turbulent velocity dispersion $\sigma_{\text{turb}, l}$ for the neutral HI gas with a temperature $\lesssim 600 \text{ K}$ is not much higher (i.e., by less than a factor of 3) than $\sim 5 \text{ km s}^{-1}$, which is mildly supersonic.

The line profiles of our galaxies cover a velocity range from ~ 20 to 130 km s^{-1} . The velocity-integrated slices lie in the thick slice regime, as implied by the asymptotes seen in Fig. 3.3. As mentioned above, our galaxies start reaching the thick regime at a channel width of $\sim 15 \text{ km s}^{-1}$ on average. With $v_T = 6.5 \text{ km s}^{-1}$ ($T_{\text{WNM, stable}} = 8000 \text{ K}$) and $\Delta v = 15 \text{ km s}^{-1}$, Eq. 3.2 gives an effective velocity slice width of 22 km s^{-1} . Therefore, to be in the thick regime defined in Inequality 1, the turbulent velocity dispersion of the thermally stable WNM should be much smaller (i.e., by at least a factor of 3) than 22 km s^{-1} . Therefore, the maximum Mach number for the thermally stable WNM components should be smaller than ~ 1 ($\sigma_{\text{turb}, l} / v_{T_{\text{WNM, stable}}} < 22/3$).

The intensity fluctuations of the velocity-integrated maps are determined by density fluctuations including all possible phases of HI. On the other hand, as explained above, the shallowing trend for power spectra of channel maps narrower than 6.5 km s^{-1} is only caused by turbulent velocity fluctuations of cooler HI, including the thermally unstable components and (possibly) some CNM. The large HI self-absorption survey by Gibson et al. (2005) found a smoothly distributed, albeit fluffy, cold phase of HI in the Milky Way Galaxy, which is in line with our finding that HI gas with a temperature of 600 K or even lower is widespread in dIrr galaxies.

Zhang et al. (2012) found that star-forming disks of most local dIrr galaxies have been shrinking at least during the past \sim Gyr. Cold atomic gas is the precursor to molecular cloud formation which shows an almost linear correlation with the SFR in nearby star-forming galaxies (e.g. Leroy et al. 2008). Possible radial variations of the β - Δv relation would reflect the relative spatial distributions of HI gas with different temperatures. We took one-dimensional (1D) power spectra of azimuthal scans at different radii (e.g. Elmegreen et al. 2003) for our galaxies. Azimuthal power spectra at different radii are shown in Fig. 3.5 for each of our galaxies. Fig. 3.6 presents the results of power spectral index variations for three of our galaxies (DDO 70, DDO 47 and NGC 4214). The 1D power spectra in Fig. 3.6 are the average of adjacent azimuthal scans with a radial extent of two synthesized beams. We used the same geometric parameters derived above for the extraction of azimuthal profiles. The *black* symbols correspond to the 2D power spectra as shown in Fig. 3.3. The *red* and *green* symbols, respectively, denote the spectral indices at inner and outer radii, in units of the V-band disk scalelength R_D^V . In an isotropic field, the 1D power spectra of azimuthal profiles are expected to be shallower than the 2D power spectra by ~ 1

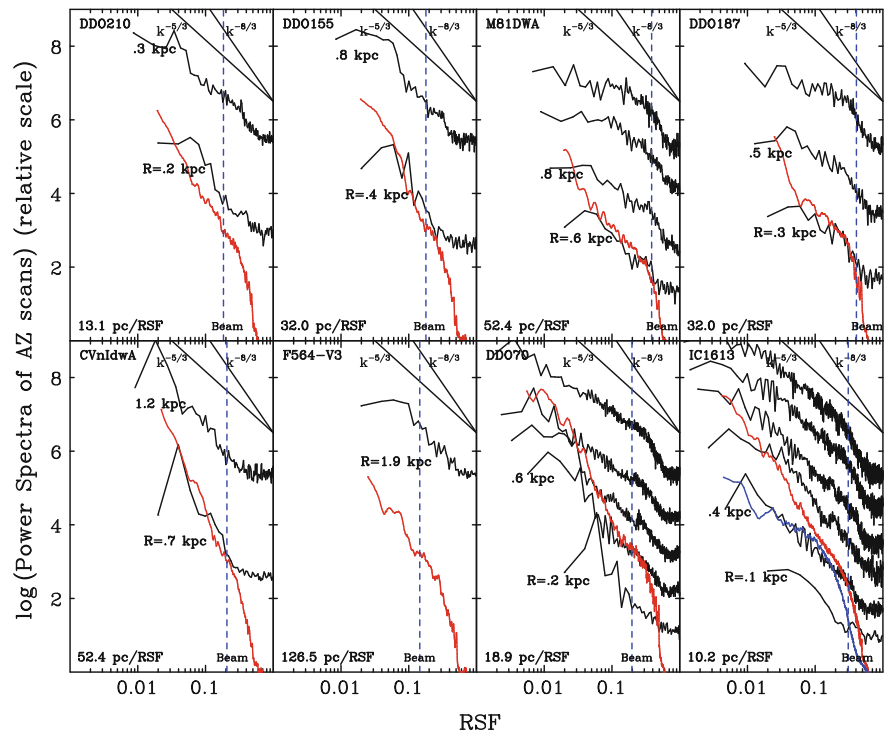


Fig. 3.5 Azimuthal power spectra at different galactocentric radii (*black curves*) of our sample galaxies. The 2D power spectra for each galaxy are also overlotted as *red curves*. One can see that for most galaxies the innermost radii have relatively steeper power spectrum than that at larger radii

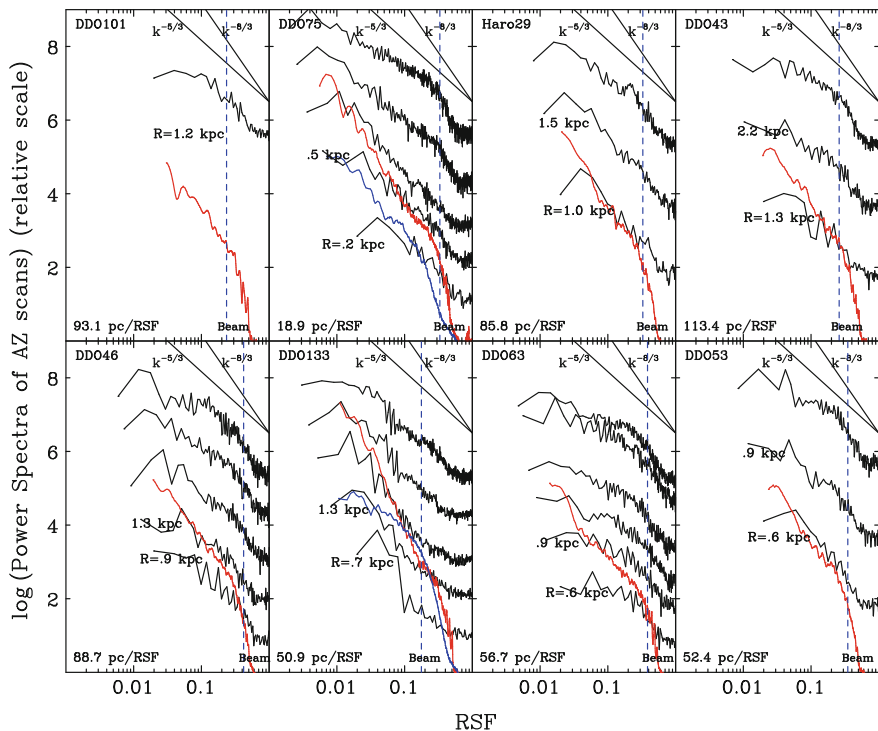


Fig. 3.5 (continued)

because of the reduced dimension (see the power spectra of inner radii in Fig. 3.6). The azimuthal scans at the outer radii have systematically shallower power spectra than those at the inner radii, which may signify a gradual change from 3D to 2D geometry, possibly due to the longer azimuthal scans at the outer radii. Obviously, the inner regions exhibit a much stronger shallowing trend toward narrower channel width. This suggests that the shallowing trend observed for the 2D power spectra, and thus the structure associated with the cooler HI, is dominantly contributed by the inner, more actively star-forming regions. The more widespread cool HI in the inner disk may be caused by a higher mid-plane gas pressure (Wong and Blitz 2002; Blitz and Rosolowsky 2004) or a higher average gas volume density (Gao and Solomon 2004) there. Braun (1997) studied the neutral HI properties of a sample of 11 nearby spiral galaxies. He found positive radial gradients of the HI kinematic temperature, and that there are more HI components with narrow ($\lesssim 6 \text{ km s}^{-1}$) emission line profiles in the inner disks.

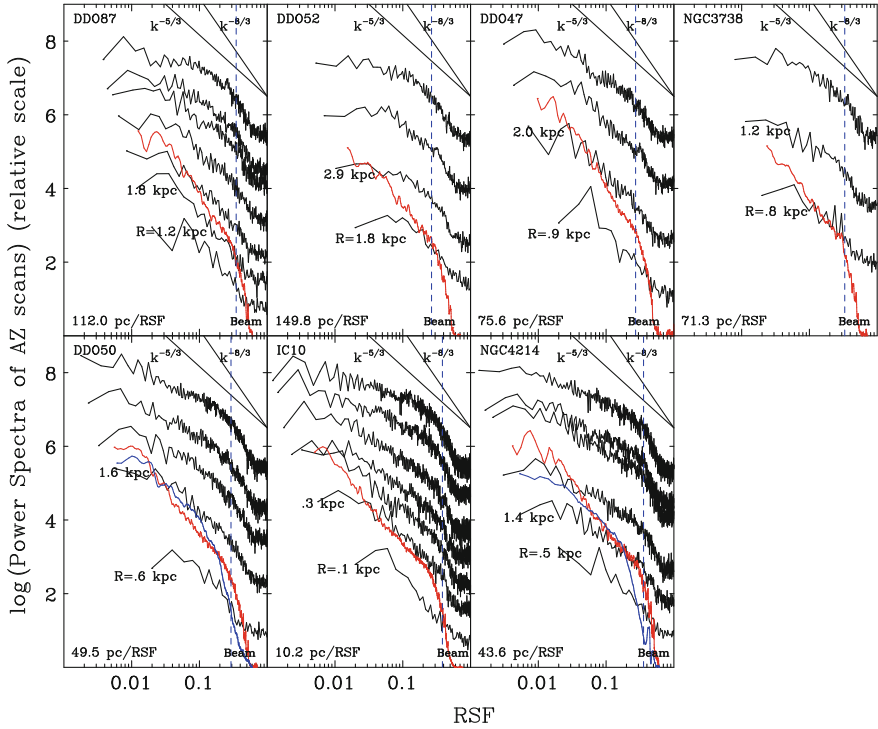


Fig. 3.5 (continued)

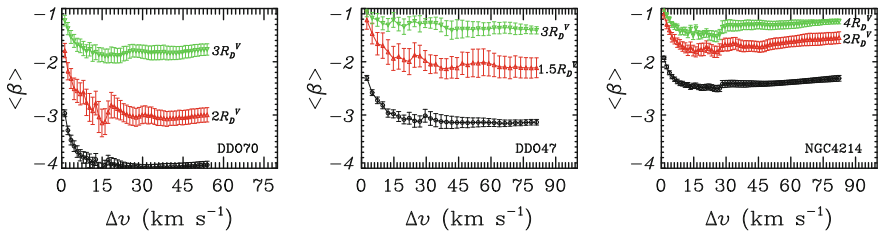


Fig. 3.6 Variations of 1D spectral indices as a function of channel width for three galaxies. The red triangles denote the spectral indices of azimuthal scans at an inner radius, measured in units of V-band disk scalelength. The green upside down triangles denote the spectral indices of azimuthal scans at an outer radius. The 2D spectral indices presented in Fig. 3.3 are shown as black circles. The figure is adapted from Zhang et al. (2012)

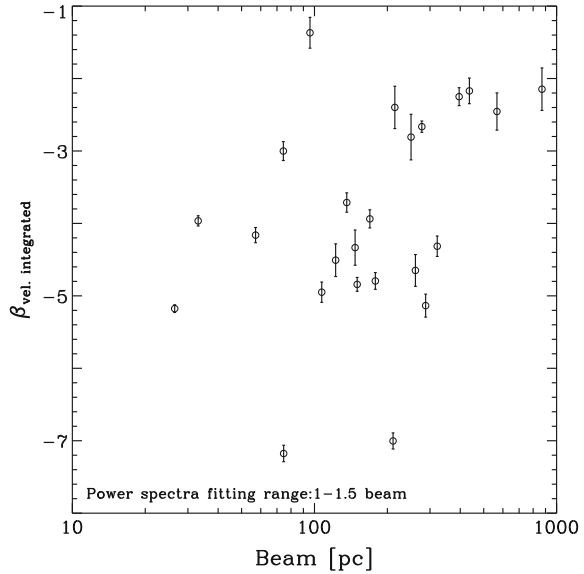
3.6 Power Spectral Index Versus SF

The ISM structure in dIrr galaxies can be significantly influenced by stellar feedback. Shells and holes of up to \sim kpc scales are often seen in the HI gas distribution of dwarf galaxies (e.g., Sargent et al. 1983; Puche et al. 1992; Young and Lo 1997; Walter and Brinks 1999; Ott et al. 2001; Muller et al. 2003; Simpson et al. 2005; Cannon et al. 2011). It has been shown that stellar feedback can provide sufficient energy to produce the observed shells and holes (Warren et al. 2011). Stellar energy, such as winds, ionizing radiation, and supernova explosions, dominates the energy injection into the ISM (Mac Low and Klessen 2004) on the corresponding scales, at least in star-forming galaxies. By studying the visibility-based power spectra of seven dwarf galaxies, Dutta et al. (2009b) found that the galaxies with higher SFR surface density tend to have steeper HI power spectra, implying more large-scale structures of HI for more intense SF. With a much larger sample, we can explore the possible relationship between the power spectra and SF.

Our thick velocity slices, especially the velocity-integrated ones, have intensity fluctuations dominated by variations in the density field. According to LP00, the spectral index of the 2D velocity-integrated map is equal to the 3D density spectral index, provided the studied scales are comparable or smaller than the line-of-sight depth. As listed in Table 3.2, for most of the galaxies, the minimum linear scales covered by our PS are \gtrsim 100 pc, which is probably comparable with the expected disk scale height of dIrr galaxies (e.g., van den Bergh 1988; Staveley-Smith et al. 1992; Carignan and Purton 1998; Elmegreen et al. 2001; Banerjee et al. 2011). A break in the power-law PS of the HI emission distribution has been observed for a few galaxies (LMC—Elmegreen et al. 2001; NGC 1058—Dutta et al. 2009a). The PS slope for smaller scales (compared to the break scale) is steeper than for larger scales by \sim 1. The flattening of the PS on larger scales is understood as the transition from isotropic 3D turbulence on smaller scales to anisotropic 2D turbulence (Bournaud et al. 2010). The break is about the average Jeans length and, thus, about the gas disk scale height (Elmegreen et al. 2001; Bournaud et al. 2010; Combes et al. 2012). Therefore, the intrinsic 3D density spectral index can be taken to be $\beta_{\text{integrated}}$ minus 1.

As described in Sect. 3.3, we did power law fitting to the power spectra for linear scales larger than 1.5 times the synthesized beam. This is because the finite size of the synthesized beam results in a pronounced decline at high spatial frequencies of the power spectra (Fig. 3.3). Nevertheless, we expect the power spectra at high spatial frequencies, although being noticeably influenced by the beam, still partially reflect the intrinsic power spectra of the galaxy at the resolution limit. Figure 3.7 presents the relation between the beam size (in units of pc) and the velocity-integrated power spectra fitted over linear scales from 1 to 1.5 times the beam size. Our galaxies fall into two groups in Fig. 3.7, separated around a beam size of \sim 200–300 pc, below which the galaxies have more negative indices. The two groups are also roughly divided by a spectral index of -3 . This may reflect the effect of the disk thickness,

Fig. 3.7 The synthesized beam size (pc) is plotted against the velocity-integrated power spectral indices determined by fitting a linear scale range from 1 to 1.5 times the beam size. The figure is adapted from Zhang et al. (2012)



because anisotropic 2D turbulence on large scales is expected to have much shallower power spectra than isotropic 3D turbulence on small scales.

The SMC, which is like the most luminous galaxies in our sample in terms of stellar and gas masses, does not have a break in the power spectrum between linear scales of 30 pc and 4 kpc (Stanimirović et al. 1999). This lack of a break indicates that the maximum transverse scale is comparable to or smaller than the HI line-of-sight depth. Perhaps the 3D behavior of the power spectrum of the SMC across a large range of linear scales is a result of the tidal interaction with the LMC during the past few Gyr. The numerical simulations by Bekki and Chiba (2007) found that almost 20% of the SMC’s gas may have been accreted by the LMC during their recent interaction, and this may explain the origin of the LMC’s intermediate-age stellar populations with distinctively low metallicities (e.g., Geisler et al. 2003). So it is possible that the SMC’s gas disk may have been stretched during the recent interaction, resulting in a thicker disk. For the two nearest galaxies in our sample, IC 10 and IC 1613, the power spectra also can be well fitted with a single power law between linear scales of ~ 50 pc and ~ 2 kpc. IC 1613 has a tidal index ~ 0.9 (Karachentsev et al. 2004), which indicates that this galaxy has been significantly influenced by the neighboring galaxies (e.g., M 33). Our HI kinematics analysis (Oh et al. 2015) suggests that these two galaxies, and also the very low luminosity galaxies, such as DDO 210 and DDO 155, have ratios of the maximum rotational velocity to velocity dispersion $\lesssim 2$, which indicates that the gas distribution may be a relatively thick disk or even triaxial ellipsoid. We note that Roychowdhury et al. (2010), (see also Sánchez-Janssen et al. 2010) found a mean intrinsic axial ratio of

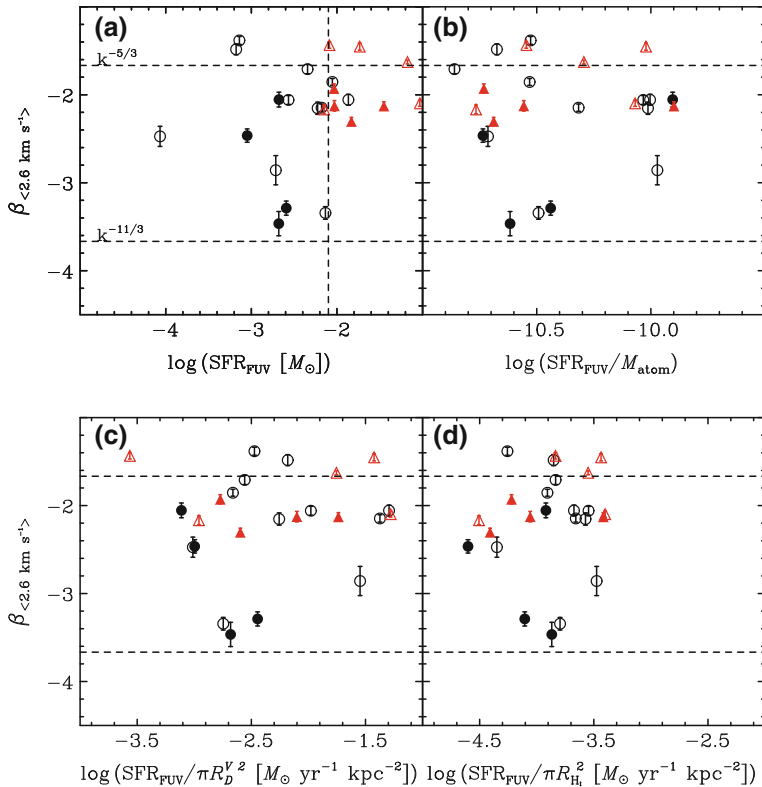


Fig. 3.8 Power spectral indices of 2.6 km s^{-1} channel maps are plotted against the SFR determined from the FUV (a), SF efficiency (b), SFR normalized by the area enclosed by the radius of one V -band disk scale length (c), and SFR normalized by the area enclosed by the radius where the HI column density falls off to 10^{19} cm^{-2} (d). The *open* and *filled* symbols respectively denote the galaxies with spectral indices measured at high spatial frequencies (linear scales between 1 and 1.5 times the beam size) more negative and less negative than -3 . The *black circles* and *red triangles* respectively denote the galaxies with $M_B > -14.5$ mag and $M_B < -14.5$ mag. The horizontal *dashed lines* mark the expected 1D ($P \sim k^{-5/3}$) and 3D ($P \sim k^{-11/3}$) power spectral indices of a Kolmogorov-type turbulence. The vertical *dashed line* in panel (a) marks the division ($\log(\text{SFR}_{\text{FUV}}) = -2.1$) of the bimodality discussed in the text. We notice that there is a slight trend for the galaxies with $M_B < -14.5$ mag in panel (d), in the sense that higher SFR surface density corresponds to shallower power spectra, but the scatter is too large to be sure. The figure is adapted from Zhang et al. (2012)

~ 0.6 for the HI disks of dIrr galaxies with $M_B > -14.5$ mag, which suggests very thick gas disks in faint dIrr galaxies.

Figures 3.8 and 3.9 plot the power spectral indices against SF-related quantities derived from the far-UV (FUV, SFR_{FUV}): SF efficiency of the atomic gas ($\text{SFR}_{\text{FUV}}/M_{\text{atom}}$), SFR surface density normalized to the area within one V -band disk scalelength ($\text{SFR}/\pi R_D^2$), and SFR surface density within the radius where the

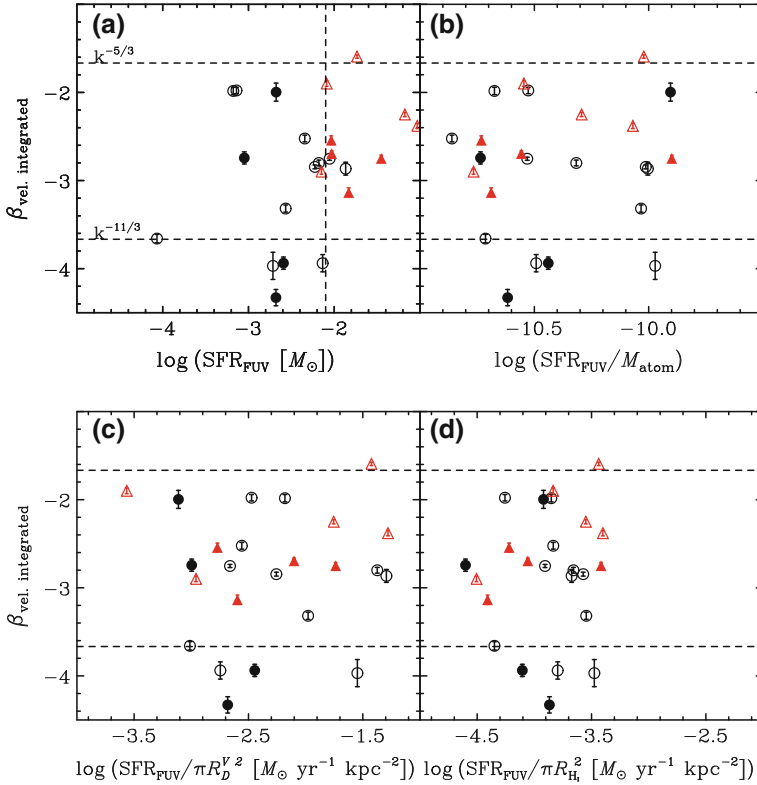


Fig. 3.9 Same as Fig. 3.8 but for velocity-integrated maps. The slight correlation found in Fig. 3.8 is also present here in panel (d). The figure is adapted from Zhang et al. (2012)

HI column density falls off to $10^{19} \text{ cm}^{-2} (\text{SFR}/\pi R_{\text{HI}}^2)$, for 1.3 and 2.6 km s^{-1} thick slices and for the velocity-integrated maps, respectively. For the formula used to derive SFR_{FUV} from the FUV, the reader is referred to Hunter et al. (2010) and Zhang et al. (2012). The total atomic gas mass M_{atom} ($1.34 \times M_{\text{HI}}$ to account for He) used here was collected from single-dish observations in the literature (see Hunter and Elmegreen 2004 for the references). The *open* and *filled* symbols respectively denote the galaxies with spectral indices measured at high spatial frequencies (1–1.5 times the beam) more negative and less negative than -3 , i.e., the two groups mentioned above. The *black circles* and *red triangles* respectively denote the galaxies with $M_B > -14.5$ mag and $M_B < -14.5$ mag. There is no strong correlation in these plots. However, Fig. 3.8 suggests that all the galaxies with $\log(\text{SFR}) > -2.1$ have narrow channel spectral indices around -2 , whereas galaxies with lower SFR exhibit a much larger scatter toward more negative spectral indices. The *vertical dashed* line in panel (a) of Fig. 3.8 marks the division at $\log(\text{SFR}) = -2.1$. Similarly, in Fig. 3.9, the spectral indices of velocity-integrated maps exhibit a larger scatter (toward more negative indices) in galaxies with lower SFR.

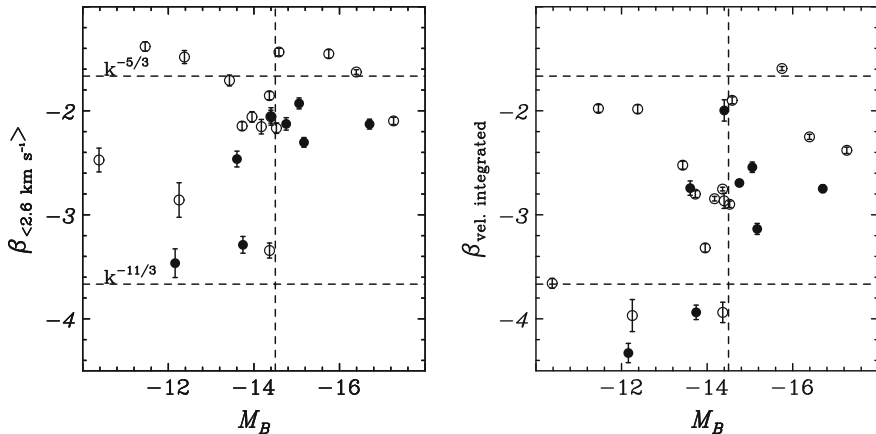


Fig. 3.10 Power spectral indices of 2.6 km s^{-1} channel maps (*left panel*) and velocity-integrated maps (*right panel*) are plotted against B -band absolute magnitude M_B . The *open* and *filled* symbols respectively denote the galaxies with spectral indices measured at high spatial frequencies (linear scales between 1 and 1.5 times the beam size) more negative and less negative than -3 . The horizontal *dashed lines* mark the expected 1D ($P \sim k^{-5/3}$) and 3D ($P \sim k^{-11/3}$) power spectral indices of a Kolmogorov-type turbulence. The vertical *dashed lines* mark the division of the bimodality ($M_B = -14.5$ mag) discussed in the text. The figure is adapted from Zhang et al. (2012)

Given that the spectral indices show bimodality with SFR but not the SFR surface density, the bimodality may just reflect the correlation between spectral indices and the mass (or size) of galaxies. In Fig. 3.10, the spectral indices of 2.6 km s^{-1} channel maps and spectral indices of velocity-integrated maps are plotted against B -band absolute magnitude M_B . There exists a similar bimodality as that present between power spectral indices and the SFR. The *vertical dashed lines* in Fig. 3.10 mark the division of the bimodality at $M_B = -14.5$ mag. Brighter galaxies tend to have flatter power spectra. This could be a result of disk thickness, in the sense that brighter galaxies tend to have a higher ratio of radial length to thickness, and so are more 2D on average. The three galaxies which have the most negative spectral indices (for both narrow channel maps and velocity-integrated maps) are CVnIIdwA, DDO 70 and DDO 133. The negative tidal indices of these three galaxies (Karachentsev et al. 2004) suggest that they do not have significant interactions with neighboring galaxies.

This ratio of radial length to thickness also affects the regularity of galactic structure because the thickness is approximately the turbulent Jeans length, and therefore the typical size of stellar complexes. When the radial length is large compared to the thickness, there is room in the disk for a lot of star-forming clumps, giving the disk a somewhat uniform appearance. But when the radial length is small compared to the thickness, there may be only a few star-forming complexes with large stochasticity, which can lead to an irregular appearance of the disk. Thus the correlation we find between the slope of the power spectrum and the galaxy absolute magnitude (or total

SFR) may explain the findings of Lee et al. (2007), who explored the distribution of the Local Volume galaxies in the M_B -H α equivalent width plane. They found a bimodality around $M_B \sim -15$ mag in the sense that galaxies with lower luminosity exhibit a larger (by a factor of 2) scatter in H α equivalent width than galaxies with higher luminosity ($-19 \lesssim M_B \lesssim -15$ mag).

The lack of a strong correlation between the inertial-range spectral indices and SFR surface density (and also SF efficiency) may be unsurprising. In the classical Kolmogorov turbulence, the energy transfer occurs locally (cascade) in the wavenumber space in the inertial range, and the driving only affects the energy input at the top of the cascade. Unlike this ideal Kolmogorov turbulence which has a single driving source on the large scale, the driving of turbulence in the ISM may span a wide range of scales. The stellar energy can drive turbulence from parsec-scale supernovae up to hundred-parsec-scale superbubbles (Mac Low and Klessen 2004). Similarly, gravitational energy may feed the turbulence through sub-parsec gravitational collapse, up to galactic-scale gravitational instabilities (e.g., Wada et al. 2002; Elmegreen et al. 2003; Agertz et al. 2009) and galaxy interactions (e.g. Elmegreen and Scalo 2004), etc. Therefore, the single power-law behavior of HI power spectra suggests that the turbulence may be driven (by whatever energy sources) over a wide range of physical scales, otherwise the power spectra should exhibit features, such as a flattening at low wavenumbers, at the primary driving scale (e.g., Nakamura and Li 2007; Padoan et al. 2009). Supernovae are the largest contributors of energy input to the ISM on scales comparable to or smaller than the disk thickness (Mac Low and Klessen 2004). However, it was suggested that supernova driven turbulence alone cannot explain the broad HI emission lines, at least in the outer parts of disk galaxies (e.g., Dib et al. 2006; Tamburro et al. 2009). Furthermore, simulations (e.g., Agertz et al. 2009; Bournaud et al. 2010) found that gravitational instabilities alone can reproduce the observed power-law power spectra; the stellar feedback does not significantly change the ISM statistical properties established by gravitational instabilities. In addition, the multiphase nature of the ISM implies that thermal instabilities (e.g., Field 1965) may also be an important driving agent of turbulence (e.g., Hennebelle and Audit 2007; Gazol and Kim 2010). Thus turbulence may be driven by many sources and the properties of this turbulence on scales smaller than the sources may be independent of these sources, so a correlation between spectral index and SFR surface density might not be expected.

The slope of the power spectrum may depend on the nature of the driving force (no matter whether it is stellar or non-stellar). Recent simulations done by Federrath et al. (2009) suggest that, at a given Mach number, compressive forcing can lead to steeper density spectra than solenoidal forcing (rotational, incompressible). Kim and Ryu (2005), Kowal et al. (2007), and Gazol and Kim (2010) found a correlation between power spectral index and Mach number from magnetohydrodynamic (MHD) simulations, in the sense that higher sonic Mach number leads to shallower density power spectra. This correlation was interpreted as the result of more small-scale density structures generated by stronger shocks in supersonic flows. In the present

observations, the lack of a correlation between the power spectral indices and the SFR surface density may imply that stellar feedback and other energy sources share similar characteristics of driving on average. Burkhart et al. (2010) also found little correlation between SF activity and Mach number in a 2D map based on kurtosis of HI line profiles in the SMC. They found that regions with the highest sonic Mach number lie around the bar. Chappell and Scalo (2001) arrived at a similar conclusion using a multifractal spectrum analysis of low-mass star-forming cloud complexes: there is little correlation between the geometrical properties of the gas and the level of internal SF.

As we discussed above, higher luminosity galaxies ($M_B < -14.5$ mag) in our sample may have 2D turbulence on the studied scales and 3D turbulence on unresolved scales, whereas lower luminosity galaxies may have only 3D turbulence because the disks are thick relative to their radial length scales. Therefore, it may be desirable to explore the relationship between SFR surface density and power spectral indices for higher luminosity and lower luminosity galaxies separately. Figures 3.8 and 3.9 suggest that our claim of a lack of a correlation between SFR surface density and spectral indices is valid for galaxies with both $M_B < -14.5$ mag or $M_B > -14.5$ mag. The lack of a correlation for the more luminous galaxies makes sense according to the above discussion if their power spectra are dominated by 2D turbulence and stellar feedback has little effect on scales larger than the disk thickness. The lack of a correlation for less luminous galaxies, which have relatively thicker disks than more luminous galaxies, suggests that local SF does not strongly affect the spectral index of turbulence.

3.7 Power Spectral Index Versus Baryonic Mass

As mentioned above, the only correlation with the spectral index found in simulations is the Mach number. The global Mach number of a galaxy may have a little relation with the galactic rotation, which in turn should be proportionally related to the baryonic mass. Furthermore, the global gravitational instability, which is presumably an important energy source of exciting the turbulence, is also tightly related to the mass. Figures 3.11 and 3.12 present the relations of the spectral indexes with stellar mass, atomic gas mass, baryonic mass (stars plus gas), and the ratios of atomic gas mass to stellar mass. No correlation shows up in these plots. The lack of correlation, again, suggests that the nonlinear development of the ISM turbulence has little to do with the exact driving source, other than the nature of driving, as was discussed above.

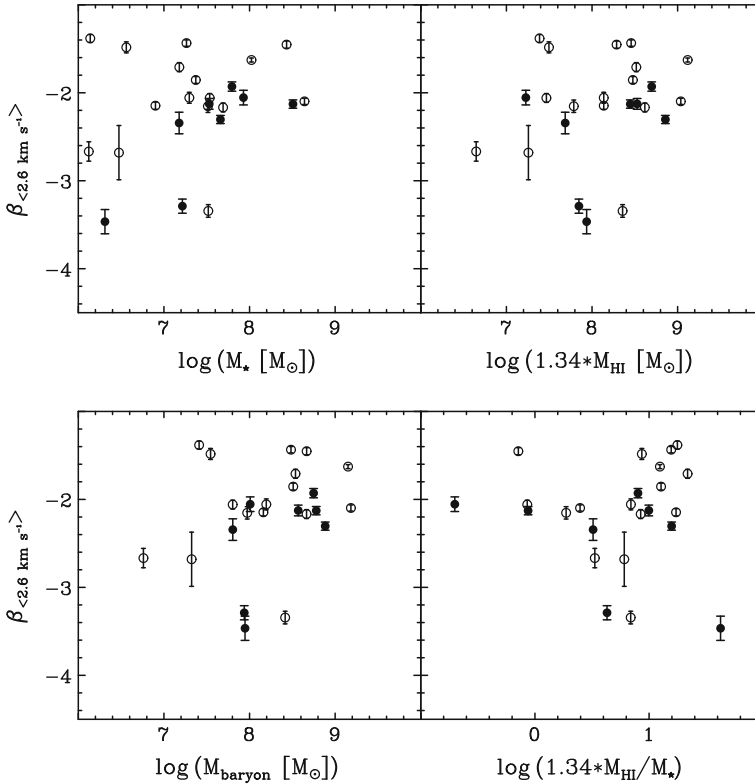


Fig. 3.11 Power spectral indices of 2.6 km s^{-1} channel maps are plotted against the stellar mass (*upper left panel*), atomic gas mass (*upper right panel*), total baryonic mass (*lower left panel*), and ratios of atomic gas mass to stellar mass (*lower right panel*). The *open* and *filled* symbols respectively denote the galaxies with spectral indexes measured at high spatial frequencies (linear scales between 1 and 1.5 beam size) more negative and less negative than -3

3.8 The Turbulent Velocity Field

Unlike the spectra that reflect density fluctuations, velocity spectra (specific kinetic energy spectra) are directly related to the turbulent energy distribution across different scales. Intensity fluctuations within channel maps are contributed by both the density and velocity fields. However, the relevant importance of density and velocity fields changes with the amplitude of the density fluctuations. For example, intensity fluctuations simply follow the velocity field if the density field is constant. Our thick velocity slices, especially the velocity-integrated ones, have intensity fluctuations dominated by variations in the density field. According to LP00, the spectral index of

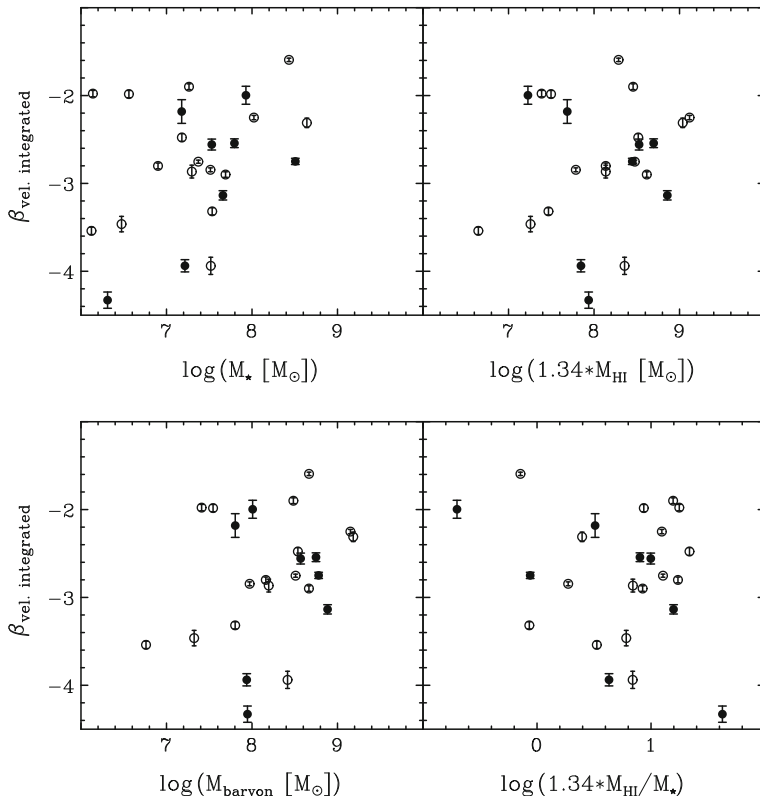


Fig. 3.12 Power spectral indices of velocity-integrated maps are plotted against the stellar mass (*upper left panel*), atomic gas mass (*upper right panel*), total baryonic mass (*lower left panel*), and ratios of atomic gas mass to stellar mass (*lower right panel*). The *open* and *filled* symbols respectively denote the galaxies with spectral indexes measured at high spatial frequencies (linear scales between 1 and 1.5 beam size) more negative and less negative than -3

(2D) thick velocity slices β_{thick} (e.g., $\beta_{\text{integrated}}$ listed in Table 3.2) is equal to the 3D density spectral index β_{density} , provided the maximum transverse scale is comparable to or smaller than the line-of-sight depth. In an isotropic 3D turbulent medium, if the density spectral index < -3 , the velocity spectral index β_{velocity} is equal to $-2\beta_{\text{thin}} - 9$, where β_{thin} is the spectral index of intensity fluctuations within thin velocity slices. β_{velocity} is equal to $-3 - 2(\beta_{\text{thin}} - \beta_{\text{thick}})$ if the density spectral index > -3 .

As discussed in Sect. 3.4, the velocity resolution of 2.6 km s^{-1} does not yet reach the thin slice regime. Assuming the 2.6 km s^{-1} velocity slice is thin (i.e., $\beta_{\text{thin}} = \beta_{2.6}$) and the line-of-sight depth is comparable to the maximum transverse scale we studied, we can obtain the velocity spectral indices β_{velocity} which are listed in Table 3.2. Sixteen galaxies have velocity power spectra steeper than that

of Kolmogorov turbulence (for which β_{velocity} would be $-11/3$ for 3D turbulence). The real velocity spectral indices can be even steeper because we do not yet reach the “thin” regime. If the line-of-sight depth is smaller than the maximum transverse scale, the measured β_{thick} and β_{thin} should be subtracted by ~ 1 to be used for the calculation of β_{density} and β_{velocity} , and thus the resultant β_{density} would be $\beta_{\text{thick}} - 1$, and β_{velocity} would be shallower than those listed in Table 3.2 by ~ 2 when the $\beta_{\text{density}} < -3$, whereas β_{velocity} determined for the galaxies with $\beta_{\text{density}} > -3$ is not affected (see the relations in the preceding paragraph). We point out that, if the steepening factor of 2D turbulence relative to 3D turbulence is not 1, then we would not know how to obtain β_{density} , and, in the case of $\beta_{\text{thick}} < -3$, β_{velocity} when the line-of-sight depth is smaller than the maximum transverse scales.

MHD isothermal simulations (e.g., Kritsuk et al. 2007; Federrath et al. 2009; Gazol and Kim 2010) suggest that fluids with higher Mach number (thus stronger compressibility) have steeper velocity power spectra (and shallower density power spectra). However, the isothermal assumption adopted in most simulations may not be valid for the multiphase HI for which thermal instabilities can be an important driving mechanism of turbulence (Hennebelle and Audit 2007; Gazol and Kim 2010). We emphasize that the multiphase nature of the HI makes the velocity spectral indices derived here questionable, because the density power spectra determined from thick velocity slices may invoke density fields of all different phases of HI, whereas the turbulent velocity fields as reflected by the shallower power spectra within narrower velocity slices only include contributions from the thermally unstable WNM and (possibly) some CNM.

3.9 Summary

We have studied the HI power spectral index variations with channel width for a sample of nearby dIrr galaxies. The majority of the 2D power spectra cover more than one decade of linear scales, from \sim hundred pc to several kpc. The main results are summarized as follows:

1. The power spectral indices asymptotically become a constant for each galaxy when a significant part of the line profile is integrated, consistent with the theoretical calculations of LP00. This indicates that density fluctuations, including all possible temperature components of HI, determine the intensity fluctuations of our “thick” velocity slices.
2. Starting at a channel width of $\sim 15 \text{ km s}^{-1}$ on average for our sample, narrower channel maps have shallower power spectra. The shallowing trend, which is caused in part by turbulent velocity dispersions of the thermally unstable WNM and possibly some CNM, continues down to the single channel maps (1.3 km s^{-1}). This continuation indicates that, first, even the highest velocity resolution of 1.8 km s^{-1} is not smaller than the thermal dispersion of the coolest HI ($\lesssim 600 \text{ K}$) which is widespread in our galaxies; if it were, then the spectral

index would remain constant. Second, the turbulent velocity dispersion of the coolest HI ($\lesssim 600$ K) probed at our highest velocity resolution is not much larger than $\sim 5 \text{ km s}^{-1}$, which means that the turbulence in this phase of HI is mildly supersonic.

3. Toward narrower channel width, the 1D power spectra of azimuthal profiles at the inner radii have a stronger shallowing trend than those at the outer radii, which implies that the shallower power spectra for narrower channel maps are mainly contributed by the inner disks, and thus the inner, more actively star-forming regions have proportionally more cooler HI than the outer regions.
4. The power spectra of IC 1613 and IC 10, which are the two nearest galaxies in our sample, can be well fitted with a single power law between linear scales of ~ 50 pc and ~ 2 kpc. This suggests that the HI line-of-sight depth may be comparable with the maximum transverse scales in these two galaxies.
5. Our sample galaxies exhibit a bimodality in the spectral indices versus M_B (and also SFR) plane. The division of the bimodality is at $M_B \sim -14.5$ mag and $\log(\text{SFR } (M_\odot \text{ yr}^{-1})) \sim -2.1$. Galaxies with higher luminosity and SFR tend to have shallower power spectra with a smaller scatter, whereas galaxies with lower luminosity and SFR exhibit a much larger scatter toward more negative spectral indices. The bimodality may signify that higher luminosity galaxies tend to have bigger gas disks compared to their thicknesses, whereas lower luminosity galaxies may be better described as thick disks or even triaxial ellipsoids.
6. The inertial-range spectral indices of single channel maps and velocity-integrated maps are not correlated with the SFR surface density. This may imply that either stellar and non-stellar energy sources can excite turbulence with about the same power spectral index, or non-stellar energy sources are more important in driving ISM turbulence. The single power-law behavior of the power spectra indicates that the ISM turbulence may be driven, from whatever energy sources (stellar or non-stellar), over a wide range of physical scales, otherwise we should see features, such as a flattening of power spectra at low wavenumbers, at the primary driving scale.

The multiphase (i.e., different temperature components) nature of galactic neutral HI means that the power spectra determined for different velocity slice widths trace different temperature components of HI. Therefore, determining the turbulent velocity spectral indices may be difficult, and more theoretical work taking into account the multiphase nature of neutral HI is needed.

References

- Agertz O, Lake G, Teyssier R et al (2009) MNRAS 392:294
 Banerjee A, Jog CJ, Brinks E, Bagetakos L (2011) MNRAS 415:687
 Bekki K, Chiba M (2007) MNRAS 381:16
 Bekki K, Stanimirović S (2009) MNRAS 395:342
 Blitz L, Rosolowsky E (2004) ApJ 612:29

- Bournaud F, Elmegreen BG, Teyssier R, Block DL, Puerari I (2010) MNRAS 409:1088
- Braun R (1997) ApJ 484:637
- Burkhardt B, Stanimirović S, Lazarian A, Kowal G (2010) ApJ 708:1204
- Cannon JM, Most HP, Skillman ED et al (2011) ApJ 735:35
- Carignan C, Purton C (1998) ApJ 506:125
- Chappell D, Scalo J (2001) ApJ 551:712
- Côté S, Carignan C, Freeman KC (2000) AJ 120:3027
- Combes F, Boquien M, Kramer C et al (2012) A&A 539:67
- Cornwell TJ (2008) IEEE J Sel Top Sign Proces 2:793
- Dib S, Bell E, Burkert A (2006) ApJ 638:797
- Dutta P, Begum A, Bharadwaj S, Chengalur JN (2009a) MNRAS 397:60
- Dutta P, Begum A, Bharadwaj S, Chengalur JN (2009b) MNRAS 398:887
- Dickey JM, McClure-Griffiths NM, Stanimirović S, Gaensler BM, Green AJ (2001) ApJ 561:264
- Elmegreen BG, Kim S, Staveley-Smith L (2001) ApJ 548:749
- Elmegreen BG, Elmegreen DM, Leitner SN (2003) ApJ 590:271
- Elmegreen BG, Scalo J (2004) ARA&A 42:211
- Federrath C, Klessen RS, Schmidt W (2009) ApJ 692:364
- Field GB (1965) ApJ 142:531
- Field GB, Goldsmith DW, Habing HJ (1969) ApJ 155:149
- Gazol A, Kim J (2010) ApJ 723:482
- Gao Y, Solomon PM (2004) ApJ 606:271
- Geisler D, Piatti AE, Bica E, Clariá JJ (2003) MNRAS 341:771
- Gibson SJ, Taylor AR, Higgs LA, Brunt CM, Dewdney PE (2005) ApJ 626:195
- Hennebelle P, Audit E (2007) A&A 465:431
- Heiles C, Troland TH (2003) ApJ 586:1067
- Hodge PW, Hitchcock JL (1966) PASP 78:79
- Hunter DA, Elmegreen BG (2004) AJ 128:2170
- Hunter DA, Elmegreen BG, Ludka BC (2010) AJ 139:447
- Hunter DA, Ficut-Vicas D, Ashley T et al (2012) AJ 144:134
- Karachentsev ID, Karachentseva VE, Huchtmeier WK, Makarov DI (2004) AJ 127:2031
- Kowal G, Lazarian A, Beresnyak A (2007) ApJ 658:423
- Kim J, Ryu D (2005) ApJ 630:45
- Kritsuk AG, Norman ML, Padoan P, Wagner R (2007) ApJ 665:416
- Leroy AK, Walter F, Brinks E et al (2008) AJ 136:2782
- Lee JC, Kennicutt RC, Funes SJ et al (2007) ApJ 671:113
- Mac Low MM, Klessen, RS (2004) RvMP 76:125
- Muller E, Staveley-Smith L, Zealey WS, Stanimirović S (2003) MNRAS 339:105
- Nakamura F, Li Z-Y (2007) ApJ 662:395
- Oh S-H, Hunter DA, Brinks E et al (2015) AJ 149:180
- Ott J, Walter F, Brinks E et al (2001) AJ 122:3070
- Padoan P, Juvella M, Kritsuk A, Norman ML (2009) ApJL 707:153
- Puche D, Westpfahl D, Brinks E, Roy J-R (1992) AJ 103:1841
- Rich JW, de Blok WJG, Cornwell TJ et al (2008) AJ 136:2879
- Roychowdhury S, Chengalur JN, Begum A, Karachentsev ID (2010) MNRAS 404:60
- Sargent WLW, Sancisi R, Lo KY (1983) ApJ 265:711
- Sánchez-Janssen R, Méndez-Abreu J, Aguerri JAL (2010) MNRAS 406:65
- Simpson CE, Hunter DA, Knezek PM (2005) AJ 129:160
- Stanimirović S, Staveley-Smith L, Dickey JM, Sault RJ, Snowden SL (1999) MNRAS 302:417
- Staveley-Smith L, Davies RD, Kinman TD (1992) MNRAS 258:334
- Tamburro D, Rix H-W, Leroy AK et al (2009) AJ 137:4424
- van den Bergh S (1988) PASP 100:344
- Walter F, Brinks E (1999) AJ 118:273
- Warren SR, Weisz DR, Skillman ED et al (2011) ApJ 738:1

- Wada K, Meurer G, Norman CA (2002) *ApJ* 577:197
Wolfire MG, McKee CF, Hollenbach D, Tielens AGGM (2003) *ApJ* 587:278
Wong T, Blitz L (2002) *ApJ* 569:157
Young LM, Lo KY (1997) *ApJ* 490:710
Zhang H-X, Hunter DA, Elmegreen BG, Gao Y, Schruba A (2012) *AJ* 143:47

Chapter 4

Blue Compact Dwarf Galaxies Formed Through Gravitational Torques

Abstract Giant star formation clumps in dwarf irregular galaxies can have masses exceeding a few percent of the galaxy mass enclosed inside their orbital radii. They can produce sufficient torques on dark matter halo particles, halo stars, and the surrounding disk to lose their angular momentum and spiral into the central region in 1 Gyr. Pairs of giant clumps with similarly large relative masses can interact and exchange angular momentum to the same degree. The result of this angular momentum loss is a growing central concentration of old stars, gas, and star formation (SF) that can produce a long-lived starburst in the inner region, identified with the BCD phase. This central concentration is proposed to be analogous to the bulge in a young spiral galaxy. Observations of star complexes in five local BCDs confirm the relatively large clump masses that are expected for this process. The observed clumps also seem to contain old field stars, even after background light subtraction, in which case the clumps may be long-lived. The two examples with clumps closest to the center have the largest relative clump masses and the greatest contributions from old stars. An additional indication that the dense central regions of BCDs are like bulges is the high ratio of the inner disk scale height to the scale length, which is comparable to 1 for four of the galaxies.

4.1 The Context: “BCD” as an Extreme Version of Dwarf Irregulars

Blue Compact Dwarfs (BCDs) are small galaxies with intense emission lines from starburst HII regions in their central regions (Sargent and Searle 1970). They are gas-rich like other dwarf irregulars (Chamaraux 1977; Gordon and Gottesman 1981; Thuan and Martin 1981), but much more centrally concentrated in stars (Noeske et al. 2003; Hunter and Elmegreen 2006), SF (Heller et al. 2000; Hunter and Elmegreen 2004), and gas (Taylor et al. 1994; Zee et al. 1998b). This concentration suggests that gas inflow following angular momentum loss led to enhanced SF in a dense and gravitationally unstable central disk (Taylor et al. 1994; Papaderos et al. 1996; Zee et al. 2001). Gas loss from the outer parts also produces a shrinking radius for SF, as observed in dwarfs (Zhang et al. 2012; Koleva et al. 2011).

Individual star-forming regions in BCDs are relatively large, giving the galaxies a clumpy, irregular appearance in $H\alpha$ (Kunth et al. 1988; Cairós et al. 2009b) and FUV (Thuan et al. 1997). Clump emission lines are supersonic and apparently virialized (Terlevich and Melnick 1981; Firpo et al. 2011), which implies the clumps could last for several internal crossing times. Low-velocity shear (Thuan et al. 1999; Zee et al. 2001; Ramya et al. 2011) and resolved stellar population studies (Dohm-Palmer et al. 1998) also suggest the clumps could be long-lived, 100 Myr or more. McQuinn et al. (2010) and Zhang et al. (2012) suggest the starburst itself can last for ~ 1 Gyr.

Surrounding many BCDs are pools of HI, sometimes as large as 4 or more optical radii (Brinks and Klein 1988; Taylor et al. 1996; Zee et al. 1998b; Putman et al. 1998; Pustilnik et al. 2001; Hoffman et al. 2003). The peripheral HI is often not simply rotating (Zee et al. 1998b) or even in a disk (Pustilnik et al. 1997, 2001). This peripheral gas led to suggestions about cloud impacts (Gordon and Gottesman 1981), weak interactions (Brinks and Klein 1988; Pustilnik et al. 2002; Bravo-Alfaro et al. 2004), merging (Bekki 2008), and tidal effects (Zee et al. 1998b; Pustilnik et al. 2001) in efforts to explain the high SF rate (SFR). Alternatively, the HI could be vestigial streams or pools of cosmological accretion (Taylor et al. 1993; Thuan and Izotov 1997; Zee et al. 1998a; Wilcots and Miller 1998), like the streams modeled for higher mass galaxies (Ceverino et al. 2010).

BCDs resemble young galaxies in many respects (Elmegreen et al. 2009b; Izotov et al. 2011; Griffith et al. 2011). They are gas-rich, low-metallicity (Izotov et al. 2001), relatively turbulent (Zee et al. 1998b, 2001; Silich et al. 2002; García-Lorenzo et al. 2008), and highly clumped with locally intense SF. They tend to lie at the edges of galactic clusters or in voids with only low-mass neighbors, and where harsh environmental effects like ram pressure stripping are minimal (Groggin and Geller 2000; Drinkwater et al. 2001; Pustilnik et al. 2002). Those with the lowest metallicity tend to be relatively young, having formed most of their stars within the last few Gyrs (Searle and Sargent 1972; Noeske et al. 2000; Johnson et al. 2000; Fricke et al. 2001; Papaderos et al. 2008). BCDs with less extreme metallicities tend to have relatively more old stars (Thuan 1983; Loose and Thuan 1986; Crone et al. 2002; Caon et al. 2005; Cairós et al. 2007, 2009a, b; Zhao et al. 2011; Zhang et al. 2012). In the most low-metal BCDs, there is little evidence for stars older than ~ 200 – 500 Myr; these include SBS 1415 + 437 (Thuan et al. 1999, Guseva et al. 2003), SBS 1129 + 576 (Guseva et al. 2003), and I Zw 18 (Papaderos et al. 2002).

Specific examples of BCDs illustrate these points. I Zw 18 is in many respects a morphologically young system. It has two giant star-forming regions inside a kpc-scale blue continuum of stars, ionized emission with an overall exponential profile (Papaderos et al. 2002), and an extensive HI envelope (Zee et al. 1998a). Inside each region the star formation is widely distributed (Hunt et al. 2005). The rotation curve is flat but steeply rising in the inner part, where baryons may dominate dark matter (Lelli et al. 2012). Radial motions in the disk of ~ 15 km s $^{-1}$ suggest a major disturbance, which Lelli et al. (2012) suggest is tidal because there is a dwarf companion galaxy and elongated peripheral HI gas. The rotation curve gives a mass of $10^8 M_{\odot}$ in which ~ 70 % is neutral gas (Conteras et al. 2011). It has very low metallicity (2–3 % solar;

Izotov et al. 2001) even though old stars are present. Recchi et al. (2004) and others have considered the selective removal of metals by winds.

Another well-studied example is VII Zw 403, which is among the nearest BCDs to the sun, having a distance of 4.5 Mpc (Lynds et al. 1998). VII Zw 403 has a half-dozen big clumps and many $H\alpha$ filaments from superbubbles (Lozinskaya et al. 2006) in the midst of a smooth elliptical background of old red giant stars (Schulte-Ladbeck et al. 1998). The dynamical mass is $2 \times 10^8 M_{\odot}$, with approximately 20% in HI (Thuan and Martin 1981). The rotation speed is only $\sim 15 \text{ km s}^{-1}$ (Simpson et al. 2011) and the metallicity is 5% solar (Martin 1997; Izotov et al. 1997). Lynds et al. (1998) used resolved stellar populations to date a major starburst to 600 Myr ago, when the star formation rate was ~ 30 times higher than it is today. The current burst produced $\sim 10^6 M_{\odot}$ within the last 10 Myr (Silich et al. 2002).

The most intense SF in BCDs can occupy very compact regions with extreme densities and local formation rates. SBS 0335-052 is a pair of extremely young interacting dwarf galaxies (Pustilnik et al. 2001; Ekta et al. 2009) without much of an underlying old population (Papaderos et al. 1998), and with a metallicity of 2.5–4% solar (Izotov et al. 2009a; Peimbert and Peimbert 2010). There are six super star clusters (Thuan et al. 1997), of which two, within ~ 200 pc of each other, have extremely intense SF. Hunt et al. (2005) and Johnson et al. (2009) found radio free-free absorption and a very high emission measure where the electron density is $\sim 10^3\text{--}10^4 \text{ cm}^{-2}$, the star formation rate is $\sim 1 M_{\odot} \text{ yr}^{-1}$, and the excitation comes from the equivalent of $\sim 10^4$ O7 stars.

Here we propose that central accretion and long-lived starbursts in some BCDs arise from gravity-driven motions and torques produced by clump formation, clump dynamical friction, and clump interactions—the same processes that could make bulges in larger galaxies (Noguchi 1999; Immeli et al. 2004; Bournaud et al. 2007). BCDs have steep stellar profiles in the inner 500 pc that are exponential (Hunter and Elmegreen 2006) or deVaucouleur’s (Doublie et al. 1999), as in the bulges of earlier Hubble types. Such high central concentrations require baryonic mass inflow and significant angular momentum redistribution in the disk. Much of this inflow could have occurred when BCDs were young, but some of today’s BCDs still look dynamically young even if there are old stars, and significant inflow could be occurring now.

Our emphasis differs from that in Governato et al. (2010), where simulations of dwarf galaxies highlight the removal of gas in order to avoid central concentrations. In these simulations, diffusion, torques, and pressure-driven inflows return some of this gas to the center (Recchi and Hensler 2006; Dalcanton and Stilp 2010), only to have it removed again by the next starburst, cycling in and out many times (Stinson et al. 2007; Revaz et al. 2009). The result is a bulge-free late-type galaxy and a time-changing central potential that converts a primordial dark matter cusp into a more uniform dark matter core (Read and Gilmore 2005). The degree of this conversion varies for different simulations (Ogiya and Mori 2011; Oh et al. 2011). Alard (2011) note that the least evolved galaxies, having the highest relative gas abundances, tend to have the steepest inner density profiles, supporting the idea that gas recycling and SF make the inner profiles shallow over time. These observations could imply that

some BCDs still have steep central dark matter profiles, if these galaxies are relatively young. Del Popolo (2011) also model low-mass galaxies and suggest that tidal torques and the baryon fraction before collapse influence the central density profile of dark matter. Steeper central profiles are predicted to occur in more remote galaxies and in those with higher dark matter fractions; BCDs could be in this category too (Grogin and Geller 2000).

BCDs are unusual in having both a central concentration and a high gas abundance. This combination also appeared in massive galaxies at redshift $z \sim 2$ (Elmegreen et al. 2009a). Observations at intermediate-to-high redshift indicate that Hubble types arise mostly since $z \sim 1$ (Papovich et al. 2005; Bundy et al. 2006). The morphology seems to depend on dynamical maturity. High-mass disks like Hubble type Sa tend to be higher density than low-mass disks like Hubble type Sd (Roberts and Haynes 1994). Thus, Sa's evolve more quickly to a centrally concentrated state with a low-gas fraction and a low specific SFR (Sandage 1986; Zhang and Buta 2007). If this trend of increasing central concentration and decreasing specific SFR continues into the future for low-mass galaxies, then some dwarf Irregulars might also evolve to a centrally concentrated state with little remaining gas. Mass loss from winds and supernovae in the low potential well of the dwarf could prevent such a central concentration however, depending on the relative rates of inflow from torques and outflow from winds. Those with dominant inflows could go through the BCD phase, as discussed here. Strong inflow depends on the presence of relatively massive clumps or tidal arms.

In what follows, we estimate the accretion time of a clumpy disk from dynamical friction (Sect. 4.2), and then consider whether observed clumps and other irregularities in BCDs are massive enough to drive significant disk evolution on a Gyr time scale (Sect. 4.3). A summary is in Sect. 4.4.

4.2 Clump Accretion in BCDs

4.2.1 *The Case with a Few Giant Clumps*

The process of clump drag and interaction leading to coalescence in the center of a galaxy has been illustrated with detailed simulations of high redshift galaxies (Elmegreen et al. 2008; Ceverino et al. 2010). The clumps in these simulations formed spontaneously in a turbulent disk and had masses of about 5% of the total galaxy mass. Migration to the center took only a few orbit times (~ 0.5 Gyr). Clump destruction by star formation feedback (Genel et al 2012) does not stop the torques and accretion if each destroyed clump is replaced by a new one. This replacement is likely as long as the conditions for forming the first clumps, such as high gas fractions and turbulent speeds, are still present. A low ratio of turbulent speed to orbit speed would stop this process, because then the clumps that form by gravitational instabilities are relatively low mass and produce proportionally weaker torques.

The biggest star-forming regions in the Milky Way are only $\sim 10^{-3}$ times the disk mass and should have little tendency to move to the center.

Dynamical friction and clump torques are important if the ratio of the disk Jeans mass to the galaxy mass is more than a few percent. This ratio scales with the square of the ratio of the gas velocity dispersion to the rotation speed. In high redshift galaxies, the rotation speed is normal for a massive disk but the dispersion is abnormally high (Erb et al. 2006; Schreiber et al. 2011) making the ratio high. In local dwarf Irregulars, the gas dispersion is normal for local galaxies, $\sim 10 \text{ km s}^{-1}$, but the rotation speed is low, $\sim 50 \text{ km s}^{-1}$ or less. In both cases, the ratio of speeds is high and the clumps that form by gravitational instabilities are massive compared to the disk. The same processes of massive clump formation and angular momentum exchange should happen in high redshift galaxies and local gassy dwarfs because both have relatively large velocity dispersions compared to rotation speeds.

The timescale for dynamical friction between an orbiting clump of mass M_c in the disk and nonrotating dark matter particles or stars in a halo is $\nu (dv/dt)^{-1}$ where

$$\frac{dv}{dt} = \frac{4\pi \ln \Lambda G^2 M_c \rho}{v^2} \left(\text{erf}[X] - \frac{2X}{\pi^{1/2}} e^{-X^2} \right) = \frac{4\pi \ln \Lambda G^2 M_c \rho \xi}{v^2} \quad (4.1)$$

(Binney and Tremaine 2008). Here, ν is the clump orbital speed, $X = \nu/(2^{1/2}\sigma)$ for halo 3D velocity dispersion σ , ρ is the halo density, $\ln \Lambda$ is the coulomb factor, and ξ is the quantity in parentheses. This formula assumes that the clump is a self-gravitating object surrounded by a uniform density of low-mass field stars or dark matter particles that have a Maxwellian velocity distribution function.

It is convenient from an observational point of view to write the local rotation speed as a power of the local radius, $\nu(r) \propto r^\beta$, since β comes from the rotation curve. Starting with $\rho(r) = \rho_0 r^{-\alpha}$ and $\nu(r)^2 = GM_{\text{dyn}}(r)/r$, we get $\nu(r)^2/(4\pi\rho[r]Gr^2) = 1/(3 - \alpha) = 1/(1 + 2\beta)$. Then the dynamical friction time, $\nu/(dv/dt)$, in units of the dynamical orbit time, r/ν , is

$$T(r) \equiv \frac{\nu^2}{r(dv/dt)} = \frac{1}{\ln \Lambda \xi (1 + 2\beta)} \times \frac{M_{\text{dyn}}(r)}{M_c} = T_0(r) \frac{M_{\text{dyn}}(r)}{M_c} \quad (4.2)$$

where M_{dyn} is the galaxy dynamical mass enclosed within the orbital radius of the clump.

Dwarf galaxies have nearly solid body rotation in the inner parts (Swaters et al. 2002). BCDs can have steeply rising rotation curves in the dense inner regions, and flatter rotation curves beyond that (Zee et al. 1998b; Lelli et al. 2012). The BCDs we consider in Sect. 4.3 have approximately linear rising rotation curves in the vicinity of the giant clumps, and some have flat rotation curves beyond that (e.g., NGC 2366; Thuan et al. 2004). Thus for the main starburst regions we can take $\beta \sim 1$ or slightly less. If $\nu \sim \sigma$, then $\xi \sim 0.20$. In that case, the dimensionless time coefficient in Eq. (4.2) is $T_0 = 0.56$ for typical $\ln \Lambda = 3$ (see below). For a clump at $r = 0.5$ kpc orbiting with $\nu = 10 \text{ km s}^{-1}$, $r/\nu = 49 \text{ Myr}$ and the dynamical friction time in

physical units is $27M_{\text{dyn}}/M_c$ Myr. This means that a clump with a mass greater than 2.7% of the enclosed galaxy mass has $T < 1$ Gyr.

Note that M_{dyn} decreases with radius, while the normalization quantity, r/v , is constant for $\beta \sim 1$. Thus the timescale gets smaller as the clump moves in. Writing the rate of change of clump angular momentum as $dL/dt = M_c r (dv/dt)$ for frictional deceleration in the azimuthal direction dv/dt , and setting this equal to $M_c v (dr/dt)$ for circular speed v and radial drift speed $dr/dt \ll v$, we get $dr/dt = v/T(r)$. For $\beta = 1$, $v \propto r$ and $M_{\text{dyn}} \propto r^3$ so $T(r) \propto r^3$ if Λ and ξ are constant. Then, the time to reach the center is 1/3 the instantaneous T in Eq. 4.2. If $\beta = 1/2$, then $v \propto r^{1/2}$ and $M_{\text{dyn}} \propto r^2$ so $dr/dt \propto r^{-3/2}$ and it takes $0.4T$ to reach the center.

One uncertainty in this result is the ratio of the disk orbit speed to the halo velocity dispersion, which enters into ξ . This ratio depends on whether the halo has a core or a cusp, and on the nature of the core. We consider two extreme cases: a (Burkert 1995) halo density profile in the case of a core, and an NFW (Navarro et al. 1996) profile for a cusp. For the Burkert profile, $\rho(x) = \rho_s ([1+x][1+x^2])^{-1}$ with $x = r/r_s$ and scale factors ρ_s and r_s . We use this with the equation of hydrostatic equilibrium in the radial direction to determine β and v/σ as functions of x . Hydrostatic equilibrium implies $dP/dr = -GM(r)\rho(r)/r^2$ where $P = \rho\sigma_{1D}^2$ for 1D dispersion $\sigma_{1D} = \sigma/3^{1/2}$ and $M(r) = \int_0^r 4\pi r'^2 \rho(r') dr'$. We assume the boundary condition $P \sim 0$ and $\sigma \sim \text{constant}$ at the edge of the halo, which is taken to be where $\rho = 10^{-4}\rho_0$. Figure 4.1 shows v/σ , ξ , β , and T_0 as functions of position x (determined by numerical integration). $\beta \sim 1$ for a solid body rotation, so x must be small in the visible part of the disk. For example, $x = 0.54$ at the half-density point, where $\rho = 0.5\rho_0$, and there $v/\sigma = 0.49$, $\xi \sim 0.03$, $\beta = 0.72$, and $T_0 \sim 4.6$. For $r = 0.5$ kpc and $v \sim 10$ km s $^{-1}$, the friction

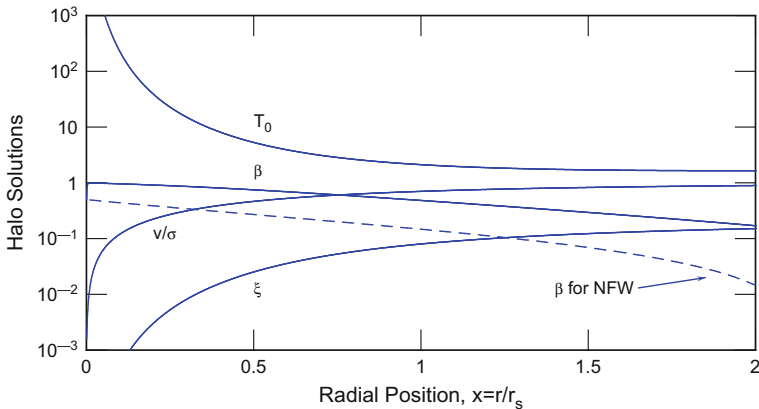


Fig. 4.1 Solutions to various parameters connected with the (Burkert 1995) dark matter density profile, which has a constant density core; ξ is the dynamical friction parameter in the parentheses of Eq. 4.1, v is the rotation speed, σ is the 3D velocity dispersion, β is the slope of the rotation curve, and T_0 is the prefactor in Eq. 4.2. The *dashed line* shows β for a Navarro et al. (1996) profile. The figure is adapted from (Elmegreen et al. 2012)

time is then $rT_0/v = 220M_{\text{dyn}}/M_c$ Myr. This implies that a clump with a relative mass of $M_c/M_{\text{dyn}} = 5\%$ takes ~ 1.5 Gyr to spiral in, considering the factor of $1/3$ that accounts for a decreasing M_{dyn} with radius, as discussed above.

The NFW dark matter profile is a little faster. For this, $\rho = \rho_s (x[1+x]^2)^{-1}$ with $x = r/r_s$ again. There is a density singularity at the center that produces a logarithmic divergence of a quantity like pressure if the equation of hydrostatic equilibrium is considered (because $M(r)\rho/r^2 \sim 1/r$ near the center). We consider instead that the halo 3D velocity dispersion is comparable to the rotation speed (Navarro et al. 1996), $v \sim \sigma$, which gives $\xi = 0.20$. Writing for the galaxy mass $M_{\text{dyn}}(x) = 4\pi r_s^3 \rho_s \mathcal{M}(x)$, where $\mathcal{M}(x) = \ln(1+x) - x/(1+x)$, the slope of the rotation curve is now given by $1 + 2\beta = x^2/(\mathcal{M}(x)(1+x)^2)$. Figure 4.1 shows β as a dashed line. We see $\beta \sim 0.5$ for small x and then $T_0 \sim 0.83$ with $\xi = 0.2$. This is a smaller prefactor than for a cored halo because of the higher v/σ . The dynamical friction time for an NFW halo is $\sim 41M_{\text{dyn}}/M_c$ Myr with $r = 0.5$ kpc and $v \sim 10$ km s^{-1} . Clumps with $M_c/M_{\text{dyn}} > 1.6\%$ take < 1 Gyr to spiral in, considering the factor of $2/5$ that accounts for a decreasing M_{dyn} with radius when $\beta = 0.5$.

Dwarf galaxies do not appear to have NFW halos at the present time (Zackrisson et al. 2006; Eymeren et al. 2009; Kuzio et al. 2009; Amorisco and Evans 2012), although it is difficult to be certain (Spekkens et al. 2005; Valenzuela et al. 2007) and it is not yet known whether BCDs differ from other dwarfs in this regard. An important point for dynamical friction is the relative velocity dispersion of the field particles, σ/V , which enters into ξ as shown above. The validity of the Chandrasekhar formula is also a question. Goerdt et al. (2010) modeled sinking massive objects like what we consider here and showed that a central cusp turns into a core inside the radius where the sinking mass equals the enclosed dark halo mass. Further sinking in their model stalled at this radius because of a decrease in dynamical friction in the core. This result was also found by Read et al. (2006) and others. In a detailed study of dynamical friction in cored galaxies, Inoue (2011) explained the loss of frictional forces as a result of orbit resonances that appear when the orbit time is independent of radius, as is the case for a constant central density. Another limitation is that after a bulge forms, tidal forces from the bulge can rip apart remaining clumps and prevent them from reaching the center (Elmegreen et al. 2008). These considerations make it plausible that in some BCDs today, giant clumps come in from larger radii and then stall at the edge of a dark matter core, building up the central region from inside out. Accretion to the center could have occurred more readily when the galaxies were young and the dark matter profiles were more cuspy.

Sánchez-Salcedo et al. (2006) considered a similar situation with in-spiraling globular clusters in dwarf galaxies. They concluded that dwarfs should have dark matter cores rather than cusps so that the globular clusters stall midway in the disk where they can still be seen. Galaxies with giant nuclear star clusters, however, may have allowed their disk clusters to reach the center (Böker 2010; Antonini et al. 2012; Hartmann et al. 2011). The resemblance of these galaxies to BCDs is compelling if we allow for a difference in the mass and size of the disk clumps that form by star formation: BCDs have relatively massive and large disk clumps that could spiral

in to form massive and large central cores, while normal dwarfs and galaxies have relatively small star clusters, which could spiral in to form small nuclear clusters.

4.2.2 Clumps with a Power Law Mass Function

As mentioned above, individual clumps need not survive the full trip to the center to drive accretion if new clumps replace dispersed clumps in a steady state. Similarly, there need not even be a single giant clump. Any irregularities moving through a slower rotating halo will have dynamical friction drag, and the total torque on the medium will depend on the mean squared mass of those irregularities. Consider the equations of disk accretion starting with the continuity equation in two dimensions (Pringle 1981)

$$\frac{d}{dt}\Sigma + r^{-1}\frac{d}{dr}r\Sigma v_r = 0; \quad (4.3)$$

the surface density is Σ and the radial drift velocity is v_r . The torque equation is

$$\frac{d}{dt}r\Sigma v + r^{-1}\frac{d}{dr}r\Sigma v_r r v = \text{torque/area} \quad (4.4)$$

where v is again the azimuthal speed. For a viscous disk, the torque per unit area is $R^{-1}dG/dR$ where $G = \nu \Sigma A r^2$ for viscous coefficient ν (comparable to the product of the clump mean free path and the rms speed), and Oort rotation constant A , which is the rate of shear. We are not concerned with viscosity in this paper because A is small for dwarf galaxies with little shear; ν is also usually small compared to dynamical torques in galaxy disks (however, see Wang et al. 2009). Here we consider dynamical friction between orbiting clumps in the disk and the halo and other parts of the disk. If an annular area has N clumps of mass M_c , then the total torque exerted on these clumps is $N M_c r dv/dt$ for deceleration in the azimuthal direction dv/dt from Eq.(4.1). This quantity depends on the mean squared clump mass because dv/dt depends on clump mass. For clump mass function $dn(M_c)/dM_c \propto M_c^{-\delta}$,

$$\langle N M_c^2 \rangle = \frac{2-\delta}{3-\delta} M_{c,\max} \langle N M_c \rangle = f M_{c,\max} \langle N M_c \rangle. \quad (4.5)$$

The prefactor f ranges between $f = 0.33$ at $\delta = 1.5$ and $f = 0.06$ at $\delta = 2$ (for δ , Heithausen et al. 1998). In the latter case, the integral over $M^2 n(M)$ gives $\ln(M_{c,\max}/M_{c,\min})$, whose value is ~ 16 for typical $M_{c,\max} \sim 10^7 M_\odot$ and $M_{c,\min} \sim 1 M_\odot$. Because $\langle N M_c \rangle / \text{Area} = \Sigma$, we have $\langle N M_c^2 \rangle / \text{Area} = f \Sigma M_{c,\max}$. Then the torque/area for the above halo model becomes $f \Sigma r dv/dt = \Sigma \gamma / r$ where $\gamma = (1 + 2\beta) f \ln A G M_{c,\max} \xi$. For a fixed galactic potential (v independent of time), the torque equation is now

$$r^2 v \frac{d\Sigma}{dt} + \frac{d}{dr} r \Sigma v_r r v = -\Sigma \gamma. \quad (4.6)$$

We can simplify this by writing $\mu = r \Sigma v_r$ and noting that $(d/dr)\mu r v = \mu(d/dr) r v + r v d\mu/dr = \mu(d/dr) r v - r^2 v (d\Sigma/dt)$ using the continuity equation. Then $d\Sigma/dt$ cancels in the torque equation and we get

$$r \Sigma v_r \frac{dr v}{dr} = -\Sigma \gamma. \quad (4.7)$$

This may be solved for v_r since everything else is a known function of r , and then the result can be put into the continuity equation to get $d\Sigma/dt$. Note that $dr v/dr = (1 + \beta)r v$; for the other radial derivative, we set $d/dr \sim 1/r$. The resultant normalized accretion timescale is

$$T = \frac{v \Sigma}{r d\Sigma/dt} \sim \frac{(1 + \beta)}{f \ln \Lambda \xi (1 + 2\beta)} \times \frac{M_{\text{dyn}}(x)}{M_{\text{c,max}}} = T_1(x) \frac{M_{\text{dyn}}(x)}{M_{\text{c,max}}}. \quad (4.8)$$

This time is larger than before by the ratio $(1 + \beta)/f$. Setting $\beta = 1$, $\ln \Lambda = 3$ and $\xi \sim 0.03$ for a Burkert core, and taking $f \sim 0.1$, we get $T_1 = 74$ and a physical accretion time of $1.2 M_{\text{dyn}}/M_{\text{c,max}}$ Gyr for $r = 0.5$ kpc, $v = 10$ km s⁻¹ with the factor 1/3 to account for a decreasing M_{dyn} with radius. For a NFW core with $\beta = 0.5$ and $\xi = 0.2$, $T_1 = 12.5$ and the accretion time is $240 M_{\text{dyn}}/M_{\text{c,max}}$ Myr for $r = 0.5$ kpc, $v = 10$ km s⁻¹ with the factor 2/5. Now we see that it takes about 1 Gyr for 10% of the ISM to accrete to the center from the inner half-kpc if the largest cloud in a power law distribution of cloud masses is 12 and 2.4% of the enclosed galaxy mass for the Burkert and NFW profiles, respectively. If the largest cloud has a mass much larger than the extrapolation of a power law distribution from the other clouds, then the previous analysis for a single cloud applies.

4.2.3 Clump–Clump Interactions

Clump–clump interactions can also drive accretion by direct gravitational forces. The acceleration on one clump by another clump is $G M_c / \Delta r^2$ for separation Δr . This acceleration cumulatively distorts the clump's motion until its velocity has changed significantly. The timescale for this change is v divided by the acceleration, and in units of the orbit time, it is v^2/r divided by the acceleration. Writing $v^2/r = G M_{\text{dyn}}/r^2$, the normalized interaction time becomes $(\Delta r/r)^2 (M_{\text{dyn}}/M_c)$. For big clumps, $\Delta r \sim r$, and the normalized interaction time is just the ratio of masses. That means $T_0 \sim 1$ in an equation like (4.2), and the accretion time is $\sim 49 M_{\text{dyn}}/M_c$ Myr for $r = 0.5$ kpc and $v \sim 10$ km s⁻¹.

Other torques will contribute to the inflow of gas, so T is an upper limit based on dynamical friction with the halo. The disk also will produce a torque if there is shear, because then the clump will drive a spiral wake (Julian and Toomre 1966) and

the wake will have its own torque that drives mass inward (Lynden-Bell and Kalnajs 1972). Small galaxies tend to have little shear, however.

4.3 Observations of Clump Properties in Dwarf Irregulars and BCD Galaxies

4.3.1 Clump Mass Fractions and Accretion Times

Many of the observations referenced in the introduction concern BCD or other dwarf irregular galaxies that have relatively large gas velocity dispersions compared to the rotation speeds, relatively thick disks compared to the galactic radii, and relatively massive star-forming regions compared to the galaxy masses. They are good candidates for the extreme torques and inward migrations discussed above. Five examples are given in Table 4.1, along with properties of their primary star formation clumps. As above, the clump mass is denoted by M_c , the galactocentric radius at the center of the clump is r_c , and the galaxy mass inside the clump radius is M_{dyn} , measured as $r_c v(r_c)^2 / G$ for local rotation speed $v(r_c)$. Also for reference, we give the total galaxy stellar mass, M_s , the total baryonic galaxy mass (gas+stars), M_b , the Coulomb factor $\Lambda \sim (R_{\text{clump}}/R_{\text{gal,tot}})(R_{\text{gal,tot}}/r_c)^{1+2\beta}(M_{\text{dyn}}/M_c)$, and the accretion time T from Eq. (4.2) for NFW and Burkert dark matter profiles. The Coulomb factor comes from the approximate expression $\Lambda \sim (R_{\text{clump}}/R_{\text{gal,tot}})(M_{\text{gal,tot}}/M_c)$ in Binney and Tremaine (2008), where R_{clump} and M_c are the clump radius and mass, and $R_{\text{gal,tot}}$ and $M_{\text{gal,tot}}$ are the total galaxy radius and mass. We take $M_{\text{gal,tot}}/M_{\text{dyn}} \sim (R_{\text{gal,tot}}/r_c)^{1+2\beta}$ for rotation curve $v \propto r^\beta$, R_{clump} equal to half the clump aperture in the table, and $R_{\text{gal,tot}}/r_c$ from Fig. 4.2. As discussed above, the NFW profile has $\beta = 0.5$, $\xi = 0.2$, and a time multiplier of 0.4 to account for faster accretion as the clump approaches the center; the Burkert profile has $\beta = 1$, $\xi = 0.03$, and a multiplier of 0.33.

Color composite images are shown in Fig. 4.2. For four galaxies, they are made with U- and J-band images from Hunter and Elmegreen (2006); for NGC 4861, they are made with u- and z-band images from the Sloan Digital Sky Survey (SDSS; Stoughton et al. 2002). The elliptical contours outline the giant star-forming clumps that we consider to be candidates for inward migration. The cross marks the center of the galaxy as defined by the outer elliptical isophotes in V band.

The HI rotation curves for our galaxies are close to solid body in the clump region. They are not accurate enough to tell if the dark matter halo is cored or cuspy (which give rotation curve slopes $\beta = 1$ or 0.5 in these two cases, respectively). To determine v at the clump radius r_c , we fit the observed rotation curve to a deprojected speed, v_t , and radius, r_t , at the limit of the observation or the turnover point, whichever comes first. Then the total galaxy mass inside the clump radius is taken to be $v_t^2 r_c^3 / (r_t^2 G)$, assuming $\beta = 1$ for this. For the different galaxies, the values of (v_t, r_t) in (km s^{-1} , kpc), are, DDO 155: (8, 0.15) (Carignan et al. 1990), Haro 29: (34, 1.7) (Stil and

Table 4.1 Sample BCD galaxies and their clump properties

Galaxy	D (Mpc)	$\log M_s (M_\odot)$	$\log M_b (M_\odot)$	$\log M_c (M_\odot)$	r_c (kpc)	Aperture (kpc)	$\log M_{\text{dyn}} (M_\odot)$	$M_c/M_{\text{dyn}}(r_c)$	$\ln \Lambda$	T Gyr
Mrk 178	3.9	7.04	7.39	5.13	0.39	0.32	6.60	0.035	3.4–4.3	0.50–1.4
DDO 155	2.2	6.47	7.22	5.46	0.21	0.24	6.78	0.048	3.2–3.9	0.12–0.37
Haro 29	5.9	7.16	8.06	6.33	0.27	0.74	6.26	1.17	1.3–2.3	0.03–0.06
NGC 2366	3.4	7.84	9.04	6.23	1.31	0.93	8.08	0.014	3.6–4.0	1.3–4.2
NGC 4861	7.6	8.04	8.83	6.89	2.07	0.67	8.48	0.026	1.8–1.8	1.7–6.3

Note— D is the distance, M_s is the galaxy stellar mass, M_b is the galaxy baryonic mass, M_c is the clump stellar mass, r_c is the clump galactocentric radius, $Aperture$ is the aperture size used for clump photometry, M_{dyn} is the galaxy dynamical mass inside r_c , Λ is the Coulomb factor, and T is the clump accretion time. For the latter two, we assume $\xi = 0.2$ and a rotation curve slope $\beta = 0.5$ in the first case (NFW core), and $\xi = 0.03$, $\beta = 1$ in the second case (Burkert core), with factors of 0.40 and 0.33 in T , respectively, to account for the decrease in M_{dyn} with radius

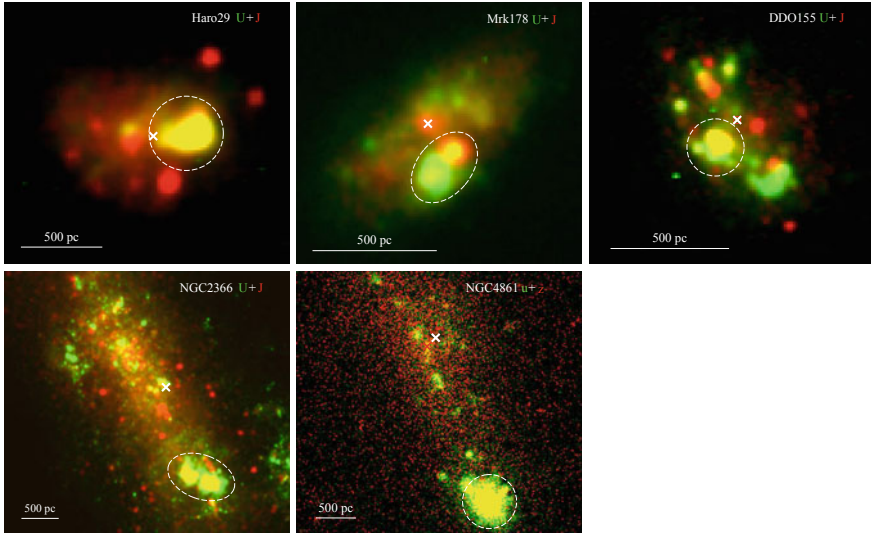


Fig. 4.2 Five clumpy irregular galaxies used to study relative clump mass and possible central migration from tidal torques. The images are a combination of U and J band from Hunter and Elmegreen (2006) except for NGC 4861, which is a combination of u and z band from SDSS. The measured clumps are indicated by *elliptical contours* and the centers of the outer V-band isophotes are indicated by “x”. The figure is adapted from (Elmegreen et al. 2012)

Israel 2002); NGC 2366: (50, 3.3) (Hunter et al. 2001; Thuan et al. 2004); NGC 4861: (40, 3.3) Thuan et al. (2004).

For DDO 155 (also known as GR8), the HI observations by Begum and Chengalur (2003) suggest that the velocity field is complex, so the dynamical galaxy mass is inaccurate. Lo et al. (1993) and Begum and Chengalur (2003) suggest the velocities have an expanding or contracting component, which Begum and Chengalur (2003) fit to a peak value of 10 km s^{-1} , with some radial variations. They also fit the rotating part to a peak value of 6 km s^{-1} at the edge (the escape speed was estimated to be $\sim 30 \text{ km s}^{-1}$). The velocity of the giant clump outlined in Fig. 4.2 is smaller than the systematic velocity, so if it is on the near side of the galaxy, then it is expanding away from the center. Begum and Chengalur (2003) consider an explosive origin for this motion but note the lack of old star clusters that might have driven this explosion; they suggest that HII regions might have had the necessary force. If the motion is inward, then Begum and Chengalur (2003) suggest that the clumps might have coalesced to form the galaxy and are now dispersing to make a disk. They note that there are no tidal features, however. This inward moving interpretation is consistent with the model presented in the present paper; tidal features are not expected because the torques are generated internally. The timescale for inward motion given in Table 4.1 is $\sim 200 \text{ Myr}$ for DDO 155. This timescale is consistent with the results of Dohm-Palmer et al. (1998), who find from resolved stellar population studies that SF lasts in each clump for $\sim 100 \text{ Myr}$. They suggest that this long time requires gravitational

self-binding of the clumps. Dohm-Palmer et al. also suggest that the clumps come and go on this time scale, with the current generation of clumps at the positions of the three main HI clouds. Thus the present model of massive clump formation by gravitational instabilities in a gas-rich galaxy, relatively long clump ages from modest gravitational self-binding, and angular momentum loss through halo, disk, and clump-interaction torques, is consistent with the HI and stellar observations and previous interpretations of DDO 155.

Mrk 178 does not have a published rotation curve, but the HI linewidth was given by Bottinelli et al. (1973), who also derived a total dynamical mass (“indicative mass”) from the equation $M_{\text{tot,dyn}} = 3 \times 10^4 r_{\text{H}} W^2 M_{\odot}$ for Holmberg radius r_{H} in kpc and linewidth W in km s^{-1} (Böker 2010). Scaling to our distance, the Holmberg radius is $r_{\text{H}} = 2.9$ kpc and the total dynamical mass is $M_{\text{H}} = 1.6 \times 10^9 M_{\odot}$. If we assume this rotation curve is solid body, then the dynamical mass inside radius r_{c} is $M_{\text{dyn}}(r_{\text{c}}) = M_{\text{H}}(r_{\text{c}}/r_{\text{H}})^3$. Setting $r_{\text{c}} = 0.39$ kpc from Table 4.1, we get $M_{\text{dyn}}(r_{\text{c}}) = 3.9 \times 10^6 M_{\odot}$.

Clump and galaxy stellar masses were derived by fitting the SEDs over a range of passbands inside deprojected circular apertures (see Zhang et al. 2012). The aperture sizes were determined from the U-band brightness contours shown in Fig. 4.2. Local background intensities came from larger annuli around the clumps and were subtracted from the clump intensities. For Mrk 178, DDO 155 and NGC 2366, the SEDs used observations in U, B, V, and J passbands (Hunter and Elmegreen 2006). For Haro 29, we used only U, B and J bands from Hunter and Elmegreen (2006) because the V-band photometry is inconsistent with the others. For NGC 4861, we used ugiz data from SDSS. The giant clump in NGC 2366 was also studied by Kennicutt et al. (1980). The giant clump in NGC 4861 is known as Mrk 59 and was studied by Izotov et al. (2009b) and others.

Although there is HI gas present in some of the clumps, and perhaps even molecular gas connected with current SF, we do not include gas in the clump masses. In DDO 155, for example, the HI mass in the clump is a few times $10^5 M_{\odot}$ (Carignan et al. 1990; Begum and Chengalur 2003), which is comparable to the stellar mass. In NGC 2366, an HI cloud at the position of the clump contains several $\times 10^5 M_{\odot}$ (Hunter et al. 2001), which is $\sim 20\%$ of the stellar mass. Considering the possible addition of gas, the clump masses and mass fractions given in Table 4.1 are lower limits.

As part of the fits for clump mass, we also obtained crude star formation histories in the clumps (Zhang et al. 2012). These are determined as relative stellar masses younger than 0.1 Gyr, in the time interval between 0.1 and 1 Gyr, and older than 1 Gyr. For the five galaxies, the relative masses in the intervals (< 0.1 Gyr, $0.1 - 1$ Gyr, > 1 Gyr) are, Mrk 178: (0.42, 0.49, 0.09), DDO 155: (0.11, 0.23, 0.66), Haro 29: (0.17, 0.15, 0.68), NGC 2366: (0.28, 0.5, 0.22), and NGC 4861: (0.27, 0.50, 0.23). Evidently the SEDs indicate significant clump components older than 1 Gyr even after background disk subtraction. The dominant appearance of these clumps in the J band (Fig. 4.2) suggests the same thing. If these old massive components are really present, then they would have to be gravitationally bound to the clump and the clump would have to be long-lived. We note that gravitational instabilities in a disk

of gas and stars can collect both gas and a significant mass of background field stars into a clump when the velocity dispersions and densities of the two components are similar (Elmegreen 2011). Background field stars also fall into the clump and get trapped because of the changing gravitational potential as its mass grows (Fellhauer et al. 2006). In our sample, the clumps that are relatively closest to the center (in Mrk 178, DDO 155 and Haro 29) contain the highest fraction of old stars. This suggests a larger total age for the more centralized clumps than for the more peripheral clumps, which is consistent with a history of inward migration.

The 9th column in Table 4.1 gives the ratio between the clump mass and the galaxy dynamical mass inside the clump radius. As shown in the previous sections, if this ratio is larger than a few percent, the clump could significantly perturb the surrounding disk and cold halo particles, leading to the loss of clump orbital angular momentum in less than ~ 1 Gyr. The tabulated mass fractions are in this range. The timescale for their migration is in the last column, assuming NFW and Burkert profiles in two cases, and using the observed rotation speed at the clump position. The mass fractions are higher and the timescales are smaller when the clumps are relatively close to the center, because only the inner parts of the galaxies are included in M_{dyn} .

4.3.2 Galaxy Thickness and Scale Length Ratios

Clump accretion can thicken the central regions because the stellar orbital energy gets mixed into three dimensions during the final merger phase (Bournaud et al. 2007). What is important is the ratio of the disk scale height, $H = \sigma^2 / (\pi G \Sigma)$, to the disk scale length R_d . Here, σ is the perpendicular velocity dispersion in the central region of the BCD, and Σ is the central mass column density of the disk. For reference values $\sigma = 10 \text{ km s}^{-1}$ and $\Sigma = 10 M_{\odot} \text{ pc}^{-2}$, we obtain $H = 740 \text{ pc}$. Most BCDs in Hunter and Elmegreen (2006) have $R_d \sim 500 \text{ pc}$ or less, so H and R_d are comparable. This means the inner parts of BCDs are 3D objects like a bulge.

Detailed consideration of the BCDs in Table 4.1 confirm that the inner disk thicknesses are comparable to or larger than the inner disk scale lengths. Putting dimensions into the thickness equation, we get

$$H = 740(\sigma/10 \text{ km s}^{-1})^2(\Sigma/10 M_{\odot} \text{ pc}^{-2})^{-1} \text{ pc}. \quad (4.9)$$

Zhang et al. (2012) determined disk stellar mass densities and scale lengths from SED fits. Values are given in Table 4.2. The average $H/R_d \sim 2.6$, so the BCDs in this study should have relatively thick inner regions. The ratio would be larger for larger perpendicular velocity dispersions—the assumed value of 10 km s^{-1} for stars seems to be a lower limit. We note that the BCDs with giant clumps closest to the center have the highest ratios of height to length.

Height-to-length ratios greater than unity in Table 4.2 are difficult to understand. They would be smaller if additional mass were in the disk. This suggests that some

Table 4.2 Inner scale heights and lengths

Galaxy	Σ ($M_{\odot} \text{ pc}^{-2}$)	H (kpc)	R_d (kpc)	H/R_d
Mrk 178	4.9	1.8	0.27	6.7
DDO 155	7.4	1.0	0.22	4.5
Haro 29	39	0.19	0.20	0.95
NGC 2366	0.66	1.3	3.7	0.35
NGC 4861	10	0.74	1.0	0.74

Note— H is the inner disk scale height assuming a perpendicular velocity dispersion of 10 km s^{-1} and the observed stellar mass column density, Σ ; R_d is the inner disk scalelength

of the BCDs in our survey have a considerable mass column density of gas in the inner disk, perhaps comparable to or larger than the stellar column density. Such high masses of gas might be expected for the clumps in which the starbursts are occurring (e.g., larger than several hundred $M_{\odot} \text{ pc}^{-2}$ in molecules, which is typical for local giant molecular clouds), but there might also be a dense molecular and atomic intercloud medium where the average exceeds the average stellar value of $10 M_{\odot} \text{ pc}^{-2}$. Alternatively, a high filling factor of star-forming gas clumps that individually have mass column densities in excess of $\sim 100 M_{\odot} \text{ pc}^{-2}$ could produce an average gas column density in the inner part that exceeds the stellar column density. This could explain why the BCDs in Table 4.2 that have their massive clumps closest to the center also have the largest height-to-length ratios, i.e., these galaxies have higher Σ than we assume because of contributions from molecular and dense atomic material in clumps. Massive clump accretion like that discussed here would drive significant gas accretion, not only in the clumps but also of the interstellar material between the clumps, which gets dragged along with the clumps by gravitational and magnetic forces.

The mass column densities of inner disk HI gas have been observed for most of these galaxies. For both DDO 155 and NGC 2366, it is $\sim 10 M_{\odot} \text{ pc}^{-2}$ (Carignan et al. 1990; Hunter et al. 2001). Haro 29 has a hole in the central HI but the clump is very close and it has an average column density of $\sim 20 M_{\odot} \text{ pc}^{-2}$ (Stil and Israel 2002). NGC 4861 has a large HI concentration in the center with a column density of $\sim 30 M_{\odot} \text{ pc}^{-2}$ (Thuan et al. 2004). Some of these values are larger than the corresponding central stellar mass column density by a factor 2 or more, which lowers H/R_d in proportion. Further studies of the gas column densities in the centers of BCD galaxies should clarify their relative thicknesses.

4.4 Summary

Young stellar clumps that form by gravitational instabilities in a galaxy disk can have such a high mass relative to the enclosed galaxy mass that they produce dynamically significant torques on the halo stars and cold dark matter particles, on the disk, and

on each other. If the clump mass fraction exceeds a few percent, then these torques can drive an inflow of the clump's amount of mass in less than 1 Gyr. This process has been suggested for the formation of bulges in disk galaxies at high redshift, but it may apply also to local clumpy galaxies. Because of the general tendency for downsizing, in which active SF occurs in galaxies with ever smaller masses as the universe ages, the clumpy phase now is mostly limited to dwarfs. We suggest that BCDs are an example of a local clumpy starbursting galaxy in which the clumps are large enough to drive significant accretion in a Gyr or less. This would explain the dense stellar inner disks of these galaxies, and the prolonged SF near the center.

The BCDs in our sample also have relatively thick inner regions, reminiscent of bulges in spiral galaxies. They are even a little too thick if only the stellar surface densities are considered. This suggests there could be a dense atomic or molecular component in the inner region that has an average surface density comparable to or exceeding that from stars.

References

- Alard C (2011) *ApJL* 728:47
 Amorisco NC, Evans NW (2012) *MNRAS* 419:184
 Antonini F, Capuzzo-Dolcetta R, Mastrobuono-Battisti A, Merritt D (2012) *ApJ* 750:111
 Bekki K (2008) *MNRAS* 388:L10
 Begum A, Chengalur JN (2003) *A&A* 409:879
 Binney J, Tremaine S (2008) *Galactic Dynamics*. Princeton University Press, Princeton
 Böker T (2010) In star clusters: basic galactic building blocks throughout time and space. In: De Grijs R, Lepine, J (eds) *Proceedings of the IAU Symposium*, vol 266, p 58
 Bottinelli L, Gouguenheim L, Heidmann J (1973) *A&A* 22:281
 Bournaud F, Elmegreen BG, Elmegreen DM (2007) *ApJ* 670:237
 Bravo-Alfaro H, Brinks E, Baker AJ, Walter F, Kunth D (2004) *AJ* 127:264
 Brinks E, Klein U (1988) *MNRAS* 231:P63
 Bundy K, Ellis RS, Conselice CJ, Taylor JE, Cooper MC, Willmer CNA, Weiner BJ, Coil AL, Noeske KG, Eisenhardt PRM (2006) *ApJ* 651:120
 Burkert A (1995) *ApJ* 447:L25
 Cairós LM, Caon N, Garca-Lorenzo B, Monreal-Ibero A, Amorín R, Weilbacher P, Papaderos P (2007) *ApJ* 669:251
 Cairós LM, Caon N, Papaderos P et al (2009a) *ApJ* 707:1676
 Cairós LM, Caon N, Zurita C et al (2009b) *A&A* 507:1291
 Caon N, Cairós LM, Aguerri JAL, Muñoz-Tuñón C (2005) *ApJS* 157:218
 Carignan C, Beaulieu S, Freeman KC (1990) *AJ* 99:178
 Ceverino D, Dekel A, Bournaud F (2010) *MNRAS* 404:2151
 Chamaraux P (1977) *A&A* 60:67
 Contreras Ramos R, Annibali F, Fiorentino G, Tosi M, Aloisi A, Clementini G, Marconi M, Musella I, Saha A, Van der Marel RP (2011) *ApJ* 739:74
 Crone MM, Schulte-Ladbeck RE, Greggio L, Hopp U (2002) *ApJ* 567:258
 Dalcanton JJ, Stilp AM (2010) *ApJ* 721:547
 Del Popolo A (2011) *MNRAS*, tmp 1818
 Dohm-Palmer RC, Skillman ED, Gallagher J, Tolstoy E, Mateo M, Dufour RJ, Saha A, Hoessel J, Chiosi C (1998) *AJ* 116:1227
 Doublier V, Caulet A, Comte G (1999) *A&AS* 138:213

- Drinkwater MJ, Gregg MD, Holman BA, Brown MJI (2001) MNRAS 326:1076
- Ekta B, Pustilnik SA, Chengalur JN (2009) MNRAS 397:963
- Elmegreen BG (2011) ApJ 373:10
- Elmegreen BG, Bournaud F, Elmegreen DM (2008) ApJ 688:67
- Elmegreen BG, Zhang H-X, Hunter DA (2012) ApJ 747:105
- Elmegreen BG, Elmegreen DM, Fernandez MX, Lemonias JJ (2009a) ApJ 692:12
- Elmegreen DM, Elmegreen BG, Marcus M, Shahinyan K, Yau M, Petersen M (2009b) ApJ 701:306
- Erb DK, Steidel CC, Shapley AE, Pettini M, Reddy NA, Adelberger KL (2006) ApJ 646:107
- Fellhauer M, Kroupa P, Evans NW (2006) MNRAS 372:338
- Firpo V, Bosch G, Hägele GF, Díaz AI, Morrell N (2011) MNRAS. 414:3288
- Förster Schreiber NM, Shapley AE, Genzel R, Bouché N, Cresci G, Davies R, Erb DK, Genel S, Lutz D, Newman S, Shapiro KL, Steidel CC, Sternberg A, Tacconi LJ (2011) ApJ 739:45
- Fricke KJ, Izotov YI, Papaderos P, Guseva NG, Thuan TX (2001) AJ 121:169
- García-Lorenzo B, Cairós LM, Caon N, Monreal-Ibero A, Kehrig C (2008) ApJ 677:201
- Genel S, Naab T, Genzel R, Förster Schreiber NM, Sternberg A, Oser L, Johansson PH, Davé R, Oppenheimer BD, Burkert A (2012) ApJ 745:11
- Goerdt T, Moore B, Read JI, Stadel J (2010) ApJ 725:1707
- Gordon D, Gottesman ST (1981) AJ 86:161
- Governato F, Brook C, Mayer L, Brooks A, Rhee G, Wadsley J, Jonsson P, Willman B, Stinson G, Quinn T, Madau P (2010) Nature 463:203
- Griffith RL, Tsai CW, Stern D, Blain A, Eisenhardt PRM, Harrison F, Jarrett TH, Madsen K, Stanford SA, Wright EL, Wu J, Wu Y, Yan L (2011) ApJ 736:L22
- Grogin NA, Geller MJ (2000) AJ 119:32
- Guseva NG, Papaderos P, Izotov YI, Green RF, Fricke KJ, Thuan TX, Noeske KG (2003a) A&A 407:105
- Guseva NG, Papaderos P, Izotov YI, Green RF, Fricke KJ, Thuan TX, Noeske KG (2003b) A&A 407:75
- Hartmann M, Debattista VP, Seth A, Cappellari M, Quinn TR (2011) MNRAS 418:2697
- Heithausen A, Bensch F, Stützi J, Falgarone E, Panis JF (1998) A&A 331:L65
- Heller AB, Brosch N, Almozniño E, van Zee L, Salzer JJ (2000) MNRAS 316:569
- Hoffman GL, Brosch N, Salpeter EE, Carle NJ (2003) AJ 126:2774
- Hunt LK, Dyer KK, Thuan TX (2005) A&A 436:837
- Hunter DA, Elmegreen BG, van Woerden H (2001) ApJ 556:773
- Hunter DA, Elmegreen BG (2004) ApJS 128:2170
- Hunter DA, Elmegreen BG (2006) ApJS 162:49
- Immeli A, Samland M, Gerhard O, Westera P (2004) A&A 413:547
- Inoue S (2011) MNRAS 416:1181
- Izotov YI, Thuan TX, Lipovetsky V (1997) ApJS 108:1
- Izotov YI, Lipovetsky VA, Chaffee FH, Foltz CB, Guseva NG, Kniazev AY (1997) ApJ 476:698
- Izotov YI, Chaffee FH, Foltz CB et al (2001) ApJ 566:222
- Izotov YI, Guseva NG, Fricke KJ, Papaderos P (2009) A&A 503:61
- Izotov YI, Thuan TX, Wilson JC (2009) ApJ 703:1984
- Izotov YI, Guseva NG, Thuan TX (2011) ApJ 728:161
- Johnson KE, Leitherer C, Vacca WD, Conti PS (2000) AJ 120:1273
- Johnson KE, Hunt LK, Reines AE (2009) AJ 137:3788
- Julian WH, Toomre A (1966) ApJ 146:810
- Kennicutt R, Balick B, Heckman T (1980) PASP 92:134
- Koleva M, Prugniel P, de Rijcke S, Zeilinger WW (2011) MNRAS 417:1643
- Kunth D, Maurogordato S, Vigroux L (1988) A&A 204:10
- Kuzio de Naray R, McGaugh SS, Mihos JC (2009) ApJ 692:1321
- Lelli F, Verheijen M, Fraternali F, Sancisi R (2012) A&A 537:72
- Lo KY, Sargent WLW, Young K (1993) AJ 106:507

- Loose HH, Thuan TX (1986) In star-forming dwarf galaxies and related objects. In: Kunth D, Thuan TX, Tran Than Van J (eds) (Gifsur-Yvette: Editions Frontie'eres), p 73
- Lozinskaya TA, Moiseev AV, Avdeev VYu, Egorov OV (2006) *Astron. Lett.* 32:361
- Lynden-Bell D, Kalnajs AJ (1972) *MNRAS* 157:1
- Lynds R, Tolstoy E, O'Neil EJ, Jr, Hunter, DA (1998) *AJ* 116:146
- Martin C (1997) *ApJ* 491:561
- McQuinn KBW, Skillman ED, Cannon JM, Dalcanton J, Dolphin A, Hidalgo-Rodriguez S, Holtzman J, Stark D, Weisz D, Williams B (2010) *ApJ* 724:49
- Navarro JF, Frenk CS, White SDM (1996) *ApJ* 462:563
- Noeske KG, Guseva NG, Fricke KJ, Izotov YI, Papaderos P, Thuan TX (2000) *A&A* 361:33
- Noeske KG, Papaderos P, Cairós LM, Fricke KJ (2003) *A&A* 410:481
- Noguchi M (1999) *ApJ* 514:77
- Ogiya G, Mori M (2011) *ApJL* 736:2
- Oh S-H, Brook C, Governato F, Brinks E, Mayer L, de Blok WJG, Brooks A, Walter F (2011) *AJ* 142:24
- Papaderos P, Loose H-H, Fricke KJ, Thuan TX (1996) *A&A* 314:59
- Papaderos P, Izotov YI, Fricke KJ, Thuan TX, Guseva NG (1998) *A&A* 338:43
- Papaderos P, Izotov YI, Thuan TX, Noeske KG, Fricke KJ, Guseva NG, Green RF (2002) *A&A* 393:461
- Papaderos P, Guseva NG, Izotov YI, Fricke KJ (2008) *A&A* 491:113
- Papovich C, Dickinson M, Giavalisco M, Conselice CJ, Ferguson Henry C (2005) *ApJ* 631: 101
- Peimbert A, Peimbert M (2010) *ApJ* 724:791
- Pringle JE (1981) *ARAA* 19:137
- Pustilnik SA, Lipovetsky VA, Izotov YuI, Brinks E, Thuan TX, Knyazev AYU, Neizvestnyi SI, Ugryumov AV (1997) *AstL* 23:308
- Pustilnik SA, Brinks E, Thuan TX, Lipovetsky VA, Izotov YI (2001) *AJ* 121:1413
- Pustilnik SA, Martin J-M, Huchtmeier WK, Brosch N, Lipovetsky VA, Richter GM (2002) *A&A* 389:405
- Putman ME, Bureau M, Mould JR, Staveley-Smith L, Freeman KC (1998) *AJ* 115:2345
- Rama S, Kantharia NG, Prabhu TP (2011) *ApJ* 728:124
- Read J, Gilmore G (2005) *MNRAS* 356:107
- Read JI, Goerdt T, Moore B, Pontzen AP, Stadel J, Lake G (2006) *MNRAS* 373:1451
- Recchi S, Matteucci F, D'Ercole A, Tosi M (2004) *A&A* 426:37
- Recchi S, Hensler G (2006) *A&A* 445:L39
- Revaz Y, Jablonka P, Sawala T, Hill V, Letarte B, Irwin M, Battaglia G, Helmi A, Shetrone MD, Tolstoy E, Venn KA (2009) *A&A* 501:18
- Roberts MS, Haynes MP (1994) *ARA&A* 32:115
- Sánchez-Salcedo FJ, Reyes-Iturbide J, Hernandez X (2006) *MNRAS* 370:1829
- Sandage A (1986) *A&A* 161:89
- Sargent WLW, Searle L (1970) *ApJ* 162:L155
- Schulte-Ladbeck RE, Crone MM, Hopp U (1998) *ApJ* 493:L23
- Searle L, Sargent WLW (1972) *ApJ* 173:25
- Silich S, Tenorio-Tagle G, Muñoz-Tuñón C, Cairos LM (2002) *AJ* 123:2438
- Simpson CE et al. (2011) *AJ* 142:82
- Spekkens K, Giovanelli R, Haynes MP (2005) *AJ* 129:2119
- Stil JM, Israel FP (2002) *A&A* 389:42
- Stinson GS, Dalcanton JJ, Quinn T, Kaufmann T, Wadsley J (2007) *ApJ* 667:170
- Stoughton C et al (2002) *AJ* 123:485
- Swaters RA, van Albada TS, van der Hulst JM, Sancisi R (2002) *A&A* 390:829
- Taylor C, Brinks E, Skillman ED (1993) *AJ* 105:128
- Taylor CL, Brinks E, Pogge RW, Skillman ED (1994) *AJ* 107:971
- Taylor CL, Thomas DL, Brinks E, Skillman ED (1996) *ApJS* 107:143
- Terlevich R, Melnick J (1981) *MNRAS* 195:839

- Thuan TX (1983) ApJ 268:667
Thuan TX, Martin GE (1981) ApJ 247:823
Thuan TX, Izotov YI (1997) ApJ 489:623
Thuan TX, Izotov YI, Lipovetsky VA (1997) ApJ 477:661
Thuan TX, Izotov YI, Foltz CB (1999) ApJ 525:105
Thuan TX, Hibbard JE, Levrier F (2004) AJ 128:617
Valenzuela O, Rhee G, Klypin A, Governato F, Stinson G, Quinn T, Wadsley J (2007) ApJ 657:773
van Eymeren J, Trachternach C, Koribalski BS, Dettmar R-J (2009) A&A 505:1
van Zee L, Westpfahl D, Haynes MP, Salzer JJ (1998a) AJ 115:1000
van Zee L, Skillman ED, Salzer JJ (1998b) AJ 116:1186
van Zee L, Salzer JJ, Skillman ED (2001) AJ 122:121
Wang J-M, Yan C-S, Li Y-R, Chen Y-M, Xiang F, Hu C, Ge J-Q, Zhang S (2009) ApJL 701:7
Wilcots EM, Miller BW (1998) AJ 116:2363
Zackrisson E, Bergvall N, Marquart T, Östlin G (2006) A&A 452:857
Zhang H-X, Hunter DA, Elmegreen BG, Gao Y, Schruba A (2012) AJ 143:47
Zhang X, Buta RJ (2007) In galaxy evolution across the hubble time. Combes F, Palous J (eds)
Proceedings of the UAU Symposium 235:184
Zhao Y, Gu Q, Gao Y (2011) AJ 141:68

Chapter 5

Summary

Abstract Putting together all of the findings from this thesis work, and taking into account the recent development in the literature, here we summarize our thoughts on the disk evolution of nearby dwarf galaxies, and try to offer some concluding remarks.

5.1 Main Findings of This Thesis Work

Nearby dwarf galaxies, especially the relatively low-mass ones ($M_{\star} \lesssim 10^8 M_{\odot}$), in the field have star formation (SF) activities that become more and more centrally concentrated over time. Both the internal mechanisms, such as stellar feedback, and the external mechanisms, such as tidal interaction, may contribute to the outside-in shrinking trend of the star-forming disks of dwarf galaxies. In accordance with this spatially evolving SF activities with time, down-bending stellar mass surface density profiles accompany down-bending SF surface density profiles.

In line with the trend of stellar disk evolution, the cold gas component, which is the fuel for SF, is also proportionally more concentrated toward the central regions of dwarf galaxies. While the overall SF disk is shrinking with time, the star-forming activities toward the center of dwarf galaxies should exhibit a large stochasticity, because the gas disk scale length of dwarf galaxies might be comparable to the disk thickness which means that only a few star-forming clumps can be held spatially at any given time. While it is observationally clear that SF activities in dwarf galaxies can significantly influence the overall morphology of gas distribution, there is no correlation between the current SF rate (SFR) and the inertial-range power spectral indices of the intensity structures of the neutral atomic gas in dwarf galaxies, suggesting that the fine properties of the star-forming gas fuel component is apparently affected but not determined by the stellar feedback.

As extreme examples of dwarf irregular galaxies, the BCD galaxies also have their SF activities concentrated toward the galactic centers, but for a reason that is probably different from ordinary dwarf irregulars. The intense starburst of BCD galaxies can be ignited through dynamical friction exerted on massive clumps by disks and cold dark matter halo particles. The dynamically hot nature of dwarf galaxies favors higher

Jeans mass scales and thus relatively massive clumps. The centrally concentrated SF in ordinary dwarf irregulars might be regarded as residual and probably relatively weak SF activities throughout the lifetime of the galaxies, whereas the starburst in BCD galaxies might be better regarded as a rejuvenescent phase of SF throughout the lifetime of the galaxies.

5.2 Recent Development in the Literature

Dwarf galaxies play a crucial role in cosmic evolution, and they also provide an ideal testbed of the Λ CDM cosmological models. Numerous studies, either theoretically or observationally, on the topic of evolution of dwarf galaxies have been published since this thesis work was finished. Those observational studies, which are mostly focused on more massive galaxies than the typical galaxies in our sample, find a gradual change of radial stellar population gradients as a function of galaxy stellar masses, and this gradual change seems to naturally connect to our findings at the relatively low-mass end of dwarf galaxies. On the theoretical or simulation side, the most prevalent idea is that the internal feedback, which is most efficient in dwarf galaxies, might be responsible for many distinct properties (including the observed outside-in trend found in this thesis work) of dwarf galaxies. It is impossible to review all of those recent development; below we will only focus on four representative studies that are closely relevant to this thesis work.

5.2.1 Observational Studies

Based on full spectrum stellar population synthesis analysis of a sample of 105 galaxies from the three-dimensional spectroscopic survey CALIFA, Pérez et al. (2013) found that the well-known inside-out disk growth trend of galaxies gradually weakens from high-mass galaxies to low-mass galaxies, and galaxies less massive than $\sim 10^{10} M_{\odot}$ show a transition from inside-out to flat or even outside-in growth (Fig. 5.1). The lowest-mass galaxies analyzed in Pérez et al. (2013) have B -band magnitude brighter than -18 , which naturally connects with our findings for even lower mass dwarf galaxies.

Based on a large sample of 11,294 galaxies selected from the GALEX+SDSS combined photometric catalog of a volume-completed sample at redshift < 0.05 , Pan et al. (2015) measured both the integrated and central NUV- r colors, and they found that the fraction of galaxies with relatively blue cores increases as the galaxy stellar mass decreases (Fig. 5.2). This finding also points to a scenario that the main galaxy assembly mode might be transitioning from the inside-out mode at $M_{\star} > 10^{10.5} M_{\odot}$ to the outside-in mode at $M_{\star} < 10^{10} M_{\odot}$.

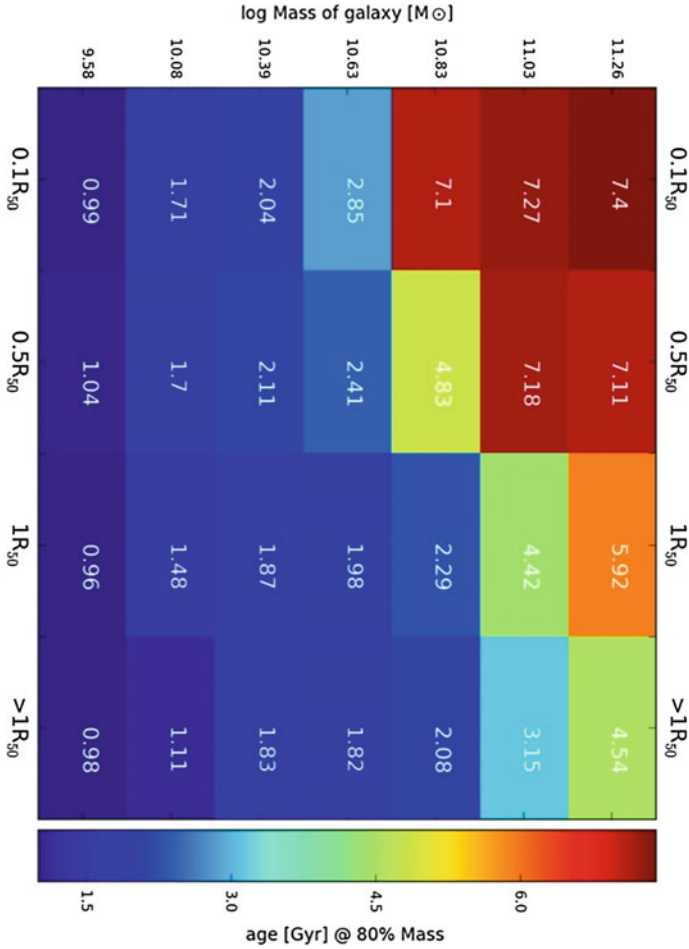


Fig. 5.1 Mean stellar age difference within different galactocentric distances (along the *horizontal axis*) of galaxies of different masses (along the *vertical axis*), based on the 3D spectroscopic survey—CALIFA—(Sánchez et al. 2012) of 105 galaxies. The radial distances annotated along the horizontal axis are in units half-light radius of galaxies. This diagram shows that more massive galaxies exhibit more remarkable inside-out disk growth trend, i.e., central regions are older than outer regions. However, moving from high-mass to low-mass galaxies, the inside-out trend gradually vanishes, with more or less flat radial age gradient for the lowest-mass bins. This figure is adapted from Pérez et al. (2013)

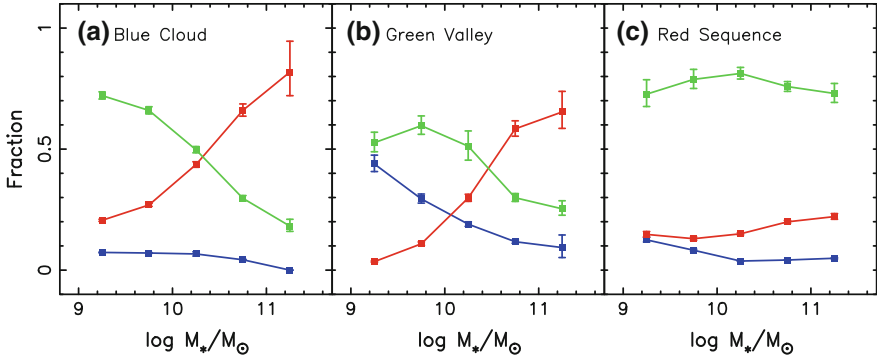


Fig. 5.2 The fraction of galaxies with blue cores (*blue*), flat color gradient (*green*), and red cores (*red*) as a function of galaxy stellar mass, based on a large sample of photometrically (GALEX+SDSS) selected galaxies at redshift <0.05 . The whole sample of galaxies is divided into three groups, i.e., blue cloud (*left*), green valley (*middle*), and red-sequence (*right*). This figure is adapted from Pan et al. (2015)

5.2.2 Theories and Numerical Simulations

Cosmic gas accretion might be important in sustaining a continuous SF over the Hubble time for most nearby disk galaxies. By assuming that the accreted gas (from halo condensation) has a lower specific angular momentum than the disk gas, Elmegreen et al. (2014) calculated the radial drift of the accreted gas and the resultant SF activities in a fountain model, and compared the prediction to the observed stellar and gas mass profiles of nearby dwarf irregulars and BCD galaxies (Fig. 5.3). As shown in Fig. 5.3, this simple toy model calculation fits the stellar and gas profiles of the BCD Haro 29 and dwarf irregular DDO 70 very well. However, the fit to NGC 1569 and NGC 3738 is not as good. Moreover, Elmegreen et al. (2014) found that the radial drift speed of gas/stellar disks is on the order of $\sim 1 \text{ km s}^{-1}$, and therefore this fountain-driven accretion model might not be an important mechanism for ordinary galaxies, with a possible exception of BCD galaxies.

Low-mass galaxies reside in low-mass dark matter halos that have shallow gravitational wells and low escape velocities, and thus their evolution can be more significantly influenced by stellar feedback than massive galaxies. Based on the FIRE (Feedback in Realistic Environments) numerical simulations, El-Badry et al. (2016) investigated the effects of stellar feedback and bursty SF on galaxies with stellar mass in range of $2 \times 10^6 - 5 \times 10^{10} M_\odot$. They found that the same stellar feedback mechanisms, which are thought to drive the formation of dark matter cores from a universal cuspy profile, might be also responsible for a significant radial migration of the newly formed stars that inherit the outflowing/infalling kinematics of gas. Stellar orbits expand and contract over short timescales, in response to the strong fluctuations of the galactic potential (Fig. 5.4). Over long timescales, the outward migration of stars, especially the older ones, lead to positive radial gradients of ages

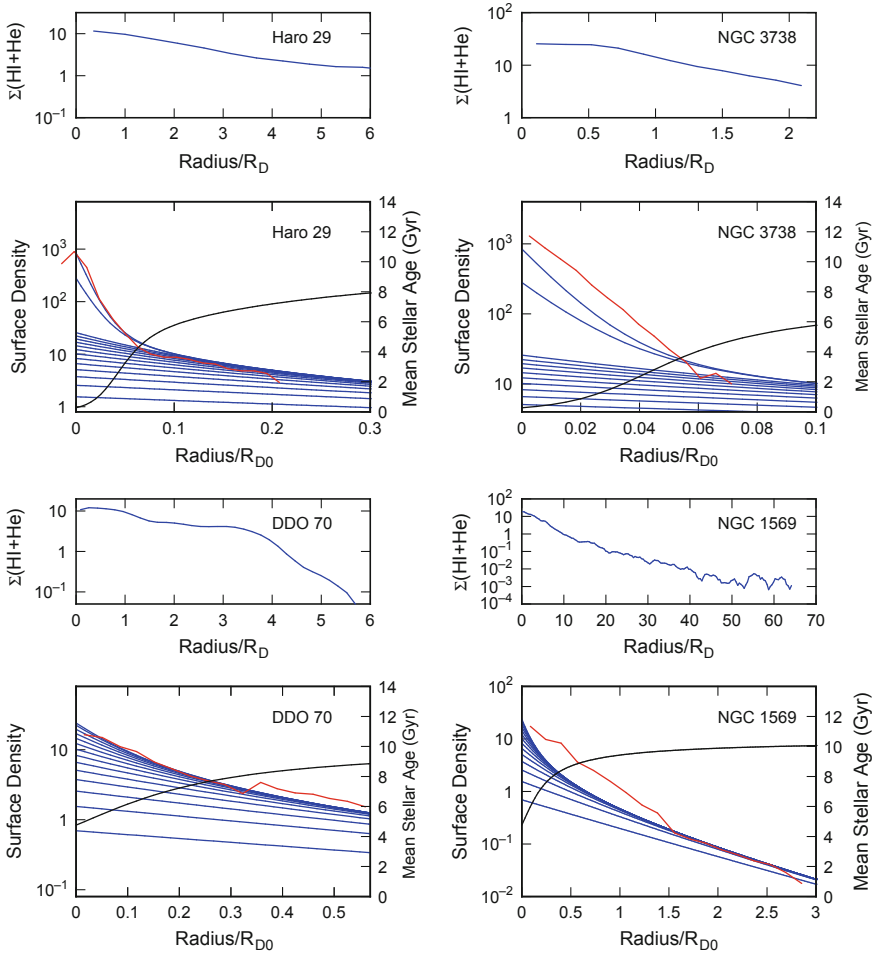


Fig. 5.3 A comparison between the mass surface density profiles in four centrally bursting galaxies (*red curves*, from Zhang et al. 2012) and models with radial accretion from low angular momentum cosmic gas (*blue curves*). The model curves increase over time as the stellar disk builds up, and they steepen toward the center as the gas disk which forms it shrinks. The radius in the models is normalized to the scale length of the initial disk, and in the observations it is varied to match the models. The vertical scale interval is the same for the models and observations. For the observations, the vertical scale is the mass surface density in units of $M_{\odot} \text{ pc}^{-2}$, while for the model, the vertical position has been adjusted to fit the observations. The *black curve* in each panel is the mean stellar age, using the scale on the right-hand axis. The deprojected HI+He gas mass surface density profiles are also shown, above each stellar profile, plotted in physical units of $M_{\odot} \text{ pc}^{-2}$ and with an abscissa equal to the ratio of the radius to the current V -band scale length. The HI+He gas mass surface density profiles extend much further than the stars in these gas-rich systems and they are not generally exponential like the stellar mass profiles. The figure is adopted from Elmegreen et al. (2014)

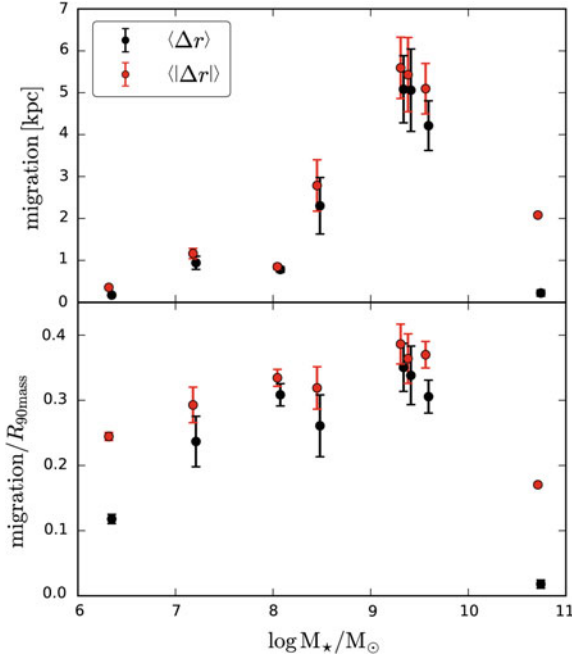


Fig. 5.4 Average radial migration of stars since their formation for all galaxies from the simulations of El-Badry et al. (2016). The top panel shows migration in units of kpc, and the bottom panel shows migration scaled by each galaxy’s 90%– M_{\odot} radius, $R_{90\text{mass}}$, at $z = 0$. *Black and red points* show average of the net and absolute radial distance, respectively, with a small horizontal offset for clarity. For each simulated galaxy, the point shows the average across 40 snapshots from $z = 0.2$ to 0, and error bars show the standard deviation across these snapshots, highlighting short-timescale variability. The highest- and lowest-mass galaxies have little short-time variability (error bars are smaller than points), because their stellar distribution does not change on short timescales. The most significant net outward radial migration occurs in galaxies with stellar masses $\approx 10^{7-9.6} M_{\odot}$. The highest- and lowest-mass galaxies show weaker systematic outward migration but do show nontrivial absolute radial migration (combination of inward and outward migration), especially when scaled to $R_{90\text{mass}}$. This significant absolute migration of the lowest-mass galaxy is likely the combined result of scattering and stars on radial but stable orbits, since the stellar distribution of these galaxies does not change on short timescales at late times. The figure is adopted from El-Badry et al. (2016)

and metallicities in the present-day dwarf galaxies. If this feedback-driven stellar migration is indeed the dominant mechanism in shaping the present-day profiles of stellar populations in dwarf galaxies, the radial SF histories inferred from present-day color gradients or color-magnitude variations can be remarkably biased, with the signature of real in situ SF history radial profiles being already largely erased by the radial migration. Nevertheless, we note that the remarkably stochastic fluctuation of stellar disks of dwarf galaxies in just a few hundred Myr, as predicted by the El-Badry et al. simulations, seems to be inconsistent with the observed tight correlation between

the size and mass of atomic gas disks of galaxies with atomic gas masses ranging from $\gtrsim 10^{11} M_{\odot}$ to $\lesssim 10^6 M_{\odot}$ (e.g., Broeils and Rhee 1997; Wang et al. 2016).

5.3 Closing Remarks

The observational studies of large samples of galaxies in the local universe suggest that the outside-in growth trend for low-mass galaxies might be primarily regulated by the internal stellar feedback, such as supernovae explosions. The energetic feedback from SF might be playing a central role in the formation and evolution of both the baryonic components and dark matter halos of dwarf galaxies, due to the much shallower gravitational potential wells of dwarf galaxies compared to massive galaxies. As is implied in the recent high-resolution simulations of isolated dwarf galaxies (Read et al. 2016), stellar feedback might hold the promise to solve at least two puzzling problems that apparently challenge the standard Λ CDM cosmological model, i.e., the “cusp/core problem” and the “too big to fail problem”. Future observational studies of larger and complete samples of dwarf galaxies down to a stellar mass of $\lesssim 10^7 M_{\odot}$ will be indispensable in firmly establishing the distribution of stellar population profiles in dwarf galaxies. More realistic numerical simulations with higher resolution will be also indispensable in firmly establishing the importance of various internal mechanisms, such as stellar scattering and stellar feedback, in regulating the properties of the baryonic components and dark matter particles of dwarf galaxies. A synergy between observations and simulations may hold the promise in understanding most of the distinct properties of dwarf galaxies, (probably) including the outside-in shrinking trend of SF in dwarf galaxies.

References

- Broeils AH, Rhee M-H (1997) *A&A* 324:877
El-Badry K, Wetzel A, Geha M et al (2016) *ApJ* 820:131. doi:[10.3847/0004-637X/820/2/131](https://doi.org/10.3847/0004-637X/820/2/131)
Elmegreen BG, Struck C, Hunter DA (2014) *ApJ* 796:110. doi:[10.1088/0004-637X/796/2/110](https://doi.org/10.1088/0004-637X/796/2/110)
Pan Z, Li J, Lin W et al (2015) *ApJ* 804:42. doi:[10.1088/2041-8205/804/2/L42](https://doi.org/10.1088/2041-8205/804/2/L42)
Pérez E, Cid Fernandes R, González Delgado RM (2013) *ApJ* 764:1. doi:[10.1088/2041-8205/764/1/L1](https://doi.org/10.1088/2041-8205/764/1/L1)
Read JI, Agertz O, Collins MLM (2016) *MNRAS* 459:2573
Sánchez SF, Kennicutt RC, Gil de Paz A et al (2012) *A&A* 538:8
Wang J, Koribalski BS, Serra P et al (2016) *MNRAS* 460:2143
Zhang H-X, Hunter DA, Elmegreen BG, Gao Y, Schrupa A (2012) *AJ* 143:47

Appendix A

Starburst Triggering Process in “Giant” Irregular Galaxies: Spiral–Spiral Merger

With imagery from *GALEX*, *HST*, *2MASS*, and *Spitzer*, and at the resolution of MIPS $24\ \mu\text{m}$ ($\sim 6''$), we study the variations of the broadband spectral energy distributions (SEDs) of star-forming regions within the nearest prototypical major merger—the Antennae galaxies. By including MIPS $24\ \mu\text{m}$ dust emission into stellar population analysis, we reliably, albeit roughly, constrain the star formation (SF) histories of these $24\ \mu\text{m}$ selected star-forming regions across the merging disks of the Antennae. Our population analysis is consistent with the SF scenario that most regions across the whole system are at a modest level of SF with the exception of some localized intense starburst sites in the well-known *overlap* regions and the *western-loop* regions of northern galaxy NGC 4038. Compared with all the other regions, the young *overlap* regions currently ($< 10\ \text{Myr}$) are experiencing much more violent enhancement of SF. Across the *overlap* regions, we suggest two sequential SF paths that we interpret as the imprints of the interpenetrating process of the two merging disks following their second close encounter. And we suggest that the SF in the southern and (especially) northwestern edges of the *overlap* zone may have been just triggered by pre-starburst shocks. The well-known mid-infrared “*hotspot*” in the *overlap* regions is also a “*hotspot*” at $4.5\ \mu\text{m}$, whose total $4.5\ \mu\text{m}$ emission ($\geq 80\%$ from both hot dust and atomic/molecular lines) is comparable with that of the two galactic nuclei.

A.1 Introduction

While dwarf irregular galaxies vastly outnumber the more massive star-forming galaxies, the rarer gas-rich giant irregular galaxies resulting from spiral–spiral mergers are the most intense sites of SF in the local universe (e.g., Gao 2008). Galaxy mergers, especially major mergers, can dramatically influence the morphological and star-forming properties of galaxies over relatively short timescales. Almost all the ultraluminous infrared galaxies (ULIRGs) — the strongest starbursts in the local Universe—are in interacting/merging systems (Sanders and Mirabel 1996).

Moreover, Conselice et al. (2003b) suggested that about two-thirds of submillimeter galaxies at $z > 1$ are undergoing major mergers. Galaxy interactions/mergers seem to be very frequent in the past (e.g., Le Fevre et al. 2000; Patton et al. 2002; Conselice et al. 2003a; Elbaz et al. 2003; Kartaltepe et al. 2007; Ravel et al. 2008; Lin et al. 2008; Conselice et al. 2009). Therefore, it is of great importance to understand how the burst of SF is triggered in the course of interacting/merging.

At a distance of 19.2 Mpc ($H_0 = 75 \text{ km s}^{-1} \text{ Mpc}^{-1}$),¹ the Antennae (NGC 4038/39, Arp 244) is the nearest prototypical major merger between two gas-rich spiral galaxies (Toomre and Toomre 1972; Hibbard et al. 2001). Thus, it provides us with a unique opportunity to study the induced SF process as a consequence of interaction in detail. It has been extensively studied at essentially all wavelengths from X-ray to radio (Hummel and van der Hulst 1986; Read et al. 1995; Vigroux et al. 1996; Mirabel et al. 1998; Nikola et al. 1998; Whitmore et al. 1999; Neff and Ulvestad 2000; Wilson et al. 2000; Fabbiano et al. 2001; Gao et al. 2001; Hibbard et al. 2001; Fabbiano et al. 2003, 2004; Wang et al. 2004; Hibbard et al. 2005; Mengel et al. 2005; Bastian et al. 2006; Gilbert and Graham 2007; Schulz et al. 2007; Brandl et al. 2009). *ISO* mid-infrared (MIR) observations (Mirabel et al. 1998) show that the most intense starburst in this system takes place in the so-called *overlap* region between the two nuclei, which indicates its intermediate merging stage, almost totally obscured in the optical. Considering the abundant molecular gas, widespread SF and overall modest SF efficiency, Gao et al. (2001) argued that Arp 244 has the potential of producing an ultraluminous extreme starburst in a later stage of merging.

In the Antennae, observations with *HST* have identified thousands of super star clusters (SSCs) (Whitmore et al. 1999) possibly being formed as part of the merging process. Both theoretical predictions (Goodwin et al. 2006) and observations (Whitmore 2004; Fall et al. 2005; Mengel et al. 2005) suggest that many of these SSCs will dissolve rapidly into the field stellar population in the course of galaxy–galaxy merging. This process was coined as star cluster’s “*infant mortality*” (Whitmore 2004). Furthermore, a large number of stars may not form in star cluster mode. In fact, star clusters found in the deep *HST* images only contribute 9, 8, 5, and 7% of the apparent total *U*, *B*, *V*, and *I* band light of the Antennae (Whitmore and Zhang 2002). Due to the uncertainties on the cluster formation history and efficiency, recently Bastian et al. (2009) pointed out the difficulty in the accurate understanding of the age distribution of star clusters in mergers like the Antennae. Therefore, in order to obtain a complete picture of SF histories in the course of merging, we must study the extended stellar populations, in addition to these star clusters.

Evolutionary population synthesis has become a powerful tool of interpretation of the integrated spectrophotometric observations of galaxies and sub-galactic regions. The most common method of model-observation comparison for stellar population analysis in galaxies is SED-fitting, with either least-squares or chi-squared

¹We note the recent debate about the distance to the Antennae. Saviane et al. (2008) determined a distance of ~ 13.3 Mpc from the tip of red giant branch, whereas Schweizer et al. (2008) estimated a distance of ~ 22.3 Mpc based on the type Ia supernovae 2007sr light curve. Throughout this work, we assumed the traditionally adopted Hubble flow distance. However, our conclusions are not affected by the controversy over the distance.

minimization technique (e.g., Kong et al. 2000; Gavazzi et al. 2002). However, the well-known age-extinction degeneracy problem prevents us from obtaining reliable information about the SF history for these galaxies or their sub-galactic regions, especially when only broadband photometry data are available. This is because these extended regions have an unknown mixture of various stellar populations, and the different populations may experience totally different extinctions (Calzetti et al. 1994; Charlot and Fall 2000).

With the inclusion of the high-quality and high-resolution *Spitzer* 24 μm dust emission data in our population analysis, we show here that the degeneracy between stellar population and dust extinction can be broken to a great extent. Thus, for the first time, we can reliably, albeit roughly, constrain the SF histories within the Antennae galaxies using SEDs over the whole spectral range from far-UV (FUV) to mid-infrared (MIR). The outline of this paper is as follows: In Sect. A.2 we introduce the multiband data that we use in this study, and give the multiwavelength photometry of star-forming regions selected mainly from the 24 μm image. Sect. A.3 gives some brief comparisons of the broadband SEDs and their variations across the whole system. Sect. A.4 presents our methodology to constrain the SF histories across the merging disks, and the main results of our population analysis. We discuss these results in Sect. A.5 and then a summary of our main findings follows in Sect. A.6.

A.2 Data and Photometry

A.2.1 Data

Both FUV ($\sim 1516 \text{ \AA}$) and near-UV (NUV; $\sim 2267 \text{ \AA}$) images were derived from the *GALEX* Ultraviolet Atlas of Nearby Galaxies distributed by Gil de Paz et al. (2007). The FWHMs of the PSFs are $5''$ and $6''$ at FUV and NUV, respectively. With these data, Hibbard et al. (2005) have studied the stellar populations of the famous tidal regions.

Four broadband (F336W, F439W, F555W, F814W) and one narrowband (F658N; $\text{H}\alpha$) images (Whitmore et al. 1999) taken with the WFPC2 aboard the *HST* were obtained as B associations from the MAST Archive,² and a mosaic containing the four chips for each image was created.

NIR *JHKs* atlas images from *2MASS* were retrieved through the Interactive *2MASS* Image Service.³

The *Spitzer* imagery (3.6, 4.5, 5.8, 8.0, 24 μm) of the Antennae was obtained with both the Infrared Array Camera (IRAC; Fazio et al. 2004) and the multiband imaging photometer for *Spitzer* (MIPS; Rieke et al. 2004) on board the *Spitzer Space*

²<http://archive.stsci.edu/hst/wfpc2/search.html>.

³<http://irsa.ipac.caltech.edu/applications/2MASS/IM/interactive.html>.

Telescope. The basic calibrated data were retrieved with the Leopard software.⁴ Background matching, cosmic-ray removal, flat-fielding, and mosaicking were performed using the Spitzer Science Center’s reduction software package MOPEX.⁵ Images of the four IRAC bands have previously been presented by Wang et al. (2004).

A.2.2 Region Selection and Photometry Extraction

Prior to our multiwavelength photometry comparison and extraction, all images were background subtracted, registered/aligned, and resampled to the same pixel scale (1.5”). Then all images (except FUV/NUV) are convolved to the same resolution of MIPS 24 μm with the convolution kernels provided by Gordon et al. (2008).

We selected star-forming regions primarily as 24 μm emission peaks, since 24 μm has been shown to be a very good local tracer of current SF (e.g., Calzetti et al. 2005). Practically, we first used the *IRAF*⁶ DAOFIND task in the DAOPHOT stellar photometry package (Stetson 1987) to find all local emission enhancements with 10 σ signal-to-noise (S/N) ratio threshold in the 24 μm image. Then we examined the findings of local enhancements visually and checked carefully to ensure that these previously detected enhancements are true star-forming regions rather than artifacts due to the Airy diffraction rings or spikes. We also included three additional FUV bright regions without any nearby 24 μm peaks associated (regions 11, 12, and 32). Finally, a total of 34 nearly non-overlapping circular apertures of 9” (~ 800 pc) in diameter (Fig. A.1) were selected. The large aperture size is mainly dictated by the PSF of 24 μm and the rather extended emission features for most regions.

Our aperture size for photometry is, in any sense, significantly larger than a typical H II region (Knapen 1998; Oey et al. 2003), and even larger than a typical central star-forming region of a starburst galaxy. However, as was already found by Zhang et al. (2001), the spatial distribution of the young star clusters tends to be correlated up to a physical scale of $\sim \text{kpc}$. Bastian et al. (2006) have studied several star cluster complexes with sizes up to several hundred parsecs in the Antennae, they found that the young cluster complexes often share the same general velocity distribution with associated giant molecular clouds (GMCs), and even some complexes themselves are clustered. Our star-forming regions are usually spatially resolved into one or few such bright star cluster complexes dominated by few bright star clusters on the high-resolution optical/NIR imaging (e.g., Whitmore et al. 1999; Mengel et al. 2005). Therefore, most of our regions should be complexes of star clusters over extended background stellar populations. We note that some regions show slight, yet not systematic, displacement ($\sim 1 - 2''$) between the 24 μm and the associated FUV

⁴ Available at <http://ssc.spitzer.caltech.edu/prookit/spot/>.

⁵ <http://ssc.spitzer.caltech.edu/postbcd/download-mopex.html>.

⁶ *IRAF* is distributed by the National Optical Astronomy Observatories, which are operated by the Association of Universities for Research in Astronomy, Inc., under cooperative agreement with the National Science Foundation.

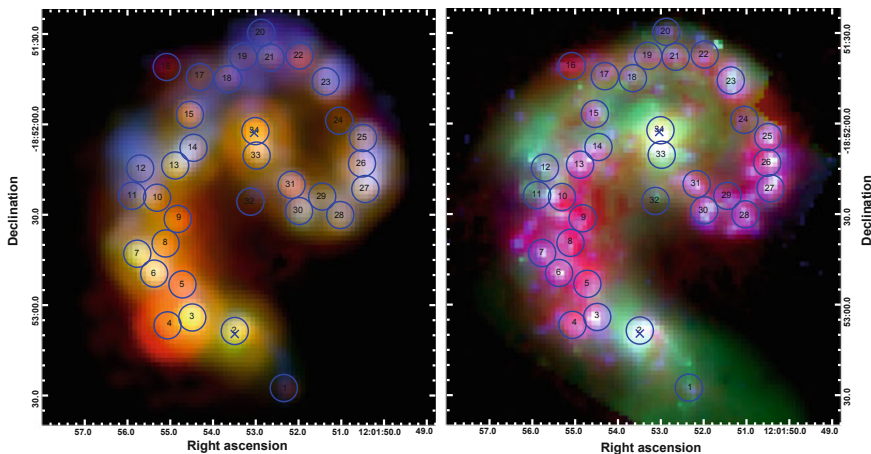


Fig. A.1 *Left* circular apertures of $9''$ in diameter were selected mainly as $24\mu\text{m}$ peaks and superposed on color-composite images generated from MIPS $24\mu\text{m}$ (red), *HST* $\text{H}\alpha$ (green), and *GALEX* FUV (blue) maps of the Antennae. The *HST* $\text{H}\alpha$ map has been degraded to match the resolution of MIPS $24\mu\text{m}$. The cross signs mark the nuclear centers of the two colliding galaxies. Pixel scales are $1.5''$. *Right* color-composite image generated from the IRAC $8\mu\text{m}$ (red), *HST* F814W (green) and $\text{H}\alpha$ (blue) maps at their original resolutions (resampled to $1.5''$ pixel scales). The pixel scales of the two figures are $1.5''$. The original resolution of IRAC $8\mu\text{m}$ is $\sim 2''$. The mosaicked *HST* images originally have $\sim 0.1''$ pixels (undersampled). At the adopted distance, $1''$ corresponds to ~ 93 pc. The figure is adapted from Zhang et al. (2010)

peaks. The displacement may indicate that IR and UV emission are dominated by different clusters within these regions.

Although the measured FWHMs of the *GALEX* PSFs are close to that of the PSFs in MIPS $24\mu\text{m}$ images, we apply point source aperture corrections to FUV ($\times 1.206$), NUV ($\times 1.269$), and other bands ($\times 1.982$). Aperture corrections are determined from photometry with increasing aperture radii of isolated field stars in the image fields. All the fluxes have been corrected for foreground Galactic extinction using a value of $E(B-V) = 0.046$ Schlegel et al. (1998) and Cardelli et al. (1989) extinction law with $R_V = 3.1$. The uncertainties assigned to the photometric values are a quadratic sum of three contributions: variance of the local background, photometric calibration uncertainty (5% for FUV and WFPC2, 3% for NUV, 10% for IRAC, and 4% for $24\mu\text{m}$), and poisson statistics noise. The multiband photometry of these 34 regions is listed in Table A.1.

Table A.1 Aperture photometry of the 34 regions studied in this work

Reg.	FUV (1)	NUV (2)	F336W (3)	F439W (4)	F555W (5)	F814W (6)	J (7)	H (8)	K _s (9)	4.5 μ m (10)	5.8 μ m (11)	7.9 μ m (12)	24 μ m (13)	H α (14)	H α (15)	H α (16)
1	-12.98±0.05	-13.44±0.03	-14.37±0.06	-15.32±0.05	-16.01±0.05	-16.67±0.05	-17.33±0.07	-17.44±0.06	-17.22±0.06	-16.54±0.11	-16.04±0.11	-17.58±0.11	-18.37±0.11	-17.38±0.11	-17.64±0.04	39.18±0.02
2	-13.85±0.05	-14.52±0.03	-15.46±0.05	-16.34±0.05	-17.07±0.05	-17.84±0.05	-18.61±0.04	-18.83±0.03	-18.61±0.03	-18.04±0.11	-17.58±0.11	-18.37±0.11	-19.34±0.11	-19.34±0.11	-20.59±0.04	40.38±0.01
3	-13.97±0.05	-14.71±0.03	-15.61±0.05	-16.05±0.05	-16.64±0.05	-17.13±0.05	-17.74±0.06	-17.43±0.05	-17.74±0.05	-17.59±0.11	-17.46±0.11	-18.95±0.11	-19.91±0.11	-18.95±0.11	-22.36±0.04	40.64±0.01
4	-12.92±0.05	-13.61±0.03	-14.49±0.06	-15.05±0.06	-15.91±0.05	-16.54±0.05	-17.24±0.08	-17.43±0.06	-17.43±0.06	-17.57±0.11	-17.63±0.11	-18.99±0.11	-20.17±0.11	-18.99±0.11	-21.29±0.04	40.16±0.01
5	-12.87±0.05	-13.52±0.03	-14.71±0.06	-15.02±0.06	-15.86±0.05	-16.55±0.05	-17.29±0.07	-17.51±0.05	-17.62±0.05	-17.36±0.11	-17.36±0.11	-19.04±0.11	-20.09±0.11	-19.04±0.11	-21.29±0.04	40.16±0.01
6	-14.36±0.05	-14.85±0.03	-15.39±0.05	-15.46±0.05	-16.05±0.05	-16.55±0.05	-17.29±0.07	-17.50±0.06	-17.45±0.05	-17.65±0.11	-17.23±0.11	-18.92±0.11	-20.07±0.11	-20.07±0.11	-21.38±0.04	40.5±0.0
7	-14.09±0.05	-14.58±0.03	-15.23±0.05	-15.34±0.06	-15.98±0.05	-16.42±0.05	-17.16±0.08	-17.35±0.06	-17.22±0.06	-17.22±0.06	-16.85±0.11	-18.37±0.11	-19.53±0.11	-19.53±0.11	-20.66±0.04	40.48±0.0
8	-12.24±0.06	-12.46±0.03	-13.96±0.06	-14.07±0.06	-15.39±0.05	-16.27±0.05	-17.24±0.08	-17.48±0.07	-17.53±0.06	-17.33±0.11	-16.99±0.11	-18.44±0.11	-19.65±0.11	-19.65±0.11	-20.83±0.04	40.21±0.0
9	-11.72±0.05	-12.19±0.03	-13.57±0.05	-13.96±0.05	-15.96±0.05	-16.32±0.05	-16.71±0.05	-17.29±0.07	-17.44±0.06	-17.51±0.06	-17.00±0.11	-18.44±0.11	-19.55±0.11	-19.55±0.11	-20.5±0.04	39.98±0.01
10	-14.78±0.05	-15.18±0.03	-15.98±0.05	-16.43±0.05	-16.67±0.05	-17.02±0.05	-17.58±0.06	-17.72±0.05	-17.85±0.05	-17.18±0.11	-16.33±0.11	-17.56±0.11	-18.64±0.11	-18.64±0.11	-19.06±0.04	39.89±0.01
11	-14.84±0.05	-15.45±0.03	-15.71±0.05	-16.09±0.05	-16.38±0.05	-16.88±0.05	-17.04±0.05	-17.84±0.05	-17.44±0.11	-17.44±0.11	-16.39±0.11	-17.62±0.11	-18.64±0.11	-18.64±0.11	-19.05±0.04	39.91±0.01
12	-15.29±0.05	-15.45±0.03	-15.69±0.05	-16.06±0.05	-16.49±0.05	-16.98±0.05	-17.04±0.05	-17.94±0.05	-17.74±0.05	-17.44±0.11	-16.97±0.11	-18.32±0.11	-19.15±0.11	-19.15±0.11	-20.16±0.04	40.34±0.01
13	-14.36±0.05	-14.7±0.03	-15.22±0.05	-16.42±0.05	-16.95±0.05	-17.61±0.06	-17.75±0.06	-17.85±0.05	-17.74±0.05	-17.44±0.11	-16.97±0.11	-18.32±0.11	-19.15±0.11	-19.15±0.11	-20.16±0.04	40.23±0.01
14	-12.73±0.05	-13.19±0.03	-14.18±0.06	-15.25±0.05	-15.62±0.05	-16.14±0.05	-16.76±0.09	-16.94±0.08	-16.61±0.08	-17.16±0.11	-16.64±0.11	-17.85±0.11	-18.79±0.11	-18.79±0.11	-19.81±0.04	39.96±0.01
15	-15.56±0.05	-15.96±0.03	-16.25±0.05	-16.23±0.05	-16.72±0.05	-17.34±0.07	-17.43±0.06	-17.18±0.06	-16.79±0.11	-15.91±0.11	-15.91±0.11	-17.35±0.11	-18.36±0.11	-18.36±0.11	-19.37±0.04	39.23±0.01
16	-14.64±0.05	-14.91±0.03	-15.33±0.05	-16.11±0.05	-16.38±0.05	-16.85±0.05	-17.51±0.07	-17.33±0.06	-16.86±0.11	-16.32±0.11	-16.32±0.11	-18.52±0.11	-18.52±0.11	-18.52±0.11	-18.68±0.04	39.56±0.01
17	-14.44±0.05	-14.7±0.03	-15.21±0.05	-15.98±0.05	-16.21±0.05	-16.64±0.05	-17.22±0.08	-17.33±0.06	-16.72±0.11	-16.14±0.11	-16.14±0.11	-17.37±0.11	-18.41±0.11	-18.41±0.11	-18.37±0.04	39.59±0.01
18	-14.03±0.05	-14.39±0.03	-15.08±0.05	-15.84±0.05	-16.0±0.05	-16.35±0.05	-16.89±0.09	-16.91±0.08	-16.69±0.08	-16.16±0.11	-15.74±0.11	-16.73±0.11	-17.62±0.11	-17.62±0.11	-17.85±0.04	39.52±0.01
19	-14.67±0.05	-14.93±0.03	-15.33±0.05	-16.02±0.05	-16.23±0.05	-16.67±0.05	-17.27±0.07	-17.27±0.06	-16.76±0.11	-16.24±0.11	-16.24±0.11	-17.49±0.11	-18.55±0.11	-18.55±0.11	-18.73±0.04	39.71±0.01
20	-14.09±0.05	-14.45±0.03	-15.11±0.05	-15.9±0.05	-16.18±0.05	-16.66±0.05	-17.28±0.07	-17.37±0.06	-17.12±0.06	-16.75±0.11	-16.26±0.11	-17.5±0.11	-18.36±0.11	-18.36±0.11	-19.3±0.04	39.69±0.01
21	-15.49±0.05	-15.76±0.03	-15.86±0.05	-16.39±0.05	-16.53±0.05	-16.92±0.05	-17.55±0.07	-17.51±0.06	-17.54±0.05	-17.16±0.11	-16.69±0.11	-17.95±0.11	-19.0±0.11	-19.0±0.11	-19.26±0.04	39.94±0.01
22	-12.11±0.05	-12.85±0.03	-14.43±0.06	-15.22±0.05	-15.78±0.05	-16.51±0.05	-17.33±0.07	-17.42±0.06	-16.83±0.11	-16.32±0.11	-16.32±0.11	-17.53±0.11	-18.65±0.11	-18.65±0.11	-18.69±0.04	39.58±0.01
23	-14.38±0.05	-14.86±0.03	-15.65±0.05	-15.94±0.05	-16.16±0.05	-16.57±0.05	-17.28±0.07	-17.42±0.06	-17.21±0.06	-16.56±0.11	-16.56±0.11	-18.11±0.11	-19.2±0.11	-19.2±0.11	-19.6±0.04	40.08±0.01
24	-15.65±0.05	-15.91±0.03	-16.25±0.05	-16.43±0.05	-16.48±0.05	-16.71±0.05	-17.26±0.07	-17.37±0.06	-17.21±0.06	-16.8±0.11	-16.8±0.11	-18.5±0.11	-19.62±0.11	-19.62±0.11	-20.25±0.04	40.31±0.01
25	-15.65±0.05	-15.91±0.03	-16.15±0.05	-16.32±0.05	-16.36±0.05	-16.53±0.05	-17.0±0.08	-17.04±0.07	-16.89±0.07	-16.84±0.11	-16.49±0.11	-18.21±0.11	-19.38±0.11	-19.38±0.11	-20.15±0.04	40.32±0.0
26	-15.56±0.05	-15.41±0.03	-15.46±0.05	-15.75±0.05	-15.96±0.05	-16.26±0.05	-16.78±0.09	-16.88±0.08	-16.58±0.11	-16.32±0.11	-16.32±0.11	-17.91±0.11	-19.04±0.11	-19.04±0.11	-19.5±0.04	40.11±0.01
27	-14.24±0.05	-14.7±0.03	-15.37±0.05	-15.72±0.05	-16.0±0.05	-16.4±0.05	-17.01±0.08	-17.1±0.07	-16.96±0.07	-16.55±0.11	-16.55±0.11	-17.85±0.11	-19.1±0.11	-19.1±0.11	-19.6±0.04	40.14±0.01
28	-14.39±0.05	-14.98±0.03	-15.56±0.05	-15.92±0.05	-16.22±0.05	-16.55±0.05	-17.09±0.08	-17.2±0.07	-16.96±0.07	-16.55±0.11	-16.55±0.11	-17.93±0.11	-19.1±0.11	-19.1±0.11	-19.38±0.04	40.06±0.01
29	-13.74±0.05	-14.37±0.03	-15.35±0.05	-15.88±0.05	-16.22±0.05	-16.72±0.05	-17.36±0.06	-17.42±0.06	-16.96±0.11	-16.55±0.11	-16.55±0.11	-18.05±0.11	-19.14±0.11	-19.14±0.11	-20.1±0.04	40.06±0.01
30	-13.0±0.05	-14.37±0.03	-14.46±0.06	-15.18±0.06	-15.95±0.05	-16.57±0.05	-17.21±0.08	-17.32±0.06	-17.03±0.07	-16.58±0.11	-16.58±0.11	-17.24±0.11	-18.24±0.11	-18.24±0.11	-18.3±0.04	39.36±0.01
31	-14.0±0.05	-14.62±0.03	-15.59±0.05	-16.41±0.05	-16.94±0.05	-17.67±0.05	-18.44±0.06	-17.92±0.11	-17.38±0.11	-17.38±0.11	-18.61±0.11	-19.72±0.11	-19.72±0.11	-19.72±0.11	-20.72±0.04	40.17±0.01
32	-13.0±0.05	-13.93±0.03	-15.3±0.05	-16.39±0.05	-17.06±0.05	-17.94±0.05	-18.75±0.05	-18.79±0.03	-18.79±0.03	-18.26±0.11	-17.84±0.11	-19.8±0.11	-19.8±0.11	-19.8±0.11	-21.37±0.04	40.18±0.01

Note—Multiband photometry of the 34 apertures of 9-arcsec in diameter each. Except for H α , which is in units of $\log[\text{erg s}^{-1}]$, all the other columns of photometry are the absolute AB magnitude, assuming a distance modulus of 31.42. Note that the photometry has been corrected for a Milky Way reddening E(B-V) of 0.046 mag

A.3 Broadband SEDs

Figure A.2 shows the broadband SEDs for some representative regions across the Antennae galaxies as compared to that of the entire Arp 220 system and the local HII galaxy NGC 2798 (Kinney et al. 1993). There are some very remarkable differences of the SEDs between different regions across the whole system of the Antennae galaxies.

In the IR dust emission bands, $24\ \mu\text{m}$ very small grains (VSGs) and $8\ \mu\text{m}$ PAH emission (for high-metallicity regions) show a very good correlation with extinction-corrected hydrogen recombination emission from starburst regions of normal galaxies to luminous IR galaxies (LIRGs) and ULIRGs (Alonso-Herrero et al. 2006; Calzetti et al. 2007). Nevertheless, the $8\ \mu\text{m}$ PAH emission is progressively depressed relative to $24\ \mu\text{m}$ with increasing SF intensities (e.g. Calzetti et al. 2005; Smith et al. 2007; Draine and Li 2007; Thilker et al. 2007). Hence, the $24/8\ \mu\text{m}$ ratio would give a rough manifestation of different strengths of *current* SF activities across the whole system.

Obviously, the *overlap* regions (3–9) generally have higher $24/8\ \mu\text{m}$ ratios than other regions in the Antennae, meaning that the *overlap* regions are the most intense *current* star-forming sites. *Spitzer* IRS spectra (Brandl et al. 2009) also show that the *overlap* regions have overall the weakest relative strength (normalized to $15\ \mu\text{m}$ continuum flux) of PAH features among all these star-forming regions. High-resolution Optical and NIR observations (Whitmore et al. 1999; Mengel et al. 2005) suggest that the *overlap* regions host most of the youngest clusters. Region 4, which hosts the well-known MIR “*hotspot*” (Mirabel et al. 1998) of the *overlap* regions, has the highest $24/8\ \mu\text{m}$ ratios, even comparable with that of Arp 220. High-quality MIR spectra (Brandl et al. 2009) obtained from *Spitzer* IRS more clearly show that region 4 is characterized by very hot dust emission and is among the regions with the strongest strength of the radiation field. The intrinsically brightest star cluster (WS95-80, Whitmore and Schweizer 1995) coincides with region 4.

The regions 16–22 in the *northern* galaxy NGC 4038 have the lowest $24/8\ \mu\text{m}$ ratios and reddest *UB* colors as compared with other regions, which is consistent with the fact that a large number of rather old (100–500 Myr) star clusters are found there (Whitmore et al. 1999; Mengel et al. 2005).

In the UV wavebands, on the contrary, the *Western-loop* regions 22–32 have the strongest UV emissions, largest UV excesses, and relatively strong $8\ \mu\text{m}$ (PAH) emissions, yet low $24/8\ \mu\text{m}$ ratios. These are in contrast with those in the *overlap* regions and indicate their relatively late SF stage, which is also evidenced by the large $\text{H}\alpha$ bubbles found there (Whitmore et al. 1999). Brandl et al. (2009) also presents the IRS spectra of the UV brightest region 26, which has significantly weaker strength of the radiation field, yet stronger PAHs emission features, than do the *overlap* regions, in agreement with our broadband analysis.

The circumnuclear star-forming region of NGC 4038, namely region 33, has $24/8\ \mu\text{m}$ ratio close to that of the *overlap* regions, suggesting its intense *current* SF activity. The prominent, yet redder, UV emission reveals that this region may also

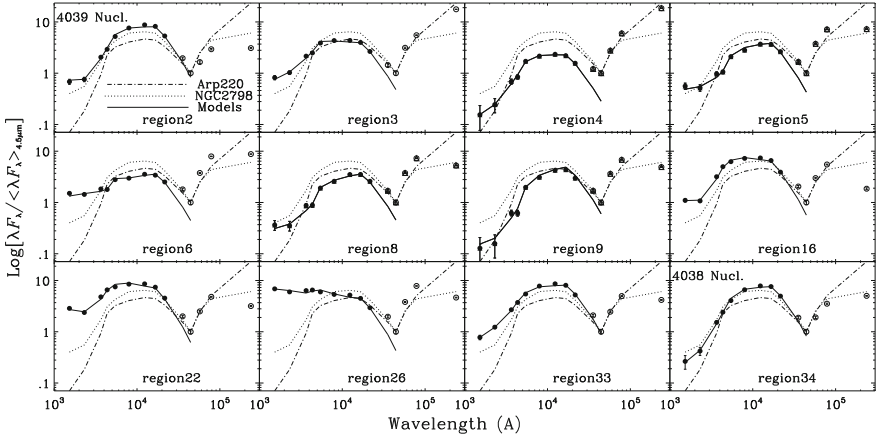


Fig. A.2 Display of FUV-24 μm broadband SEDs of some representative star-forming regions marked in Fig. A.1 and compared to Arp 220 and local HII galaxy NGC 2798. The broadband photometry data points from FUV to K_s , which are fitted with 3-SSP superpositions, are represented by filled circles and the *Spitzer* data points by open circles. For the purpose of comparison, the broadband WPC2 data have been transformed to standard *UBVI* system with the transformation coefficients provided by Holtzman et al. (1995). The best-fit (FUV- K_s) composite stellar broadband SED models have been plotted as solid lines. The figure is adapted from Zhang et al. (2010)

hold large post-starburst (> 10 Myr) stellar populations. For the two nuclei regions, NGC 4039 has both weaker 8 μm PAH emission and 24 μm dust emission indicating its lower SF activity, whereas NGC 4038 has almost the same broadband SEDs as that of the local HII galaxy NGC 2798 in the plotted wavelength range. Thus far, there is no strong evidence for the presence of AGN activity in the two nuclei. The IRS spectrum (Brandl et al. 2009) suggest that both nuclei regions have significantly weaker strength of the radiation field than the *overlap* regions. In comparison with the southern nucleus region, the northern nucleus region has flatter MIR continuum, stronger PAHs fluxes, yet smaller PAHs equivalent widths. These are consistent with our broadband analysis, i.e., both nuclei regions have weak *current* SF strength compared to the *overlap* starburst regions, and the southern nucleus region has even weaker current SF strength than does the northern nucleus. The stronger high excitation lines in the southern nucleus region (Brandl et al. 2009) should be attributed to supernovae shocks, which are also strongly evidenced by its very steep radio spectrum (Neff and Ulvestad 2000). We point out that our apertures covering the two nuclei (regions 2, 34) are so large that the surrounding star-forming regions are also included.

When we examine the SEDs variations across the *overlap* regions, we see an interesting phenomenon. From the central regions, i.e., regions 6 and 7, to both the northwestern (e.g. regions 8, 9) and southeastern (e.g. regions 4) regions, the UV/optical emission gradually become redder and weaker, accompanying by a comparable amount of the energy fraction reemitted as IR dust emission. In the following

sections, we show that the obvious trends of the SEDs variations across the *overlap* regions may reflect the SF modes in the *overlap* regions.

A.4 Stellar Population Analysis

A.4.1 Methodology

The availability of $H\alpha$ and MIPS $24\mu\text{m}$, which traces the SF (unobscured and obscured) on timescales of ~ 10 Myr, FUV and NUV (tracing SF on timescales of ~ 100 Myr), and the $U(F336W)$ and $B(F439W)$, whose combination in U/B ratio is sensitive (straddles the 4000 \AA break) to the fraction of populations younger than a few hundred Myr relative to the old populations, makes it reasonable to roughly probe the SF histories across the whole merging disks of the Antennae. With χ^2 minimization technique, we fit the broadband SEDs (FUV- K_s) plus the narrowband $H\alpha$ photometry for the above selected star-forming regions with superpositions of three single stellar populations (SSPs), namely young (< 10 Myr), intermediate (10–300 Myr), and old (> 300 Myr) populations. In our fitting, we account for the different extinctions experienced by different populations.

For population synthesis models, we use the new version Starburst99 (Vazquez and Leitherer 2005) SSP models with the Padova 2000 stellar evolution tracks, which include the full AGB evolution. We adopt the multipower law Kroupa initial mass function (Kroupa 2002). Adoption of the bottom-heavy Salpeter IMF would not change our main conclusions in this paper. Using the metallicity sensitive Mg I line at 8806.8 \AA , Mengel et al. (2002) found a handful of star clusters in Arp 244 with solar metallicity, which is consistent with recent metallicity estimates (Bastian et al. 2009) from more absorption and emission lines in the Antennae. Thus, we fix solar metallicity for all the SSPs models. Since we have narrowband $H\alpha$ imagery data, and the regions we studied are all actively star-forming regions, we include gaseous emission into the SSP models. Besides the nebular continuum emission and several hydrogen emission lines provided by Starburst99, we also account for other strong hydrogen emission lines (i.e., Balmer, Paschen, Brackett and Pfund lines) assuming case B recombination and strong non-hydrogen element emission lines using the line ratios of typical Galactic HII regions compiled by Anders and Fritze (2003).

For dust extinction, we use the two-phase dust attenuation recipes developed by Charlot and Fall (2000). The effective absorption curve is proportional to $\lambda^{-0.7}$. One adjustable parameter μ defines the ratio of the total effective extinction experienced by intermediate/old (> 10 Myr) to young (< 10 Myr) populations.

It is known, from the works of the SINGS team, that the combination of $H\alpha$ and $24\mu\text{m}$ accounts for both the unobscured and obscured current SF for star-forming regions in galaxies (Calzetti et al. 2007; Kennicutt et al. 2007). We adopt the relationship between extinction-corrected $H\alpha$, observed $H\alpha$ and $24\mu\text{m}$ calibrated for the HII regions in the 33 SINGS galaxies (Eq. 5 in Calzetti et al. 2007) to obtain the

H α extinction, and then use the Charlot and Fall (2000) extinction curve to derive the approximate A_V of the young stellar populations from the following equation

$$A_V = 2.825 \log \left[1 + 0.031 \frac{L_{24\mu m}}{L_{H\alpha}} \right] \quad (\text{A.1})$$

where $L_{24\mu m}$ is the dust-only 24 μm monochromatic luminosity and $L_{H\alpha}$ is the observed H α luminosity.

Therefore, we first restrict the variations of the three SSPs to their corresponding age ranges mentioned above in order to model the SEDs of various star-forming regions across the merging disks in the Antennae galaxies. Then we try to find the best-fit composite models with the χ^2 minimization technique

$$\chi^2 = \sum_{i=\text{FUV}}^{K_s} \left(\frac{F_{obs,i} - aF_{mod,i}}{\sigma(F_{obs,i})} \right)^2 \quad (\text{A.2})$$

by minimizing Eq. A.2. In this way, we obtain the four best-fit parameters, namely, the mass of the old (M_o), intermediate (M_i), and young (M_y) populations, the extinction ratio (μ) of intermediate/old to young populations. It should be stressed here that we first fix the extinction A_V with Eq. A.1 prior to SED modeling, which affects mostly the young stellar populations. This makes our stellar population analysis presented in this paper much less affected by the degeneracy between stellar population and extinction.

A.4.2 Results of SED-Fitting

A.4.2.1 Best-Fit Parameters

Our main fitting results are summarized in Table A.2. One should keep in mind that we are actually comparing relatively clustered younger stellar populations with relatively extended older populations. Hence, the absolute values for the mass ratios between different populations should be sensitive to the size of photometric apertures and the average density of the underlying stellar populations. On that account, we mainly focus on the relative changes of the mass ratios between different populations across the system.

We notice that the SED-fitting quality for some *overlap* regions (i.e., regions 8, 9), is not as good as for most other regions (Fig. A.2). The possible reason can be either the significant starlight contamination by nearby bright regions or the very faint nature (low S/N ratio) of these two regions at short wavebands. To check the significance of the starlight contamination by nearby bright regions, we also present the broadband SEDs for the four optically faint regions in the *overlap* region in Fig. A.3. It can be seen that the contamination by nearby bright regions does not change the overall

Table A.2 SED-fitting results

Reg.	χ_r^2	μ	M_i/M_\odot	M_y/M_\odot	M_y/M_i	$\frac{M_y/Ag_{e,y}}{M_i/Ag_{e,i}}$	$\frac{M_y/Ag_{e,y}}{M_\odot/Ag_{e,\odot}}$	log[Total Abs.](erg/s)
NGC4039 arms								
1	1.1	0.1	0.003	7.0e-4	0.23	2.6	0.5	41.71
Southern nucleus								
2	2.2	0.9	0.03	6.0e-4	0.02	3.8	1.7	42.72
Overlap regions								
3	2.5	0.6	0.03	0.003	0.1	6.3	20.2	43.09
4	2.7	0.3	0.01	0.007	0.7	10.4	11.3	43.21
5	4.3	0.4	0.002	0.001	0.5	7.5	12.6	42.67
6	2.3	0.8	0.008	0.002	0.2	3.7	29.0	42.82
7	4.5	1.0	0.007	0.002	0.3	8.0	9.6	42.53
8	4.2	1.0	0.004	7.0e-4	0.2	11.1	6.1	42.61
9	5.9	0.8	<1.0e-4	4.0e-4	>4.0	>40.0	3.0	42.46
Eastern regions								
10	3.0	0.9	0.01	5.0e-4	0.03	1.5	5.3	42.55
11	1.8	1.0	0.05	5.0e-4	0.01	0.2	2.1	42.46
12	1.9	0.9	0.05	4.0e-4	0.008	0.4	5.0	42.55
13	2.8	1.0	0.01	7.0e-4	0.07	1.3	3.4	42.60
14	2.1	0.3	0.01	6.0e-4	0.06	2.0	8.7	42.28
15	0.9	0.5	0.04	5.0e-4	0.01	1.3	4.3	42.36
Northern regions								
16	1.3	0.1	0.07	6.0e-4	0.008	1.5	1.7	41.57
17	1.5	0.2	0.1	6.0e-4	0.005	1.1	1.7	41.82
18	1.1	0.2	0.04	3.0e-4	0.007	0.7	4.3	41.91
19	1.0	0.3	0.05	3.0e-4	0.006	0.6	3.7	41.89
20	1.1	0.2	0.07	4.0e-4	0.006	0.6	3.4	41.62
21	1.2	0.1	0.04	4.0e-4	0.009	0.9	5.8	41.78
22	2.2	0.1	0.06	0.001	0.02	1.7	2.8	41.92
Western-loop regions								
23	0.5	0.5	0.03	6.0e-4	0.02	0.3	4.4	42.42
24	2.3	0.7	0.09	4.0e-4	0.004	0.7	2.9	42.09
25	3.1	0.8	0.03	8.0e-4	0.02	0.8	11.6	42.46
26	1.9	0.7	0.2	0.007	0.04	0.5	50.0	42.72
27	3.1	1.0	0.2	0.006	0.03	0.4	29.6	42.72
28	3.8	1.0	0.2	0.002	0.01	1.3	17.4	42.30
29	3.1	1.0	0.2	0.003	0.02	1.8	3.0	42.26
30	3.0	1.0	0.1	0.002	0.02	0.6	3.2	42.43
31	2.5	0.7	0.03	7.0e-4	0.02	1.2	7.4	42.50
32	2.6	0.1	0.02	0.002	0.1	8.0	1.5	42.05

(continued)

Table A.2 (continued)

Reg.	χ_r^2	μ	M_i/M_o	M_y/M_o	M_y/M_i	$\frac{M_y/Ag_{e_y}}{M_i/Ag_{e_i}}$	$\frac{M_y/Ag_{e_y}}{M_o/Ag_{e_o}}$	log[Total Abs.](erg/s)
Circumnuclear regions of NGC4038								
33	1.1	0.8	0.03	4.0e-4	0.01	0.3	1.3	42.90
Northern nucleus								
34	1.4	0.6	0.01	7.0e-4	0.05	1.5	1.4	43.03

χ_r^2 is the reduced minimum χ^2 value. μ is the extinction ratio of intermediate/old to young populations. M_y , M_i and M_o represent the mass of young, intermediate and old populations, respectively. $\frac{M_y/Ag_{e_y}}{M_i/Ag_{e_i}}$ and $\frac{M_y/Ag_{e_y}}{M_o/Ag_{e_o}}$ represent the corresponding age-averaged mass fraction ratios. The total starlight absorption obtained from the models is listed in the last column

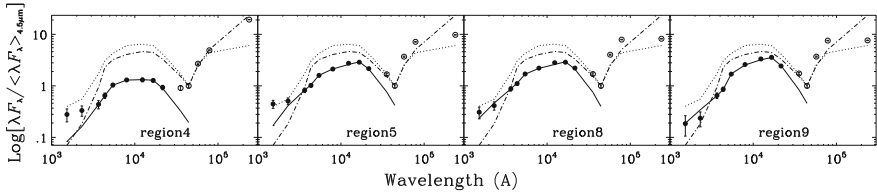


Fig. A.3 Display of FUV-24 μm broadband SEDs (extracted from the images with their *original resolutions*) of four *overlap* star-forming regions, which may have significant starlight contamination by nearby bright regions at short wavebands. Lines and symbols are the same as in Fig. A.2, except that FUV/NUV data are not used in the SED-fittings. It can be seen that the overall shapes of the SEDs do not change as compared with the SEDs extracted from the smoothed images (Fig. A.2). The figure is adapted from Zhang et al. (2010)

SEDs shape for these regions. In fact, when we fit the SEDs (excluding the FUV/NUV data) extracted from the images at their original resolutions for these regions, our main conclusions for the *overlap* regions do not change. Table A.3 lists the fitting results for the *overlap* regions using SEDs extracted from the images at their original resolutions. According to our best-fitting results for these regions, the best-fit ages of intermediate populations $\lesssim 100$ Myr, and the best-fitting ages of old stellar population ≥ 3 Gyr.

For the mass ratios of intermediate to old populations M_i/M_o , the *overlap* regions have overall smaller values compared to other regions, suggesting the *overlap* star-forming regions are very young. The northern edge of the *overlap* regions, i.e., region 9, for example, has the lowest M_i/M_o , whereas the *western-loop* regions of NGC 4038 have overall the largest M_i/M_o across the whole system, and they are the brightest regions in the UV. The *western-loop* regions host most of the intermediate populations. The ratios of most other regions across the whole system fall in between the *overlap* and *western-loop* regions.

For the mass ratios of young to old populations M_y/M_o , the *overlap* regions and some *western-loop* regions have M_y/M_o larger than all the other regions. A similar contrast could also be seen from the age-averaged mass fraction ratios of young to old populations ($\frac{M_y/Ag_{e_y}}{M_o/Ag_{e_o}}$). The *overlap* and *western-loop* regions host most of the

Table A.3 Fitting results for the SEDs (without FUV/NUV) extracted from the images at their original resolutions. Only results for some of the *overlap* regions that may have significant mutual light contamination are listed

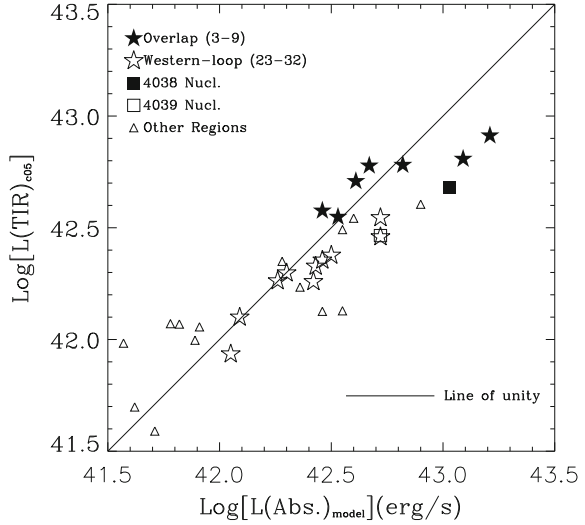
Overlap regions								
Reg.	χ_r^2	μ	M_i/M_o	M_y/M_o	M_y/M_i	$\frac{M_y/Agc_y}{M_i/Agc_i}$	$\frac{M_y/Agc_y}{M_o/Agc_o}$	log[Total Abs.] (erg/s)
3	1.0	0.5	0.04	0.01	0.3	5.0	40.0	42.97
4	0.3	0.3	0.01	0.05	4.5	9.4	100.1	43.50
5	0.7	0.8	0.004	0.005	1.3	4.7	13.5	43.11
6	1.9	1.0	0.05	0.01	0.2	1.5	73.0	42.94
7	1.8	0.3	0.02	0.004	0.2	2.9	42.5	42.54
8	0.9	1.0	0.04	0.002	0.05	0.6	8.8	42.82
9	1.0	0.7	0.002	0.001	0.5	5.0	4.2	42.52

young populations, and they are the most intense current star-forming sites across the whole system.

For the mass ratios of young to intermediate populations M_y/M_i , the *overlap* regions hold the largest values, while the *northern* regions have overall small M_y/M_i , conforming with their weak *current* SF activities. We also point out here one interesting finding. That is, across the *overlap* regions, the northwestern edge, namely region 9, and the southeastern edge, region 4, have M_y/M_i ratios significantly larger than the central regions, e.g., region 6. We note that the trend still exists after we normalize the mass fraction ratios with their corresponding best-fit ages ($\frac{M_y/Agc_y}{M_i/Agc_i}$).

In the last column of Table A.2, we also list the corresponding total starlight absorbed by dust, which should be equal to the total infrared (TIR) dust emission. Calzetti et al. (2005) exploited a relationship between $24\mu\text{m}/\text{TIR}$ and $8/24\mu\text{m}$ for the star-forming regions in NGC 5194. Considering the similar global properties between the Antennae and NGC 5194, such as similar PAH abundances (the PAH index ~ 4.5 according to Draine and Li (2007) dust emission models), comparable TIR (Sanders et al. 2003) and total molecular gas surface density (Wilson et al. 2003), we compare the total starlight absorption from our models with the TIR estimated from dust-only 8 and $24\mu\text{m}$ using the relation (Eq. 1 in Calzetti et al. 2005) exploited for the star-forming regions of NGC 5194. The comparison is shown in Fig. A.4. Obviously, almost all of our selected star-forming regions in Arp 244 generally follow the same relation derived in the star-forming regions of NGC 5194. Considering the general consistency, in the following sections, we take the total starlight absorption from our SED-fitting models as the best estimate of TIR for our selected star-forming regions.

Fig. A.4 Total starlight absorption obtained from the SED-fitting models is compared with total infrared luminosity estimated from dust-only 24 and 8 μm using the relation calibrated in NGC 5194 by Calzetti et al. (2005) (hereafter TIR_{c05}). The line with slope of unity and null intercept is also plotted (solid line). The figure is adapted from Zhang et al. (2010)

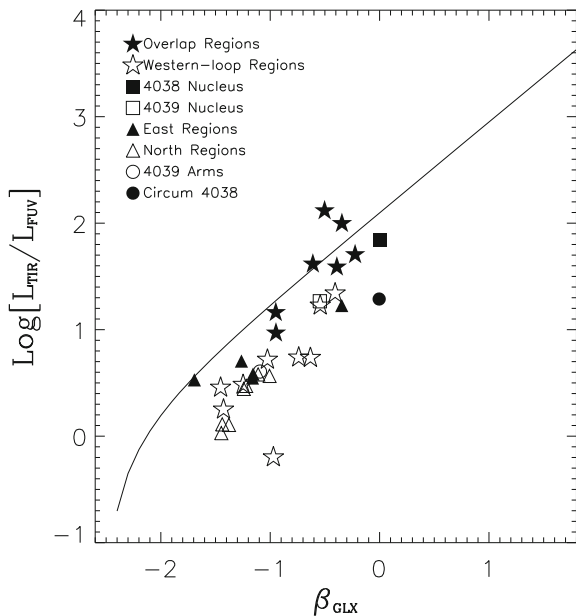


A.4.2.2 Star-Forming Regions of Arp 244 on the IRX-UV Plane

Kong et al. (2004) found that while the dust extinction is the main factor driving the strong correlation between $L_{\text{TIR}}/L_{\text{FUV}}$ (hereafter IRX) and UV spectral slope, it is the SF history that affects the degree of deviation of a star-forming galaxy from the locus of starbursts in the IRX-UV color indices’ plane. It is surely meaningful to plot these indices for the star-forming regions of the Antennae on the IRX-UV color plane. Figure A.5 shows the ratio of $L_{\text{TIR}}/L_{\text{FUV}}$, where TIR is set to be equal to the total starlight absorption obtained from our models, as a function of β_{GLX} ($\beta_{\text{GLX}} = \frac{\log F_{\text{FUV}} - \log F_{\text{NUV}}}{\log \lambda_{\text{FUV}} - \log \lambda_{\text{NUV}}}$, see Kong et al. 2004). The solid line represents the tight correlation for starburst galaxies (Kong et al. 2004). Obviously, except the *overlap* regions, almost all the star-forming regions in Arp 244 lie below the locus followed by starbursts. The three regions that lie above the starburst locus are regions 4, 5, and 9. Hence, it can be stated here that except for some localized starburst sites, mainly in the *overlap* regions, most regions across the whole system are forming stars at a level weaker than that of the starbursts. This is also consistent with our further analysis of SF histories.

Figure A.6 plots the ratios of $L(H\alpha_{\text{corr}})/L(Ks)$ versus $L_{\lambda}(U)/L_{\lambda}(B)$. Star-forming regions in NGC 5194 selected (mainly as 24 μm peaks) by Calzetti et al. (2005) are shown as small *pluses*. Also plotted is the archetypical starburst galaxy NGC 7714 as a whole (*large cross*). The modest total SF rate (SFR, $\sim 3.4 M_{\odot} \text{yr}^{-1}$) and SF intensity ($\sim 0.015 M_{\odot} \text{yr}^{-1} \text{Kpc}^{-2}$) of NGC 5194 place it among the quiescently star-forming galaxies, although it hosts a LINER-type nucleus. Calzetti et al. (2005) found that the star-forming regions in NGC 5194 have properties quite similar to that of normal star-forming galaxies, rather than that of starbursts. Assuming $L_{\lambda}(U)/L_{\lambda}(B)$ and $L(H\alpha_{\text{corr}})/L(Ks)$ roughly represent the ratios of recent-to-past and current-to-past

Fig. A.5 Ratio of TIR (set to total starlight absorption from models) to FUV luminosity as a function of equivalent ultraviolet spectral slope (the IRX-UV diagram). Data for different star-forming regions within the Antennae are plotted with different symbols. The *solid line* represents the mean IRX-UV relation for 50 starburst galaxies fitted by Kong et al. (2004). The figure is adapted from Zhang et al. (2010)



SF strengths, respectively, Fig. A.6 reveals similar results as that of the IRX-UV diagram. Namely, almost all the star-forming regions of Arp 244 have current SF strength comparable with star-forming regions in quiescently star-forming galaxies (low $L(H\alpha_{corr})/L(Ks)$), except for some of the *overlap* and *western-loop* regions.

A.4.2.3 Emission Excess at IRAC 3.6 and 4.5 μm

Since we have done relatively sophisticated SED-fitting for these star-forming regions, we could estimate the hot dust emission at IRAC 3.6 and 4.5 μm which are often assumed to be dominated by stellar photospheric emission in the literature. With the average of 3.6 and 4.5 μm fluxes as the underlying stellar continuum level, Wang et al. (2004) concluded that most of the emission (>90%) in these two bands comes from direct stellar contribution for the whole system. From our stellar SED-fitting, we can easily see (Figs. A.2 and A.3) the prominent emission excess at 3.6 μm (~10–65%) and 4.5 μm (~10–80%) for most of these star-forming regions relative to the stellar (plus nebular continuum) emission, especially for the *overlap* regions. The significant emission excess at 3.6 and 4.5 μm brings out the caution needed in using them as a representation for the underlying stellar mass, particularly when studying active star-forming regions. Since we have largely accounted for hydrogen/helium recombination emission in our SED-fitting, according to the existing spectra in these two bands for compact HII regions (e.g., Martin-Hernandez et al.

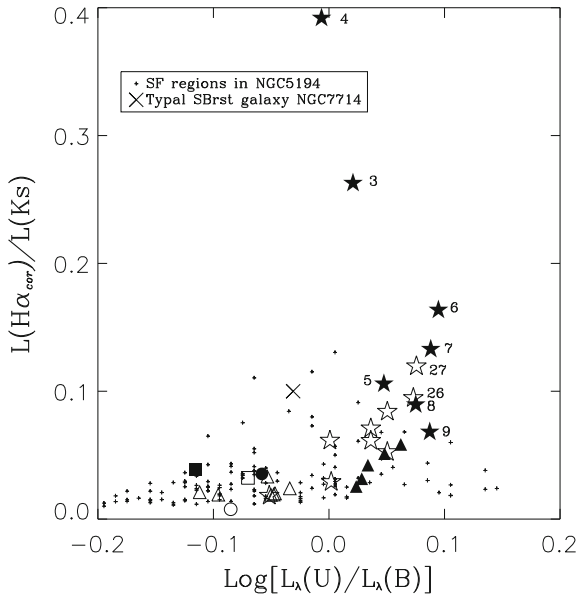


Fig. A.6 Ratio of extinction-corrected (using $24\ \mu\text{m}$) $L(H\alpha_{\text{corr}})$ to $L(Ks)$ versus $\log[L_{\lambda}(U)/L_{\lambda}(B)]$. The symbols are as Fig. A.5. The star-forming regions selected by Calzetti et al. (2005) in the quiescently star-forming galaxy NGC 5194 are shown by small *pluses*. The archetypal starburst galaxy NGC 7714 as a whole is represented by *large cross*. Obviously, just like the majority of star-forming regions in NGC 5194, most regions (except some of the *overlap* and *western-loop* regions) in Arp 244 host a significant fraction of older stellar populations and have relatively lower current SF strength compared to typical starbursts. See the text for further explanation. The figure is adapted from Zhang et al. (2010)

2000; Peeters et al. 2002), the other possible main mechanisms of the emission excess could be vibrationally excited molecular hydrogen emission, atomic fine-structure lines, or very small hot dust (e.g., $3.3\ \mu\text{m}$ PAH feature) emission.

For region 4, the MIR “*hotspot*”, the excess emission components contribute ≥ 65 and 80% ⁷ of the total emission at 3.6 and $4.5\ \mu\text{m}$ respectively. As is already pointed out by Wang et al. (2004), the extremely high obscuration of region 4 must be responsible for the large excess to some extent. The high-quality MIR spectrum of this region obtained with IRS on board *Spitzer* is characterized by prominent PAHs and very hot VSGs emission (Brandl et al. 2009). Given the prominent PAH feature emission of region 4, the exceptionally low excess emission flux ratio of $3.6/4.5\ \mu\text{m}$ (~ 0.9) can not be accounted for by the pure dust emission models of Draine and Li (2007). Furthermore, the *K*-band spectra (Gilbert et al. 2000) in the observations of the compact star clusters coincident with the MIR “*hotspot*” are characterized by prominent nebular and fluorescent H_2 emission with slightly rising continuum toward the red (due to hot dust emission). The fact that region 4 has a very

⁷Considering the hot dust emission contribution to *Ks* band, our estimation should be lower limits.

flat radio spectrum (Neff and Ulvestad 2000) and prominent PAH feature emission excludes the shock origin of the possible molecular/atomic emission. Thus, the fine-structure lines from heavy elements, the molecular lines from FUV fluorescence in dense photodissociation regions (PDRs), and hot dust (including PAHs) emission may all have significant contribution to the emission excess at IRAC 3.6 and 4.5 μm .

Interestingly, the total 4.5 μm flux of region 4 is even $\sim 20\%$ higher than that of the southern nucleus and nearly equal to that of northern nucleus. In short, the excess emission (either from hot dust or molecule/ionized atoms) at IRAC 4.5 μm bands have a nonnegligible ($> 18\%$ ⁸) contribution to the total flux for the whole system.

A.5 Discussion

A.5.1 Star Formation Histories Across the Whole System

Since we have the mass ratios between the three stellar populations for these star-forming regions, using the best-fit ages of the three populations for each region, we could easily derive the ratios between the age-averaged SFR for the three (i.e., current, recent, and past) SF epoches related to our three populations (Tables A.2 and A.3). We find that except for some of the *overlap* regions and the *western-loop* regions of NGC 4038, which have the ratios of *current-to-past* age-averaged SFR (defined approximately as $\frac{M_y/\text{Age}_y}{M_o/\text{Age}_o} \gtrsim 10$), almost all the other star-forming regions have the ratios $\gtrsim 1$. Specifically, the regions that have the ratios $\gtrsim 10$ are 3, 4, 5, 6, 25, 26, 27, and 28. Hence, it can be said that some of the *overlap* and *western-loop* regions are experiencing bursts of SF, whereas most of the other regions are forming stars at a moderate level comparable with normal star-forming galaxies. The location of these star-forming regions on the IRX-UV plane (Fig. A.5) is also consistent with the fact that most of the regions are at a modest SF intensity. For the ratios of *current-to-recent* age-averaged SFR (defined as $\frac{M_y/\text{Age}_y}{M_i/\text{Age}_i}$) (see Table A.2), the *overlap* regions have the ratios $\gtrsim 3$, whereas almost all the other regions have the ratios ~ 1 . The high $\frac{M_y/\text{Age}_y}{M_i/\text{Age}_i}$ for the two nuclei may be attributed to their surrounding star-forming regions. Hence, comparing with the *overlap* regions, the SF of most regions across the whole system is not only modest (except the *western-loop* regions) but also continuous during the recent tens of million years (typical best-fit ages of the intermediate stellar populations for these regions). Namely, while both the *overlap* regions, and the *western-loop* regions are the most intense *current* star-forming sites across the whole system, the *overlap* regions are now experiencing much more violent enhancement of SF compared to all the other regions.

⁸This is obtained by the sum of flux of excess emission for all the star-forming regions selected in this work divided by the total flux for the whole system. So here our estimation is a lower limit for the whole system.

In fact, the SF histories for these star-forming regions could also be simply probed through the ratios of $L_\lambda(U)/L_\lambda(B)$ and $L(H\alpha_{corr})/L(Ks)$, which roughly represent ratios of the recent-to-past star formation strength and the current-to-past SF strength, respectively. Figure A.6 clearly shows that except for the *overlap* and *western-loop* regions, most regions are forming stars at moderate level (low $L(H\alpha_{corr})/L(Ks)$) comparable with star-forming regions in quiescently star-forming galaxies. And meanwhile, these regions host a remarkable fraction of aging stellar populations (small $L_\lambda(U)/L_\lambda(B)$), just like the star-forming regions in NGC 5194. The overall larger ratios $L_\lambda(U)/L_\lambda(B)$ for the *overlap*, the *western-loop*, and the *eastern* (to a lesser extent) regions compared with the star-forming regions in quiescently star-forming galaxies indicate that these regions may have just experienced a period of intense starburst in the recent few hundred million years. It is also notable of the much higher ratios of current-to-past SF strength for some of the *overlap* and *western-loop* regions. Wang et al. (2004) also got similar results from the flux ratio of the dust-only IRAC 8 μm and the underlying stellar continuum.

A.5.2 *The 20 cm-to-CO Ratio Map as Star Formation Efficiency Map*

Taking advantage of the tight correlation between FIR and radio continuum (Condon 1992; Yun et al. 2001; Bell 2003), which appears to be valid at least on kiloparsec scales in galaxies (Lu et al. 1996), Gao et al. (2001) constructed a SF efficiency map using the 20 cm-to-CO ratio. Overall, our results of population analysis are consistent with their SF efficiency map, viz, except some localized starburst sites mainly in the *overlap* and *western-loop* regions, most regions across the whole system are forming stars at a quite moderate level comparable with normal star-forming galaxies. This verifies the practice of using radio continuum as an indicator of the SF and the radio-to-CO ratio maps as a representation of SF efficiency maps in most cases.

Nevertheless, some exceptions do exist, like for some overlap regions of galaxy pairs in a high-speed collision. For instance, in the Taffy galaxy a large portion of the synchrotron radio emission may be related to gas collision shocks, rather than supernovae remnants (SNRs, most likely related to recent SF) shocks (Gao et al. 2003; Zhu et al. 2007). In the *overlap* regions of the Antennae, Gao et al. (2001) found that the radio-to-CO ratios progressively increase from the southeastern side to the northwestern edge across the *overlap* regions. However, we note that the lower radio-to-CO ratio of the southeastern region (4) compared to other *overlap* regions may be, rather than due to lower SF efficiency, assigned to other various causes. First, the very flat radio continuum suggests that the 20 cm continuum in region 4, rather than being dominated by synchrotron emission from (maybe) SNRs shocks like other *overlap* regions, is primarily thermal free-free emission from young, compact H II regions. This means that in such violent overlap starburst environment, large numbers of supernovae events associated with current SF epoch have not happened. Second,

studies on the local IR/radio correlation within nearby galaxies (e.g., Hughes et al. 2006; Murphy et al. 2006) demonstrate the weak trend of increasing IR/radio ratio with increasing IR luminosity within an individual galaxy. Both our TIR estimates (equal to the total starlight absorption) and recent IR estimate based on the 15 and 30 μm continuum fluxes (Brandl et al. 2009) suggest that region 4 has the largest IR luminosity across the whole system. Finally, the very hot dust emission, as we have shown above, for the southeastern side (i.e., region 4) implies that most energy there may emit in the MIR regime, which again is different from most of the other regions. Therefore, unlike the usually continuous SF in a relatively long timespan ($\geq 10^8$ yr), in violent galaxies interaction regions, both strong shocks as a result of cloud–cloud collisions and strong variations of SFR over short timescales (tens of Myr) may all make the 20 cm-to-CO ratio fails to be an efficient SF efficiency indicator.

A.5.3 *Sequential Star Formation Paths in the Overlap Regions*

Across the *overlap* regions (Tables A.2 and A.3), the northwestern edge and the southeastern edge have both higher mass ratios of young to intermediate populations M_y/M_i (i.e. regions 9 and 4) and higher correspondingly age-averaged SFR ratios $\frac{M_y/\text{Age}_y}{M_i/\text{Age}_i}$ than do the central regions (e.g., regions 6). We like to interpret the trends as two sequential SF paths. One is from the central regions (i.e., regions 6) to the *southern* edge (e.g., region 4), and the other is from the central to the *northwestern* edge (e.g., region 9).

To check if there are any trends in the spatial distributions of the star clusters across the *overlap* regions, we refer to the cluster distribution maps derived by Zhang et al. (2001). We find a slightly proportionally deficit of clusters with ages of tens of Myr for both the northwestern (corresponding to our region 9) and the southern edges compared to the central regions (e.g. region 6). Recently, Mengel et al. (2005) also obtained the spatial distributions for clusters with Br γ -determined and CO-index-determined ages. Interestingly, the distributions also show the relative deficit of intermediate-age (~ 10 Myr) clusters for both the northwestern and southern edges, although the sample size and the probed age range are all small compared to that of Zhang et al. (2001). The cluster distributions are in agreement with the sequential SF paths mentioned above, i.e., both the *northwestern* and *southern* regions are just beginning their recent SF episode.

Jog and Solomon (1992) proposed a physical mechanism to explain the origin of the enhanced SF occurring in situ in the overlapping regions of a pair of colliding galaxies like the Antennae. In their model, following a collision between galaxies, the HI cloud–cloud collisions from the two galaxies lead to the formation of hot, ionized, high-pressure remnant gas that compresses the outer layers of preexisting GMCs in the overlapping regions. This makes the GMCs’ shells become gravitationally unstable, which triggers a starburst in the initially barely stable GMCs. Although

generally H I cloud–cloud collisions should be more efficient than that of the GMCs due to the much smaller mean free path of an H I cloud than a GMC, the huge concentration of molecular gas in the *overlap* regions of Arp 244 (Wilson et al. 2000; Gao et al. 2001) may make GMC collisions also possible.

Based upon this model, across the *overlap* regions of Arp 244, the sequential SF paths we have found can be explained naturally. As the two colliding disks begin to interpenetrate each other, the regions that overlap first, e.g., region 6, may have more layers of gravitationally unstable GMCs form first, leading to in situ starburst there first. As the colliding/merging proceeds and the overlapping zone between the two colliding disks bulks up, cloud collisions from the two colliding disks spread to more and more regions, i.e., both the northwest (e.g., to regions 8, 9) and southeast (e.g., to regions 5, 4) of the *overlap* regions. This leads to progressively lagging starbursts triggered by radiative shock compressions toward both the northwest and southeast directions of the *overlap* regions. In short, the identified sequential SF paths could be imprints of the interpenetrating process of the two colliding galaxy disks.

Both kinematic analysis (Hibbard et al. 2001) and numerical simulations (Toomre and Toomre 1972; Barnes 1988) suggest that the two galaxies of the Antennae system began their first close encounter several hundred million years ago, and the two colliding galaxies may have passed their first close encounter (Mihos et al. 1993). The first peak of large-scale starburst phase may have just passed in the Antennae (Mihos and Hernquist 1996), evidenced by the moderate SF strengths shown in Figs. A.5 and A.6, consistent with the SF efficiency map across the whole system (Gao et al. 2001). While the moderate, continuous (recent) SF for most regions is consistent with this scenario, the currently violent enhancement of SF and the sequential SF paths for the *overlap* regions may suggest that now the two colliding galaxies are just launching their second close encounter.

After analyzing $H_2 \nu = 0 - 0 S(3) \lambda = 9.66 \mu\text{m}$ line emission obtained by ISOCAM CVF, Haas et al. (2005) found that both the southwestern and northwestern edges of the *overlap* regions, which are very close to the star-forming region 5 and region 9, respectively, have exceptionally high $L(H_2)/L(FIR)$ ratios that exceed that of all other known galaxies. But the absolute current/recent SF there (especially the northwestern edge) are very weak, just as we find from population analysis (see Tables A.2 and A.3). They suggest that the high H_2 emission there should be excited by pre-starburst shocks that are caused by cloud–cloud collisions. The low mass fractions of intermediate populations and the very high (age-averaged) mass ratios of young to intermediate populations for the two edges, especially the northwestern edge, indicate there indeed are very young star-forming sites, which are most probably triggered by pre-starburst shocks following the second close encounter between the two galaxies. However, recent high-quality observations from *Spitzer* (Brandl et al. 2009) detected about five times less integrated $H_2 S(3)$ line flux than does ISOCAM CVF, and did not find the previously claimed strong H_2 emission peak in the northern *overlap* zone. These new observations cast doubt on the pre-starburst shock origin of the H_2 emission in the *overlap* regions.

A.6 Summary

To summarize, taking advantage of the availability of multiwavelength imagery from FUV to $24\ \mu\text{m}$ from *GALEX*, *HST*, *2MASS* and *Spitzer* in both high resolution and high sensitivity:

- We compare the broadband SEDs of star-forming regions selected as $24\ \mu\text{m}$ peaks across the whole merging disks of the Antennae galaxies, which provides us a basis to comprehend the complete picture of SF histories. The large ratios of $24/8\ \mu\text{m}$ for the *overlap* regions and the blue, strong UV emission for the *western-loop* regions demonstrate that currently they are the most intense star-forming sites, although the *western-loop* regions are at a relatively later SF stage compared to the *overlap* regions. Most of the other regions, which have redder *UB* color, weaker IR dust emission and UV emission, across the whole system are forming stars at a quite moderate level during the past ~ 100 Myr.
- We roughly constrain the SF histories of these active star-forming regions across the whole system, with the degeneracy between stellar population and extinction broken, by including $24\ \mu\text{m}$ dust emission into population analysis. Compared with other regions, the *overlap* regions are now experiencing much more violent enhancement of SF, although both the *overlap* and the *western-loop* regions are the most intense *current* star-forming sites across the whole system. Our analysis is in general agreement with the findings of Gao et al. (2001), i.e., except for some localized violent starbursts confined mainly in the *overlap* regions and the *western-loop* regions of NGC 4038, the bulk of SF is at a moderate level comparable to that of star-forming regions in quiescently star-forming galaxies.
- We suggest two sequential SF paths across the famous *overlap* regions, which may reflect the (second) interpenetrating process of the second passage between the two colliding galaxy disks. We also suggest that the recent SF of both the northern and southern edges of the *overlap* zone might be just triggered by pre-starburst shocks.
- We report the nonnegligible ($>18\%$) excess emission contribution to the total IRAC $4.5\ \mu\text{m}$ for the whole system. The well-known brightest MIR “hotspot” in the *overlap* regions has total $4.5\ \mu\text{m}$ emission ($\geq 80\%$ excess emission) even higher (by $\sim 20\%$) than that of the nuclear region of NGC 4039 and nearly equals that of the nuclear region of northern galaxy NGC 4038. The unusually low ratio of $3.6/4.5\ \mu\text{m}$ implies that in addition to hot dust emission, other emission mechanisms, such as atomic fine-structure lines and vibrationally excited molecular hydrogen lines from dense PDRs, have a significant contribution to IRAC $4.5\ \mu\text{m}$.

References

- Alonso-Herrero A, Rieke GH, Rieke MJ, Colina L, Perez-Gonzalez PG, Ryder SD (2006) ApJ 650:835
- Anders P, Fritze-v. Alvensleben U (2003) A&A 401:1063

- Barnes JE (1988) *ApJ* 331:699
- Bastian N, Emsellem E, Kissler-Patig M, Maraston C (2006) *A&A* 445:471
- Bastian N, Trancho G, Konstantopoulos LS, Miller BW (2009) Preprint (astro-ph/09062210)
- Bell EF (2003) *ApJ* 586:794
- Brandl BR, Sniijders L, den Brok M et al (2009) Preprint (astro-ph/09051058)
- Calzetti D, Kinney AL, Storchi-Bergmann T (1994) *ApJ* 429:582
- Calzetti D, Kennicutt RC, Bianchi L et al (2005) *ApJ* 633:871
- Calzetti D, Kennicutt RC, Engelbracht CW et al (2007) *ApJ* 666:870
- Cardelli JA, Clayton GC, Mathis JS (1989) *ApJ* 345:245
- Charlot S, Fall SM (2000) *ApJ* 539:718
- Condon JJ (1992) *ARA&A* 30:575
- Conselice CJ, Bershadsky MA, Dickinson M, Papovich C (2003a) *AJ* 126:1183
- Conselice CJ, Chapman SC, Windhorst RA (2003b) *ApJ* 596:L5
- Conselice CJ, Yang C, Bluck AFL (2009) *MNRAS* 394:1956
- de Ravel L, Le Fevre O, Tresse L et al (2008) *A&A* 498:379
- Draine BT, Li A (2007) *ApJ* 657:810
- Elbaz DM, Cesarsky CJ (2003) *Science* 300:270
- Fabbiano G, Zezas A, Murray SS (2001) *ApJ* 554:1035
- Fabbiano G, Krauss M, Zezas A, Rots A, Neff S (2003) *ApJ* 598:272
- Fabbiano G, Baldi A, King AR, Ponman TJ, Raymond J, Read A, Rots A, Schweizer F, Zezas A (2004) *ApJ* 605:21
- Fall SM, Chandar R, Whitmore BC (2005) *ApJ* 631:133
- Fazio GG, Hora JL, Allen LE et al (2004) *ApJS* 154:10
- Gao Y (2008) *Nature* 452:417
- Gao Y, Lo KY, Lee S-W, Lee T-H (2001) *ApJ* 548:172
- Gao Y, Zhu M, Seaquist ER (2003) *AJ* 126:2171
- Gavazzi G, Bonfanti C, Sanvito G, Boselli A, Scodreggio M (2002) *ApJ* 576:135
- Goodwin SP, Bastian N (2006) *MNRAS* 373:752
- Gordon KD, Engelbracht CW, Rieke GH, Misselt KA, Smith J-DT, Jr Kennicutt RC (2008) *ApJ* 682:336
- Gilbert AM, Graham JR (2007) *ApJ* 668:168
- Gilbert AM, Graham JR, McLean IS et al (2000) *ApJ* 533:57
- Gil de Paz A, Boissier S, Madore BF et al (2007) *ApJS* 173:185
- Haas M, Chini R, Klaas U (2005) *A&A* 17:L20
- Hibbard JE, van der Hulst JM, Barnes JE, Rich RM (2001) *AJ* 122:2969
- Hibbard JE, Bianchi L, Thilker DA et al (2005) *ApJ* 619:L87
- Holtzman J et al (1995) *PASP* 107:1065
- Hummel E, van der Hulst JH (1986) *A&A* 155:151
- Hughes A, Wong T, Ekers R, Staveley-Smith L, Filipovic M, Maddison S, Fukui Y, Mizuno N (2006) *MNRAS* 370:363
- Jog CJ, Solomon PM (1992) *ApJ* 387:152
- Kartaltepe JS, Sanders DB, Scoville NZ et al (2007) *ApJS* 172:320
- Knapen JH (1998) *MNRAS* 297:255
- Kennicutt RC, Calzetti D Jr, Walter F et al (2007) *ApJ* 671:333
- Kong X, Zhou X, Chen JS et al (2000) *AJ* 119:2745
- Kong X, Charlot S, Brinchmann J, Fall SM (2004) *MNRAS* 349:769
- Kinney AL, Bohlin RC, Calzetti D, Panagia N, Wyse RFG (1993) *ApJS* 86:5
- Kroupa P (2002) In: Grebel EK, Brandner W (eds) *ASP conference series. Modes of star formation and the origin of field populations*, vol 285. ASP, San Francisco, p 86
- Le Fevre O, Abraham R, Lilly SJ et al (2000) *MNRAS* 311:565
- Lin L, Patton DR, Koo DC et al (2008) *ApJ* 681:232
- Lu NY, Helou G, Tuffs R, Xu C, Malhotra S, Werner MW, Thronson H (1996) *A&A* 315:L153
- Martin-Hernandez NL, Peeters E, Damour F et al (2000) *ESASP* 456:135

- Mirabel LF, Vigroux L, Charmandaris V et al (1998) *A&A* 333:L1
Mengel S, Lehnert MD, Thatte N, Tacconi-Garman LE, Genzel R (2002) *ApJ* 383:137
Mengel S, Lehnert MD, Thatte N, Genzel R (2005) *A&A* 443:41
Mihos JC, Hernquist L (1996) *ApJ* 464:641
Mihos JC, Bothun GD, Richstone DO (1993) *ApJ* 418:82
Murphy EJ, Braun R, Helou G et al (2006) *ApJ* 638:157
Nikola T, Genzel R, Herrmann F, Madden SC, Poglitsch A, Geis N, Townes CH, Stacey GJ (1998) *ApJ* 504:749
Neff SG, Ulvestad JS (2000) *AJ* 120:670
Oey MS, Parker JS, Mikles VJ, Zhang XL (2003) *AJ* 126:2317
Peeters E, Martin-Hernandez NL, Damour F et al (2002) *A&A* 381:571
Patton DR, Pritchett CJ, Carlberg RG et al (2002) *ApJ* 565:208
Read AM, Ponman TJ, Wolstencraft RD (1995) *MNRAS* 277:397
Rieke GH, Young ET, Engelbracht CW et al (2004) *ApJS* 154:25
Sanders DB, Mirabel IF (1996) *ARA&A* 34:749
Sanders DB, Mazzarella JM, Kim D-C, Surace JA, Soifer BT (2003) *ApJ* 126:1607
Saviane I, Momany Y, da Costa GS, Rich RM, Hibbard JE (2008) *ApJ* 678:179
Schweizer F, Burns CR, Madore BF et al (2008) *AJ* 136:1482
Schlegel DJ, Finkbeiner DP, Davis M (1998) *ApJ* 500:525
Schulz A, Henkel C, Muders D, Mao RQ, Rollig M, Mauersberger R (2007) *A&A* 466:467
Smith JDT, Draine BT, Dale DA et al (2007) *ApJ* 656:770
Stetson PB (1987) *PASP* 99:191
Thilker DA, Boissier S, Bianchi L et al (2007) *ApJ* 173:572
Toomre A, Toomre J (1972) *ApJ* 178:623
Vazquez GA, Leitherer C (2005) *ApJ* 621:695
Vigroux L, Mirabel F, Altieri B et al (1996) *A&A* 315:L93
Wang Z, Fazio GG, Ashby MLN et al (2004) *ApJS* 154:193
Wilson CD, Scoville N, Madden SC, Charmandaris V (2000) *ApJ* 542:120
Wilson CD, Scoville N, Madden SC, Charmandaris V (2003) *ApJ* 599:1049
Whitmore B, Schweizer F (1995) *AJ* 109:960
Whitmore BC (2004) The formation and evolution of massive young star clusters. *ASPC* 322:419
Whitmore BC, Zhang Q (2002) *AJ* 124:1418
Whitmore BC, Zhang Q, Leitherer C, Fall SM, Schweizer F, Miller BW (1999) *AJ* 118:1551
Yun MS, Reddy NA, Condon JJ (2001) *ApJ* 554:803
Zhang Q, Fall M, Whitmore BC (2001) *ApJ* 561:727
Zhang, H. -X., Gao, Y., Kong, X. (2010) *MNRAS* 401:1839
Zhu M, Gao Y, Seaquist ER (2007) *AJ* 134:118